Ground based FTIR and MAX-DOAS observations of greenhouse and trace gas emissions in the Rhine valley (Germany), St. Petersburg and Yekaterinburg (Russia)

Zur Erlangung des akademischen Grades eines

DOKTORS DER NATURWISSENSCHAFTEN (Dr. rer. nat.)

von der KIT-Fakultät für Physik des

Karlsruher Instituts für Technologie (KIT)

genehmigte

DISSERTATION

von

M.Sc. Carlos Armando Alberti Arroyo

Aus El Rosario, El Salvador, C.A.

Referent:	Prof. Dr. Johannes Orphal
Korreferent:	Prof. Dr. André Butz
Tag der mündlichen Prüfung:	04.11.2022

To Sophya, Gabriel, Mark and Areli

ABSTRACT

The anthropogenic emissions of greenhouse gases and air pollutants in the atmosphere have increased and worsened since the beginning of the industrial era, resulting in considerable impact on the environment and the atmosphere. Global warming, mainly caused by the anthropogenic emissions of CO_2 , is one of the most alarming and discussed consequences that keep the planet under threat of rising Earth temperatures above 1.5°C within the coming two decades (IPCC, 2021). Pinning down the anthropogenic emissions of GHGs emission is a pending task that requires enormous political and societal efforts, will, and immediate actions. For several years this topic has been discussed on the transnational level. The negotiations translate into international agreements, the most recent being the Paris agreement in 2016. Therefore, precise and accurate methods for monitoring and quantifying those GHGs in the atmosphere are vital. Additionally, it is crucial to study the natural sources and sinks of GHGs into the atmosphere to understand climate change better and allow for reliable projections of their future under climate change conditions. Both applications require representative measurements, as achievable by remote sensing techniques. However, measuring relatively minor changes in column-averaged GHG concentrations on top of an extensive accumulated background requires high-accuracy instrumentation and calls for continuous efforts to improve the instrumental and data processing state-of-the-art.

The work presented in this thesis encompasses the crucial topics mentioned before. In the first part, improved calibration procedures for the COllaborative Carbon Column Observing Network (COCCON) are presented. COCCON is an emerging global network of portable EM27/SUN FTIR spectrometers for deriving precise and accurate column-averaged atmospheric abundances of greenhouse gases. The original laboratory open-path lamp measurements for deriving the spectrometer's instrumental line shape (ILS) from water vapour lines have been refined and extended to the second detector channel incorporated in the EM27/SUN spectrometer for the detection of carbon monoxide (CO). The refinements encompass improved spectroscopic line lists for the relevant water lines and a revision of the laboratory pressure measurements used to analyze the spectra. Finally, a revision and extension of the COCCON network instrument-to-instrument calibration factors for XCO_2, XCO, and XCH_4 is presented, incorporating 47 new spectrometers (of 83 in total by now).

In the second part, the results of the city emission campaign carried out in St. Petersburg as a case study in Eastern Europe, aiming at empirically quantifying the CO_2, CO, and CH_4 city emissions, are presented and compared with available inventories sources. This campaign utilized two portable EM27/SUN FTIR instruments operated at daily variable locations based on St. Petersburg's forecasted wind direction. After the mobile campaign, one instrument remained in a continuous mode of operation in Peterhof (a suburb of St. Petersburg), and the other instrument was moved to Yekaterinburg in 2019 and 2020. The

v

collected measurements, during approximately one year, were analyzed, and the results are compared to all available satellite products (TROPOMI, OCO-2, GOSAT, and MUSICA IASI), showing generally good agreement with COCCON observations. As a final result, the gradients between both cities are analyzed and compared with Copernicus Atmosphere Monitoring Service (CAMS) model data. Satellite and ground-based observations at high latitudes are much sparser than at low or mid-latitudes, which makes direct coincident comparisons between remote-sensing observations more difficult, but at the same time, assigns these measurements a great scientific value.

The final chapter presents the results of the remote sensing measurements used for the study case region in the Rhine valley area. This area was selected due to the variety of the emission sources located in the surrounding: industry, urban, power, forest, and agricultural sectors. TCCON and MAX-DOAS observations were performed at KIT Campus North from 2019 to 2021 in order to investigate the ratios of column-averaged abundance ($\Delta XCO/\Delta XCO_2$ and $\Delta NO_{2,VCD}/\Delta XCO_2$) for separating the anthropogenic emissions of CO_2; the results were compared to the in-situ, and TNO high-resolution inventory data results. The $\Delta proxy/\Delta ffCO_2$ ratios found are in the range of the TNO emissions ratios corresponding to the industry sector, which is supported by the predominant wind direction, advecting air from an industrial area located in the South-West of the Campus. Several significant transport events have been detected.

PREFACE

This Ph.D. thesis reuses material already published in the following peer-review papers where the primary author is the doctoral candidate and project reports written by himself. The Doctoral candidate confirms that the results, analysis, calculations, algorithms, plots, and illustrations presented in this thesis contain solely scientific contributions made by himself with the guidance of his supervisors. Otherwise, the appropriate credits are given by proper referencing. The Introduction, Chapter 8, Chapter 9, Appendix A, Appendix B, and Conclusions contains material from Alberti et al. (2022a,b). These papers had been published by Copernicus Publications under the Creative Commons Attribution 4.0 License (see https://www.atmospheric-measurement-techniques.net/policies/, last access: 04 October 2022.). Finally, Chapter 10 uses some parts from Deliverable 2.7 of the Verify Project (Jäschke et al., 2021). However, the results presented in this thesis encompass a much larger period with new findings, plots, and conclusions that surpass those presented there. Partners authored this deliverable from the University of Heidelberg for the in-situ section and KIT for the remote sensing results. The parts included in this thesis were written by myself under the supervision of PD. Dr. Frank Hase.

LIST OF AUTHOR'S PUBLICATIONS

Alberti, C., F. Hase, M. Frey, D. Dubravica, T. Blumenstock, A. Dehn, P. Castracane, G. Surawicz, R. Harig, B. C. Baier, C. Bès, J. Bi, H. Boesch, A. Butz, Z. Cai, J. Chen, S. M. Crowell, N. M. Deutscher, D. Ene, J. E. Franklin, O. García, D. Griffith, B. Grouiez, M. Grutter, A. Hamdouni, S. Houweling, N. Humpage, N. Jacobs, S. Jeong, L. Joly, N. B. Jones, D. Jouglet, R. Kivi, R. Kleinschek, M. Lopez, D. J. Medeiros, I. Morino, N. Mostafavipak, A. Müller, H. Ohyama, P. I. Palmer, M. Pathakoti, D. F. Pollard, U. Raffalski, M. Ramonet, R. Ramsay, M. K. Sha, K. Shiomi, W. Simpson, W. Stremme, Y. Sun, H. Tanimoto, Y. Té, G. M. Tsidu, V. A. Velazco, F. Vogel, M. Watanabe, C. Wei, D. Wunch, M. Yamasoe, L. Zhang, and J. Orphal (2022a). "Improved calibration procedures for the EM27/SUN spectrometers of the COllaborative Carbon Column Observing Network (COCCON)." In: *Atmospheric Measurement Techniques* 15.8, pp. 2433–2463. DOI: 10.5194/amt-15-2433-2022. URL: https://amt.copernicus.org/articles/15/2433/2022/.

Alberti, C., Q. Tu, F. Hase, M. V. Makarova, K. Gribanov, S. C. Foka, V. Zakharov, T. Blumenstock, M. Buchwitz, C. Diekmann, B. Ertl, M. M. Frey, H. Kh. Imhasin, D. V. Ionov, F. Khosrawi, S. I. Osipov, M. Reuter, M. Schneider, and T. Warneke (2022b). "Investigation of spaceborne trace gas products over St Petersburg and Yekaterinburg, Russia, by using COllaborative Column Carbon Observing Network (COCCON) observations." In: *Atmospheric Measurement Techniques* 15.7, pp. 2199–2229. DOI: 10.5194/amt-15-2199-2022. URL: https://amt.copernicus.org/articles/15/2199/2022/.

Ionov, D. V., M. V. Makarova, F. Hase, S. C. Foka, V. S. Kostsov, C. Alberti, T. Blumenstock, T. Warneke, and Y. A. Virolainen (2021). "The CO_2 integral emission by the megacity

of St Petersburg as quantified from ground-based FTIR measurements combined with dispersion modelling." In: *Atmospheric Chemistry and Physics* 21.14, pp. 10939–10963. DOI: 10.5194/acp-21-10939-2021. URL: https://acp.copernicus.org/articles/21/10939/2021/.

Jäschke, Cornelia, Carlos Alberti, Samuel Hammer, Frank Hase, and Claudius Rosendahl (Jan. 29, 2021). *Observation-based system formonitoring and verification of greenhouse gases. Temporal variations of proxy/ffCO2 ratios*. Tech. rep. University of Heidelberg and Karlsruhe Institute of Technology. 69 pp.

Makarova, M. V., C. Alberti, D. V. Ionov, F. Hase, S. C. Foka, T. Blumenstock, T. Warneke, Y. A. Virolainen, V. S. Kostsov, M. Frey, A. V. Poberovskii, Y. M. Timofeyev, N. N. Paramonova, K. A. Volkova, N. A. Zaitsev, E. Y. Biryukov, S. I. Osipov, B. K. Makarov, A. V. Polyakov, V. M. Ivakhov, H. Kh. Imhasin, and E. F. Mikhailov (2021). "Emission Monitoring Mobile Experiment (EMME): an overview and first results of the St. Petersburg megacity campaign 2019." In: *Atmospheric Measurement Techniques* 14.2, pp. 1047–1073. DOI: 10.5194/amt-14-1047-2021. URL: https://amt.copernicus.org/articles/14/1047/2021/.

CONTENTS

LIST OF FIGURES

LIST OF TABLES

INTRODUCTION

Since human beings have existed on the Earth's surface, their activities have deteriorated the environment in several ways. The activities of modern civilisation require the use of vast amounts of energy, among which fossil fuels such as coal, oil, and natural gas have been the primary sources since the industrial era. The increase in the global population, the globalization of the economy, the growing industry, and the transport sector are only some of the most important causes which have increased anthropogenic emissions and, therefore, negatively impacted the Earth's atmosphere. Global warming is one of the most severe adverse effects caused by the anthropogenic emissions of greenhouse gases (GHGs). CO_2 from fossil fuel combustion is the most important driver of climate change; but also methane (CH_4), and nitrous oxide (N_2O) contribute significantly. These gases directly affect the Earth's radiative balance by reducing the thermal infrared emission to space. Consequently, the Earth's surface temperature increases, melting glaciers and the Greenland and Antarctic ice sheets, rising sea levels, but also creating droughts, and other harmful effects. Unfortunately, these gas emissions affect the climate for decades or centuries due to their long atmospheric lifetime.

The reduction of anthropogenic GHGs emissions is thus recognized as an essential and urgent political and societal task requiring urgent actions at all levels. Countries have debated anthropogenic climate change for more than three decades, and international conferences on the topic produced several important agreements. In 1992, the first global deal on climate change was created: the UN Framework Convention on Climate Change (UNFCCC), which established the annual Conference of the Parties (COP). Based on this meeting, the Kyoto Protocol and the Paris Agreement were created. The Kyoto Protocol became active in 2005, and its main aim was to commit industrialized economies to reduce the emission of GHGs following defined and agreed-on targets. Unfortunately, the global anthropogenic emissions of GHGs continued to increase (Harris, Chow, and Symons, 2012). The Paris Agreement came into force on November 2016, which aims to limit global warming below 2 °C or even below 1.5 °C. Such an objective can only be achieved by a very significant reduction of GHG emissions. Although most cities have enacted initiatives to measure and control pollution, most interventions are only localized (Miller et al., 2013; Seinfeld and Pandis, 2016). Most countries' governments have generally failed to enact effective measures for reducing anthropogenic emissions (Meetham, Bottom, and Cayton, 2016). Consequently, global warming is expected to reach and most likely exceed 1.5°C within the coming two decades (IPCC, 2021).

Monitoring and quantifying those gases – thereby pinning down their sources and sinks and their links with various human activities – are essential tasks for appropriate decision-making in order to mitigate climate change. In general, atmospheric concentrations of GHGs are measured by in-situ and remote sensing techniques; the first of these techniques offers very high accuracy but faces problems due to its high sensitivity to

local sources and details of the vertical transport. Ground-based remote sensing techniques using solar absorption spectroscopy deliver column-averaged atmospheric GHG abundances but suffer from lower precision, accuracy, and sensitivity for local sources. Nevertheless, these observations are well suited for validating satellite missions and for dedicated observations of source regions on local and regional scales. Both applications require measuring relatively minor changes superimposed on a large background concentration, which requires high accuracy instrumentation and calls for continuous efforts to improve the instrumental and data processing state of the art.

Currently, several dedicated GHG satellite missions are in orbit: the Greenhouse Gases Observing Satellite (GOSAT) and GOSAT-2 (Kuze et al., 2009; Morino et al., 2011; Suto et al., 2021; Yoshida et al., 2013), the Orbiting Carbon Observatory-2 (OCO-2) and OCO-3 (Crisp et al., 2017; Eldering et al., 2019, 2017; Frankenberg et al., 2015), the Copernicus Sentinel-5 Precursor (S5P) (Veefkind et al., 2012), and the Chinese Carbon Dioxide Observation Satellite (TanSat) (Liu et al., 2018). The TCCON network was established in 2004 to obtain accurate measurements of column-averaged dry-air mole fractions of XCO_2, XCO, XCH_4, and N_2O. The TCCON stations operate high-resolution Fourier transform IFS125HR spectrometers (FTS) manufactured by Bruker. The network has 29 operational sites worldwide (Wunch et al., 2011). Although these TCCON stations are distributed around the globe, there are still considerable geographic gaps that need the addition of further stations. The COCCON network emerged in 2016 based on the portable low-resolution 0.5 cm^{-1} EM27/SUN FTIR spectrometer developed by KIT in cooperation with Bruker (Gisi et al., 2012; Hase et al., 2016), delivers similar precision and accuracy as TCCON, assuming a careful calibration of each spectrometer. Several studies have revealed its previously unprecedented high level of performance and stability (Frey et al., 2015, 2019; Sha et al., 2021). In addition, the portability of the EM27/SUN spectrometer allows the realisation of campaigns for observing selected sources (as cities, landfills, power plants, coal mining areas), and numerous campaigns have already successfully been conducted by various investigators (Butz et al., 2017; Chen et al., 2020, 2016; Dietrich et al., 2021; Hase et al., 2015; Hedelius et al., 2016; Jones et al., 2021; Kille et al., 2019; Luther et al., 2019; Makarova et al., 2021; Viatte et al., 2017; Vogel et al., 2019).

The number of EM27/SUN spectrometers deployed worldwide continues to grow. Therefore it is essential to continuously assess the quality assurance/quality control (QC/QA) work and apply the best available procedures for instrumental characterization of new units to maintain and further improve the collected atmospheric data. Enabled by the European Space Agency (ESA) support, KIT has launched the Collaborative Carbon Colmn Network (COCCON), which delivers a framework for assuring instrumental and data processing standards for the EM27/SUN spectrometer. One of the key characteristics that needs to be specified for the quantitative spectral analysis of measurements collected with measurements Fourier Transform InfraRed (FTIR) spectrometers is the instrumental line shape (ILS). Several studies have shown that the actual ILS deviates from the ideal one (Bernardo and Griffith, 2005; Hase, 2012; Hase, Blumenstock, and Paton-Walsh, 1999), e.g., due to interferometric misalignment, optical aberrations, or uneven illumination or sensitivity of the detector element. An out-of-range ILS result points to instrumental is-

sues which need to be alleviated by realignment or replacement of optical or mechanical components. Portable spectrometers must demonstrate their ability to preserve their ILS characteristics during transport events and over sufficiently long periods. Stable instrumental characteristics of the EM27/SUN spectrometer have been demonstrated despite harsh transport and operation conditions for up to several years (Frey et al., 2015).

In the first part this thesis, the open-path (OP) method for ILS calculation of EM27/SUN spectrometers, as described by Frey et al. (2015), is significantly improved and applied in the commissioning of further spectrometers (Alberti et al., 2022a). Additionally, a new calibration cell filled with C_2H_2 was designed, built, and used in addition to the open-path method since January 2020. This provides additional redundancy of the ILS characterization and allows the comparison of both approaches, OP and cell measurement. The meanwhile seven-year long-term trace gas measurements of the reference EM27/SUN spectrometer operated at KIT are used as a fixed point for the instrument-specific gas calibration factors (also called side-by-side solar measurements) of the other EM27/SUN units, has been continued. These atmospheric measurements are compared with the trace gas amounts derived from low-resolution spectra collected with the co-located 125HR spectrometer of the Karlsruhe TCCON station. The open-path measurements and list the instrument-specific calibration factors for each spectrometer done in the past had been re-evaluated, considering the detected variations in the reference unit during the first three years of operation.

A considerable part of this doctoral thesis' work has been done in the framework of the EU project VERIFY work-packages (WP) 2 and 3 (https://verify.lsce.ipsl.fr/, last access: 01 October 2022), which aimed to quantify and estimate the anthropogenic and natural GHG emissions based on atmospheric measurements, emission inventories, and ecosystem data. As a task of VERIFY, two cities in Russia (St. Petersburg and Yekaterinburg) were selected to improve our understanding of a key important region with anticipated massive biosphere fluxes and potentially extensive carbon sinks (Reuter et al., 2014). Two different campaigns using a pair of COCCON spectrometers were carried out in Russia in the framework of VERIFY: (1) continuous measurements at fixed locations in both places and (2) a mobile city campaign targeting St Petersburg emissions (Emission Monitoring Mobile Experiment, EMME), using a pair of spectrometers in St Petersburg. During the city campaign in spring 2019, the spectrometers were placed upwind and downwind of St Petersburg. With the obtained results, the emission ratios for the city emissions were quantified and compared with the bottom-up estimation and with the results presented by Makarova et al. (2021). Furthermore, the complete set of COCCON measurements collected in the framework of VERIFY was used to validate and compare TROPOMI, OCO-2, GOSAT, MUSICA IASI, and Copernicus Atmosphere Monitoring Service (CAMS). Additionally, a method was developed for upscaling the COCCON measurements for better inter-comparison with satellite products. In that regard, the gradients for XCO_2, XCH_4, and XCO are calculated between both studied cities during the shared measurement period. Finally, a city-scale transport event that occurred during the city campaign and was tracked by TROPOMI has been investigated.

The final part of this thesis presents the results obtained in the "key-study" region of VERIFY: the Rhine valley in South-Western Germany (Karlsruhe). This location was selected because it comprises a mixture of urban, industrial, forest, and agricultural sectors, which implies a variety of possible biogenic and anthropogenic CO_2 emission sources. This complex structure can be taken as a typical case for European urban agglomerations. Additionally, it took advantage of the vast amount of collocated in-situ and remote sensing measurements continuously carried out in this region, plus the instrumentation added by VERIFY. The main aim was to quantify anthropogenic emissions from fossil-fuel combustion ($ffCO_2$) on a local/urban scale. Because their fossil and non-fossil CO_2 components cannot easily separate based on total CO_2 concentration measurements alone, observations of co-emitted species were used. Because there is no way to retrieve $ffCO_2$ with remote sensing techniques, an approach that uses the short-term variability of NO_2, CO, and CO_2 to separate the signals from local sources have been developed. The NO_2 vertical integrated column density is retrieved from MAX-DOAS observations, while the XCO and XCO_2 are from the TCCON station at KIT CN. The main results obtained during the whole campaign period from the total column measurements are presented, followed by a comparison with the events found with in-situ ICOS measurements and TNO inventory data.

SCIENTIFIC BACKGROUND: EARTH'S ATMOSPHERE AND TROPOSPHERIC CHEMISTRY

2.1 THE EARTH'S SYSTEM

The Earth system can be considered an integrated system, subdivided into four main components that are tightly interconnected: the geosphere, atmosphere, hydrosphere, and biosphere, see Figure 2.1.
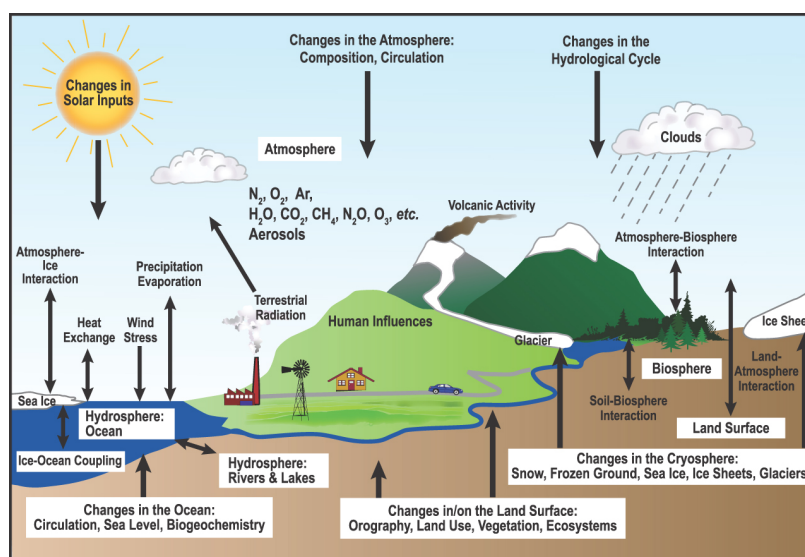
Figure 2.1: Overview of the different global components of the Earth's climate system. Figure taken from https://www.ipcc.ch/report/ar4/wg1/historical-overview-of-climate-change-science/faq-1-2-fig-1/ last access : August, 02 2022.

The Earth's system components are interconnected and affect the climate. For example, the stratospheric ozone layer is responsible for absorbing the solar UV radiation, protecting the biosphere. The temperature on the Earth is regulated by the interaction of the solar radiation with the atmosphere and Earth's surface. Atmospheric circulation is responsible, among other things, for the transport of smoke, seeds, dust, and trace gases. The oceans are essential because of their role in the global heat transport and for the carbon cycle, which regulates the CO_2 concentrations in the atmosphere.

2.1.1 *The terrestrial biosphere*

The terrestrial biosphere is composed of forests, grasslands, tundra, and deserts. Changes in any of these components affect Earth's climate via:

- **Grasslands and forests**: These components help to cool down the Earth's surface during high temperatures. Their leaves absorb parts of the incoming solar radiation, and the evapotranspiration process helps to release the water from Earth's surface to the atmosphere.

- **Local albedo**: This is defined as the amount of scattered solar radiation by the Earth's surface, clouds and aerosols.

- **Land surface roughness**: Over tundras and flat soils, the wind speeds are higher than in forests areas.

2.1.2 *The hydrologic cycle*

The water cycling between different Earth's reservoirs is vital to allow life on Earth, see Figure 2.2. Here, one important term is "residence time," which refers to the time water lasts in a defined reservoir. Table 2.1 shows the type of reservoir, its mass, and the typical residence time within the Earth's system.

Reservoirs of water	Mass	Residence time
Atmosphere	0.01	Days
Fresh water: lakes and rivers	0.6	Days to years
Fresh water: underground	15	Up to hundred years
Alpine glaciers	0.2	Up to hundred years
Greenland ice-sheet	5	10,000 years
Antactic ice sheet	53	100,000 years
Oceans	2700	
Crust and mantle	20,000	10^{11} years

Table 2.1: Masses and residence time for diverse water's reservoirs in Earth's system. Data taken from Wallace and Hobbs (2006).

From Table 2.1, it can be observed that in the atmosphere water resides the shortest time. Due to the significant exchange rate and having the highest known heat of vaporization, water transports latent heat from the Earth's surface into the atmosphere.

2.1.3 *Carbon cycle*

The carbon cycle is essential because it moderates the atmospheric amounts of the two most important greenhouse gases (GHGs) in the atmosphere: carbon dioxide (CO_2) and methane (CH_4). Table 2.2 collects the carbon reservoirs within the Earth's system, their capacity, and the usual residence time. Additionally, Figure 2.3 presents how the carbon exchanges between these reservoirs.
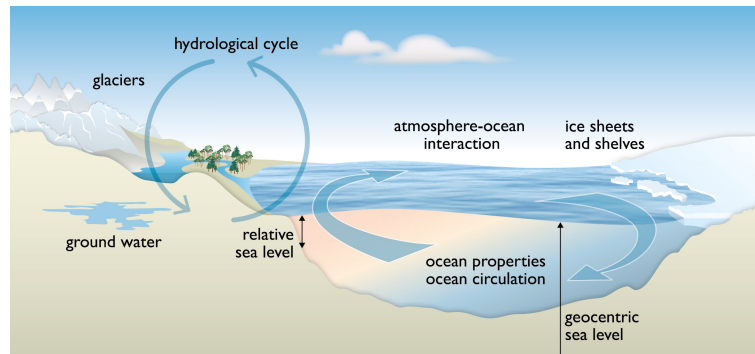
Figure 2.2: Overview of the Earth's hydrologic cycle. Figure taken from `https://www.agci.org/earth-systems/hydrosphere` last access : 23 July 2022.

Reservoir	Capacity	Residence time
Atmospheric CO_2	1.6	10 years
Atmospheric CH_4	0.02	9 years
Green part of the biosphere	0.2	Days to seasons
Tree trunks and roots	1.2	Up to centuries
Soil and sediments	3	Decades to millenia
Fossil fuels	10	-
Organic C in sedimentary rocks	2×10^{11}	
Ocean dissolved CO_2	1.5	12 years
Ocean CO_3^{2-}	2.5	6,500 years
Ocean HCO^-	70	200,000 years
Inorganic C in sedimentary rocks	80,000	10^8 years

Table 2.2: Major carbon reservoirs within the Earth's system and their corresponding capacities. Data taken from Wallace and Hobbs (2006)

2.1.3.1 *Carbon reservoirs*

- **Atmosphere:** CO_2 is the dominant form of carbon within the atmosphere, which is found fairly well mixed because of its inert state. Out of well-known natural sources of CO_2 like forest areas or close to vegetation, its concentrations vary $\sim 1\%$ over Earth's surface. CH_4 is also found in the atmosphere but smaller amounts than CO_2. Nevertheless, this is sufficient to contribute to the so-called greenhouse effect (see Section 3.6.2) being its emissions responsible for approximately 1 W m^{-2} radiative forcing in 2011 (Holmes, 2018).

- **Biosphere:** Vast amounts of carbon are exchanged between the biosphere and the atmosphere, which involves photosynthesis and respiration, and decay reactions summarized in a simplified way by Equations 2.1, which remove and return CO_2 into the atmosphere, respectively. In that equation, CH_2O stands for "organic matter" in general (Van Niel, 1949).
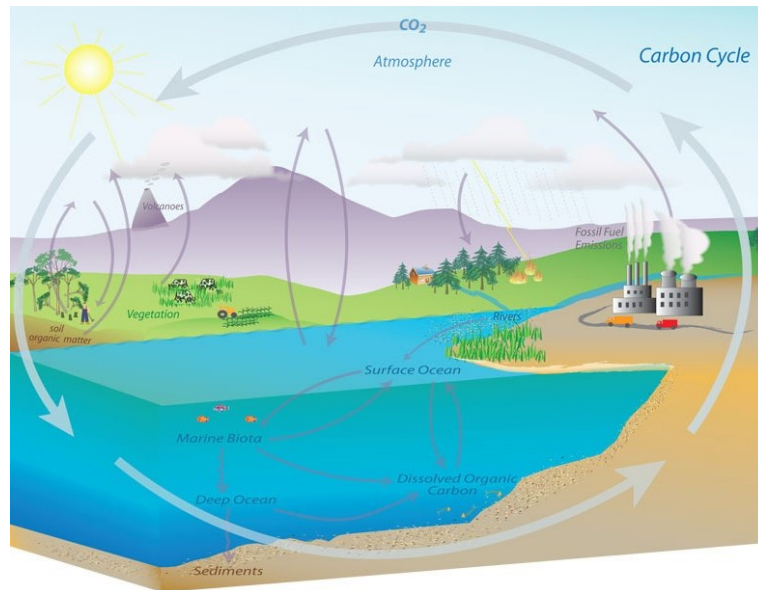
Figure 2.3: Carbon cycle between different reservoirs within the Earth's system. Taken from `https://www.noaa.gov/education/resource-collections/climate/carbon-cycle`, last access: August 2, 2022.

$$
\begin{aligned}
CO_2 + H_2O &\xrightarrow{h\nu} CH_2O + O_2 \\
CH_2O + O_2 &\xrightarrow{h\nu} CO_2 + H_2O
\end{aligned}
$$
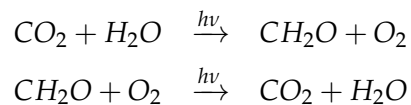
$$(2.1)$$

The photosynthesis reaction needs sunlight, which is absorbed in the visible range, while the decay releases energy in a heat form. The residence time of CO_2 is $\sim$ 10 years; however, excess amounts of CO_2 injected into the atmosphere last longer because the biosphere can only store $\sim$ 10% of the total carbon in the atmosphere independent of time.

- **Oceans:** The ocean plays an essential role in the carbon cycle because of its ability to store $\sim$ 50 times more CO_2 than the atmosphere. In the ocean, the anthropogenic CO_2 is dissolved more effectively than other gases like CH_4 and Chlorofluorocarbons (CFCs), and for that reason, it is called a carbon sink. Carbon exists in three different forms: carbonic acid, carbonate ions paired with Ca^{2+} and Mg^{2+}, and bicarbonate ions, accounting for $\sim$ 91% of the total. The exchange between ocean and atmosphere occurs over several hundred years.

  The CO_2 solubility changes with seawater temperature, salinity, and alkalinity; therefore, if any of these variables are affected, this directly affects the ocean uptake of CO_2. Ocean circulation plays a vital role in the transport of carbon from natural sink areas to natural source regions.

2.2 THE EARTH'S ATMOSPHERE

The Earth's atmosphere is composed of different layers consisting of several main and various trace gases. It is responsible for keeping Earth warm enough, protecting living species on Earth from harmful UV radiation by absorbing it and making life possible. In the following subsection, each layer of the atmosphere and the processes taking part there are described.

2.2.1 *Chemical composition*

The atmosphere is a thin gaseous layer extending from the Earth's surface to space. It is mainly composed of diatomic Nitrogen (N_2), Oxygen (O_2), Argon (Ar) and water vapor (H_2O). There are many more gases that constitute the atmosphere but in much smaller amounts, as described in Table 2.3.

Constituent	Molecular weight	Percentage or fractional concentration per volume
Nitrogen (N_2)	28.013	78.08%
Oxygen (O_2)	32.000	20.95%
Argon (Ar)	39.95	0.93%
Water vapor (H_2O)	18.02	**0-5%**
Carbon dioxide (CO_2)	44.01	**417.42 ppm**
Neon (Ne)	20.18	18 ppm
Helium (He)	4.0	5 ppm
Methane (CH_4)	16.04	**1908.74 ppb**
Krypton (Kr)	83.80	1 ppm
Hydrogen (H_2)	2.02	0.5 ppm
Nitrous oxide (N_2O)	56.03	**335.47 ppb**
Ozone (O_3)	48.00	**0-0.1 ppm**

Table 2.3: Major atmospheric constituents of the Earth atmosphere. The values for CO_2, CH_4 and N_2O were taken from Dlugokencky (2022), and the others species from Wallace and Hobbs (2006). In **bold** marked are the GHGs.

The sole presence of oxygen (O_2) in the troposphere, and the stratospheric ozone (O_3) layer makes the Earth different from other planets in our solar system. Considerably scientific efforts have been invested to estimate how much oxygen existed before life began and what exactly produced its rise. Geological and geochemical evidence suggests that oxygen levels were very low $\sim$ 2.45 billion years (Gyr) ago and that the rise had occurred between 2.22 and 2.32 Gyr (Bekker et al., 2004).

In the lowermost layers of the atmosphere, clouds are formed then droplets fall out as precipitation. Additionally, water vapour is an essential source of infrared opacity in the Earth's atmosphere.

Due to the large variability of water vapor into the atmosphere, gas concentrations are preferably expressed in terms of dry air molar fractions: for convenience minor trace gases are quantified in parts-per-million (ppm) or parts-per-billion (ppb) by volume. The (stratospheric) O_3 layer absorbs hazardous UV solar radiation, the GHGs, mainly H_2O, CO_2, CH_4 and N_2O trap outgoing thermal radiation from Earth's surface which keeps Earth warm enough to make life possible on Earth's surface.

2.2.2 *Vertical structure*

The most important meteorological variables: temperature, pressure, density, and the essential components of the Earth's atmosphere show differences with geolocation, season, day, night, etc. Only the vertical structure of each of these elements is summarized within this section. Despite the horizontal variation of the atmospheric temperature, the vertical distribution is comparatively similar everywhere. The value of the atmospheric pressure at a defined altitude directly relates to the mass located above that height. Both pressure and density decrease with altitude. The relationship describing the stratification of pressure as function of altitude is the so-called hydrostatic balance, which mathematically can be written as:

$$\frac{\partial p}{\partial z} + g\rho = 0 \qquad p(z + dz) = p(z)e^{\frac{-dz}{H}} \tag{2.2}$$

H is defined as scale height and p_0 as reference pressure from the last equation, usually at z=0, i.e. at sea level. The scale height H varies between 7 to 8 km in the lowermost layers of the atmosphere.

The mixing ratios of the gases N_2, O_2, Ar , CO_2 and others long lived constituents are quite constant at different altitudes. Nevertheless, most of the other trace gases have more variable vertical profiles due to chemical reactions, solubility, and photolysis (Wallace and Hobbs, 2006). Usually the atmosphere is split into layers according to the temperature vertical profile. Following that approach, the atmosphere can be divided in four different layers starting from the Earth's surface: Troposphere, Stratosphere, Mesosphere and Thermosphere (see Figure 2.4).

The results presented in this thesis deal with gases and processes occurring within the troposphere; therefore, the other atmospheric layers are are only briefly described here.

- **Stratosphere:** In this layer, a temperature inversion occurs; the temperature increases with altitude due to the absorption of UV radiation by stratospheric O_3. This phenomenon makes the Earth suitable and habitable for life.

- **Mesosphere:** The layer is located just above the stratosphere between the stratopause and the mesopause. In this layer, the temperature decreases with height, similar to the troposphere, until it reaches the lowest temperature value that defines mesopause.
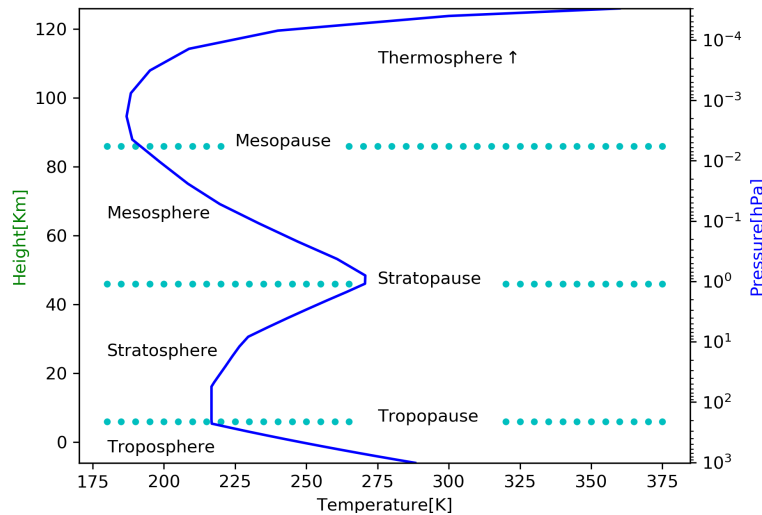
Figure 2.4: Vertical structure of the atmosphere. Data taken from libradtran input files: US Standard Atmosphere 1976 (Mayer and Kylling, 2005).

- **Thermosphere:** This layer is located above the mesopause. Here again, a temperature inversion occurs, which increases with height mainly due to the absorption of solar radiation by N_2 and O_2.

2.2.2.1 *Troposphere*

The troposphere is the lowermost layer of the atmosphere that extends from the Earth's surface until the tropopause (the boundary between the troposphere and the stratosphere). In this layer, the temperature decreases with height with a rate of around 6.5 °C.km^{-1}, named "lapse rate". Most of the air of the entire atmosphere is located in this layer; it contains $\sim 80\%$ of the total mass of the atmosphere.

2.3 ATMOSPHERIC CHEMISTRY

Atmospheric chemistry has evolved from purely studying the most important gases in the Earth's atmosphere to identifying natural and anthropogenic sinks, sources, properties, interaction with the biosphere, etc., of various chemical species in the atmosphere. Thinking about spatial and temporal scales of the chemical constituents in the atmosphere, by assuming globally averaged amounts (which do not change dramatically in a defined time) and within a steady-state of the atmosphere, the rate at which the species are injected into and removed from the atmosphere must be equal, and thus in equilibrium. Under these conditions, the so-called "residence time" is defined as (see Equation 2.3):

$$\tau = \frac{M}{F} \quad \text{, where} \quad [M] = kg \quad \text{, and} \quad [F] = kgs^{-1} \tag{2.3}$$

Figure 2.5 shows how the atmospheric constituents vary in the space and time domain. The residence time of a defined species is proportional to the variation in concentration

in the spatial domain; high concentrations of constituents with short residence time are likely to be found close to local sources and in low amounts far away from them.
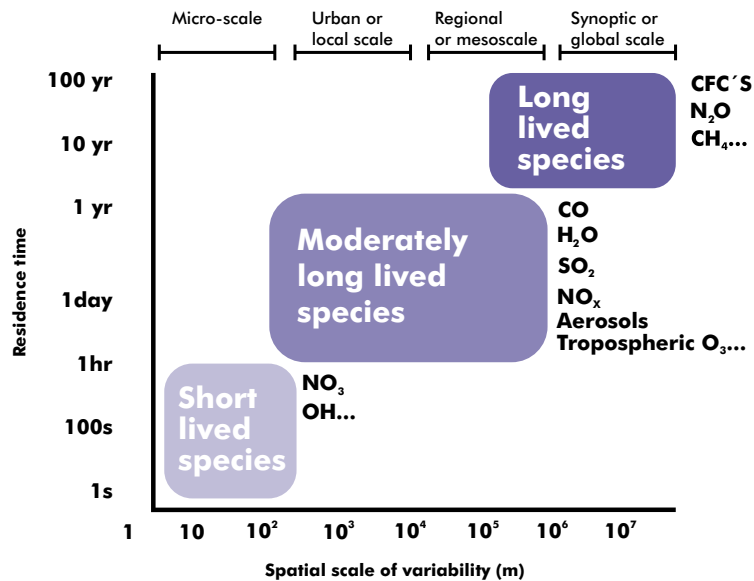
Figure 2.5: Space-time variability for some important atmospheric constituents. Adapted from Wallace and Hobbs (2006).

Atmospheric chemistry is much more complex than described in this chapter; however, the essential concepts of tropospheric chemistry are briefly summarized here, emphasizing the trace gases and GHGs studied in this thesis.

2.4 TROPOSPHERIC CHEMISTRY

Various chemically active species are emitted from the Earth's surface; such emissions vary with the geolocation. The troposphere is well mixed for long-lived species. However, gases with short lifetimes can exhibit large gradients. Like in the stratosphere, tropospheric O_3 chemistry is associated with the formation and destruction of ozone. Here, O_2 cannot be the ozone source because the photons with the required energy have already been absorbed in the stratosphere; NOx[1] serves instead. Apart from NOx species, many anthropogenic and natural hydrocarbons and organic species are present in the troposphere. CH_4 is the leading hydrocarbon, a critical component for tropospheric chemistry. Although short-wave UV radiation has already been absorbed in the stratosphere, sufficient radiation still reaches the troposphere leading to photochemical reactions. The troposphere is well known to be an oxidant medium, the essential reaction is driven by the hydroxyl radical OH, which is very reactive and attacks most trace gases. For that reason, OH is known as the "detergent of the atmosphere" (Ball, 2000).

---

[1] $NOx = NO_2 + NO$

2.4.1 *Ozone: O_3*

Tropospheric O_3 is a highly toxic and reactive species, which can cause human health problems and damage vegetation and ecosystems. As described before, O_3 is very important within the stratosphere whereby it is called "good ozone"; however, tropospheric O_3 has many harmful effects and, for that, is called "bad ozone." Additionally, tropospheric O_3 absorbs IR radiation, turning it into the third most important GHG after CO_2 and CH_4 (D. et al., 2001). Within the troposphere, O_3 has a critical role in the oxidation capacity of this layer. Photolysis of O_3 occurs in the wavelength region between 300 and 320 nm:

$$
\begin{aligned}
O_3 + h\nu(\lambda < 310nm) &\Rightarrow O_2 + O(^1D) \\
O_3 + h\nu(\lambda > 310nm) &\Rightarrow O_2 + O(^3P)
\end{aligned}
$$

$$(2.4)$$
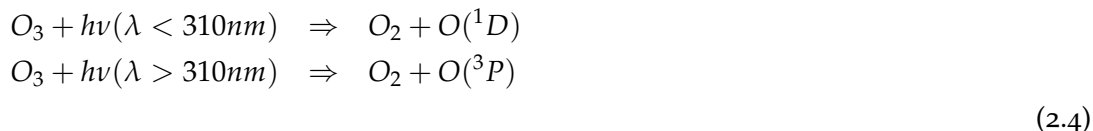
The produced $O(^1D)$ yields OH production, whilst, $O(^3P)$ regenerates O_3. An important fraction of tropospheric O_3 is formed by oxidation reactions of CH_4 and CO with OH in the presence of NOx.

2.4.2 *Nitrogen oxides: NOx*

Nitrogen oxides (NOx): NO (nitric oxide) and NO_2 (nitrogen dioxide) are important pollutants due to their role in atmospheric chemistry. They are mainly produced at high temperatures. Several studies demonstrate that the concentration of nitrogen oxides in the atmosphere has been increasing steadily due to anthropogenic emissions (Rosa Eugene and Thomas, 2012). These gases are also very important due to their relationship with the photochemical ozone production in the troposphere and the estimation of its distribution over the Earth (Crutzen, 1979). This ozone located in the troposphere is harmful and produces several pulmonary diseases like asthma (EPA, 2022b).

2.4.2.1 *Natural sources*

Denitrification and nitrification processes, which occur in undisturbed terrestrial environments, are the primary sources of NOx in the atmosphere. Lightning, animal wastes, and the transport of NO_2 from the stratosphere are also sources of NOx in the troposphere (Rosa Eugene and Thomas, 2012).

2.4.2.2 *Anthropogenic sources*

Human activity is the primary source of NO releases in the troposphere. Electricity generation, road transport, ships, and the heat sector are the primary sources of anthropogenic NOx (Rosa Eugene and Thomas, 2012). These emissions are concentrated in urban and industrial areas (Dix, 2007). A photochemical reaction occurs between the unburned motor vehicle's exhaust and NO, producing ozone (Crutzen, 1979). Chemically it can be expressed as,

$$\begin{aligned}
R + O_2 + M &\Rightarrow RO_2 + M \\
RO_2 + NO &\Rightarrow RO + NO_2 \quad \lambda \leq 400nm \\
NO_2 + h\nu &\Rightarrow NO + O \\
O + O_2 + M &\Rightarrow O_3 + M \\
R + 2O_2 &\Rightarrow RO + O_3
\end{aligned}$$

(2.5)

(2.6)

(2.7)
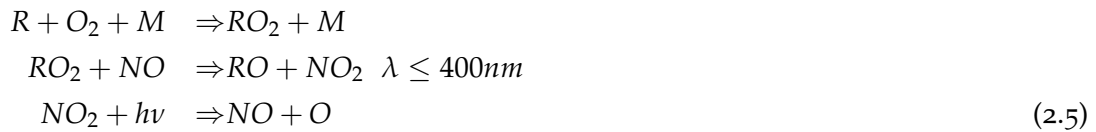
Where R is a radical like H, CH_3 or $CH_3C(O)$. These components are intermediate products of hydrocarbons combustion (Crutzen, 1979).

2.4.2.3 *Photochemical cycle*

In the troposphere, NOx species are responsible for O_3 formation. For that, the presence of three actors is required: NO, NO_2, and sunlight, the last one photolyzing NO_2. Reactions 2.5 and 2.6 produce O_3. This O_3 then reacts with NO and brings back NO_2. However, when the NO concentration is much higher than O_3, reaction 2.8 leads to O_3 depletion; this usually occurs at night in urban areas.

$$NO + O_3 \quad \Rightarrow \quad NO_2 + O_2$$

(2.8)

2.4.2.4 *Urban photochemistry*

In general, urban air can be subdivided into two categories depending on the anthropogenic source and light intensity as follows:

1. **Photochemical smog (or Los Angeles-type)**: Both sunlight intensity and emissions are high. Moreover, the emission source is the fossil-fuel combustion type. It is produced from reactions of "reactive organic gases" (ROGs) such as NO and NO_2 with sunlight, as described above.

2. **London-type smog**: This occurs when high amounts of sulphur oxide emissions from coal-fired power plants and high relative humidity are present in the troposphere. Unlike type 1, here, the sunlight intensity is moderate.

O_3 production is different in the free-troposphere compared to polluted urban air because the ROGs radicals involve the NO to NO_2 conversion.

2.4.3 *Formaldehyde: HCHO*

Formaldehyde is the most crucial intermediate in the oxidation of methane and other biogenic and anthropogenic organic compounds like hydrocarbons in the troposphere (Brasseur, Orlando, and Tyndall, 1999). On average, its lifetime in the troposphere is about 5 hours (Arlander et al., 1995). Furthermore, its photolysis and reaction with OH are the

major sources of CO (Brasseur, Orlando, and Tyndall, 1999). Formaldehyde is hazardous and can cause some types of cancer (EPA, 2022a). Like NOx, it is found in industrialized cities. Formaldehyde is also a primary emission product of biomass burning and fossil fuel combustion (Dix, 2007).

2.4.3.1 *HCHO degradation*

Formaldehyde is removed by the reaction with OH radicals and photolysis, as follows:

$$
\begin{aligned}
HCHO + h\nu(\lambda < 330nm) &\Rightarrow H + HCO \\
HCHO + h\nu &\Rightarrow H_2 + CO \\
HCHO + OH &\Rightarrow HCO + H_2O
\end{aligned}
$$

$$(2.9)$$
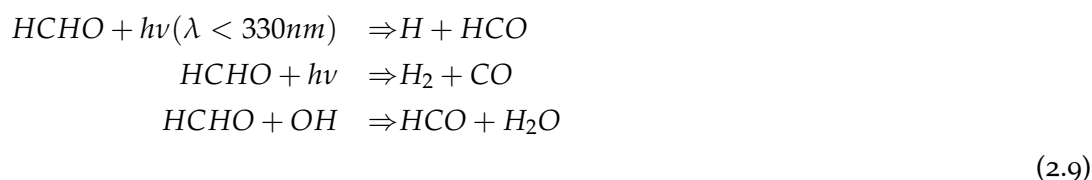
The hydrogen, and the radical HCO reacts quickly with O_2 as follows:

$$
\begin{aligned}
H + O_2 + M &\Rightarrow HO_2 + M \\
HCO + O_2 &\Rightarrow HO_2 + CO
\end{aligned}
$$

$$(2.10)$$

The formed HO_2, later reacts with NO. Therefore, the oxidation chain for HCHO/NOx follows:

$$
\begin{aligned}
HO_2 + NO &\Rightarrow NO_2 + OH \ (2\times) \\
NO_2 + h\nu &\Rightarrow NO + O \ (2\times) \\
O + O_2 + M &\Rightarrow O_3 + M \ (2\times) \\
\hline
Net: HCHO + 4O_2 + h\nu &\Rightarrow CO + 2OH + 2O_3
\end{aligned}
$$

$$(2.11)$$

$$
\begin{aligned}
HCHO + OH &\Rightarrow HCO + H_2O \\
HCO + O_2 &\Rightarrow HO_2 + CO \\
HO_2 + NO &\Rightarrow NO_2 + OH \\
NO_2 + h\nu &\Rightarrow NO + O \\
O + O_2 + M &\Rightarrow O_3 + M \\
\hline
Net: HCHO + 2O_2 + h\nu &\Rightarrow CO + OH + O_3 + H_2O
\end{aligned}
$$

$$(2.12)$$
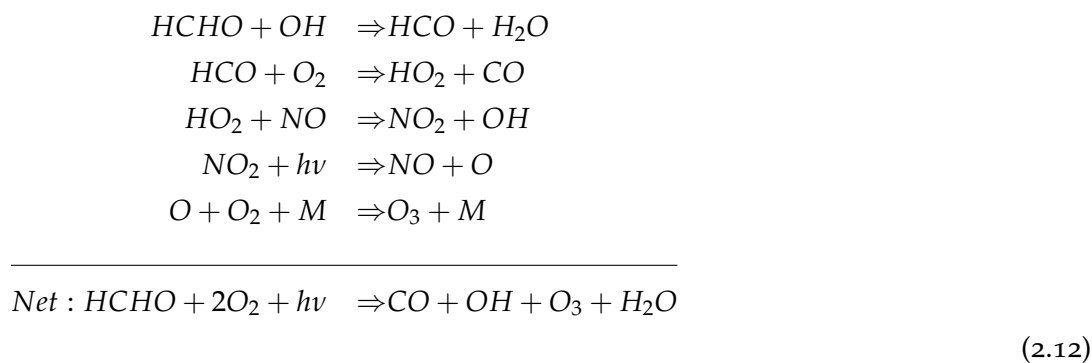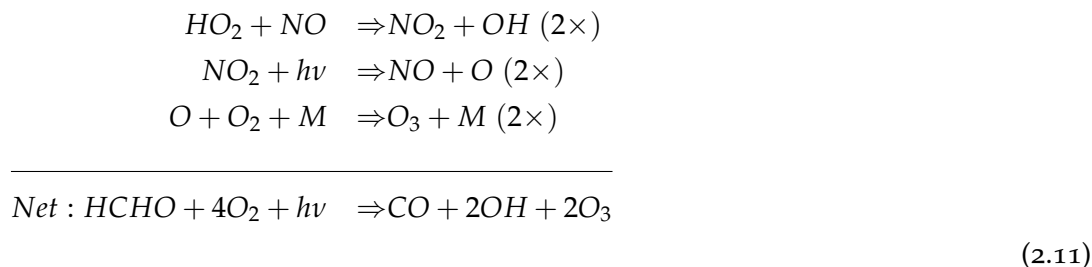
2.4.4 *Carbon monoxide: CO*

There are several sources of CO; one of them is the oxidation of CH_4 with the so-called Non-Methane HydroCarbons (NMHC); another critical source is anthropogenic emissions such as biomass burning and fossil fuel combustion. CO is not considered a GHG because it does not absorb the outgoing infrared radiation from Earth's surface. Its biggest sink is the oxidation by OH as follows:

$$
\begin{aligned}
CO + OH &\Rightarrow CO_2 + H \\
H + O_2 + M &\Rightarrow HO_2 + M \\
HO_2 + NO &\Rightarrow NO_2 + OH \\
NO_2 + h\nu &\Rightarrow NO + O \\
O + O_2 + M &\Rightarrow O_3 + M \\
\hline
Net : CO + 2O_2 + h\nu &\Rightarrow CO_2 + O_3
\end{aligned}
$$

$$(2.13)$$
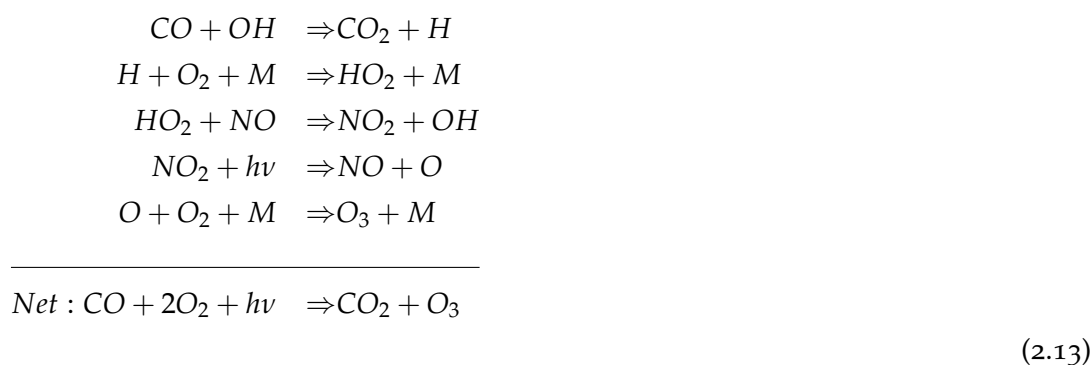
Because of the last reaction, in rural areas and non-forested places, OH concentrations are determined by CO. In extratropical locations, CO presents a seasonal cycle directly linked to its OH removal, i.e., it accumulates in winter when OH is low and decreases in spring.

2.4.5 *Methane: CH_4*

CH_4 is the most abundant hydrocarbon within the atmosphere. High-resolution measurements of CH_4 have been performed to determine its temporal and spatial distribution within the troposphere and stratosphere. These reveal that in the stratosphere, its variability is relatively small (D. et al., 2001).

CH_4 is the second most important anthropogenic GHG after CO_2. Latest preliminary reports from NOAA's analysis have shown that the CH_4 concentrations during 2021 were $\approx$ 1896 ppb, which is 162% higher than the pre-industrial levels. CH_4 global emissions are 15% higher than the estimated levels during the 1984 to 2006 period (NOAA, 2021). Figure 2.6 shows the global CH_4 budget with its sources and sinks. Sources include fossil-fuel and oil production, and use like leakages from natural gas pipelines and coal mines, agriculture and waste, biomass burning, and wetlands. From the chemical point of view, it is a reactive gas with an atmospheric residence time of $\sim$ 9 years, which is mainly removed by its reaction with the hydroxyl radical (OH) as shown in Equation 2.14 which consequently leads to CO_2, H_2O, O_3, and HCHO formation.

$$CH_4 + OH \xrightarrow{O_2} CH_3O_2 + H_2O$$

$$(2.14)$$
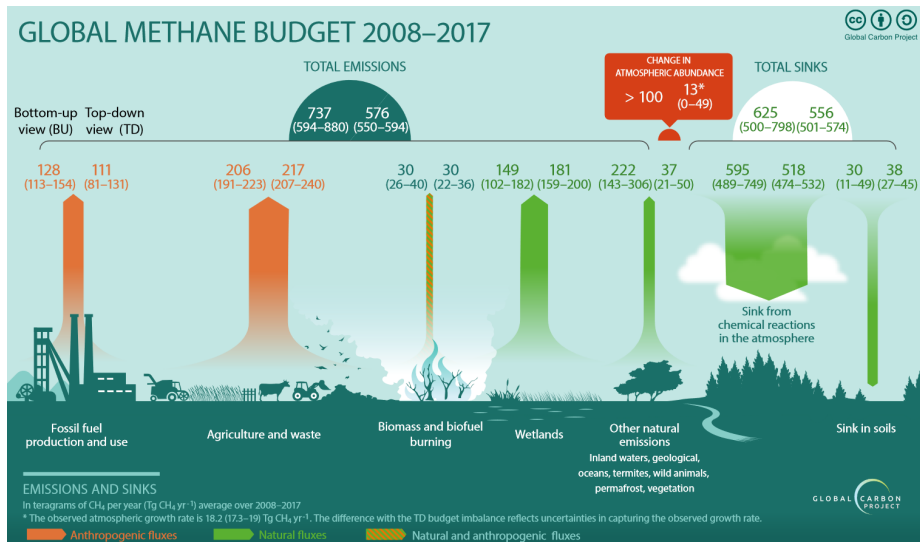
Figure 2.6: Global emission sources and sinks of CH_4 during 2008-2017. Taken from `https://www.globalcarbonproject.org/methanebudget/`, last access: August 1, 2022.

2.4.6 *Tropospheric aerosols*

Atmospheric aerosols are small solid or liquid suspended particles in the air; their atmospheric role depends on their size, which is illustrated in Figure 2.7
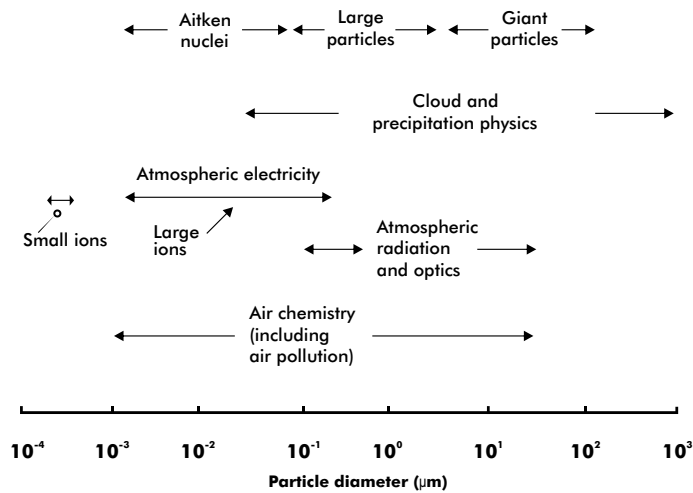
Figure 2.7: Particle size distribution within the atmosphere and their importance. Adapted from Wallace and Hobbs (2006)

2.4.6.1 *Sources and sinks*

The primary natural sources of tropospheric aerosols are sea salt, smoke from wildfires, and particles from the Earth's surface, released by semi-arid regions and deserts. These particles can be transported over long distances. Particles are injected into the atmosphere by volcanic eruptions. Aerosols can also form from the gas phase (eg. secondary organic

aerosol formation from pined emissions). The most important anthropogenic sources are biomass-burning, fuel combustion, industrial processes, dust from roads, etc. In general, tiny particles are converted into larger ones by coagulation processes; this increase in size reduces their mobility and contributes to their atmospheric removal by other mechanisms.

RADIATIVE TRANSFER IN THE ATMOSPHERE

3.1 ELECTROMAGNETIC WAVES AND PHOTONS

[1]Electromagnetic radiation (commonly known as light) is a transversal wave traveling at a speed of light c $\sim 2.998 \times 10^8 \ ms^{-1}$ (in vacuum). Light has a dual (wave-particle) behavior, which means it can behave equally as an electromagnetic wave (with a coupled electric and magnetic field) or as a particle simultaneously. This duality perfectly explains the emission and absorption of the light (photon) in the atmosphere (Hilboll, 2014).

The energy of a photon depends on the value of the electromagnetic field's wavelength: $E = \frac{hc}{\lambda}$, where h = Planck's constant $\sim 6.63 \times 10^{-34}$ Js, and λ = wavelength.

The radiative transfer process in the atmosphere requires the consideration of the contribution of different spectral regions (with different wavelengths and frequencies). The available range of values for wavelength and frequencies are given in Figure 3.1.
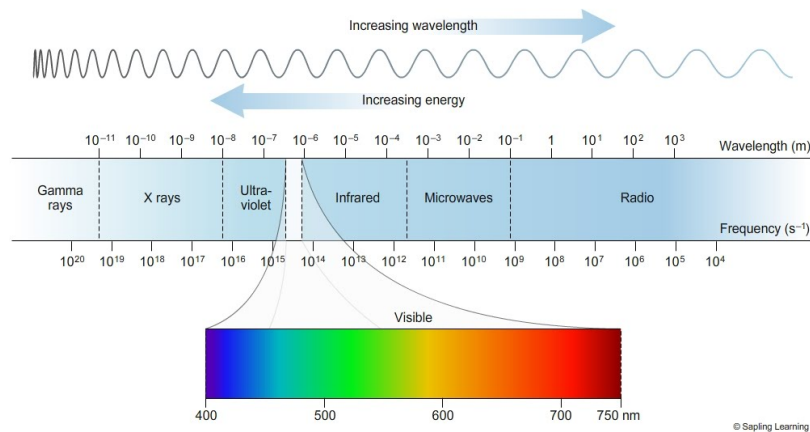
Figure 3.1: The electromagnetic spectrum. Taken from https://sites.google.com/site/chempendix/em-spectrum.

3.2 RADIANT POWER, IRRADIANCE AND RADIANCE

In the following sections, the radiative processes that take place in the atmosphere are quantitatively described; for this, it is necessary to introduce the following concepts:

- Radiant power (Φ): It is the radiant energy dQ per time unit dt.

$$\Phi = \frac{dQ}{dt} [W] \tag{3.1}$$

1 This chapter is based on overview from the following books: Petty (2006) and Wallace and Hobbs (2006).

- Irradiance E: Is the radiant power on a given surface dA.

$$E = \frac{dQ}{dAdt} \left[\frac{W}{m^2} \right]$$ (3.2)

- Radiance L: Is the irradiance per solid angle $d\Omega$. Here θ and ϕ are the zenith and azimuth angle respectively, see Figure 3.2.

$$L = \frac{dQ}{dA \cos \theta d\Omega dt} \left[\frac{W}{m^2 sr} \right]$$ (3.3)
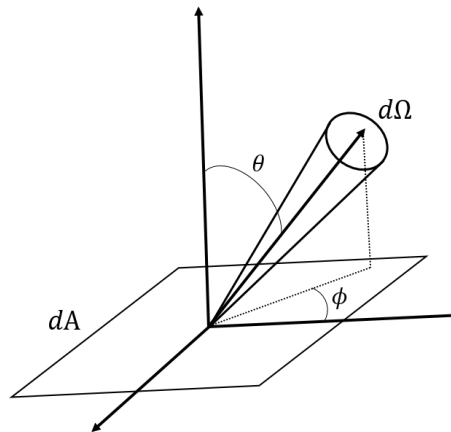
Figure 3.2: Definition of the angles involved in the radiance's definition

3.3 BLACK BODY RADIATION

All existent bodies emit thermal radiation. A blackbody is considered a surface capable of absorbing all the incoming radiation. Substances like coal and a small hole in a much larger cavity are examples. For the last one, the small aperture must look black, although the interior surfaces can be very reflective. However, only a tiny portion of the entered light is reflected back to the aperture, which entails the light absorption in the cavity's interior due to the multiple reflections occurring inside.

3.3.1 *Planck function, Wien's and Stefan Boltzmann's law*

[2]Any "body" at equilibrium emits radiation depending on its temperature. The so-called blackbody is the ideal physical body capable of emitting the maximum radiative energy. Mathematically this process is described by Planck's law:

$$B(\lambda, T) = \frac{2hc^2}{\lambda^5} \frac{1}{\exp\{\frac{hc}{\lambda.k_B T}\} - 1}$$ (3.4)

2 This subsection is based on an overview from Sportisse (2010).

Where $k_B = 1.38 \times 10^{-23} JK^{-1}$ is the Boltzmann constant.

Wien's displacement law gives the wavelength at which the maximum emission occurs at a defined temperature:

$$\lambda_{max} = \frac{2898 \times 10^3 \ [nm \ K]}{T \ [K]} \tag{3.5}$$

The total emitted radiance can be found by integrating the last equation over the whole wavelengths, that is the so-called Stefan-Boltzmann Law:

$$B(T) = \int_0^\infty B(\lambda, T) d\lambda = \sigma T^4 \tag{3.6}$$

3.3.2   *Radiative properties of nonblack materials*

Strictly speaking, a perfect blackbody does not exist. Non-black bodies like gaseous samples or mediums, unlike blackbodies that absorb all the incoming radiation, also scatter and transmit it. Despite their individual characteristics, the behavior of the non-black materials can still be understood based on the blackbody equations described before. For this reason, it is essential to define some better connections between the monochromatic intensity of the emitted radiation by the body and the corresponding blackbody, which are: the monochromatic emissivity ε_λ (Equation 3.7), absorptivity α_λ, reflectivity R_λ, and transmissivity T_λ, see Equation 3.8.

$$\varepsilon_\lambda = \frac{I_\lambda(emitted, T)}{B_\lambda(T)} \tag{3.7}$$

$$\alpha_\lambda = \frac{I_\lambda(absorbed)}{I_\lambda(incident)}, \qquad R_\lambda = \frac{I_\lambda(reflected)}{I_\lambda(incident)}, \text{ and } \qquad T_\lambda = \frac{I_\lambda(transmitted)}{I_\lambda(incident)} \tag{3.8}$$

3.3.3   *Kirchhoff's Law*

As described before, the Planck distribution function describes the radiation absorbed by a blackbody. In reality, i.e., in non-ideal cases, objects or mediums absorb at some wavelength ranges, not in all.

Kirchhoff's Law expresses that the emissivity of any object at any particular wavelength is equal to its absorptivity.

$$\varepsilon_\lambda = \alpha_\lambda \tag{3.9}$$

Where $\varepsilon_\lambda(T)$ is called emissivity. Typical values of this constant can be found in Table 3.1

Surface	ε_{IR}	Surface	ε_{IR}
Sea	0.95 - 1	Grass	0.90 - 0.95
Fresh snow	0.99	Desert	0.85 - 0.90
"Old snow"	0.80	Forest	0.95
Liquid water clouds	0.25 - 1	Concrete	0.70 - 0.90
Cirrus	0.10 - 0.90	Urban	0.85

Table 3.1: Values of emissivity in the IR range. Taken from (Sportisse, 2010)

3.4 SOLAR OUTPUT

Assuming that the Sun emits electromagnetic radiation resembling a blackbody with a surface temperature of around 5800 K and by applying Wien's displacement law, the maximum emission occurs at $\sim$ 500 nm, referred to as shortwave radiation.

In reality, the Sun is not a perfect blackbody. The solar spectrum results from emission and absorption through the whole photosphere; the photospheric temperature increases with depth, therefore the resulting spectrum is more complex than the blackbody spectrum. The solar irradiance spectrum contains numerous absorption lines due to some absorbers in the Sun's atmosphere, called "Fraunhofer lines". Finally, the solar spectral irradiance that reaches the Earth's surface is modified due to the absorbers in the Earth's atmosphere. Figure 3.3 is an example of the spectral irradiances calculated at the top of the atmosphere (TOA), and the Earth's atmosphere compared with the Planck function evaluated for the sun. The irradiances have been calculated with the radiative transfer model libRadtran (Emde et al., 2016; Mayer and Kylling, 2005).

3.5 PHYSICS OF SCATTERING, ABSORPTION AND EMISSION

3.5.1 *Scattering by air molecules and particles*

Particles are considered omnipresent, including aerosols of all possible sizes and shapes, ice crystals, and cloud droplets. Therefore it is crucial to describe their interaction with the incoming electromagnetic radiation; here, the scattering is described, and for that, particles are considered spherical with radius r.

3.5.2 *Elastic scattering*

This is defined as the scattering process in the atmosphere that only changes the direction of propagation of the photon but not the energy, and consequently the wavelength remains unchanged. Elastic scattering is produced when the incoming radiation interacts with air molecules (Rayleigh scattering), and aerosol particles (Mie scattering).
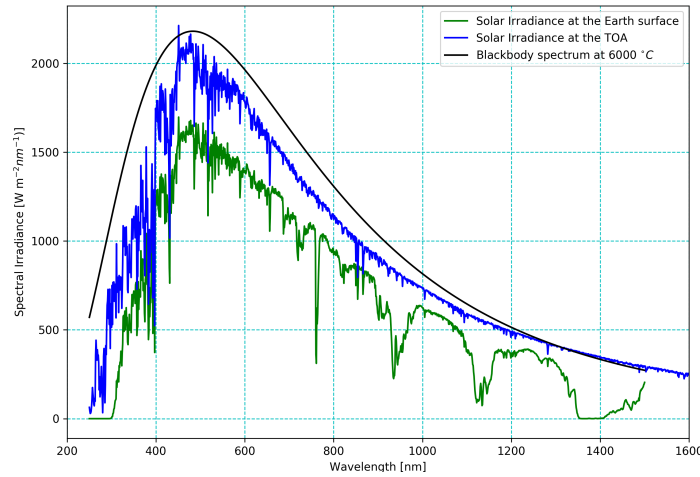
Figure 3.3: The solar spectrum irradiance at the Top Of the Atmosphere (TOA) and the Earth's surface is compared to the ideal blackbody at 6000°C. The irradiances have been calculated with libRadtran (Emde et al., 2016; Mayer and Kylling, 2005) with the following inputs: U.S. Standard atmosphere, solar zenith angle: 30°, the extraterrestrial spectrum from Kurucz (1992), surface albedo: 0 and wavelength range: $100 - 1500$ nm.

3.5.3 Rayleigh Scattering

Rayleigh scattering is caused by air particles with radius smaller than the incoming radiation wavelength λ (e.g air molecules). The Rayleigh scattering cross section σ depends strongly on the wavelength:

$$\sigma_R \propto \lambda^{-4} \tag{3.10}$$

It is the cause of the blue color of the sky owing to its effectiveness in the UV range by scattering the light with small wavelength (Grossmann, 2014). The Rayleigh phase function is described by:

$$\Phi(\cos \vartheta) = \frac{3}{4}(1 + \cos^2 \vartheta) \tag{3.11}$$

Where ϑ is the angle between the incoming and outgoing (scattered) direction of the photon. The Figure 3.4 shows an example of the Rayleigh phase function.

3.5.4 Mie Scattering

Mie Scattering is caused by particles with radius comparable to the wavelength of the incoming radiation. The Mie theory assumes spherical aerosol particles. For a typical particle distribution the Mie scattering cross section can be approximated as follow (Grossmann, 2014),

$$\sigma_M \propto \lambda^{-1.3} \tag{3.12}$$
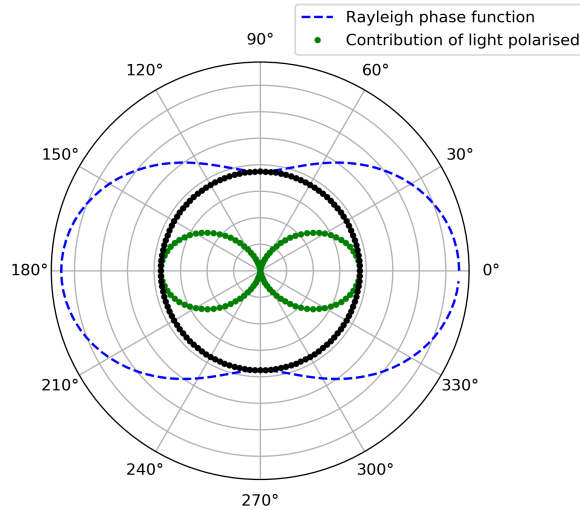
Figure 3.4: Typical Rayleigh scattering phase function. Adapted from Platt and Stutz (2008) and Yilmaz (2012).

The Mie scattering phase function P_{HG} is more complex to obtain. An analytical parametrization proposed by Henyey and Greenstein (1941) is often used:

$$P_{HG}(\mu) = \frac{1 - g^2}{(1 + g^2 - 2g\mu)^{3/2}} \tag{3.13}$$

Where g is the so-called asymmetry parameter, and $\mu = \cos\theta$. Here θ is the scattering angle.
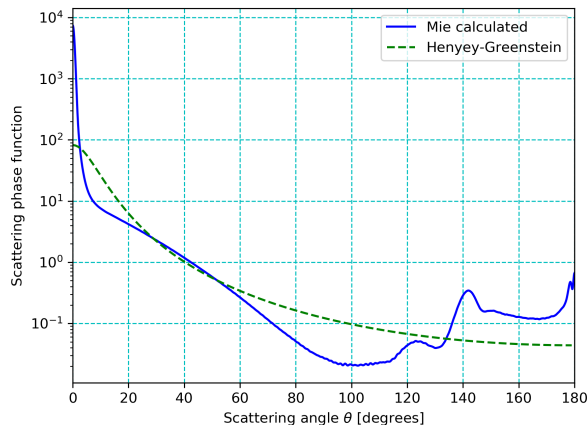
Figure 3.5: Mie Scattering phase function for water clouds with effective radii of 10 μm (solid blue line), calculated with libRadtran (Emde et al., 2016; Mayer and Kylling, 2005) and also the Henyey Greenstein approximation is shown (dashed green line).

3.5.5 *Inelastic scattering (Raman Scattering)*

[3]Inelastic scattering can be defined as the scattering process in the atmosphere in which the direction and the energy of the scattered photon changes. This is called Raman scattering. During this scattering process the photon can either loose or gain energy:

- **Stokes-Raman Scattering**: The photon transfers part of its energy to the molecule and the emitted photon has lower energy than the absorbed one. See Figure 3.6.

- **Anti-Stokes Raman Scattering**: The photon take out part of the molecule's excitation energy and the scattered photon has higher energy than the absorbed one. See Figure 3.6.
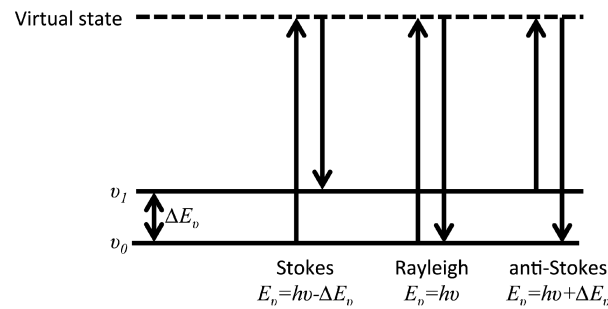
Figure 3.6: Schematic drawing of rotational and vibrational Raman lines of a diatomic molecule. Taken from Hosseinpour and Magnus (2017).

3.5.6 *Aerosol optical properties*

Besides scattering the incoming radiation, aerosols may absorb it depending on its composition. Aerosols are usually characterized due to their optical properties by the following parameters: "extinction coefficient" (β_{ext}) and "single scattering albedo (SSA)."

3.5.6.1 *Extinction coefficient*

It is defined as the sum of the scattering coefficient $\beta_{scat}(\lambda)$ and the absorption coefficient $\beta_{abs}(\lambda)$.

$$\beta_{ext}(\lambda) = \beta_{scat}(\lambda) + \beta_{abs}(\lambda) \tag{3.14}$$

The wavelength dependence of β_{ext} is described by the Ångström exponent α:

$$\beta_{ext}(\lambda) = \beta_{ext}(\lambda)(\frac{\lambda}{\lambda_0})^{-\alpha} \tag{3.15}$$

Where λ_0 is the reference wavelength, α on average is ~ 1.3 (Ångström, 1930).

---

3 The following part is based on an overview from Grossmann (2014) and Yilmaz (2012).

The aerosol optical thickness τ can be obtained by:

$$\tau = \int_0^z \beta_{ext}(\lambda, z')dz'$$ (3.16)

3.5.6.2 Single scattering albedo (SSA)

The SSA ω_0 is defined as the ratio between the scattering coefficient and the extinction coefficient:

$$\omega_0(\lambda) = \frac{\beta_{scat}(\lambda)}{\beta_{scat}(\lambda) + \beta_{abs}(\lambda)}$$ (3.17)

The value of the SSA is between 0 and 1. Thereby, "0": no scattering, and "1": all light scattered.

3.5.7 Extinction by an atmospheric layer

When considering the path of a radiation beam through the atmosphere, the initial monochromatic beam radiation decreases due to the presence of molecules and particles on its way to the Earth's surface. This phenomenon can be quantitatively described by using Equation 3.18 (see Figure 3.7):

$$dL_\lambda = -L_\lambda \frac{N\sigma}{A} = -L_\lambda n\sigma dz = -L_\lambda d\tau_{abs}$$ (3.18)

where $n = \frac{N}{V}$, and $\frac{N}{V} = \frac{N}{Adz}$
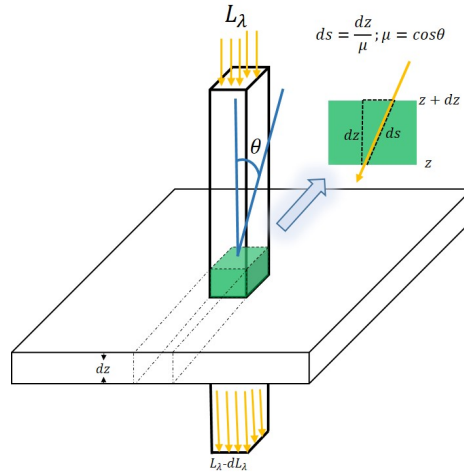
Figure 3.7: Solar radiation extinction by a infinitesimally thin atmospheric layer

Here, N is the number of particles in volume V, n is the number density, σ is the particle/molecule cross-section. The product $\mu\sigma$ defines the volume absorption coefficient, so β_{abs}, and the product $\beta_{abs}dz$, the optical thickness $d\tau_{abs}$. For the slant incidence beam

shown in Figure 3.7, where ds is the differential optical path length, and $\mu = cos\theta$ is the zenith angle; the Equation 3.18 change to:

$$dL_\lambda = -L_\lambda \frac{d\tau_{abs}}{\mu} \quad , \text{where} \quad ds = \frac{dz}{\mu} \quad , \text{and} \quad \tau_{abs} = n\sigma ds = n\sigma \frac{dz}{\mu} \tag{3.19}$$

The solution of Equation 3.19 is given by:

$$L_\lambda = L_0 \exp\left(-\frac{\tau_{abs}}{\mu}\right) \quad = L_0 \exp\left(-\frac{n\sigma z}{\mu}\right) \tag{3.20}$$

Where:

$$\tau_\lambda = \int_{z_1}^{z_2} \beta_{abs}(z)dz \quad \text{and} \quad T_\lambda = e^{-\frac{\tau}{\mu}} \tag{3.21}$$

The terms in Equation 3.21 are the so-called *layer transmissivity*, and the optical *density/thickness*, respectively.

Finally, the monochromatic absorptivity of the layer is defined as $1 - T_\lambda$, i.e.:

$$\alpha_\lambda = 1 - T_\lambda = 1 - e^{-\frac{\tau}{\mu}} \tag{3.22}$$

3.5.8 *Reflection and absorption by an atmospheric layer*

Applying the conservation of energy for every atmospheric layer that the incoming radiation is passing through, leads to:

$$\alpha_\lambda{}^f + R_\lambda{}^f + T_\lambda{}^f = 1 \tag{3.23}$$

α, R, and T are every layer's absorptivity, reflectivity, and transmissivity fluxes. The incoming radiation can be scattered multiple times when it passes through a given layer, resulting in diverse ray paths. The initial parallel beam can be deviated on multiple scattering or isotropic radiation if there is no absorption. There are three essential parameters utilized for the optical characterization of aerosols, cloud droplets, and ice crystals:

- **The volume extinction coefficient** $N\sigma\beta_\lambda$: describes how particles decrease the incoming radiation intensity by absorption or scattering.

- **Single scattering albedo:** See subsection 3.5.6.2.

- **The asymmetry parameter:** It is defined as:

$$g(\lambda) = \frac{1}{2} \int_{-1}^{1} P(\cos\theta') \cos\theta' d\cos\theta' \tag{3.24}$$

Here, $P(\cos\theta')$ is the so-called scattering phase function and θ' is the angle between the incoming and the scattered radiation.

3.6 ATMOSPHERIC WINDOWS AND GREENHOUSE EFFECT

3.6.1 *Atmospheric windows*

Atmospheric windows are defined as the range of wavelengths where the atmosphere becomes transparent, i.e., there is a relatively small absorption of the incoming radiation by the atmospheric gases. Figure 3.8 shows the most important and well-known window between 8 and 13 μm (AMS, 2022).
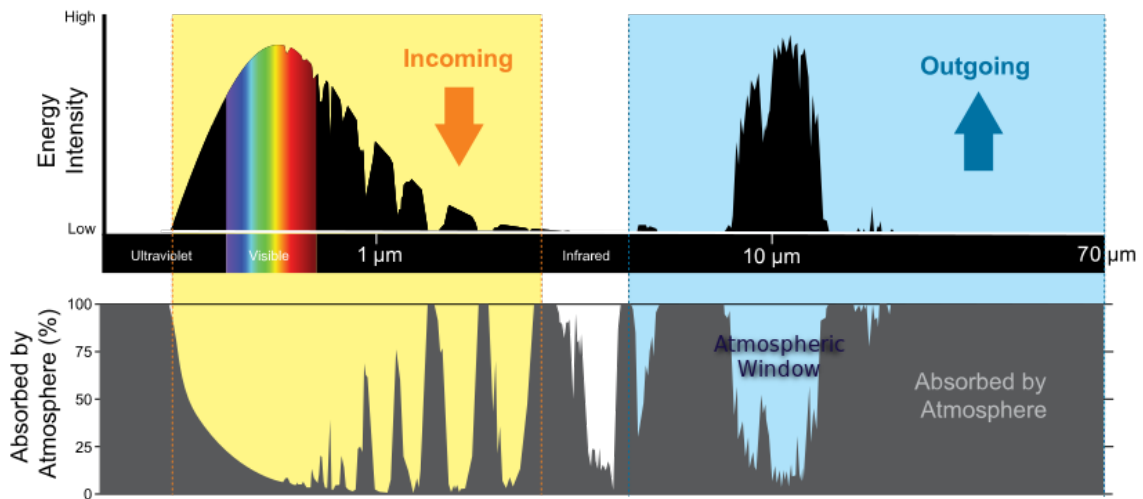
Figure 3.8: Upper panel: Incoming solar energy and outgoing thermal energy to the atmosphere. The bottom panel shows the energy absorbed by the atmosphere including the atmospheric window. Figure taken from https://www.weather.gov/jetstream/absorb, last access 26 July 2022.

3.6.2 *The greenhouse effect*

The Sun is the primary energy source for Earth. From the solar radiation balance as outlined in Figure 3.9, approximately one-third of the radiation that reaches the TOA is directly reflected back into the space. The other 2/3 are mainly absorbed by the Earth's surface and the atmosphere. In order to balance the energy absorbed, the Earth has to radiate the same amount back to space. The temperature on Earth's surface is much colder than that on the Sun; therefore, it thermally emits at much longer wavelengths, which are partly absorbed by the atmosphere and re-radiated back to the Earth's surface. This so-called greenhouse effect is responsible for an additional heating of the Earth's surface. Without the natural greenhouse effect, life on Earth may not be possible because the ground temperature would be below 0° C. However, humankind's activities, especially those linked to burning fossil fuels and deforestation, have seriously increased the greenhouse effect and raised Earth's surface temperature, leading to a global warming of $\sim$ 1.5°C above pre-industrial levels (Forster et al., 2021).

As described in Table 2.3, the atmosphere is mainly composed of nitrogen (78%) and oxygen (21%), whose effect on the greenhouse effect is almost negligible. The greenhouse
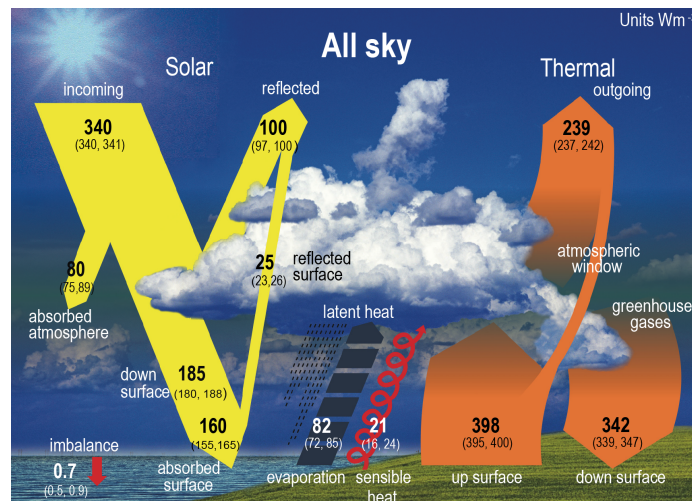
Figure 3.9: Diagram showing all the components of the Earth's energy budget. Taken from (Forster et al., 2021)

effect depends on the atmospheric abundance of other molecules which are effectively interacting with thermal infra-red (IR) radiation. In terms of their abundances, water vapor is the most important GHG, followed by CO_2. Other gases contribute to the greenhouse effect, but their atmospheric concentrations are much lower than H_2O and CO_2. Naturally, multiple parts of the Earth's climate system affect the abundance of greenhouse gases in the atmosphere; for example, plants remove atmospheric CO_2 via photosynthesis during daylight. However, anthropogenic emissions, mainly from burning fossil fuels and coal, injected a tremendous amount of greenhouse gases during the industrial era and have not stopped until now. The increase of GHGs in the atmosphere by human activities increases the greenhouse effect and, therefore, the warming of the Earth's climate. As temperature rises, atmospheric water vapor increases too, further intensifying the greenhouse effect. Since the greenhouse effect has a tremendous repercussion on the energy budget of Earth (incoming and outgoing radiation), it is essential to introduce a variable called "Effective Radiative Forcing (ERF)," which accounts for the atmospheric change in the energy flux caused by biogenic or anthropogenic sources as measured at the TOA, which are summarized in Figure 3.10 (Forster et al., 2021).

3.7 THE RADIATIVE TRANSFER EQUATION (RTE)

[4]Radiative transfer in the atmosphere is critically important because accurate knowledge of it:

1. Helps to quantify the greenhouse effect and, therefore, climate change;

2. allows us to determine the efficiency of the photochemical reaction on Earth's atmosphere; and

---

4 This subsection is based on the book Guzzi, Lanzerotti, and Platt. (2011).
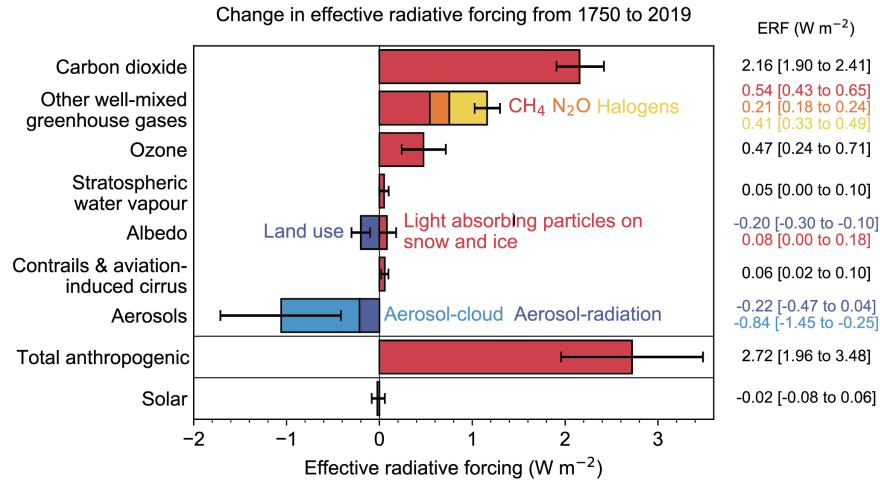
Figure 3.10: Diagram showing the change in Effective Radiative Forcing (ERF) from 1750 to 2019 due to CO_2, other well-mixed GHGs, O_3, H_2O, surface albedo, contrails, and aviation-induced cirrus, aerosols, total anthropogenic contribution, and solar radiation. Figure taken from Forster et al. (2021)

3. electromagnetic radiation sources and their atmospheric transport within the atmosphere are crucial for the trace gases and aerosol retrievals used in this thesis.

In real life, radiative transfer models are complex because they are composed of systems of equations that cannot be solved analytically, and this demands substantial computational resources.

Considering a stream of radiation travelling through the atmosphere the RTE represents all the possible interactions of the radiation with the atmosphere constituents: emission, single or multiple scattering, and absorption. The RTE integrates the changes in the radiance L_λ while crossing the atmosphere, which changes dL_λ after passing through an layer of thickness dz, and described by Equation 3.25:

$$\frac{dL_\lambda}{dz} = \underbrace{-\beta_{ext}(\lambda)L_\lambda}_{1} + \underbrace{\beta_{abs}(\lambda)B(\lambda,T)}_{2} + \underbrace{\frac{\beta_{scat}(\lambda)}{4\pi}\int_{4\pi} P(\Omega',\Omega)L_\lambda(\Omega')d\omega'}_{3} \qquad (3.25)$$

Here, the term **1** is the loss due to absorption and scattering of incoming radiation, and the term **2** is the increase of radiance due to thermal self emission. The term **3** describes the scattering of radiation into the direction of the beam under consideration. Calculation of this term is especially difficult, as it requires knowledge of the radiance from all directions, moreover, the resulting contribution depends on the directional characteristics of the scattering molecules and particles (see Section 3.5).

Generally, Equation 3.25 cannot be solved by analytical methods. However, depending on the wavelength range, two simplifications are possible:

- **Short wavelengths (UV-Vis):** The Planck term is neglected, transforming Equation 3.25, into:

$$\frac{dL_\lambda}{dz} = -\beta_{ext}(\lambda)L_\lambda + \frac{\beta_{scat}(\lambda)}{4\pi} \int\limits_{4\pi} P(\Omega',\Omega)L_\lambda(\Omega')d\omega' \qquad (3.26)$$

- **Thermal infrared radiation:** For direct solar absorption spectroscopy in this spectral range, scattering effects become negligible, and then the Equation 3.25 is reduced to:

$$\frac{dL_\lambda}{dz} = \beta_{abs}(\lambda)(B(\lambda,T) - L_\lambda) \qquad (3.27)$$

by using the optical density definition for this case $d\tau = \beta_{abs}dz$, last equation simplifies to the so-called Schwarzschild's equation (3.28):

$$\frac{dL_\lambda}{d\tau} = B(\lambda,T) - L_\lambda \qquad (3.28)$$

When working in the near infrared (NIR), Equation 3.27 can be further simplified by neglecting the thermal self emission source term, reducing the RTE into a simple description of attenuation by absorption, as described by the Beer-Lambert equation:

$$\frac{dL_\lambda}{dz} = -\beta_{abs}(\lambda)L_\lambda \qquad (3.29)$$

3.8 INTERACTION OF ELECTROMAGNETIC RADIATION WITH MOLECULES

The ground-based remote sensing techniques utilized in this thesis derive the atmospheric abundances of greenhouse and trace gases based on the interaction of the incoming electromagnetic radiation with matter. The accuracy of the retrieved species amount depends on the knowledge of these interactions; for that reason, a short introduction is given in the following subsections.

3.8.1 Photochemistry

In a photochemical process, a given molecule AB absorbs a photon switching its state to an often short-lived intermediate excited state AB*. Following the excitation several processes are possible to return or to keep thermochemical equilibrium, Table 3.2 shows the most important processes.

C_1, C_2, and M are other molecules. If a photon is absorbed, there is a probability that more than one of these routes will happen. The bond energy and the photon wavelength, which is equivalent to it, are essential because photolysis occurs when the photon has

Photolysis	$AB^* \rightarrow A + B$
Ionization	$AB^* \rightarrow AB + e$
Luminiscence	$AB^* \rightarrow AB + h\nu\prime$
Intramolecular transfer	$AB^* + AB \rightarrow AB + AB^{**}$
Intermolecular transfer	$AB^* + M \rightarrow AB + M^*$
Collisional deactivation	$AB^* + M \rightarrow AB + M$
Photochemical reaction	$AB^* + M \rightarrow C_1 + C_2$

Table 3.2: Photochemical processes that a molecule AB can go through. Data taken from Grainger (2013).

energy larger or equal to the bond energy to break the bond. It is important to note that only solar photons provide enough energy to create notable atmospheric photolysis. In the electromagnetic wavelength range, photons of visible or higher frequencies are required in photolysis reactions. In Table 3.3 these values are shown for several atmospheric species, and the most important photolysis reactions that occur in the atmosphere are shown in Table 3.4.

Bond	Energy [kJ mol^{-1}]	Photon's wavelength [nm]
$C \equiv C$	812	147.3
$C = O$	728	164.3
$C = C$	615	194.5
$O = O$	498	240.2
$H - H$	436	274.4
$H - O$	464	257.8
$C - H$	414	289.0
$C - O$	360	332.3
$C - C$	347	344.7
$Cl - Cl$	244	490.3
$F - F$	158	757.1

Table 3.3: Example of bond energy for some atmospheric gases. Data taken from Grainger (2013)

3.8.2 *Absorption molecular spectrum*

A molecule's absorption spectrum is much more complex than those for a single mono-atomic gas because, in the molecule, there could be transitions between different energy states involving nuclei vibrations and rotations. In the Born-Oppenheimer approximation,

Reaction	Taking place in:	Importance
$O_2 + h\nu \rightarrow O + O$	Stratosphere	Formation of O_3
$O_3 + h\nu \rightarrow O_2 + O$	Stratosphere	Balance between atomic oxygen and O_3
$O_3 + h\nu \rightarrow O_2 + O^{1D}$ $O^{1D} + H_2O \rightarrow 2OH$	Troposphere	Formation of OH
$NO_2 + h\nu \rightarrow NO + O$ $O + O_2 + N_2 \rightarrow O_3 + N2$	Troposphere	Formation of O_3

Table 3.4: Some of the most important photolytic reactions happening in the Earth's atmosphere. Data have been taken from Grainger (2013).

the total energy of an individual molecule is given by the sum of the electronic (E_{el}), vibrational (E_{vib}), and rotational energy (E_{rot}).

$$E = E_{el} + E_{vib} + E_{rot} \tag{3.30}$$

The associate energy change for the electron's excitation ($\delta E_{el} \sim 1$ eV) is larger than that for the molecular vibration ($\delta E_{vib} = h\nu_{vib} \sim 10^{-2} eV$). Therefore, $h\nu_{el} \gg h\nu_{vib} \gg h\nu_{rot}$.

The various transitions occurring within the rotation, vibration, and electronic energy level belong to the far-infrared - microwave, infrared, and ultraviolet-visible spectral range, respectively. Generally, vibrational and electronic transitions also incorporate changes in the rotational and vibrational and rotational modes, respectively.

Absorption takes place when a given molecule interacts with the incoming electromagnetic radiation. Such a molecule has to have an electronic variable dipole moment that oscillates during the transition. Trace gases like H_2O, and O_3 are complicated, and they indeed own both permanent electric dipoles and vibrationally induced moments. However, the two more abundant atmospheric gases, N_2 and O_2, do not interact via the electric dipole; therefore, these gases do absorb weakly in the infrared region.

3.8.3 *Vibration and rotation*

Within the infrared spectral region, the vibrational and rotational molecular transitions and several additional electronic transitions of atoms and molecules occur. This spectral region is essential for molecular spectroscopy because each molecule's vibrational bands are unique. In this section, two phenomena are described: (1) rotating molecules produce stretching in the molecule's chemical bonds due to centrifugal forces, having an effect on the rotational spectra; and (2) the atoms in a molecule do not remain in relatively fixed locations but instead, vibrate about a mean position. Here, the case of diatomic and polyatomic molecules are considered .

3.8.3.1 *The harmonic oscillator*

The harmonic oscillator is a fundamental and straightforward quantum mechanics model used to describe the vibration of diatomic and polyatomic molecules. The harmonic os-

cillator is described by a particle moving in a straight line constraint by the potential $V = \frac{kx^2}{2}$, where k is Hooke's constant. The Hamiltonian and the wave equation of the system is given by:

$$H = \frac{p^2}{2m} + \frac{1}{2}kx^2 \quad \text{,and} \quad \frac{d^2\psi}{dx^2} + \frac{8\pi^2 m}{h^2}\left(E - \frac{1}{2}kx^2\right)\psi = 0 \tag{3.31}$$

Introducing the following abbreviations, and changing variables accordingly:

$$\alpha = \frac{8\pi^2 m}{h^2}E \quad , \quad \beta = \frac{2\pi\sqrt{mk}}{h} \quad , \quad \xi = \sqrt{\beta}x \quad \text{, and} \quad \frac{d^2}{dx^2} = \beta\frac{d^2}{d\xi^2} \tag{3.32}$$

We find 3.33:

$$\frac{d^2\psi}{d\xi^2} + \left(\frac{\alpha}{\beta} - \xi^2\right)\psi = 0 \tag{3.33}$$

From Equation 3.33, we have to infer the form of ψ for large values of ξ. If ξ is large enough the ratio $\frac{\alpha}{\beta}$ can be neglected in comparison to ξ^2 so that the equation turns into:

$$\frac{d^2\psi}{d\xi^2} - \xi^2\psi = 0 \tag{3.34}$$

The solution to the last equation is:

$$\psi(\xi) = u(\xi)e^{-\frac{\xi^2}{2}} \tag{3.35}$$

By substitution of Equation 3.35 into Equation 3.33, it is found that the energy E is quantized as follows:

$$E = \frac{h}{2\pi}\left(n + \frac{1}{2}\right)\sqrt{\frac{k}{m}} = \left(n + \frac{1}{2}\right)h\nu \quad , \quad n = 0, 1, \dots \tag{3.36}$$

And finally, the normalized wave function is found to have the following form:

$$\psi_n(\xi) = N_n H_n(\xi)e^{-\frac{\xi^2}{2}} \quad \text{with} \quad N_n = \left(\sqrt{\frac{\beta}{\pi}}\frac{1}{2^n n!}\right)^{1/2} \tag{3.37}$$

where H_n are the Hermite polynomials.

In conclusion, in an ideal case of harmonic oscillation behaviour, the energy levels are equidistant.

3.8.3.2 *Vibration of diatomic molecules*

Here the vibrations of the two atoms relative to each other are considered. The fundamental vibration in this kind of molecule is when each atom moves back and forth from the other in a harmonic way. Homonuclear molecules like Cl_2 have zero dipole moment, i.e., they do not have electric dipole-allowed pure rotational/vibrational spectra. Nevertheless, these molecules have weak electric quadrupole vibrational transitions that can be measured with long path distances. Electric quadrupole transitions are $\sim 10^{-6}$ weaker than typical infrared transitions occurring on heteronuclear molecules such as HCl that own electric dipole (Bernath, 2016).

The assumption of an harmonic oscillator potential is very approximative for molecules. A more realistic potential V is defined by the *Morse function*, see Figure 3.11 as,

$$V(r) = D(1 - e^{-\beta(r-r_e)})^2 \tag{3.38}$$

Where D is the molecular dissociation energy resulting when $r \to \infty$; and β is a constant different for each molecule.
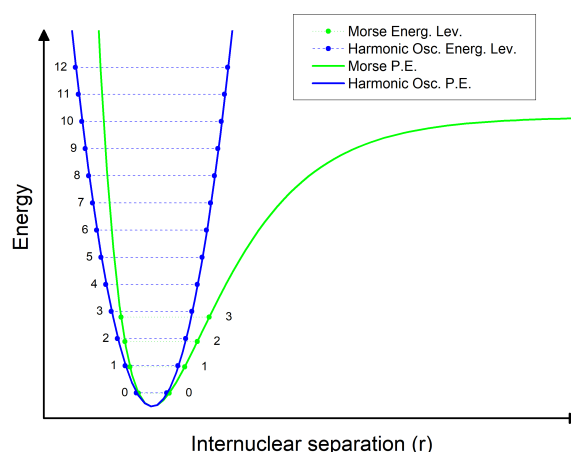
Figure 3.11: Illustration of the potential energies and their vibrational states given by the harmonic oscillator and Morse function, respectively.

Another essential quantity that is necessary for determining the vibrational energy is the so-called reduced mass (see Equation 3.39).

$$\mu = \frac{m_1 m_2}{m_1 + m_2} \tag{3.39}$$

Assuming that r_1 and r_2 are the distances of each to the molecule's center of mass, we have:

$$m_1 r_1 = m_2 r_2 \quad \text{if} \quad r = r_1 + r_1 \quad \text{then} \quad r_1 \quad \text{and} \quad r_2 \quad \text{are given by:} \tag{3.40}$$

$$r_1 = \frac{m_2}{m_1 + m_2} r \quad , \quad r_2 = \frac{m_1}{m_1 + m_2} r \tag{3.41}$$

The Kinetic energy, Hamiltonian, and Schrödinger equation of the system are then defined by Equations 3.42, 3.43, and 3.44 respectively.

$$K = \frac{1}{2}m_1\dot{r}_1^2 + \frac{1}{2}m_2\dot{r}_2^2 = \frac{1}{2}\mu\dot{r}^2 \qquad (3.42)$$

$$H = \frac{1}{2}\mu\dot{r}_1^2 + V(r) \quad \text{with} \quad V(r) = \frac{1}{2}k(r - r_e)^2 \qquad (3.43)$$

$$\frac{d^2\psi}{dr^2} + \frac{8\pi^2\mu}{h^2}[E - V(r)]\psi = 0 \qquad (3.44)$$

The solution of Equation 3.44 provides the wave function and energy of the diatomic molecule, as follows:

$$\psi_n(\xi) = \left(\frac{\sqrt{\beta/\pi}}{2^n n!}\right)^{1/2} H_n\left(\sqrt{\beta}x\right) e^{-\frac{1}{2}\beta x^2} \quad \text{with} \quad \beta = 2\pi\frac{\sqrt{\mu k}}{h} \qquad (3.45)$$

$$E = \frac{h}{2\pi}\left(v + \frac{1}{2}\right)\sqrt{\frac{k}{\mu}} = \left(v + \frac{1}{2}\right)h\nu \qquad (3.46)$$

3.8.3.3 Rotation of diatomic molecules

In addition to the space coordinates (x_i, y_i, z_i), the masses m_i and the distance R between both atoms; the center of mass coordinates (x, y, z), and the spherical coordinates (r, θ, ϕ) are utilized, see Figure 3.12.
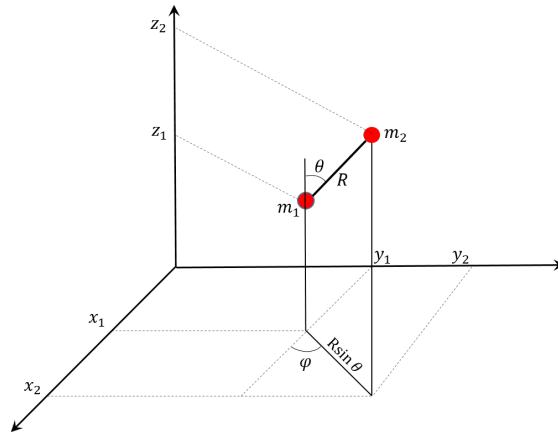
Figure 3.12: Rigid rotator coordinates. Modified from Griffiths and Haseth (2007)

In our system, the spherical coordinates follow:

$$x_2 - x_1 = R\sin\theta\cos\phi \quad , \quad y_2 - y_1 = R\sin\theta\sin\phi \quad , \text{and} \quad z_2 - z_1 = R\cos\theta \qquad (3.47)$$

The center of mass of the system is given by:

$$x = \frac{m_1 x_1 + m_2 x_2}{m_1 + m_2} \quad , \quad y = \frac{m_1 y_1 + m_2 y_2}{m_1 + m_2} \quad , \text{ and } \quad z = \frac{m_1 z_1 + m_2 z_2}{m_1 + m_2} \tag{3.48}$$

Raising the variables a, and b:

$$a = \frac{m_2}{m_1 + m_2} R \qquad b = \frac{m_1}{m_1 + m_2} R \tag{3.49}$$

The kinetic energy of the system is then written as follows:

$$K = \frac{m_1 a^2 + m_2 b^2}{2} \left[\left(\frac{d\theta}{dt} \right)^2 + \sin^2 \theta \left(\frac{d\phi}{dt} \right)^2 \right] \tag{3.50}$$

The quantum mechanical Hamiltonian in spherical coordinates can be written as (Zdunkowski, Trautmann, and Bott, 2007)

$$H = -\frac{h^2}{8\pi^2 m} \left[\frac{1}{r^2} \frac{\partial}{\partial r} \left(r^2 \frac{\partial}{\partial r} \right) + \frac{1}{r^2 \sin \theta} \frac{\partial}{\partial \theta} \left(\sin \theta \frac{\partial}{\partial \theta} \right) + \frac{1}{r^2 \sin^2 \theta} \frac{\partial}{\partial \varphi^2} \right] + V \tag{3.51}$$

Assuming no external forces, $r = 1$, and $mr^2 = m = I$; Schrödinger's equation is found to be:

$$\frac{1}{\sin \theta} \frac{\partial}{\partial \theta} \left(\sin \theta \frac{\partial \psi}{\partial \psi \theta} \right) + \frac{1}{\sin^2 \theta} \frac{\partial^2 \psi}{\partial \varphi^2} + \frac{8\pi^2 I E}{h^2} \psi = 0 \tag{3.52}$$

Because this differential equation has two independent variables, we need a solution of the form: $\psi = \Theta(\theta)\Phi(\varphi)$. Omitting all the math required to solve the equation, we come up with the solution and the energy in Equations 3.53 to 3.56.

$$\Phi(\phi) = \Phi_M(\phi) = \frac{1}{\sqrt{2\pi}} e^{\pm iM\phi} \quad , \quad M = 0, 1, \dots \tag{3.53}$$

$$\Theta(\theta) = \Theta_J^{|M|}(\theta) = \sqrt{\frac{(2J+1)}{2} \frac{(J-|M|)!}{(J+|M|)!}} P_J^{|M|}(\cos \theta) \tag{3.54}$$

$$\psi_{J,M} = \Phi_M(\phi) \Theta_J^{|M|}(\theta) \tag{3.55}$$

$$\frac{8\pi^2 I E}{h^2} = J(J+1) \quad \text{or} \quad E = \frac{h^2}{8\pi^2 I} J(J+1) \quad , \quad J = 0, 1, \dots \tag{3.56}$$

The suitable wave functions depend on the rotational J and magnetic M quantum numbers. As a rule, for every value of J, there will be $2J + 1$ values for M, which is called degeneracy, because all these wave functions have the same energy.

As mentioned earlier, the molecule needs to have a permanent dipole moment to either interact with the radiation and produce molecular rotation or for a rotating molecule to emit or absorb radiation. The selection rule governing the rotational transitions follows:

$$\Delta J = J' - J'' = \pm 1 \tag{3.57}$$

A rotating molecule's absorbed/emitted frequencies ν_R are linked to the ΔE between adjacent energy levels. Using the Equation 3.56, we find:

$$\nu_R = \frac{h}{8\pi^2 I}[J'(J' + 1) - J''(J'' + 1)] = \frac{h}{4\pi^2 I}(J'' + 1) \quad , \quad J' > J'' \tag{3.58}$$

3.8.3.4 Vibration-rotation of diatomic molecules

Interaction of the molecule with infrared radiation changes its vibrational and rotational states. For describing the rotational state of the molecule the non-rigid rotator is used, which consists of two punctual masses connected by a spring with negligible mass. Using the Hamiltonian of the system we found the following wave function:

$$\frac{1}{r^2}\frac{\partial}{\partial r}\left(r^2\frac{\partial\psi}{\partial r}\right) + \frac{1}{r^2\sin\theta}\frac{\partial}{\partial\theta}\left(\sin\theta\frac{\partial\psi}{\partial\theta}\right) + \frac{1}{r^2\sin^2\theta}\frac{\partial^2\psi}{\partial\varphi^2} + \frac{8\pi^2\mu}{h^2}[E - V(r)]\psi = 0 \tag{3.59}$$

The procedure to solve and find the energy is similar to the one described in the previous section. The Schrödinger equation for the r-variable of the wave function has the form:

$$\frac{1}{r^2}\frac{\partial}{\partial r}\left(r^2\frac{\partial\psi}{\partial r}\right) + \left(\frac{8\pi^2\mu}{h^2}[E - V(r)] - \frac{J(J+1)}{r^2}\right)\psi_r = 0 \tag{3.60}$$

And the energy of the system,

$$E = \left(v + \frac{1}{2}\right)h\nu_e + J(J+1)\frac{h^2}{8\pi^2 I} - \frac{J^2(J+1)^2 h^4}{128\pi^6\nu_e^2 I^2} \quad \text{with} \quad \nu_e = \frac{1}{2\pi}\sqrt{\frac{k}{\mu}} \tag{3.61}$$

As in the previous section, the Morse function is used to find a solution for the frequency, which yields to:

$$\begin{aligned}
\bar{\nu} = \frac{E}{hc} &= \bar{\nu}_e\left(v + \frac{1}{2}\right) - x_e\bar{\nu}_e\left(v + \frac{1}{2}\right)^2 + J(J+1)B_e - J^2(J+1)^2 D_e \\
&- \alpha_e\left(v + \frac{1}{2}\right)J(J+1)
\end{aligned} \tag{3.62}$$

where:

$$\bar{\nu}_e = \frac{\beta}{2\pi c}\left(\frac{2D}{\mu}\right)^{1/2} \quad , \quad D_e = \frac{h^3}{128\pi^6\mu^3\bar{\nu}_e{}^2c^3r_e{}^6} \quad , \quad B_e = \frac{h}{8\pi Ic} \quad ,$$

$$x_e = \frac{h\bar{\nu}_e c}{4D} \quad , \quad \alpha_e = \frac{3h^2\bar{\nu}_e}{16\pi^2\mu r_e{}^2D}\left(\frac{1}{\beta r_e} - \frac{1}{\beta^2 r_e{}^2}\right)$$

(3.63)

From Equation 3.62, the first term is the harmonic oscillator, the second corrects the anharmonicity as described by the Morse function, the third and fourth describe the rotational energy, and the fifth, the coupling of vibration and rotation. The selection rule for J keeps the same as before. The vibrational transitions are not restricted to $\Delta\nu > \pm 1$, but transitions with $\Delta\nu > \pm 2$ are very weak. In terms of the energy level diagram, the following equation is useful:

$$\bar{\nu}_0 = \bar{\nu}_e(\nu' - \nu'') - x_e\bar{\nu}_e\left[\left(\nu' + \frac{1}{2}\right)^2 - \left(\nu'' + \frac{1}{2}\right)^2\right] \quad , \quad \nu' > \nu''$$

(3.64)

Equation 3.64 describes the vibrational energy difference caused by the transition ν'' to ν'. The absorption and emission processes are considered between levels with quantum numbers ν'' and J'' and ν' and J' (ν' and ν'' are fixed values.)

If $J' - J'' = 1$ or -1, yields to Equation 3.65, as follows:

$$\bar{\nu}_R = \bar{\nu}_0 + 2(J+1)B_e \quad , \text{and} \quad \bar{\nu}_P = \bar{\nu}_0 + 2JB_e$$

(3.65)

These transitions are forming the R or P branch, respectively (See Figures 3.13 and 3.14). In one branch $\Delta\nu$ should increase with J, and in the other drecrease. In a few molecules, the transitions corresponding to $\Delta J = 0$ are permitted; such transitions generate the Q branch. Diatomic and polyatomic molecules having electronic angular momentum in the ground electronic state, such as NO, have a Q-branch. However, most diatomic molecules own a small angular momentum, so no Q-branch is observed.

3.9 SPECTRAL LINE SHAPE

A freely rotating molecule has rotational kinetic energy of the following form:

$$E_r = \frac{1}{1}I_x\omega_x{}^2 + \frac{1}{1}I_y\omega_y{}^2 + \frac{1}{1}I_z\omega_z{}^2$$

(3.66)

The rotation axis is given by x, y, and z; their corresponding moments of inertia are I_x, I_y, and I_z, which help to classify molecules in the four categories shown in Figure 3.15.

3.9.0.1 *Spectral line shapes*

Three properties mainly define the absorption line:
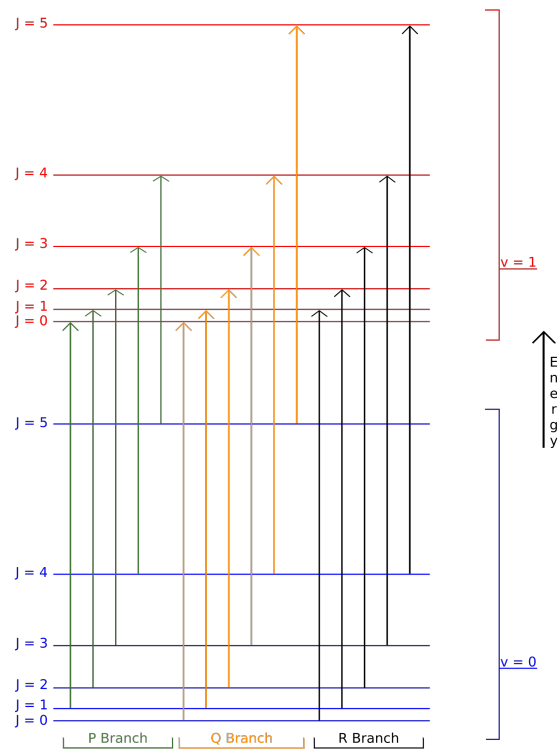
Figure 3.13: First P, Q and R transitions of the vibration-rotation for a diatomic molecule. Taken from https://commons.wikimedia.org/wiki/File:Vibrationrotationenergy. svg, last access: September 25, 2022.
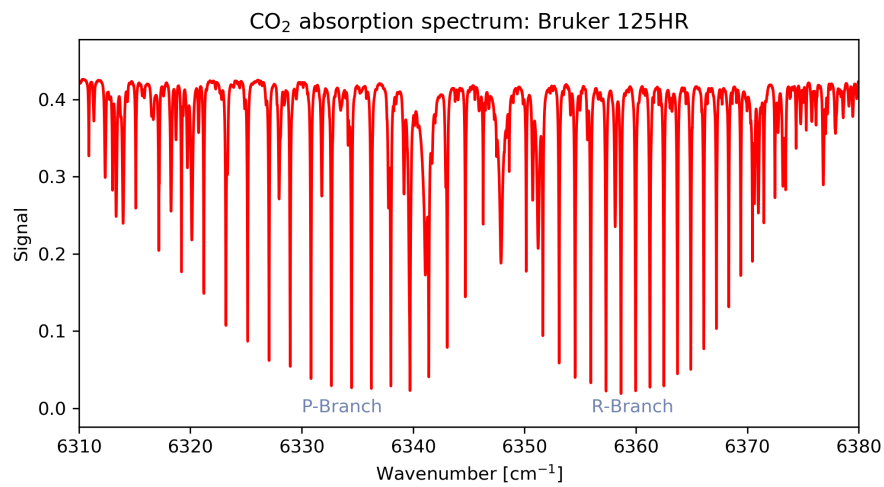
Figure 3.14: IR absorption spectrum of CO_2 measured with the Bruker 125HR spectrometer.

- Central position (frequency v_o or wavenumber ν_o)

- The intensity of the line (or strength, S)

- The shape (or profile, $f(x)$) of the line
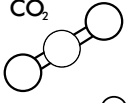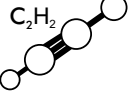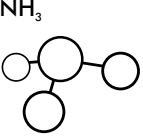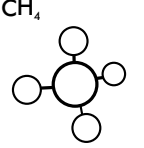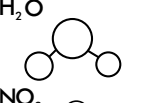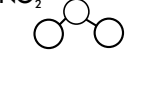
Types of molecules

Types	Linear molecules	Symmetric Tops	Spherical Tops	Asymmetric rotors
Relative Magnitudes of I a,b,c	$I_b = I_c$; $I_a \approx 0$	$I_b = I_c \neq I_a$; $I_a \neq 0$	$I_b = I_c = I_a$	$I_b \neq I_c \neq I_a$
Examples	CO_2 C_2H_2	NH_3	CH_4	H_2O NO_2

Relatively simple	No dipole moment	Largest category

Figure 3.15: Electronic rotors and their moments of inertia respectively.

These combined define the so-called mass absorption coefficient as follows:

$$k^{abs}(\tilde{v}) = S f(\tilde{v} - \tilde{v}_0) \tag{3.67}$$

The line strength is defined as:

$$S = \int_0^\infty k^{abs}(\tilde{v}) d\tilde{v} \tag{3.68}$$

$\tilde{v}_0$ is defined as the line center, and all the frequencies far from that value are called line wings. The shape factor is normalized to 1, so:

$$\int_0^\infty f(\tilde{v} - \tilde{v}_0) d\tilde{v} = 1 \tag{3.69}$$
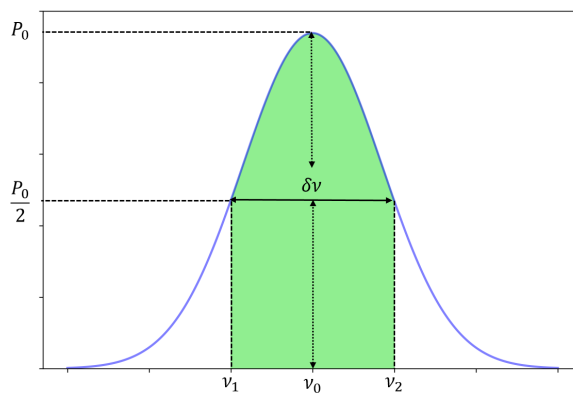
Figure 3.16: Line shape of a spectral line. Adapted from Demtröder (2006)

The broadening of a line is produced by tiny changes in the energy levels involved in a transition. Due to the limited duration of the transition every absorption line has a width,

referred to as the natural broadening of a spectral line. There are two processes occurring in the atmosphere dominating the resulting broadening of a given molecule's spectral line, such that:

1. Pressure broadening: due to the collisions between molecules

2. Doppler broadening: caused by the molecular thermal momentum.

3.9.0.2 *Natural linewidth*

A spontaneous emission caused by an excited atom can be described with the classical model of a damped harmonic oscillator with mass "m", spring constant "D", and eigenfrequency $\omega_0 = \sqrt{D/m}$. Therefore, the equation of motion is the following (where gamma is the damping constant)

$$\ddot{x} + \gamma \dot{x} + {\omega_0}^2 x = 0 \tag{3.70}$$

The solution to this equation is given by:

$$x(t) = x_0 e^{-(\gamma/2)t}[\cos \omega t + (\gamma/2\omega) \sin \omega t] \tag{3.71}$$

The damped oscillator frequency is given by $\omega = \sqrt{{\omega_0}^2 - (\gamma/2)^2}$, which is a bit lower than ω for the undamped oscillator. Generally, the damping constant δ is much smaller for excited atoms than ω_0. Then, the second term of the equation can be neglected resulting $\omega \sim \omega_0$, and then the previous solutions become more straightforward as:

$$x(t) \approx x_0 e^{-(\gamma/2)t} \cos \omega_0 t \tag{3.72}$$

Here and because $x(t)$, the frequency will not necessarily be monochromatic. Therefore and applying a Fourier transformation it is possible to get the frequency distribution of the amplitudes as follows:

$$\begin{aligned} A(\omega) &= \frac{1}{\sqrt{2\pi}} \int_{-\infty}^{+\infty} x(t) e^{i\omega t} dt \\ &= \frac{1}{\sqrt{2\pi}} \int_0^{+\infty} x_0 e^{-(\gamma/2)t} \cos \omega_0 t e^{i\omega t} dt \end{aligned} \tag{3.73}$$

The integration leads to:

$$A(\omega) = \frac{x_0}{\sqrt{8\pi}} \left[\frac{1}{i(\omega_0 - \omega) + \gamma/2} + \frac{1}{i(\omega_0 + \omega) + \gamma/2} \right] \tag{3.74}$$

The second term is neglected because in the proximity of the resonance frequency $|\omega - \omega_0| \ll \omega_0$.

The power spectral radiation density can be derived because $A(\omega)$ is $E(\omega)$, a Fourier component of the emitted radiation's electric field.

$$P_\omega(\omega) \propto A(\omega)A^*(\omega) = \frac{C}{(\omega - \omega_0)^2 + (\gamma/2)^2} \tag{3.75}$$

And the constant C satisfies:

$$\int_0^\infty P_\omega(\omega)d\omega = P_0 \tag{3.76}$$

The integration and solution of that integral yields to the Equation 3.77, called the "Lorentzian profile," and the fullwidth at half-maximum (FWHM) is then derived as:

$$\delta\omega_n = \gamma \Rightarrow \delta\nu_n = \gamma/2\pi \tag{3.77}$$

Finally, this FWHM is called "natural linewidth".

3.9.0.3 *Doppler Broadening*

The random motion of the molecules in the atmosphere produces this effect. Assuming that an excited atom moves with velocity $v = v_x, v_y, v_z$, the emitted wave is Doppler shifted; if the wave travels in the z direction, then:

$$\omega_a = \omega_0 + k_z v_z = \omega_0(1 + v_z/c) \tag{3.78}$$

At thermal equilibrium, the atom's velocities follow the Maxwell-Boltzmann distribution, and then the number density of atoms absorbing within $z + dz$ is:

$$n_i(v_z)dv_z = \frac{N_i}{v_\omega\sqrt{\pi}}e^{-(v_z/v_\omega)^2}dv_z \tag{3.79}$$

Where $v_\omega = (2k_BT/m)^{1/2}$, $N_i = \int_{-\infty}^{+\infty} n_i(v_z)dv_z$ and k_B is the Boltzmann constant.

Likewise before, the power spectral radiation density can be derived because is proportional to $n(\omega)d\omega$. Altogether yields to the Doppler-broadening of the emitted or absorbed lines, as follows:

$$n_i(\omega)d\omega = \frac{cN_i}{\omega_0 v_\omega\sqrt{\pi}}e^{-[c(\omega-\omega_0)/(\omega_0 v_\omega)]^2}d\omega \tag{3.80}$$

Equation 3.80 is a Gaussian function symmetric to ω_0; therefore, the FWHM can be derived as follows:

$$\delta\omega_D = |\omega_1 - \omega_2| \quad \text{with} \quad P(\omega_1) = P(\omega_2) = \frac{1}{2}P(\omega_0) \tag{3.81}$$

Using $v_\omega = (2k_BT/m)^{1/2}$, we get:

$$\delta\omega_D = 2\sqrt{\ln 2}\,\omega_0 v_\omega/c = (\omega_0/c)\sqrt{8k_BT\ln 2/m} \tag{3.82}$$

Doppler broadening is proportional to ω_0 and $\sqrt{T}$.

3.9.0.4 *Pressure (Collision) broadening*

This broadening is associated with molecular collisions that reduce the lifetime of a given excited state as compared to the natural broadening (see Equation 3.77) and is described with the Lorentzian function.

$$\phi(\nu)_{coll} = \frac{1}{\pi} \frac{\Delta\nu_c/2}{\pi(\nu - \nu_0)^2 + (\Delta\nu_c/2)^2} \tag{3.83}$$

In the last equation, the FWHM is determined by:

$$\Delta\nu_P = \frac{1}{2\pi\tau_{coll}c} \propto p \quad \text{with} \quad \tau_{coll} \propto \frac{\sqrt{T}}{p} \tag{3.84}$$

3.9.0.5 *The Voigt line shape*

The Voigt profile is defined as the convolution of Lorentzian and Gaussian profiles, which characterizes broadening under low-pressure conditions, see Figure 3.17. This profile is essential for atmospheric spectroscopy, where the accurate measurement of the line wings grants the separation of Doppler-broadening and natural broadening or pressure broadening.
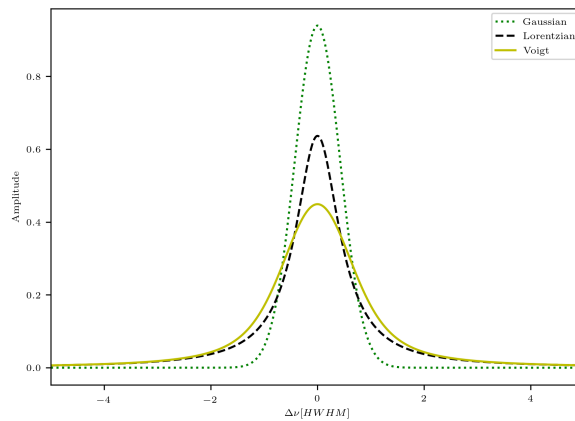
Figure 3.17: Gaussian, Lorentzian and Voigt profiles

FOURIER-TRANSFORM INFRARED SPECTROSCOPY

[1]Some important aspect as electromagnetic radiation, blackbody spectrum, and molecular shape are already described in Chapter 3.

4.1 THE FTIR SPECTROMETER

[2]An FTIR spectrometer is used to observe the chemical composition of the atmosphere. This instrument uses the rovibrational transitions discussed in Chapter 3, and especially in Figure 3.14. Therefore, in this section the most relevant aspects of these instruments are described.

4.1.1 *Michelson interferometer*

Generally the interferometers used in IR spectroscopy are based on the original two-beam interferometer built by the American physicist Albert Abraham Michelson approximately in the 19th/20th century. The instruments used for measuring the GHGs in the atmosphere within this thesis are also based on this spectrometer.

When incoming radiation passes through the Michelson interferometer, the beam is divided into two paths and recombined after adding a path difference; this setup allows to observe interference between both beams. The beam's intensity variability is measured by a detector as a function of the path difference. The elemental model of this interferometer is shown in Figure 4.1.

The ideal interferometer is composed of two mutually perpendicular plane mirrors, F and M, in Figure 4.1. M is moving along the axis perpendicular to its plane. Bisecting F and M has located the beamsplitter, which partially reflects and transmits the incoming collimated radiation beam to F and M, respectively ideally achieving a 50/50 division ratio. Once the beams reach F and M, they return to the beamsplitter, producing interference, and are partially reflected and transmitted again. The occurring interference affects the intensity of the recombined beam that reaches the detector/radiation source, which depends on the path difference of the beams in the interferometer's arms. This intensity variation as a function of the path difference yields the spectral information in Fourier transform spectrometers.

4.1.2 *Interferogram creation*

The interferogram, which is the final output of this kind of spectrometer, is the recorded interference as a function of the optical path difference (OPD). The signal that reaches the detector ($I'(\delta)$) is composed of two parts: a constant (DC) and modulated part (AC); this

---

1 This chapter is described based on Demtröder (2006) and Zdunkowski, Trautmann, and Bott (2007).
2 The notation here used follows Griffiths and Haseth (2007).
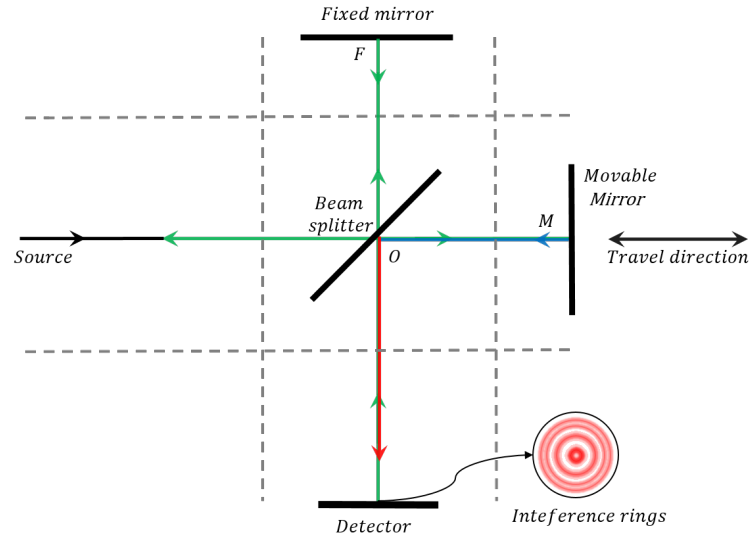
Figure 4.1: Illustration of the Michelson interferometer. Modified from (Griffiths and Haseth, 2007)

modulated part refers to the interferogram $I(\delta)$, which is the only important component for spectroscopic measurements. In case of monochromatic input, the signal becomes:

$$I'(\delta) = \frac{1}{2} I(\bar{v}_0)(1 + \cos 2\pi \bar{v}_0 \delta) \quad , \text{where} \quad \bar{v}_0 = \frac{1}{\lambda_0} \tag{4.1}$$

The AC part becomes:

$$I(\delta) = \frac{1}{2} I(\bar{v}_0) \cos 2\pi \bar{v}_0 \delta \tag{4.2}$$

It is essential to say that the amplitude of the interferogram as observed by the detector not only depends on the source's intensity but also on the beamsplitter efficiency, detector response, and amplifier details. Therefore the Equation 4.2 can be re-written as:

$$\begin{aligned} S(\delta) &= \frac{1}{2} H(\bar{v}_0) G(\bar{v}_0) I(\bar{v}_0) \cos 2\pi \bar{v}_0 \delta \\ &= B(\bar{v}_0) \cos 2\pi \bar{v} \delta \end{aligned} \tag{4.3}$$

Where, $B(\bar{v}_0)$ accounts for $H(\bar{v}_0)$ and $G(\bar{v}_0)$, which represent a wavenumber-dependent correction factor and the response of the detector/amplifier, respectively. When repeated measurements with the same interferometer hardware and operational settings are performed, mainly $I(\bar{v}_0)$ varies from one measurement to another.

4.1.3 *The Fourier transformation*

The interferogram $S(\delta)$ and the spectrum $B(\bar{v})$ are related via the Fourier Transformation. The mathematical formulation for the recorded interferogram and spectrum when the radiation source is a continuum, like sunlight, is given by:

$$
\begin{aligned}
S(\delta) &= \mathcal{F}^{-1}(B(\bar{v})) = \int_{-\infty}^{+\infty} B(\bar{v}) \cos 2\pi\bar{v}\delta d\bar{v} \\
B(\bar{v}) &= \mathcal{F}(S(\delta)) = \int_{-\infty}^{+\infty} S(\delta) \cos 2\pi\bar{v}\delta d\delta = \int_{0}^{+\infty} S(\delta) \cos 2\pi\bar{v}\delta d\delta
\end{aligned}
\tag{4.4}
$$

In reality, interferograms must be sampled discretely; therefore, the frequency range covered by the interferogram needs to be limited according to the *Nyquist criterion*. The discretization of Equation 4.4 leads to the so-called Discrete Fourier Transformation (DFT). The sampling interval h needs to be adjusted to the frequency range covered by the interferogram. The maximum sampling interval h in the interferogram needs to obey the condition $2h \leq (\bar{v}_{max} - \bar{v}_{min})^{-1}$.

The integral is changed to a summation and the intensity $B'(\bar{v}_1)$ is computed at any wavenumber $\bar{v}_1$, being $S_a(n)$ the interferogram value at this point, where N is the total number of sampled points.

$$
B'(\bar{v}_1) = S_a(0) + 2\sum_{k=1}^{N-1} S_a(k) \cos 2\pi\bar{v}_1 kh
\tag{4.5}
$$

4.1.4 *Finite resolution and instrumental line shape (ILS)*

The spectral resolution of a given interferometer depends on its maximum retardation or maximum optical path difference (OPD_{max}). So, the best resolution, $\Delta\bar{v}$ of an interferometer with OPD_{max} can be defined as:

$$
\Delta\bar{v} = \frac{1}{\text{OPD}_{max}}
\tag{4.6}
$$

When the interferometer is scan path restricted to OPD_{max}, it is understood that the interferogram's size is finite. For connecting this truncated with the full interferogram a boxcar truncation function $D(\delta)$ is imagined. Limiting the maximum retardation for a given interferogram to OPD [cm], the boxcar function adopts the following values:

$$
D(\delta) = \begin{cases} 1, & \text{if } -\text{OPD} \leq \delta \leq +\text{OPD} \\ 0, & \text{if OPD} > |\text{OPD}| \end{cases}
\tag{4.7}
$$

Multiplying by D(δ):

$$
B(\bar{v}) = \int_{-\infty}^{+\infty} S(\delta)D(\delta) \cos 2\pi\bar{v}\delta d\delta
\tag{4.8}
$$

By using the convolution theorem (Equation 4.9) stating that the Fourier transform (FT) for the product of the two functions is the convolution of the FT of each function, it can be shown that the FT of the first term $S(\delta)$ yields to the true spectrum, $B(\bar{v})$, while the FT of the second one D(δ), yields to $f(\bar{v})$, see Equation 4.10.

$$G(\bar{v}) = B(\bar{v}) \cdot f(\bar{v})$$
$$= \int_{-\infty}^{+\infty} B(\bar{v}')f(\bar{v} - \bar{v}')d\bar{v}' \tag{4.9}$$

$$f(\bar{v}) = 2(\text{OPD})\frac{\sin(2\pi\bar{v}\text{OPD})}{2\pi\bar{v}\text{OPD}}$$
$$\equiv 2(\text{OPD})\,\text{sinc}(2\pi\bar{v}\text{OPD}) \tag{4.10}$$

For a low-resolution spectrum measured with a monochromator, the true spectrum must be convolved with the slit function of the instrument; the equivalent for FT spectrometers is the *Instrumental Line Shape* (ILS) function $f(\bar{v})$. There are several criteria to specify the resolution of a given spectrometer, one of the more used techniques are the Rayleigh and the FWHM criteria. The first is commonly used for diffraction-limited grating spectrometers, while the second is for monochromators with triangular slit functions. The FWHM of a line that has a shape of the *sinc* function given by the Equation $f(\bar{v})$ results in:

$$\Delta\bar{v} = \frac{0.6035}{\text{OPD}_{max}} \tag{4.11}$$
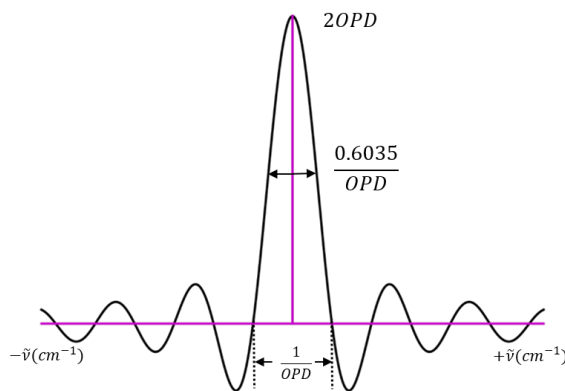
Figure 4.2: FT of a boxcar sinc x function, with amplitude = 1 and extending from +OPD to −OPD. Modified from (Griffiths and Haseth, 2007)

4.1.5 *Apodization*

The *sinc* function often results from the convolution with the boxcar function, provides the lowermost line representation; however it generates negative sidelobes in the spectrum if the line is not fully resolved. A method used to address this problem and reduce

these artifacts down to an acceptable level is known as apodization. Here, instead of the previous boxcar function, different functions A(δ) are used, see Figure 4.3 and Table 4.1.
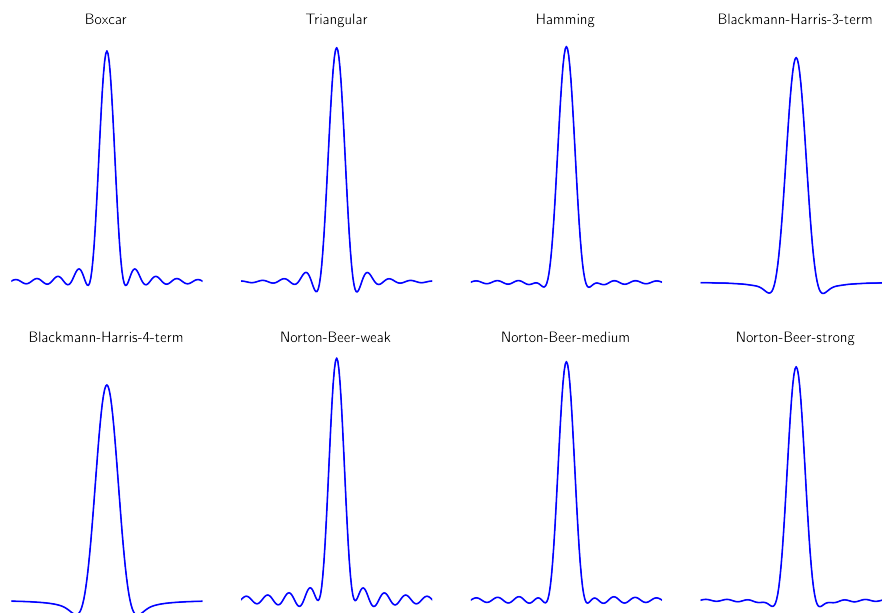
Figure 4.3: ILS calculated with different apodization functions for COCCON's reference unit SN37 by using LINEFIT

A(δ) can be used instead of the previous boxcar function. Then, as before, the FT of A(δ) is convolved with the true spectrum; this function would then determine the ILS. Depending on choices for apodization resolution criteria, different resolution values result, therefore it is useful to define as nominal resolution the factor: $\dfrac{1}{\text{OPD}}$ or to specify OPD$_{max}$ directly.

Name	Apodization function
Boxcar	$D(\delta) = \begin{cases} 1, & \text{if } |\delta| \leq \text{OPD} \\ 0, & \text{if } |\delta| > \text{OPD} \end{cases}$
Triangular	$D(\delta) \cdot \left[1 - \frac{|\delta|}{\text{OPD}} \right]$
Hamming (Happ–Genzel)	$D(\delta) = 0.54 + 0.46 \cos(\pi \frac{\delta}{\text{OPD}}$
Blackman	$D(\delta) = 0.35875 - 0.48829 \cos\left(2\pi \frac{\delta}{\text{OPD}} \right)$ $+ 0.14128 \cos\left(4\pi \frac{\delta}{\text{OPD}} \right) - 0.01168 \cos\left(6\pi \frac{\delta}{\text{OPD}} \right)$
Norton-Beer (weak)	$0.384093 - 0.087577 \left(1 - \frac{\delta}{\text{OPD}} \right) + 0.703484 \left(1 - \frac{\delta}{\text{OPD}} \right)^2$
Norton-Beer (medium)	$0.152442 - 0.136176 \left(1 - \frac{\delta}{\text{OPD}} \right) + 0.983734 \left(1 - \frac{\delta}{\text{OPD}} \right)^2$
Norton-Beer (strong)	$0.045335 + 0.554883 \left(1 - \frac{\delta}{\text{OPD}} \right)^2 + 0.399782 \left(1 - \frac{\delta}{\text{OPD}} \right)^4$

Table 4.1: Examples of apodization and ILS functions shown in Figure 4.3. The mathematical description was adapted from (Griffiths and Haseth, 2007; Parker et al., 1991)

DIFFERENTIAL OPTICAL ABSORPTION SPECTROSCOPY (DOAS)

[1]This chapter summarizes the most important aspects of the Differential Optical Absorption Spectroscopy (DOAS) technique, which, together with the FTIR one described in the previous chapter, are the central techniques used for the data presented in this thesis.

5.1 THE DOAS BASICS

The DOAS technique was introduced for the very first time by Perner and Platt (1979). Since then, and for more than four decades has become one of the most powerful techniques for measuring atmospheric trace gas and aerosol abundances. One of the most remarkable points is that many species were finally measured for the first time, e.g., OH by Perner et al. (1976), HONO by Perner and Platt (1979) and Platt, Perner, and Pätz (1980), NO_3 by Platt, Perner, and Pätz (1980), tropospheric BrO in the Artic by Hausmann and Platt (1994) and IO in the marine boundary layer by Alicke et al. (1999), stratospheric OClO, and BrO by Sanders et al. (1988), CHOCHO by Volkamer et al. (2005). Additionally, several other essential trace gases which absorb in the UV-Vis wavelength range, like O_3, NO_2, SO_2, HCHO, and ClO, have been extensively retrieved with this technique (Bobrowski et al., 2003; Dix et al., 2009; Friess et al., 2011; Halla et al., 2011; Heckel et al., 2005; Hendrick et al., 2014; Hönninger et al., 2004a,b; Leser, Hönninger, and Platt, 2003; Macdonald et al., 2012; Stutz et al., 2011; Theys et al., 2007).

The DOAS technique is very sensitive for all these gases, which have structured absorption cross-section structure in the UV-Vis spectral range. It allows the retrieval of reactive species such as halogen oxides (BrO, IO, etc.), OH, and NO_2. Furthermore, the fact that several species can be retrieved within a single wavelength range reduces measurement and analysis time.

Depending on the light source used, the DOAS technique can be either active or passive, as described below:

Active DOAS: Uses an artificial light source like Light Emitting Diodes (LEDs).
Passive DOAS: Uses a natural light source, mainly the Sun and Moon.

5.2 THE BEER-LAMBERT'S LAW

The DOAS method is based on the application of Beer-Lambert's law to the atmosphere in a specific wavelength range, which describes the attenuation of the initial light intensity I_0 (incoming radiation) due to the absorption that occurs in the atmosphere on its way from the Sun to the ground-based instrument's detector (for the instruments used in this thesis). For a simple absorber the Beer-Lambert's law can be written as:

$$I(\lambda) = I_0(\lambda)e^{-\sigma(\lambda)cL} \tag{5.1}$$

---

1 All the concepts and terminology are based on Platt and Stutz (2008).

Where I is the intensity measured at the surface, I_0 is the initial intensity, σ is the absorption cross-section of the trace gas, c is its concentration at the TOA, and L is the light path length through the atmosphere (see Figure 5.1).
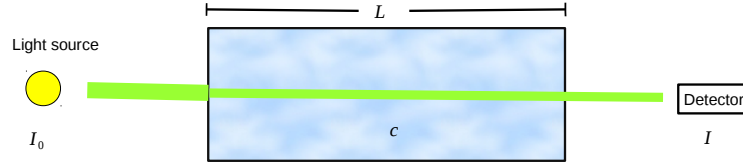
Figure 5.1: Scheme of the DOAS technique principles, described by Beer-Lambert's law. Adapted from Platt and Stutz (2008)

In this thesis, a passive DOAS technique using scattered sunlight was used; therefore, Equation 5.1 has to be transformed for an experiment with the Sun as the light source and including all the processes occurring in the atmosphere; with those considerations the extended version of that equation is:

$$I(\lambda) = I_0(\lambda) \exp\{- \int [\sum_{i=1}^{n} \sigma_i(\lambda,s)\rho_i(s) + \sigma_{Ray}(\lambda,s)\rho_{air}(s)+ \\ + \sigma_{Mie}(\lambda,s)\rho_{aer.}(s)]ds\} + I_{Raman} \tag{5.2}$$

Here n indicates the trace gases that absorb in the wavelength range in which the DOAS fit is performed. In the following, the rotational (called Ring effect) scattering is represented by a pseudo cross section σ with its density ρ. The Mie, and Rayleigh scattering are not pseudo cross sections because they are proportional to the density of the atmosphere and aerosols respectively. Therefore, Equation 5.2 can be re-written and a new term called *optical density* $\tau(\lambda)$ is defined as follows:

$$\tau(\lambda) = \ln \frac{I_0(\lambda)}{I(\lambda)} = \int [\sum_{i=1}^{n} \sigma_i(\lambda)\rho_i(s) + \sigma_{Ray}(\lambda)\rho_{air}(s)+ \\ + \sigma_{Mie}(\lambda)\rho_{aer.}(s)]ds \tag{5.3}$$

Then, another critical quantity is defined, the so-called Slant Column Densities (SCD) S_i, which is the concentration of a given trace gas along the optical light path:

$$S_i = \int \rho_i(s)ds \tag{5.4}$$

5.3 DIFFERENTIAL OPTICAL ABSORPTION SPECTROSCOPY

The retrieval of the SCD by Equation 5.4 requires that I_0 in Equation 5.3 is known. However, in MAX-DOAS (Multi AXis DOAS) applications, I_0 at TOA cannot be measured. Additionally, the measured absorption structure already contains the broad-banded spectral

fingerprints caused by Rayleigh and Mie scattering, which depend on the actual observing parameters like ground albedo, solar zenith angle, and aerosol information (Friess, 2001). To overcome these restrictions, the DOAS technique uses *differential quantities*, which is explained in the following.

Extinction by molecules and particles show a broad spectral behaviour. Many trace gases create highly structured spectral signatures. DOAS separates the broad and narrow-band structures from the cross sections according to:

$$\sigma_i(\lambda) = \sigma_i'(\lambda) + \sigma_i^b(\lambda) \tag{5.5}$$

Where $\sigma_i(\lambda)$ is the total absorption cross-section, while $\sigma_i'(\lambda)$, and $\sigma_i^b(\lambda)$ are the narrow, and smooth (broad) variation of the cross sections with respect to wavelength, respectively. In practice, this can be done in two different ways; the first one is applying a high pass filter to the absorption cross-sections and the measured spectrum, and the second one; by simply including a polynomial ($p_(\lambda)$) into the DOAS fit. Figure 5.2 shows an example of this approach applied on a NO$_2$ cross-section at 298 K (Vandaele, 1996).
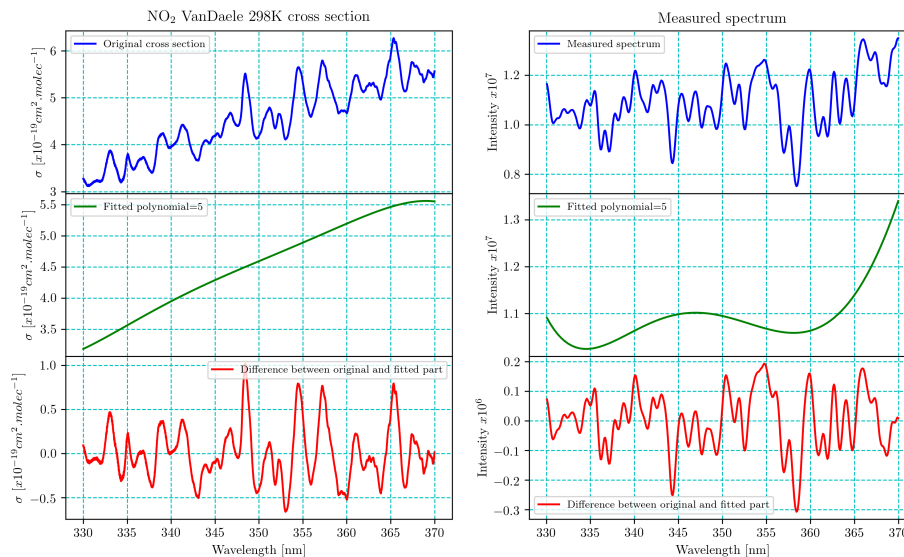
Figure 5.2: Separation of the NO$_2$ cross section into broad and narrow spectral components. The top panel shows the original cross-section and the measured spectrum, left to right respectively; the middle one shows a polynomial of order five fitted to both of them, which represents the smooth variation with wavelength; and finally, the bottom panel shows the differential cross-section and measured spectrum. The NO$_2$ data was taken from the MPI-Mainz UV/Vis spectral atlas of gaseous molecules of atmospheric interest www.uv-vis-spectral-atlas-mainz.org, last access: 03 October 2022.

In Equation 5.6 σ_i' explains the construction of the so-called *differential* absorption cross-section. The use of this quantity explains the name of the technique, *differential* absorption spectroscopy.

$$\sigma_i'(\lambda) = \sigma_i(\lambda) - p(\lambda) \tag{5.6}$$

The DOAS polynomial represents all the contributions that vary slowly with respect to the wavelength. Due to their smooth variation, including Rayleigh and Mie scattering. At this point, the strong fluctuation of the trace gas absorption structure can be isolated and analyzed with the DOAS method. Therefore, the Equation 5.3 is converted as follows:

$$\tau'(\lambda) = \ln \frac{I_0'(\lambda)}{I(\lambda)} = \sum_{i=1}^{n} \sigma_i'(\lambda) \text{SCD}_i + \sum_n c_n \lambda^n \tag{5.7}$$

where $I_0'(\lambda)$ includes $I_0(\lambda)$ and the broad-band structure produced by the trace gas absorption cross-section, and the Mie and Rayleigh extinction. $\tau'(\lambda)$ is the *differential* optical density. The second term of the equation is a low-order polynomial, usually between 2 and 5, representing the broad-band contributions of the trace gas absorption structure as described above. It is essential to mention that the Ring effect (rotational scattering) is included as an additional or pseudo-cross-section, see Section 5.6.3.

Therefore, trace gas SCDs in the atmosphere can be determined based on the optical density, the differential cross sections, and the fitted polynomial.

5.4 EXPERIMENTAL PROCEDURE

[2]A typical DOAS experiment is described in Figure 5.3. Light with intensity I_0 traverses the atmosphere and is collected in a telescope; it has been attenuated by the extinction processes in the atmosphere and now has a lower value I which goes through the slit's entrance of the spectrograph and it is dispersed by the grating, see Figure 5.3 a). Because of the limited spectral resolution of the spectrograph, the size, and shape of I changes. Mathematically, this is described by the convolution of I with the spectrograph's function H (see Figure 5.3 b).

$$I^*(\lambda, L) = I(\lambda, L)^* H \tag{5.8}$$

And finally, in order to be able to save the data in a digital computer, I^* has to be converted to binary data, which is done by an analog-digital converter (see Figure 5.3 c)

5.4.1 *Spectrograph's function H*

H is the spectrometer response to a received monochromatic light (λ_0). In real life, this is solved by using measurements of well-known narrow-band emission lines, such as from Mercury or Neon. This function is vital because it allows us to transform the high-resolution (HR) cross-section (σ_{HR}) to the resolution of a specific instrument, i.e., as if they had been measured with our equipment (σ_{LR}). Mathematically this process is described by the convolution of the cross-sections with H, as follows:

$$\sigma_{LR}(\lambda) = H * \sigma_{HR} = \int H(\lambda_0, \lambda) \sigma_{HR}(\lambda_0) d\lambda_0 \tag{5.9}$$

---

2 The following description is based on the overviews of Platt and Stutz (2008) and Stutz and Platt (1996).
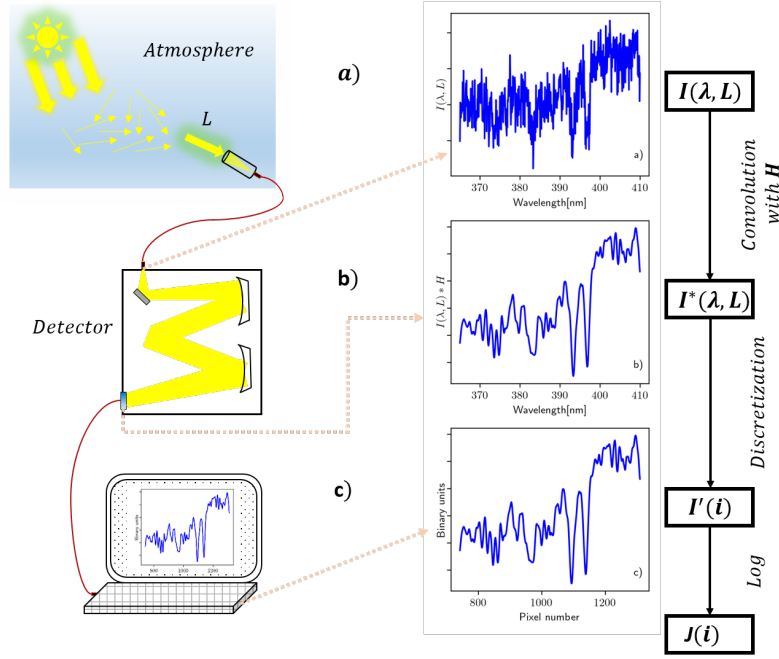
Figure 5.3: Description of the DOAS procedure, starting with the scattered sunlight collected in the telescope and ending with the final DOAS results. Modified from Hönninger (2002)

From the last equation, $H(\lambda_0, \lambda)$ is commonly not constant over λ_0 due to the optical characteristic of the instrument. The variation of the H over the wavelength can be approximated from the surrounding emission lines (Friess, 2001; Yilmaz, 2012).

As an important note, in most literature sources, the instrument function H is also called Slit Function Parameter (SFP_λ). In the following sections, we decide to name it like that.

5.5 DOAS RETRIEVAL

Having performed DOAS measurements in the atmosphere, the SCD can be derived by applying a least-squares fit to Equation 5.7 in a defined wavelength range (Platt and Stutz, 2008). During the fitting process, a Levenberg-Marquardt algorithm (Levenberg, 1944; Marquardt, 1963) minimizes the chi-square (χ^2) described in the following equation:

$$\chi^2 = \sum_k \left(\ln I(\lambda_k) - \ln I'_0(\lambda_k) + \sum_i \sigma'_i(\lambda_k) SCD_i + \sum_n c_n \lambda_k^n \right)^2 \overset{!}{\to} min \tag{5.10}$$

In the ideal case, χ^2 in Equation 5.10 must be integrated over the considered wavelength range; however, in practice, the integral is replaced for the sum over the discrete pixels covering the spectral window range instead ($\sum_k$).

Other significant quantities that help to define the quality of the DOAS fitting results are described as follows:

- **The residual:** It is the difference between the optical density of the observed and modeled spectrum. Mathematically defined as:

$$R_k = \ln I(\lambda_k) - \ln I_0'(\lambda_k) + \sum_i \sigma_i'(\lambda_k)\text{SCD}_i + \sum_n c_n \lambda_k^n \tag{5.11}$$

- **The χ^2:** defined as: $\chi^2 = \sum_k R_k^2$

- **The Root Mean Square (RMS):** defined as: $\text{RMS} = \sqrt{\dfrac{\chi^2}{k}} = \sqrt{\dfrac{1}{k}\sum_k R_k^2}$

  An unstructured Residual with values $< 10^{-3}$ is ideal for a good fit.

5.6 PASSIVE DOAS

When using the Sun as the light source several effects needs to be considered, these are briefly described in the following sections.

5.6.1 *Fraunhofer Lines*

The incoming radiation at the TOA has structured spectral lines due to the interaction of sunlight with the Sun's atmosphere. Those are called Fraunhofer lines, and their optical densities are around 2-3 orders of magnitude higher than the optical density of the trace gases in the UV-Vis range (Grossmann, 2014; Yilmaz, 2012). For that reason, it is essential to consider this effect in our analysis. In practice, this is considered by including a so-called Fraunhofer reference spectrum (FRS) which is a spectrum taken at an elevation angle of 90°, which also serves as I_0' spectrum in the DOAS fitting analysis.

5.6.2 *Solar I_0 effect*

This effect is caused by the limited spectral resolution of the spectrograph that measures the absorbed sunlight and the cross sections measured in the lab with a smooth light source, producing an incomplete removal of the Fraunhofer lines during the DOAS fit. This is basically because the exponent and convolution do not commute, i.e, $H * (e^{-\sigma s}) \neq e^{-(H*\sigma s)}$. Using modified absorption cross sections helps to overcome this problem (Wagner et al., 2001).

The modified cross sections can be calculated with the following equation proposed by Johnston (1996).

$$\sigma_{corr}(\lambda, S) = \frac{-ln\left(\frac{I^*(\lambda,S)}{I_0^*(\lambda)}\right)}{S} \tag{5.12}$$

Where I_0^* is the HR solar spectrum convolved with the spectrograph function. I_0^* is a modeled absorption spectrum calculated from the HR solar spectrum, convolved with

the spectrograph function, and S is an atmospheric column that has to be assumed. This effect is significant for strong absorbers, and it can be omitted for weak ones.

In this thesis, only NO_2 and O_3 are I_0 corrected. The usual values for S are: $1e^{-19}$ for O_3 and $1e^{-16}$ for NO_2. More details can be found in the analysis settings in Appendix C.1.

5.6.3 Ring effect

Inelastic rotational scattering in the atmosphere, also called the "Ring effect," produces a "filling-in" of the Fraunhofer lines. The observed measured intensity (I_{Meas}) at the ground can be written as:

$$I_{Meas} = I_{Rayleigh} + I_{Mie} + I_{Ring} = I_{elastic} + I_{Ring} \tag{5.13}$$

In the DOAS analysis, the optical densities are determined by comparing the logarithm of the intensities. Because the Raman (inelastic) component of the scattered light is small in comparison with the elastic one when taking the logarithm of Equation 5.13, a Taylor expansion can be applied and yields:

$$
\begin{aligned}
\ln(I_{Meas}) &= \ln(I_{elastic} + I_{Raman}) \\
&= \ln(I_{elastic}) + \ln\left(1 + \frac{I_{Raman}}{I_{elastic}}\right) \\
&\approx \ln(I_{elastic}) + I_{Ring}
\end{aligned}
\tag{5.14}
$$

where $I_{Ring} = \frac{I_{Raman}}{I_{elastic}}$. In this thesis, the Ring effect is considered by including a pseudo-cross-section (additional cross-sections) in the DOAS fit, which was calculated with QDOAS using the HR solar spectrum published by Chance and Kurucz (2010).

5.7 MULTI-AXIS DOAS (MAX-DOAS)

The MAX-DOAS technique was introduced by Hönninger G. and Platt (2004). The main difference from other DOAS approaches is its capability to measure the scattered sunlight at different elevation angles[3]. Each of those angles has its own sensitivity to the state of the atmosphere at the measurement time, which depends on the meteorological conditions, vertical distribution of the trace gases, aerosols, etc., in the atmosphere. The lower the elevation angle, the longer the atmospheric light path, resulting in high sensitivity to trace gases located in the very first kilometers of the atmosphere. With good meteorological conditions (sunny and clear days), this technique can retrieve the vertical profile of trace gases and aerosols.

Figure 5.4 shows in a very simplified way the MAX-DOAS geometry. An instrument located at a fixed place at ground measures the scattered sunlight at different elevation

---

[3] MAX-DOAS instruments can optionally measure at different azimuth angles as well, which is the case of the instruments used in this thesis.

angles and either at different azimuth viewing directions or at a fixed one. The elevation angles are measured with respect to the horizon, and the Solar Zenith Angle (SZA) measures the Sun's position relative to the horizontally oriented line of sight.
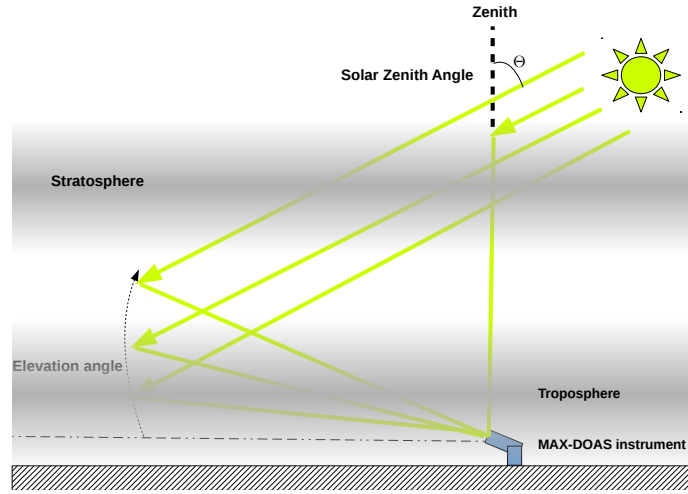
Figure 5.4: MAX-DOAS geometry and its principal elements. As it can be seen, the light path in the upper atmosphere does not depend on the elevation angle of the observation; in contrast, it does for the lowermost layers of the atmosphere, which means that the light path increases with decreasing the elevation angle.

For MAX-DOAS measurements, the output from the DOAS fitting procedure as described in Equation 5.4 is the integrated concentration of a given trace gas along the line of sight through the atmosphere, here for convenience we call it SCD_{retr}, which, thus, includes the tropospheric (SCD_{trop}) and stratospheric (SCD_{strat}) components:

$$S_{retr} = S_{trop} + S_{strat} \tag{5.15}$$

The S_{retr} also contains atmospheric absorption of the analyzed trace gas. Therefore the result of the DOAS spectral fitting is then given by:

$$dS_{retr} = S_{retr} - S_{ref} \tag{5.16}$$

where dS_{retr} is the *differential* Slant Column Density.

In this thesis, the FRS was taken at an elevation angle $\alpha = 90°$ for each elevation angle sequence. In this thesis, the DOAS fitting considered the closest temporal FRS to every measurement at $\alpha \neq 90°$; this cancels out the stratospheric component of the measurement and the reference by assuming that they are the same during one elevation sequence ($S_{strat}(\alpha) = S_{strat}(90°) = S_{strat}$), as follows:

$$\begin{aligned} dS_{retr}(\alpha) &= S_{trop}(\alpha) + S_{strat} - S_{trop}(90°) - S_{strat} \\ &= S_{trop}(\alpha) - S_{trop}(90°) \end{aligned} \tag{5.17}$$

5.7.1 *Air mass factor (AMF)*

The final output of the DOAS analysis is the dSCD of a given trace gas as described by the Equation 5.17. Nevertheless, the light path s is not easy to calculate due to its dependence on the actual state of the atmosphere[4] (Grossmann, 2014). Then, to interpret its vertical distribution, it is helpful to introduce the so-called "Vertical Column Density" (VCD), which represents the vertically integrated trace gas concentration along the altitude.

The conversion of the dSCD into VCD needs an additional parameter called "AMF",A, which is defined as:

$$A(\lambda, \theta, \alpha, \phi) = \frac{\mathrm{dS}(\lambda, \theta, \alpha, \phi)}{V} \tag{5.18}$$

The AMF calculations require the use of a radiative transfer model (See Section 6.6.2 in Chapter 6).

5.8 SPECTRAL CORRECTIONS

The DOAS basics described in the preceding subsections hold for an ideal case. For actual DOAS observations, several corrections must be done in the measured data before starting the DOAS analysis. All those corrections are described in the following sub-sections.

5.8.1 *Spectral calibration*

The wavelength calibration is a crucial point in the DOAS analysis because the quality of the retrieval fit depends on the correct alignment of the measured and reference spectrum and the cross sections. There are several reasons why small misalignments or minor uncertainties in the wavelength position can occur, like thermal changes in the spectrograph, inaccuracy in the grating position, and calibration errors in the literature cross-sections[5]. Therefore it is very important to perform a spectral calibration (Platt and Stutz, 2008).

In this sub-section, we introduce two different methods to determine the spectral calibration, which is the pixel-to-wavelength mapping of the instrument, i.e., the dispersion relation $\lambda_k = p(k)$, where k is the pixel number.

5.8.1.1 *Emission line calibration*

With this method, we determine the pixel-to-wavelength relationship using the well-known positions of the mercury lamp emission lines within the wavelength range of the spectrometer. The emission line width is assumed to be much smaller than the actual instrument's resolution and therefore is neglected.

The spectrometer has a limited resolution; therefore, a measured spectral line must have a finite width. The resolution is determined by the width of the instrument's function (ΔH), see Section 5.4.1, which is mathematically expressed by the FWHM.

---

4 Scattering process on the atmosphere, meteorological conditions, etc.
5 The absorption cross-sections are taken from the literature.

In practice, the emission lines of a mercury lamp are measured with the spectrometer; then, a Gaussian fit is done over every single observed peak in order to get the center position k_n of the nth emission line, which is then linked to a defined λ_n by searching into the literature emission lines, which can be found for example in `https://lweb.cfa.harvard.edu/amp/ampdata/kurucz23/sekur.html`, last access: August 08, 2022. Figure 5.5 shows an example of a single emission line of HR measurement from Sansonetti, Salit, and Reader (1996). Then a polynomial $p(k)$ is fitted to the points (k_n, λ_n) by using a least-square method; finally the dispersion relation $\lambda(k) = p(k)$ is determined. The spectral resolution is determined directly by the width of the measured emission line. Figure 5.6 shows an example of this method performed for the UV spectrometer of the instrument located at the Karlsruhe Institute of Technology(KIT)-Institute of Meteorology and Climate Research - Department Troposphere Research (IMK-TRO) tower.
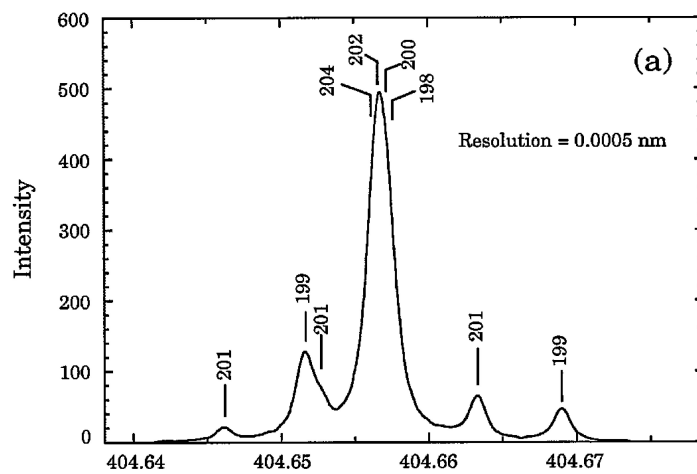
Figure 5.5: Example of a HR spectrum of a Mercury emission peak. Taken from Sansonetti, Salit, and Reader (1996)
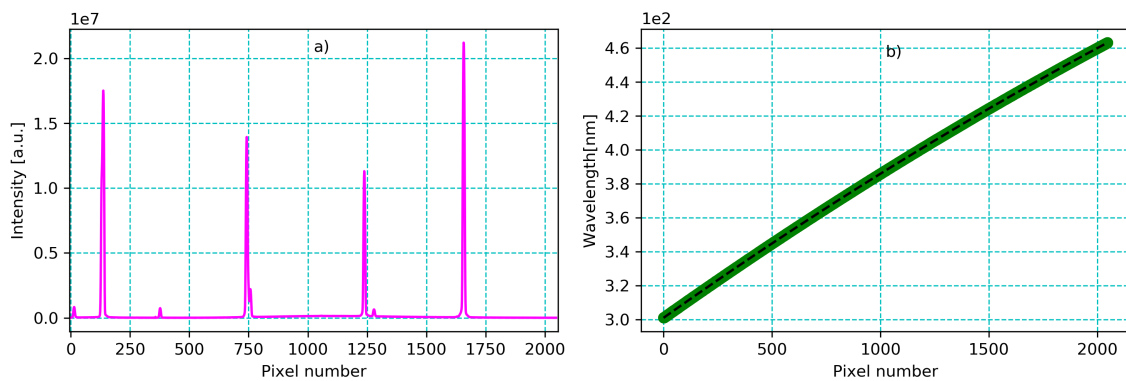
Figure 5.6: Mercury emission lines measured with the UV spectrometer of the instrument installed at the KIT-TRO tower and the respective polynomial fit as determined using Gaussian fits to the emission lines in a) and b) respectively.

5.8.1.2   *HR solar spectrum calibration*

The previous method has the disadvantage that the mercury lamp has a limited number of emission lines[6] to find the dispersion relation, which can lead to interpolation errors. This can be solved by using a well-structured absorption spectrum covering the whole wavelength range of the spectrometer; the solar spectrum for example.

QDOAS (Danckaert et al., 2017) offers a tool to make this process by aligning a measurement taken with the spectrometer at 90° to an HR Fraunhofer spectrum such as the published by Chance and Kurucz (2010), using a nonlinear least-squares fit algorithm. The steps followed by QDOAS are summarized in the chart shown in Figure 5.7. The required settings for the calibration are briefly described as follows:

- The wavelength calibration interval in which the calibration is going to be made needs to be defined. Such interval is split in N sub-windows that must also be set.

- A non-linear least squares fitting in each N sub-windows selected is made, and during this process, the following calculations are carried out:

    – The shift between (Δn_{shift}) the $I_{solar,n}$ and $I_{0,n}$.

    – The slit function parameter (SFP_n) is derived.

    – The new wavelength calibration is calculated by fitting a polynomial previously set by the user through the N individual Δn_{shif} values.

    – The dependence of the SFP with the wavelength is calculated by fitting a polynomial previously set by the user over the SFP_n values.

- Fitting routine: HR Fraunhofer spectrum is convoluted with line shape and wavelength calibration as fit parameter, and fitted to the measured spectrum.

Figure 5.8 shows a typical calibration result. The plot at the top of the figure shows the original HR solar spectrum and the adjusted one; the plots below show the residual, shift and slit function parameters calculated during the calibration process. More details can be found in Section 5.10.

5.8.2   *Electronic offset*

The electronic offset is an artificial electronic signal added to every single measurement due to the limitation of the Analog-to-Digital (AD)-converter to process negative values. Therefore, the electronic offset has to be subtracted for every single measurement (Platt and Stutz, 2008). The electronic offset can be measured by recording a spectrum with a high scan number and a very low integration time (e.g., 10000 scans at 3 milliseconds). A typical example is shown in Figure 5.9 a).

---

6 Some of them are not well separated and therefore cannot be used either for calibration or spectrograph resolution calculations.
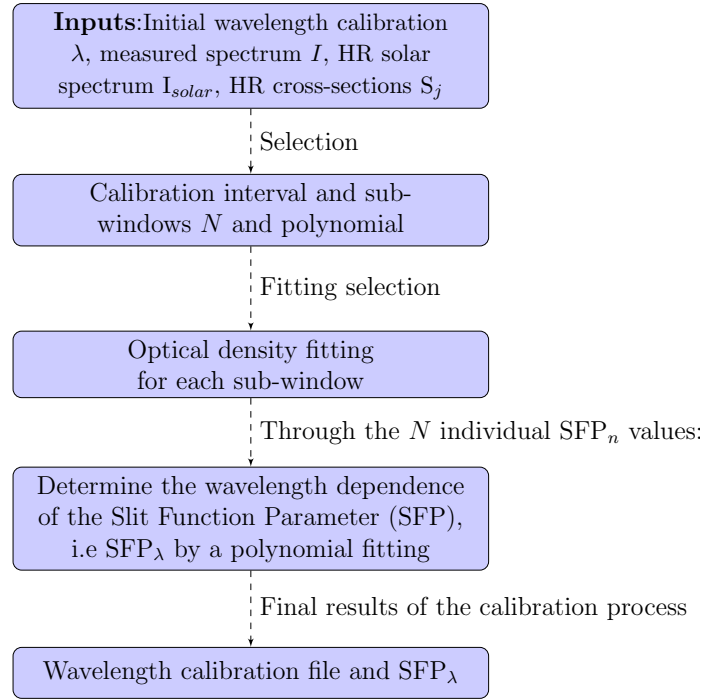
Figure 5.7: Chart diagram of the steps followed by QDOAS for the HR Fraunhofer calibration.

Mathematically the correction of the spectrum is made by:

$$I_{corr} = I_{meas} - \frac{N_{meas}}{N_f}O_f \tag{5.19}$$

Where I_{corr}: corrected spectrum, O_f: offset spectrum, N_{meas}: scans number of the measured spectrum, N_f: scans number of the offset spectrum and I_{meas}: intensity of the measured spectrum (Shaiganfar, 2012).

5.8.3 *Dark current*

The dark current effect occurs when thermally excited electrons pass from the valence band to the conducting band, which is proportional to the Boltzmann function. Then, this effect strongly depends on the detector temperature (Grossmann, 2014; Shaiganfar, 2012). Experimentally this effect can be quantified by measuring a spectrum without light entering the spectrograph (no illumination) using longer integration time than for normal measurements. For deriving the pure dark current spectrum, the offset signal needs to be subtracted from the dark current measured spectrum. See Figure 5.9.

Mathematically this correction is done by the following equation:

$$I_{corr} = I_{meas} - \frac{t_{meas}}{t_{DC}}I_{DC} \tag{5.20}$$

Where I_{meas}: Measured spectrum intensity, I_{DC}: Dark Current spectrum, t_{meas} and t_{DC}: integration time of the measured and Dark Current spectrum respectively.
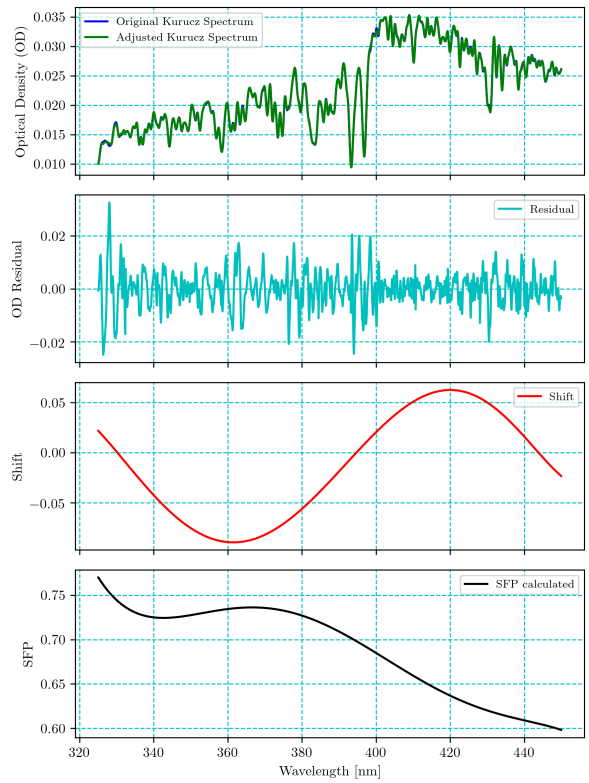
Figure 5.8: HR Fraunhofer spectrum calibration using QDOAS for a single spectrum at an elevation angle of 90°, on 25 July 2019 and around noon, measured with UV spectrometer of the instrument set-up at the KIT-TRO tower. More details can be found in section 10.3.3.
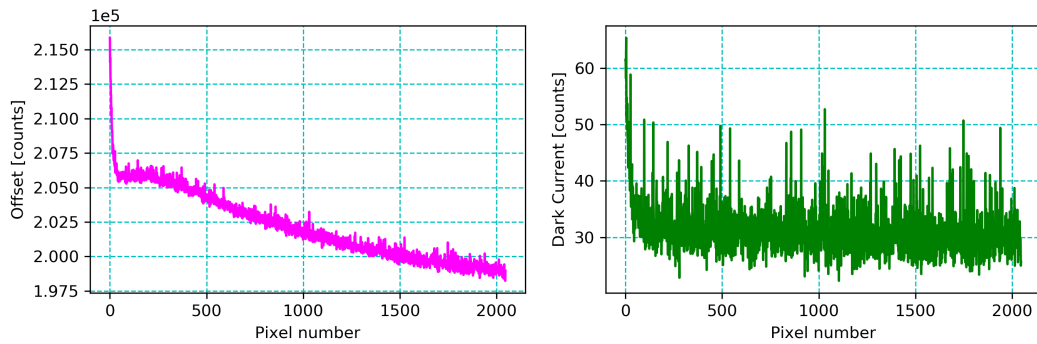
Figure 5.9: Example of a usual electronic offset in a), and dark-current spectrum in b) taken with UV spectrograph of the 2D MAX-DOAS instrument installed at the KIT-TRO tower (details of this instrument can be found in the Chapter 7, Section 7.1.1). The electronic offset was taken with 3 milliseconds of integration time and 20000 scans, while the dark-current spectrum was taken with an integration time of 3 seconds and 20 scans.

5.8.4 *CCD non-linearity effect*

It is assumed that the spectrometer's Charge Coupled Device (CCD)[7] has a linear response to the illumination, but in reality, it does not. The nonlinearity of the detector is

---

7 An array of elements that serve to record the spectra. It is located in the spectrometer.

a necessary correction, especially for weaker absorbers like HONO. This non-linear effect of the spectrograph's CCD can be calibrated by scaling the measured spectrum with an adequate polynomial that represents the pixels response of the CCD, see Figure 5.10.
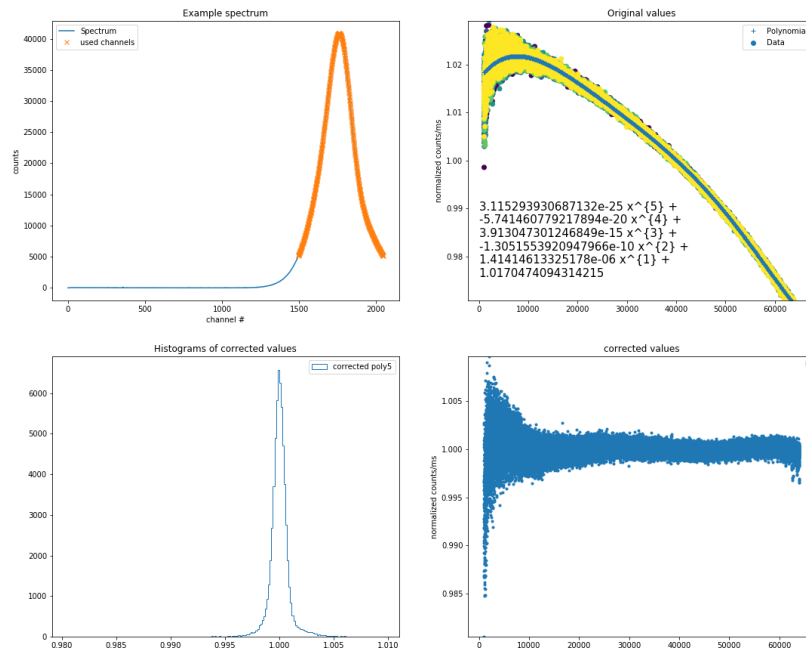
Figure 5.10: Nonlinearity effect example of one of the UV spectrometer of the 2-D MAX-DOAS installed at KIT-TRO tower, see Chapter 7, Section 7.1.1 for more details on the instrument.

5.9 DOAS FITTING PARAMETERS USED

5.9.0.1 *Wavelength range*

For the DOAS fit a wavelength range has to be selected depending on the trace gas to be analyzed. The wavelength range used for the retrieval of each trace gas presented in this thesis can be found in Appendix C.1.

5.9.0.2 *Absorption cross sections*

The absorption cross sections are measured with HR instruments in laboratory conditions. Then, to use them in the DOAS fit, it is necessary to convolve them with the spectrograph's spectral resolution (instrument's slit function) used for the measured spectrum. The wavelength range used for the analysis depends on the cross sections. Once the wavelength range to be used has been defined, all the cross sections that absorb in that range might be considered. An example of cross sections absorbing in the UV-Vis range can be seen in Figure 5.11.

The convolution process is performed during the DOAS analysis. Additionally to the standard convolution, the following has to be taken into account:
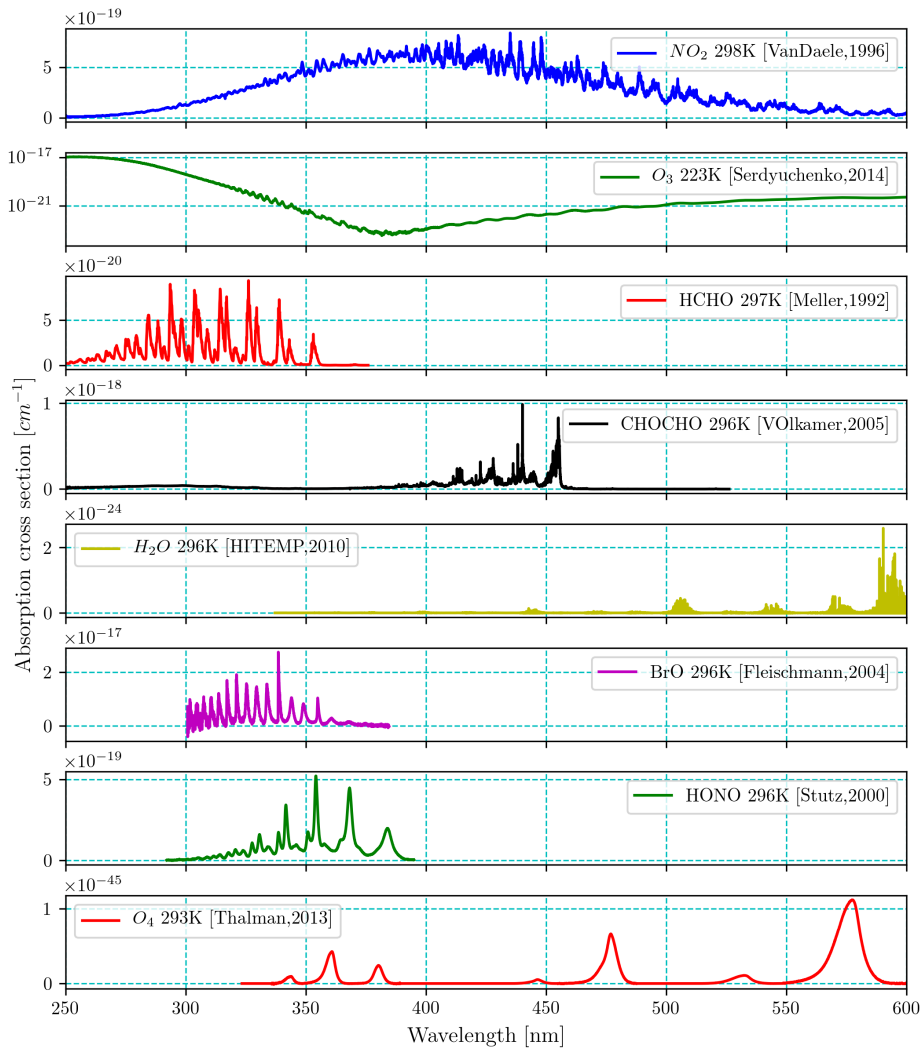
Figure 5.11: Differential absorption cross-sections of the standard atmospheric trace gas compo-
nents that can be measured with the DOAS technique in the wavelength range from
250 to 600 nm. The data set has been taken from `satellite.mpic.de/spectral_`
`atlas/`, last access: 03 October 2022.

5.9.0.3 *Fraunhofer reference*

Since the atmosphere changes rapidly, in this thesis, a sequential reference is used, which
means that a spectrum measured at $\alpha = 90°$ in the same elevation angle sequence is taken.

5.9.0.4 *Shift and stretch*

In order to correct possible misalignments between most of the inputs that have wave-
length dependencies during the DOAS fit, a shift and stretch are applied in this thesis for
all the cross sections and the reference spectrum.

5.9.0.5 *Polynomial*

Depending on the trace gas fitting range, a defined polynomial with a degree between 2 and 5 is set to separate the smoothest part of the spectral absorbance, as explained above.

5.9.0.6 *Non-linear offset correction*

It considers additional offset sources like instrumental stray-light and dark current in the detector (Danckaert et al., 2017). Different values are used depending on the fitting interval; these values can be found in Appendix A.

5.9.0.7 *Taylor terms*

AMF is assumed to be constant in a defined wavelength range; nevertheless, it is well known that AMF depends on the wavelength. A Taylor series approach described in Pukite et al. (2010) is used to correct the wavelength dependency of the NO_2 AMF. It is important to say that this is relevant for weak absorbers like HONO. For more details, see Appendix C.1.

5.10 APPLIED DOAS FITTING PROCEDURE

In this thesis, the DOAS fit analysis is performed using the DOASIS software (Kraus, 2006). Figure 5.12 shows the resume of all the steps until the dSCD is obtained. The retrieval is composed of three main processes:

1. *CCD nonlinear-effect correction:* This correction is the first to be made in all the spectra measured, even for the corrections (offset and dark current), to have more realistic spectra by scaling it with the non-linear polynomial response of the spectrographs CCD.

2. *Spectral calibration:* Here, a similar algorithm to the one presented in sub-section 5.8.1 was implemented in DOASIS. The main results of this process are the instrumental slit function and the wavelength-pixel relation. To achieve this, the following steps are needed:

   a) The background spectra (offset, dark current) and the Mercury absorption spectrum measured with the spectrometer are loaded. Then, the initial calibration is made by using the Mercury absorption peaks.

   b) The required inputs are the measured Fraunhofer spectra (I_0) at the zenith, background spectra (offset and dark current), and the HR solar spectrum (I_{solar}). Here the published solar spectrum by Chance and Kurucz (2010) is used, which is convoluted with the preliminary SFP_λ from step 1, resulting in the HR solar spectrum calibration is made.

3. **DOAS fitting process:** It is mainly composed of 3 processes:

   a) Cross-section processing:

Pre-processing: CCD non-linear effect
correction over all the measured spectra.

Initial Mercury calibration

Inputs:Measured Hg spectrum, back-
ground spectra (offset and dark current).

HR Solar spectrum calibration

Inputs: Initial wavelength calibra-
tion λ, Measured Fraunhofer spec-
trum I_0, HR Solar Spectrum I_{solar}

Final results of the calibration process

Wavelength calibration file and SFP_λ

Cross sections and reference spectrum processing

Wavelength calibration of
I and convolution of S_j

DOAS fitting method used

Optical density fitting

Application of a Non-Linear Least Squares Fit (NLLS)

Differential slant column densities (dSCD)

Figure 5.12: Flow chart of the DOAS technique retrieval used in this thesis.

- The wavelength calibration and the SFP_λ are applied to convolve σ_j. In the case of O_3 and NO_2, a I_0 correction is also done using a HR solar spectrum, as previously explained. See Figure 5.13, as an example, showing the original HR cross-section for NO_2 at 298 K measured by Vandaele et al. (1998), and the corresponding cross-section convolved with the instrument function for the UV spectrometer operated at the KIT-TRO tower

- The Ring spectrum is calculated as an additional cross-section as explained in 5.6.3.

- Taylor terms: In the case of using them, those are calculated based on the convolved cross sections as it is described above.

b) Spectra processing: Dark current and Offset corrections are applied to the measured spectrum.
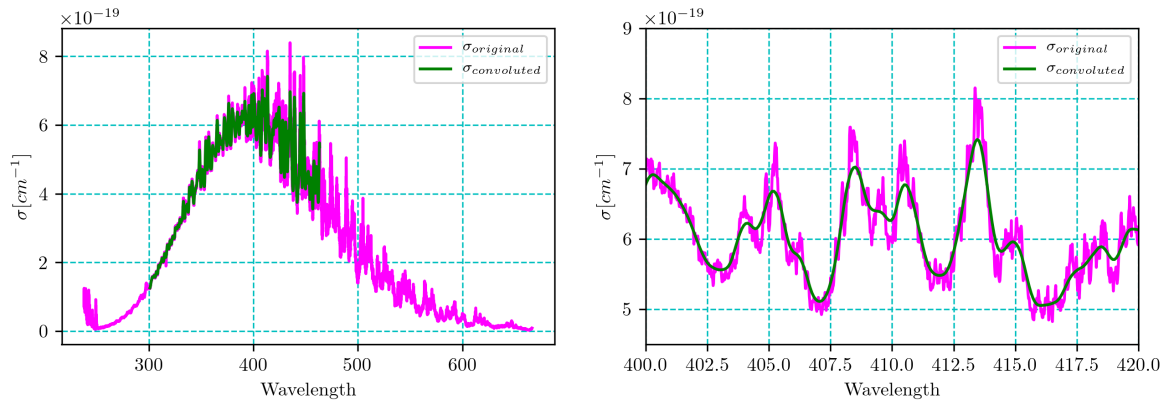
Figure 5.13: Example of the convolution effect over the HR NO$_2$ at 298K with the instrument function for the UV spectrometer at the KIT-TRO tower.

c) The DOAS fitting process uses all the parameters defined in 5.9. A Non-Linear-Least-Squares (NLLS) method is used to deduce the Slant Column densities and their errors, as explained in Section 5.5.

6

INVERSION THEORY FOR GROUND-BASED FTIR AND MAX-DOAS OBSERVATIONS

[1]The retrieval of atmospheric abundances of CO_2, CO, CH_4, and H_2O, derived from ground-based FTIR remote sensing observations, is possible making use of the inversion theory. The following sections describe the most important features of this theory.

6.1 RETRIEVAL ALGORITHM

Retrieving atmospheric variables and constituents based on remote sensing observations is a well-known ill-posed inverse problem (Rodgers, 1976), i.e., there is no unique solution. The algorithm comprises two main parts: The forward model $F(x)$ and the inverse model used to solve the problem, see Figure 6.1. In this thesis, the approach described by Rodgers (1976) and Rodgers (2000) is summarized for a basic understanding of the inversion problem and solution.
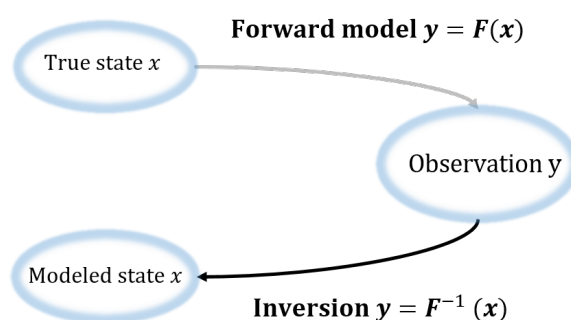
Figure 6.1: Illustration of the retrieval algorithm components

6.2 FORWARD RADIATIVE TRANSFER MODEL

The measurement $\mathbf{y}$ can be written in terms of the measured variables (radiances), considering the general radiative transfer formulations in the atmosphere, as follows:

$$\mathbf{y} = \mathbf{F}(\mathbf{x}, \mathbf{b}) + \epsilon \tag{6.1}$$

Where $\mathbf{F}$ is the so-called forward model, $\mathbf{x}$ represents the atmospheric state vector, $\mathbf{b}$ describes all the model parameters affecting the measurement but not included in the fit, and ϵ is the measurement error or noise.

6.3 THE OPTIMAL ESTIMATION METHOD (OEM)

This method retrieves the values of variables $\hat{x}$ assembled in the state vector assuming the model $\mathbf{F}$ is locally linearizable. It should be based on the best possible knowledge of the atmospheric state prior to the measurement and its variability; this is comprised of the mean state $\mathbf{x}_a$ and its covariance matrix, $\mathbf{S}_a$; both refer to the n-dimensional state vector $\mathbf{x}$ (in our case, the discrete vertical profile of any gas of interest). The OEM solution results from a weighting between the a priori state $\mathbf{x}_a$ and the information contained in the vector of the spectral measurement $\mathbf{y}$. The weighting is determined by the covariance matrix of the a priori profile and the spectral measurement noise $\mathbf{S}_a$ and $\mathbf{S}_\epsilon$, respectively. If the forward model is linear, $\mathbf{y} = \mathbf{F}(\mathbf{x}, \mathbf{b}) + \epsilon = \mathbf{K}\mathbf{x} + \epsilon$, where $\mathbf{K}$ is the jacobian matrix or weighting function $\mathbf{K} = \frac{\partial \mathbf{F}}{\partial \mathbf{x}}$, which does not depend on the state vector. The optimal solution is given by:

$$\hat{\mathbf{x}} = (\mathbf{S}_a^{-1} + \mathbf{K}^T \mathbf{S}_\epsilon^{-1} \mathbf{K})^{-1} (\mathbf{S}_a^{-1} \mathbf{x}_a + \mathbf{K}^T \mathbf{S}_\epsilon^{-1} \mathbf{y}) \tag{6.2}$$

Because the radiative transfer equation is not linear; iterative methods are used to minimize the cost function:

$$\chi^2 = (\mathbf{F}(\mathbf{x}, \mathbf{b}) - \mathbf{y})^T \mathbf{S}_\epsilon^{-1} (\mathbf{F}(\mathbf{x}, \mathbf{b}) - \mathbf{y}) + (\mathbf{x} - \mathbf{x}_a)^T \mathbf{S}_a^{-1} (\mathbf{x} - \mathbf{x}_a) \tag{6.3}$$

The minimization of the cost function 6.3, and therefore the finding of the optimal state vector $\hat{x}$ can be derived by:

$$\vec{\nabla}\chi^2(\hat{\mathbf{x}}) = 0 \longrightarrow \vec{\nabla}\mathbf{F}(\hat{\mathbf{x}})^T \mathbf{S}_\epsilon^{-1} [\mathbf{K}\hat{\mathbf{x}} - \mathbf{y}] + \mathbf{S}_a^{-1} [\hat{\mathbf{x}} - \mathbf{x}_a] = 0 \tag{6.4}$$

Subject to the state vector and the model function, solving Equation 6.4 can be linear or nonlinear.

6.3.1 *Nonlinear inversion case*

For a non-linear inversion problem like aerosol retrievals (Deutschmann et al., 2010; Friess et al., 2006; Grossmann, 2014; Yilmaz, 2012), the Gauss-Newton iteration method described in Equation 6.5 is applied to solve the Equation 6.4.

$$x_{i+1} = x_i + (\mathbf{S}_a^{-1} + \mathbf{K}_i^T \mathbf{S}_\epsilon^{-1} \mathbf{K}_i)^{-1} [\mathbf{K}_i^T \mathbf{S}_\epsilon^{-1} (\mathbf{y} - \mathbf{F}(x_i)) - \mathbf{S}_a^{-1} (x_i - \mathbf{x}_a)] \tag{6.5}$$

Levenberg (1944) and Marquardt (1963) presented a method that uses a barely modified version of Equation 6.5. The main advantage is its faster convergence rate compared to the Newton-Gauss method:

$$x_{i+1} = x_i + \left[(1 + \gamma_i)\mathbf{S}_a^{-1} + \mathbf{K}_i^T \mathbf{S}_\epsilon^{-1} \mathbf{K}_i \right]^{-1} \{ \mathbf{K}_i^T \mathbf{S}_\epsilon^{-1} [\mathbf{y} - \mathbf{F}(x_i)] - \mathbf{S}_a^{-1} [x_i - \mathbf{x}_a] \} \tag{6.6}$$

The cost function is minimized by selecting an appropriate γ_i value at each iteration.

6.3.2 *Retrieval properties*

6.3.2.1 *Gain function* G

G characterizes how sensitive the retrieval is to the measurement. Mathematically it is defined as:

$$\mathbf{G} = \frac{\partial \hat{\mathbf{x}}}{\partial \mathbf{y}} = (\mathbf{S}_a^{-1} + \mathbf{K}^T \mathbf{S}_\epsilon^{-1} \mathbf{K})^{-1} \mathbf{K}^T \mathbf{S}_\epsilon^{-1} \tag{6.7}$$

6.3.2.2 *Averaging kernel matrix* A

A determines the sensitivity of the retrieved state vector $\hat{x}$ to the true state vector x. Mathematically it is given by:

$$\mathbf{A} = \frac{\partial \hat{\mathbf{x}}}{\partial \mathbf{x}} = \mathbf{GK} = (\mathbf{S}_a^{-1} + \mathbf{K}^T \mathbf{S}_\epsilon^{-1} \mathbf{K})^{-1} \mathbf{K}^T \mathbf{S}_\epsilon^{-1} \mathbf{K} \tag{6.8}$$

For an ideal measurement (without noise), $\hat{x}$ and x follows:

$$\hat{\mathbf{x}} = \mathbf{x}_a + \mathbf{A}(\mathbf{x} - \mathbf{x}_a) \tag{6.9}$$

6.3.2.3 *Degrees of freedom (DOFs):* d_s

The degrees of freedom d_s quantifies the number of independent pieces of information that can be measured, mathematically, given by:

$$d_s = tr(\mathbf{A}) \tag{6.10}$$

6.3.3 *Retrieval errors*

Model uncertainties, spectral noise and experimental errors lead to retrieval inaccuracies, which are calculated based on Bayes's theorem; more information can be found in Rodgers (2000). Mathematically these errors are given by:

- **Smoothing error:**
$$\mathbf{S}_s = (\mathbf{A} - \mathbf{I}_n)\mathbf{S}_a(\mathbf{A} - \mathbf{I}_n)^T \tag{6.11}$$

- **Retrieval noise:**
$$\mathbf{S}_m = \mathbf{GS}_\epsilon \mathbf{G}^T \tag{6.12}$$

- **Parameter error:**
$$\mathbf{S}_p = \mathbf{GK}_p \mathbf{S}_p \mathbf{K}_p^T \mathbf{G}^T \tag{6.13}$$

- **Total error:**
$$\hat{\mathbf{S}} = \mathbf{S}_s + \mathbf{S}_m + \mathbf{S}_p \tag{6.14}$$

6.4 OEM FOR GROUND-BASED FTIR REMOTE SENSING OBSERVATIONS

Radiative transfer forward models predict synthetic spectra based on:

1. **Spectroscopic line lists** containing information on line positions, intensities, broadening and shifting parameters and/or tabulated cross-sections as function of pressure and temperature, as provided by spectroscopic databases like HITRAN (Gordon et al., 2022; Gordon et al., 2017; Rothman et al., 2013).

2. **The atmospheric state**: pressure p(h) and temperature T(h) as function of the altitude , a-priori profiles of the trace gases (H_2O, CO_2, CH_4, CO, O_2).

3. **The Solar Zenith Angle (SZA)** of the observation place.

4. **Instrumental characteristics** or instrumental resolution.

Figure 6.2 shows an example of synthetic atmospheric transmittance in the solar spectral range for a cloudless sky calculated (off-line) with the two–stream radiative transfer solver described in Kylling, Stamnes, and Tsay (1995) as part of libradtran.
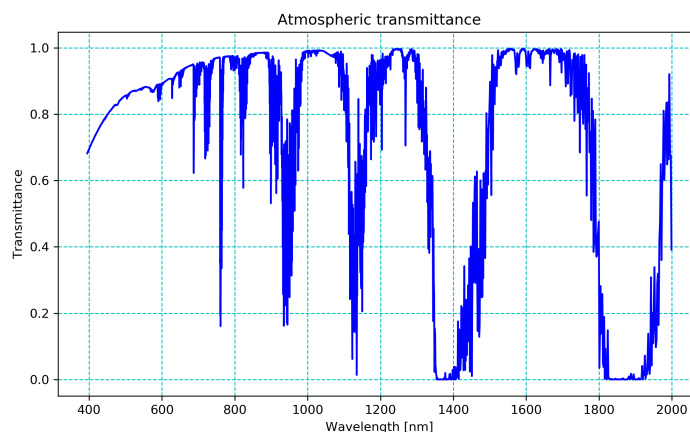
Figure 6.2: Atmospheric transmittance for a cloudless sky. The calculations were made with the two–stream radiative transfer solver described in Kylling, Stamnes, and Tsay (1995) as part of the libradtran (Emde et al., 2016).

The forward codes used for the retrieval of atmospheric species here are PROFFWD and PCXS (used by PROFFAST) and described in the following sections.

6.5 RETRIEVAL SOFTWARE FOR GROUND-BASED FTIR REMOTE SENSING

The retrieval of atmospheric trace gas abundances in the infrared spectral region using ground-based remote sensing observations are commonly done with GFIT, SFIT2, PROF-FIT, and for low-resolution mobile spectrometers PROFFAST.

GFIT is the official software for processing the NIR observations carried out by the TC-CON network, while COCCON uses PROFAST, and SFIT2 and PROFFIT are dedicated to analyze the MIR observations made by NDACC. GFIT and PROFFIT have been developed

by G. Toon from CALTECH (Toon et al., 1992; Wunch et al., 2011) and F. Hase from KIT (Hase et al., 2004), respectively. In this thesis, the data acquired with the low-resolution mobile spectrometer EM27/SUN (see Section 7.2) are analyzed; therefore, the PROFFAST retrieval code is described in the next section.

6.5.1 *PROFFAST retrieval algorithm*

The processing and analysis of the low-resolution EM27/SUN measurements are summarized in Figure 6.3. This process requires two main steps: (1) the generation of spectra from the pre-processing of the raw interferogram, which are the direct observations recorded by the computer; and (2) the retrieval of the wanted trace gas abundances based on the absorption spectra obtained in step 1; this requires a radiative transfer and inversion algorithm to fit synthetic data to the actual observations. These steps are included in two open-source tools developed by F. Hase from KIT in the framework of the COCCON-PROCEEDS project (supported by the European Space Agency (ESA)); for the pre-processing (i.e., the tool PREPROCESS) and the subsequent quantitative trace gas analysis (i.e., the tool PROFFAST), respectively.
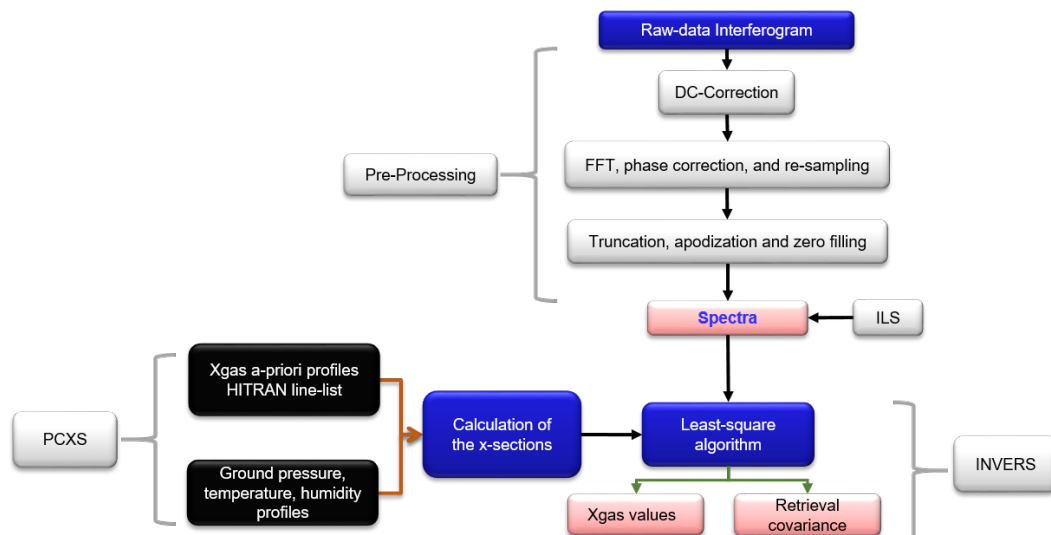
Figure 6.3: PROFFAST processing flux diagram.

6.5.1.1 *PREPROCESS*

The preprocess code generates a spectrum from the raw DC-coupled double-sided interferogram, which is recorded by the EM27/SUN FTIR spectrometer. This step incorporates a so-called DC-correction for removing variations in atmospheric transmission during interferogram recording. Several quality checks for ensuring that the quality of generated spectra is adequate for trace gas analysis are performed (no spectrum is generated if, e.g., the variability of atmospheric transmission during the interferogram recording was too big, if spectral out-of-band artifacts are too strong, if the spectral signal-to-noise level is too low, or if a significant spectral detuning is detected). The Fourier Transform is per-

formed by using an FFT algorithm. It uses the fact that the EM27/SUN phase spectrum is very smooth. A numerical apodization function (Norton-Beer medium) is applied to avoid excessive ringing in the resulting under-resolved spectrum. A final spectral interpolation is performed on the spectrum resulting from the FFT (by performing a convolution with a truncated sinc-function) for achieving a minimally sampled spectrum (using the maximum path difference of the spectrometer).

6.5.1.2 *PROFFAST*

PROFFAST is performing the trace gas analysis of the spectra generated by PREPROCESS. In order to achieve high computational speed, the code is split into two sub-programs: pre-calculation of cross-sections (PCXS) and INVERS.

- **PCXS**

  The code PCXS generates a daily lookup table of optical depth for each gas to be used by INVERS. The table is generated by performing line-by-line calculations assuming Voigt profiles, using line lists in the HITRAN format. Input parameters are ground pressure, the temperature and humidity profiles, and the a priori dry-air mixing ratio profiles for each relevant gas. In the near-infrared region, the relevant absorbers are H_2O (+ HDO), CO_2, N_2O, CO, CH_4, and HF.

  The final table of cross-sections does not provide the optical depth for each gas as a function of altitude, but the optical depth along the vertical line-of-sight and a polynomial expansion as function of SZA. This expansion considers the geometric curvature of the atmosphere and the bending of the line of sight due to atmospheric refraction. Along the spectral abscissa, a grid width proportional to the wavenumber is used for the table because the width of the Doppler broadening of spectral lines is proportional to wavenumber; a denser sampling is required at lower wavenumbers. The resulting presentation reduces table size and allows an effective reconstruction from the tabulated values.

- **INVERS**

  The code INVERS performs for each measured spectrum recorded during the day the retrieval of the atmospheric abundances of each gas by performing least squares fits. Therefore, the code uses the contains of the lookup table for calculating the atmospheric transmission:

$$T(S_{i,gas}, \alpha) = e^{-\sum S_{i,gas} \tau_{gas}(\alpha)} \tag{6.15}$$

  Here, the $S_{i,gas}$ are the scaling factors for each gas (the a priori profile has $S_{i,gas} = 1$). The equation is written for a particular spectral position; T and τ are vector quantities (their values are evaluated for each spectral grid point of the cross-section table). The scaling factors are the sought-for quantities derived from the spectral fit. Note that the radiative transfer equation is straightforward: only absorption along

the line-of-sight needs to be taken into account, while scattering and emission are negligible atmospheric processes in the near-infrared solar absorption measurement. The pure Lambert-Beer equation's applicability is the reason for the reference character of solar absorption measurements. The measurement is self-calibrated because the contrast between a spectral absorption line and the adjacent spectral continuum informs about the amount of the absorbing gas.

INVERS determines the required derivatives with respect to all fitted quantities (the scaling factors and additional variables, as the background continuum level C and the spectral scale) and performs the iterative retrieval. The final calculated spectrum S follows from the convolution of the transmission with the instrumental line shape ILS. In this step, a re-gridding to a coarser, spectrally equidistant grid is performed to match the spectral sampling of the measured spectra resulting from PREPROCESS.

$$S = C(\nu)\text{ILS} * T \tag{6.16}$$

Here, C is assumed to be a function that slowly varies as a function of wave number. The parameters determining the background continuum C are among the parameters to be fitted.

The required derivatives are all sampled on the spectrally equidistant grid set by the spectrum generated by PREPROCESS and assorted into the Jacobean matrix. The spectral dimension sets the column dimension of the matrix, and the row dimension is set by the total number of parameters to be fitted.

The inversion is performed by calculating:

$$\Delta\vec{\mathbf{p}} = (\mathbf{K}^T\mathbf{K})^{-1}\mathbf{K}^T(\vec{\mathbf{S}}_{meas.} - \vec{\mathbf{S}}_{calc.}) \tag{6.17}$$

Because the retrieval problem is slightly nonlinear, the resulting set of improved fit parameters is updated several times using $\Delta\vec{p}$ as predicted by the linearized retrieval equation above.

Note that INVERS has no access to altitude-resolved optical densities $\tau(h_1, h_2)$; the tabulated τ-values refer to the complete atmosphere from the observer level to the top of the atmosphere.

So INVERS cannot compute column sensitivities required to characterize the retrieval. For this reason, the calculation of the column sensitivity vector is already performed by PCXS, while the optical depth for each species is still available as a function of altitude. For this purpose, PCXS performs simplified retrievals on synthetic spectra for a set of α values. In these calculations, the a priori gas profiles are disturbed at each model altitude level i (thereby affecting a particular adjacent layer

in the model atmosphere, resulting in a change of the total column: $\delta c(i)$). If the retrieval performed on the spectrum calculated from the disturbed profile detects (via scaling of the a priori profile) a total column change of δc_{inv}, then the column sensitivity at model level i is:

$$colsens(i) = \delta c_{inv}/\delta c(i) \tag{6.18}$$

The values of the resulting column sensitivities are provided daily for each gas in a two-dimensional table stored together with the lookup table of cross-sections (dimensions: altitude and solar zenith angle).

6.5.2 PROFFAST: inputs and final outputs

In order to successfully retrieve the atmospheric trace gas abundances like water vapor, carbon dioxide, methane, and carbon monoxide with PROFFAST, apart from the EM27/SUN observations, several inputs are required, summarized in the following sections.

6.5.2.1 Inputs

- **Ground pressure (p) and temperature profile (T(h))**: Determines the total mass and stratification of the atmosphere. Intra-day variations in pressure (and temperature) are considered.

- **Climatology (a-priori profiles)**: A-priori map files are used; they are provided online by the TCCON network to ensure identical choices for the temperature and water vapor profiles, as well as for the a-priori vertical profiles of all relevant atmospheric trace gases for each site and day.

- **Fitting interval**: These are not adjusted by the user; however, it is essential to mention that they have been selected, taking into account the absorption lines of the retrieved atmospheric species. In this thesis, we derived XCO_2, XCH_4, XCO, XH_2O, and XAir; their fitting micro-windows, and an additional scaling factor that executes the air mass independent correction (AICF) are listed in Table 6.1.

6.5.2.2 Outputs

- **Fitting example**: Here we present an example of the fitting results for one single measurement to understand better the species retrieved, the microwindows used during the retrieval (see Table 6.1), and the fitting quality. Figure 6.4 shows the fitting results for one observation of the COCCON's reference unit SN37 at the KIT campus north on May 17, 2022 at $\approx$ 10:00 A.M.

- **Column-averaged volume mixing ratios** (X_{gas}): To minimize potential error sources, the retrieved total column abundance of a particular gas is converted into a column-averaged dry air mole fraction (DMF) using the observed O_2 column amounts. For

Species	Micro-window (MW)	AICF
XCO_2	(6173.0, 6390.0)	0.9862
XCH_4	(5897.0, 6145.0)	0.9905
XCO	(4208.7, 4318.8)	0.9250
XH_2O	(8353.4, 8463.1)	0.8300
$XAir$	(7765.0, 8005.0)	0.9737
$XCH_4{}^*$	(4208.7, 4318.8)	0.9727

Table 6.1: Fitting MW intervals and their AICFs for each retrieved species. The last factors are summarized in next section. * MW, which is retrieved in the second channel of the EM27/SUN spectra. This MW coincides with the utilized for the retrieval of the Sentinel-5 Precursor product.

instance, such error sources are related to the accuracy of the SZA or the ground pressure. The DMF of a target gas is denoted as and calculated by the following expression:

$$X_{gas} = \frac{VC_{gas}}{VC_{O_2}} 0.2095 \tag{6.19}$$

where 0.2095 is the dry-air mole fraction of O_2. The construction of Xgas by referencing to the O_2 column reduces various error sources.

In order to be consistent and to reference the results to the WMO (World Meteorological Organization) in-situ trace gas scale, the EM27/SUN retrieval PROFFAST also includes a post-processing consisting of an empirical air mass-dependent and independent corrections as follows:

$$X_{gas} = Scale_{gas}^{WMO} \frac{VC_{gas}}{VC_{O_2}} 0.2095 \tag{6.20}$$

These $Scale_{gas}^{WMO}$ are listed in Table 6.1 as AIC.

- **Sensitivities for all target gases**: The sensitivities are one of the outputs of the INVERS code; they are not calculated for each measurement but for the whole day instead as a function of the solar zenith angle. Here, we show and briefly discuss the resulting pressure-dependent column sensitivities for CO_2, CH_4, and CO; for measurements carried out with the COCCON's reference instrument SN37 at KIT campus north (49.094, 8.437) on May 17, 2022, see Figure 6.5.

    – **XCO₂**: CO_2 signals are generally slightly overestimated in the troposphere and underestimated at higher altitudes. This tendency increases with a larger solar zenith angle, i.e., increasing air mass, see Figure 6.5.
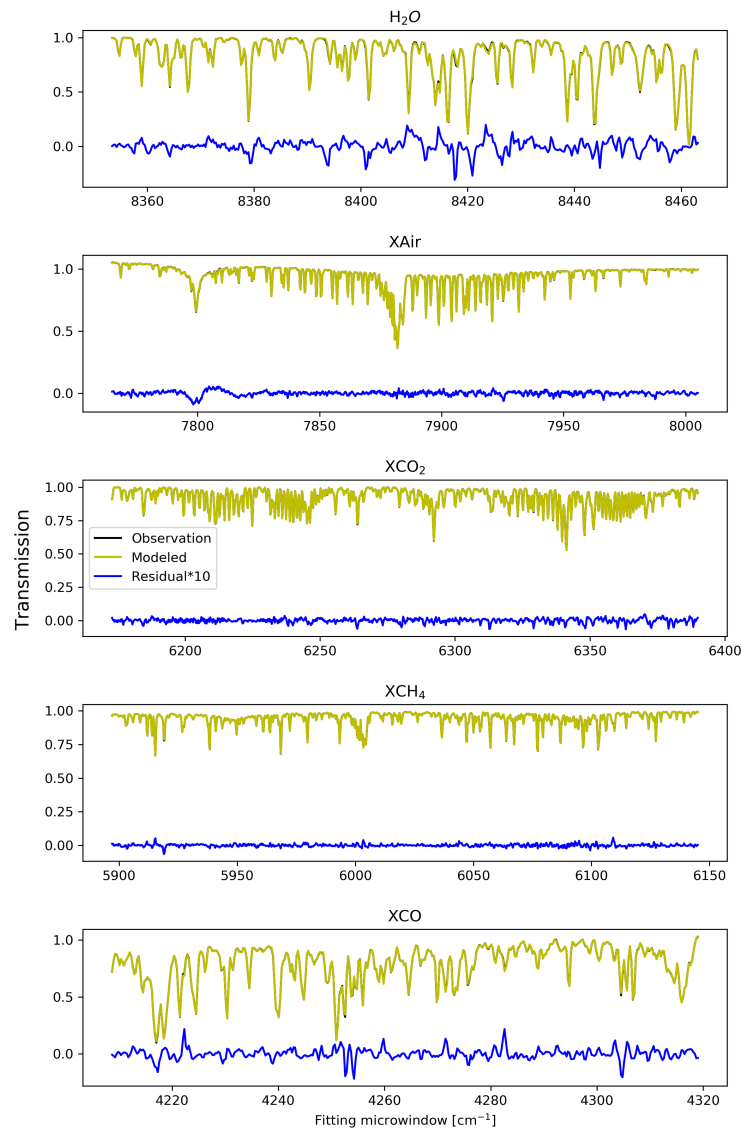
Figure 6.4: Fitting example using PROFFAST version 1.0 for a measurement taken on May 17, 2022 at $\approx$ 10:00 A.M at the KIT campus north. The observation was taken with the COCCON's reference unit, SN37. The plot shows the measurement (yellow) and the modeled (black) transmission and the residual times 10 (to be observed with more detail) for each of the most important quantities retrieved in their respective microwindows: H_2O, XAir, XCO_2, XCH_4, and XCO, respectively.

– **XCH_4**: The sensitivity pattern qualitatively compares to that of carbon dioxide. However, the imbalance between increased tropospheric sensitivity and decreased stratospheric sensitivity is less pronounced. However, for small solar zenith angles, the sensitivity is nearly ideal across the whole altitude range, see Figure 6.5.

– **XCO**: This sensitivity differs from those found for CH_4 and CO_2. The sensitivity variation as a function of solar zenith angle is less pronounced. The sensitivity slope as a function of altitude is reversed (increasing sensitivity with altitude)
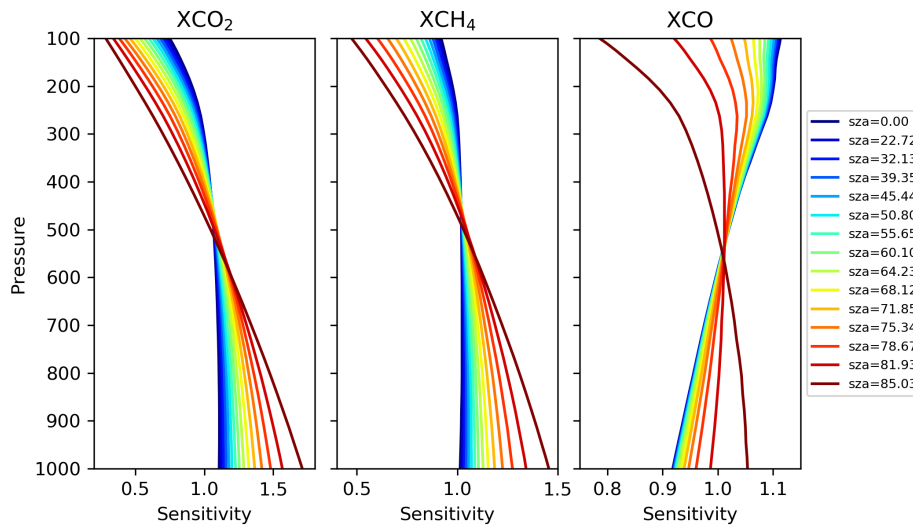
Figure 6.5: XCO_2, XCH_4 and XCO sensitivities for observations with the COCCON's reference unit SN37 on May 17 2022 at KIT campus north.

and moderate, see Figure 6.5. This is due to the fact that the CO lines are optically thin.

6.6 MAX-DOAS: INVERSION ALGORITHMS FOR VERTICAL PROFILE RETRIEVALS

MAX-DOAS is an atmospheric sounding technique with a horizontal spatial coverage of about 3-15 km, which offers the possibility to retrieve information on a large horizontal and vertical extent of the atmosphere (Irie et al., 2011).

This method aims to acquire profiles of the atmospheric constituents based on the slant column densities measured with MAX-DOAS, which an inverse model determines. In this thesis, an updated[2] version of the Heidelberg Profile Retrieval Algorithm (HEIPRO, Yilmaz (2012)) has been used to invert the measurements and calculate the aerosol and trace gas profiles. HEIPRO uses SCIATRAN radiative transfer model version 2.1.5[3] (Rozanov et al., 2014) to calculate the light path in the atmosphere for a given state by using the so-called optimal method.

Like most of the MAX-DOAS inversion retrievals, HEIPRO uses a two-step procedure, summarized as follows: (1) the aerosol profile is derived using the O_4 dSCDs as a measurement vector, and (2) the trace gas profile is derived using the previously calculated aerosol profile and the trace gas dSCDs.

---

2 Udo Frieß updated it in order to be able to process the measurements done in this work.
3 With the following mode: discrete ordinate, full multiple-scattering, full-spherical geometry for single-scattering, and plane-parallel geometry for multiple-scattering light.

6.6.1 *OEM for Aerosol retrieval by using tetraoxygen (O_4)*

[4]Because O_4 has a well-known vertical profile[5], any change in the measured concentrations under clear sky conditions contains information about the atmospheric light path, which can then be used to retrieve information about the atmospheric aerosols and clouds (Wagner et al., 2021). The O_4 concentration is proportional to the square of the O_2 concentration, and therefore decreases as function of altitude. The main partial column of O_4 is located near the ground; therefore, the optical depth of O_4 is very sensitive to changes in the first kilometers of the atmosphere. O_4 has several absorption bands over the UV-Visible range that a DOAS instrument can easily detect, see Figure 6.6. Therefore O_4 measurements help to retrieve the aerosol extinction as a function of the wavelength (Friess et al., 2006).
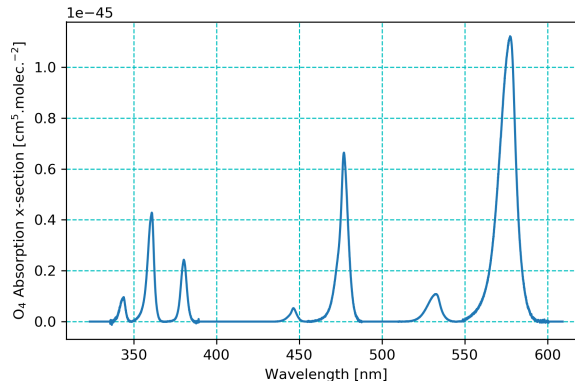
Figure 6.6: O_4 cross section at 293 K (Thalman and Volkamer, 2013). Data taken from http://satellite.mpic.de/spectral_atlas/, last access: 03 October 2022.

6.6.1.1 *Aerosol inversion remarks*

An essential quantity containing information about aerosol properties is the relative intensity (Friess et al., 2006; Vlemmix et al., 2010). It is defined as the ratio between any elevation angle and the corresponding zenith angle in the measurement sequence (elevation angle sequence used in this work: 1°, 2°, 3°, 5°, 10°, 20°, 40° and 90°).

$$I_\alpha^{rel} = \frac{I_\alpha}{I_{90^0}} \tag{6.21}$$

Only relative intensities can be compared to the simulated ones because most of the DOAS instruments are not radiometrically calibrated, i.e., solely relative changes in the intensity depending on the measurement geometry can be deduced (Vlemmix et al., 2010).

$F(x,b)$ on Equation 6.1 is the forward model operator implemented, in our case in the SCIATRAN radiative transfer model.

---

4 The following sections are based on overviews of Friess et al. (2006), Rodgers (2000), and Wagner et al. (2004).
5 Additionally to the O_4 dependency with height, its atmospheric concentrations show only minor variations with temperature, pressure, and humidity (Wagner et al., 2021).

Retrieving the aerosol extinction profile by just using the measurement vector y is not straightforward because for x there are many solutions, i.e., it is an ill-posed problem. Therefore, to solve it, the OEM is applied (Rodgers, 2000). This method has been widely used in retrieving vertical profiles by using the MAX-DOAS dSCDs as input vector (Friess et al., 2006; Grossmann, 2014; Lampel, 2014; Peters, 2013; Wagner et al., 2004; Yilmaz, 2012).

The a priori constitute an approximation of a given state of the atmosphere which can be obtained, for example, from other independent measurements (Friess et al., 2006).

In Equation 6.3, for the aerosol extinction profile, the variance σ_a has to be set: typical values are 50% and 100% of the a priori extinction profile, and the aerosol extinction is assumed to be correlated through the altitudes; therefore S_a can be expressed as:

$$\mathbf{S}_{a_{ij}} = \sigma_{a_i}\sigma_{a_j}\exp\left(-\frac{|z_i - z_j|}{\eta_{corr}}\right) \tag{6.22}$$

Where z is the layer altitude and η_{corr} is the correlation length representing a constraint of the measurement vector y smoothness (Friess et al., 2006). The typical values for it are 0.5 to 1.0 km.

In Equation 6.4, the Jacobian matrix [6] is calculated by SCIATRAN.

The retrieval of aerosol extinction coefficient profiles based on MAX-DOAS measurements represents a non-linear inversion problem which is solved as described in Section 6.3.1. Once this is solved, trace gas retrieval can be initiated as described in Section (6.6.2).

6.6.2 *Trace gas inversion retrieval*

In contrast to aerosols, the retrieval of trace gases is a linear problem that can be solved with one iteration. Here the forward model is described by $\mathbf{K} = \frac{\partial \mathbf{F}}{\partial \mathbf{x}}$, composed of the so-called Box Air Mass Factors (BAMFs) modeled by SCIATRAN.

As described in Section 5.7.1, to calculate the VCD, having the dSCD, the AMF is required. Here, the atmosphere is divided into vertical layers. The $BAMF_{ij}$ is calculated using the modeled $dSCD_i$ at an angle α, and the respectively VCD_j modeled on that layer.

The trace gas profiles' calculations depend directly on the aerosol information previously calculated. This information is used to calculate the BAMF for a single wavelength located at one of the O_4 absorption bands; in this thesis, 360 nm and 477 nm are used for trace gases analyzed in the UV and Visible range, respectively. Such BAMF is assumed to be constant over the DOAS fitting interval, i.e., no wavelength dependencies are considered.

Because the trace gas profiles change with time, the BAMFs need to be re-modeled and updated for every single measurement, i.e., for a given elevation angle, azimuth viewing

---

6 The Jacobian matrix describes how the measurement changes in a specific altitude layer when the aerosol extinction profile also changes

direction, time, and height level; using the aerosol extinction profile previously calculated. Mathematically the BAMF can be written as:

$$B_{ij} = \frac{\partial S_i}{\partial V_j} \tag{6.23}$$

From 6.23:

$$dS_i = \sum_j B_{ij} \times \Delta z_j \times c_j \tag{6.24}$$

Where i stands for the elevation angle, and j is the height level. The layer settings are the same as in the aerosol retrieval. From the Equation 6.24 the vertical profile can be acquired (its concentration c_j at the height level j). The trace gases profile retrieval represents a linear inversion model as described in Deutschmann et al. (2010), Friess et al. (2006), and Yilmaz (2012).

Following the Equation 6.24, a set of linear equations can be obtained for every elevation angle i at a given height level j. Getting the trace gas profile by using a small number of measurements is impossible; for that reason, a linear OEM is applied with a two-step approach to regularize the inversion, as is explained in Friess et al. (2006) and Yilmaz (2012). The system of linear equations can be written as,

$$\hat{\mathbf{x}} = \mathbf{x}_a + (\mathbf{S}_a^{-1} + \mathbf{K}^T\mathbf{S}_\epsilon^{-1}\mathbf{K})^{-1}\mathbf{K}^T\mathbf{S}_\epsilon^{-1}(\mathbf{y} - \mathbf{K}\mathbf{x}_a) \tag{6.25}$$

Where $\hat{\mathbf{x}}$ is the solution of Equation 6.25, $\mathbf{x}_a$ is the a priori trace gas profile, $\mathbf{S}_\epsilon$ and $\mathbf{S}_a$ are the covariances matrices of the measurements, $\mathbf{y}$ is the measurement vector, and $\mathbf{K}$ is calculated in the same way than for aerosols.

6.6.3 *Aplication to MAX-DOAS observations*

Here the measurement and state vector are mathematically defined for MAX-DOAS observations as follows:

6.6.3.1 *Aerosols*

MEASUREMENT VECTOR

$$\begin{aligned}
\mathbf{y} &= (\mathbf{y}_{dSCD_{O_4}}, \mathbf{y}_I)^T \\
&= \{[dSCD_{O_4}(\lambda_1, \mathbf{\Omega}_1), ..., dSCD_{O_4}(\lambda_1, \mathbf{\Omega}_n), dSCD_{O_4}(\lambda_m, \mathbf{\Omega}_1), ..., dSCD_{O_4}(\lambda_m, \mathbf{\Omega}_n)]^T, \\
&\quad \underbrace{[I(\lambda_1, \mathbf{\Omega}_1), ..., I(\lambda_1, \mathbf{\Omega}_n), I(\lambda_m, \mathbf{\Omega}_1), ..., I(\lambda_m, \mathbf{\Omega}_n)]^T}_{Optional}\}
\end{aligned} \tag{6.26}$$

Where,

- $\mathbf{\Omega}_1, ..., \mathbf{\Omega}_n$: is the viewing geometry, with $\mathbf{\Omega} = (\alpha, \theta, \phi)$ where α, θ, ϕ are the elevation, solar zenith and solar azimuth angles respectively.

- $\lambda_1, ..., \lambda_m$ are the O_4 absorption bands wavelengths, and;

$$\Delta SCD_{O_4} = SCD_{O_4}(\lambda, \mathbf{\Omega}_n) - SCD_{O_4}(\lambda, \mathbf{\Omega}_{90})$$
$$\hat{I}(\lambda, \mathbf{\Omega}_n) = \frac{I(\lambda, \mathbf{\Omega}_n)}{I(\lambda, \mathbf{\Omega}_{90})} \tag{6.27}$$

STATE VECTOR

$$\mathbf{x} = [\epsilon_M(z, \lambda_{ref}), \underbrace{\omega_0(\lambda_1), ..., \omega_0(\lambda_m), g(\lambda_1), ..., g(\lambda_m), \alpha_M}_{Optional}] \tag{6.28}$$

Where,

- $\epsilon_M(z, \lambda_{ref})$: Aerosol extinction profile at reference wavelength.

- $\lambda_1, ..., \lambda_m$: As described before.

- ω_0: Aerosol single scattering albedo.

- g: Asymmetry parameter for Henvey-Greenstein parametrization.

- α_M: Ångström exponent

6.6.3.2 *Trace gases*

MEASUREMENT VECTOR: All the *dSCDs* for a given trace gas to analyze. Specifically in this thesis, NO_2 in the UV and VIS range, and HCHO.

STATE VECTOR:

$$\mathbf{x} = [\Delta V(z_0), ..., \Delta V(z_l)]^T \quad , \text{with} \quad \Delta V(z) = \int_{z-\frac{\Delta z}{2}}^{z+\frac{\Delta z}{2}} c(z')dz' \tag{6.29}$$

Where,

$\Delta V(z)$: Partial vertical column density in a column of height Δz. Furthermore, the BAMFs are given by the weighting functions:

$$BAMF(\lambda, \Omega, z) = \frac{\partial dSCD(\lambda, \Omega)}{\partial \Delta V(z)} \tag{6.30}$$

6.7 RETRIEVAL PROCEDURE

As previously mentioned, in this thesis, HEIPRO (Yilmaz, 2012) was used for the measurements' inversion to derive the aerosol and trace gas vertical content in the atmosphere. Figure 6.7 shows the retrieval steps starting from the spectra and ending with the aerosol and trace gas profile information as a final output.
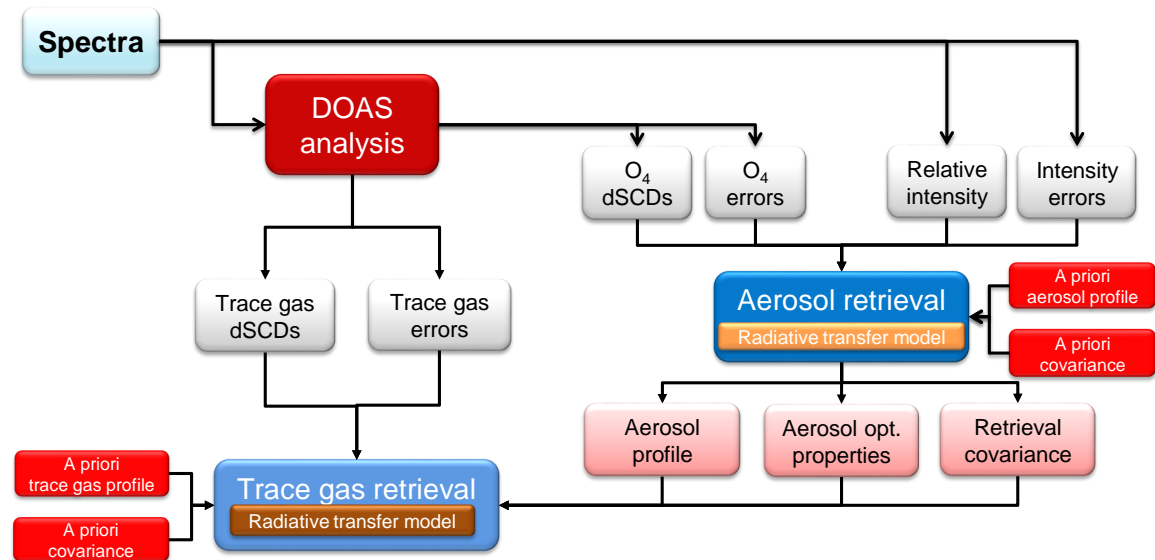
Figure 6.7: Retrieval scheme of the aerosol and trace gas profile retrieval adapted from Yilmaz (2012) and modified for the here used algorithm.

The complete retrieval is composed of three main processes:

1. **The DOAS analysis**: It is deeply explained in Chapter 5. Starting from the actual observations, it ends with the dSCD[7] of aerosols and trace gases of interest.

2. **The non-linear inversion of the aerosol extinction profile**: The measurement vector used consists of the O_4 dSCD and its errors which represent the measurement covariance matrix. An a priori aerosol extinction profile is used, exponentially decreasing with height. The $O_4 dSCD$ are modeled using SCIATRAN; then, the OEM optimizes the aerosol extinction profile by comparing the measured and modeled O_4 dSCD until both agree on a defined limit difference.

   In recent studies, it has been demonstrated that the modeled and measured O_4 dSCD do not match; therefore, a scaling factor ($0 < SF < 1$) must be applied to the O_4 observations to correct this inconsistency (Clémer et al., 2010; Wagner, Deutschmann, and Platt, 2009).

3. **Linear inversion of the trace gases profile**: The retrieved aerosol extinction profile calculated above, together with the dSCD of the trace gas of interests obtained with the DOAS fit, is used. Furthermore, depending on the wavelength range used for the

---

7 And their respective errors, which are later used as measurement vector.

DOAS analysis, an absorption band of O_4 is selected to calculate the BAMFs, which are calculated with SCIATRAN. Finally, an a priori trace gas extinction profile is provided with an exponential decay function. Then a linear inversion is performed using the OEM to calculate the trace gas profile. More details on the algorithm and procedure can be found in Yilmaz (2012).

7

INSTRUMENTATION: DESCRIPTION AND SET-UP.

7.1 MAX-DOAS INSTRUMENT

7.1.1 *Airyx SkySpec 2D MAX-DOAS*

7.1.1.1 *Description and set-up*

The MAX-DOAS instrument used within this thesis is a two-dimensional (2D) unit built by Airyx, commercially called "Airyx SkySpec 2D". Figure 7.1 comprises all instrumental components, measurement geometry, and basic features. Briefly, the instrument has two spectrometers covering the UV and Vis range; this feature allows the user to have a broader spectral interval for retrieving more trace gases and aerosol properties, with higher resolution than using only one spectrometer covering the whole range. The instrument collects scattered sunlight at different elevation angles using a motorized prism inside a quartz tube; this arrangement prevents misalignments in the optical adjustment of the telescope by not moving the entire telescope unit but only the prism employing a small servo motor. Furthermore, an azimuth motor allows the instrument to measure in different horizontal directions (azimuth angles). The instrument includes a motorized light diffuser, allowing direct-sun measurements. The instrument is temperature stabilized and includes an inclination sensor to adjust the elevation angle automatically (Airyx, 2022).
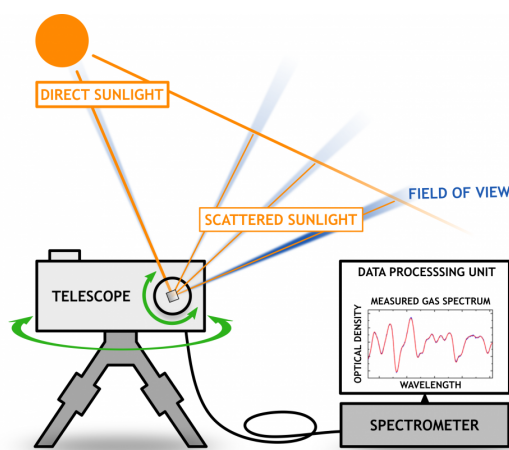
Figure 7.1: Illustration of the Airyx 2D MAX-DOAS's components and basics. Taken from Airyx (2022)

Figure 7.2 shows all the parts of the instrument, which are explained below:

- **Part A**: Quartz tube containing the scanning telescope and a small stepper motor that allows to measure at different elevation angles. The scanning telescope itself

Figure 7.2: The main components of the 2D MAX-DOAS are shown in Figure. A., B., C. and D represent the external parts of the 2-D MAX-DOAS while E. is the outdoor part of the instrument.

is composed of a prism reflector that redirects the sunlight to the entrance of the telescope box (B.).

- **Part B**: A telescope, a rotating housing box containing the focusing lenses to receive scattered sunlight, an integrated motorized diffusor for direct sun measurements, an integrated mercury lamp for wavelength calibration, and an optical fiber entrance transporting the collected light to the spectrometer box (E.).

- **Part C**: The optical fiber bundle which carries the sunlight from the telescope box to the entrance of the two spectrometers, i.e., the spectrometer box (E.)

- **Part D**: Contains a stepper motor that controls the azimuth viewing direction.

- **Part E**: Due to the sensitive elements that form this part, and the necessity of temperature stabilization , it needs to be indoors. It is composed of two Avantes AvaBench-75 spectrometers, which use Hamamatsu CCD detectors; brief information about them is described in Table 7.1 :

Besides the spectrometers, the box contains all the connecting cables between E. and B., including the power supply for the stepper motors and a USB cable that connects B. to a computer that controls the instrument.

Spectrometer name	Spectral range	Spectral resolution
UV	$300 \sim 460nm$	$\sim 0.6nm$
Vis	$405 \sim 550nm$	$\sim 0.6nm$

Table 7.1: Airyx 2D SkySpec spectrometers information

- Software: This instrument is operated by an external computer, which uses "MS-DOAS"[1] to control the instrument and, therefore, the measurements.

7.1.1.2 *Elevation angle calibration*

The SkySpect instruments utilized in this thesis were bought under the premise that they were ready to use, calibrated, and tested. However, during the first months of measurements, one of the instruments showed different failures, one of which was the elevation angle and all related components. Once this was fixed, we perform, together with a colleague from IUP-Heidelberg[2] an elevation angle calibration procedure similar to the one described in Donner et al. (2020). A sketch of the method is provided in Figure 7.3, and is briefly described in the following.

A thin neon-light stick was used as a target placed at ~ 5 meters far from the instrument telescope. Because an artificial light source was utilized, this calibration was made at night. The lamp was fixed on a tripod at an altitude that was aligned with the telescope unit's center, so with the elevation angle $\alpha = 0$ The alignment described before was possible using a laser level, which illuminated both the telescope unit and the target lamp on the tripod. Such laser level has a total uncertanty of ~ 0.1 degrees[3]. After all, it is set up; it is turned to measure. A simple routine was run, which includes two steps:

1. Using the eye, we moved the instrument's azimuth angle ϕ to an initial position relatively close to the target in a straight line. At that initial position, we collected measurements at different elevation angles with a step of 0.1 degrees, with the idea of sampling until the lamp was found.

2. If the lamp was not found in 1., we moved the azimuth angle by a step of 0.1 degrees, and then we sampled in the vertical axis as described before.

Once the lamp position was found, we fixed the azimuth angle, then took measurements at different elevation angles with a step of $\sim 0.01°$.

Figure 7.4 shows that our hypothesis that the instrument's elevation angle was not properly calibrated was true. We found that the elevation angle was off by about -1.8°. After this finding, the instrument was sent to Airyx for complete calibration.

---

1 Software written by Udo Frieß.

2 Jan-Lukas Tirpitz

3 The laser level used is the same described by Donner et al. (2020). Furthermore, they experimentally measured its uncertainty to $\sim 0.1°$, summing up to $\sim 0.04°$ due to the beam width of ~ 2 mm.
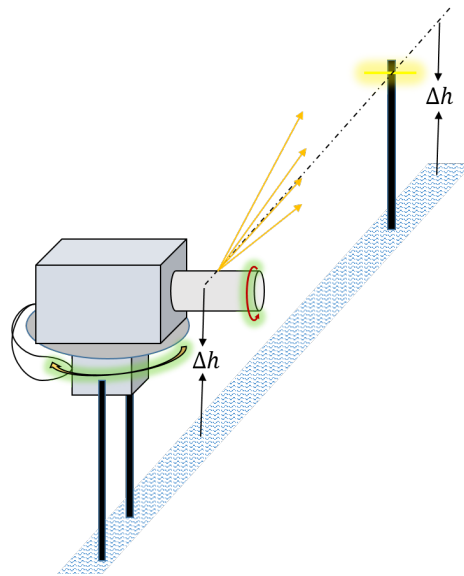
Figure 7.3: MAX-DOAS set-up for calibration of the elevation angle.
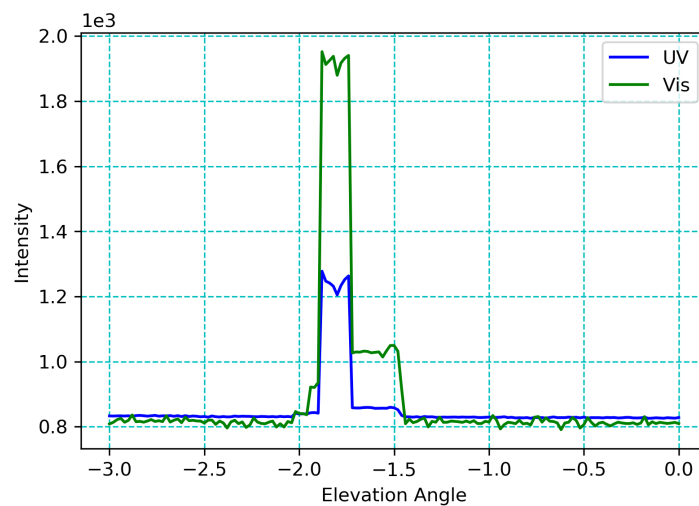
Figure 7.4: Example of elevation angle calibration test results for one of the instruments used in this thesis.

7.1.1.3 *Instrumentation software*

MS-DOAS: The software written by Udo Frieß from the University of Heidelberg controls the SkySpect 2D instrument. It requires a routine script to set up the desired measurement sequence. For the instruments used in this thesis, the script provided by Airyx was extended and adjusted accordingly.

7.2.1 *EM27/SUN FTIR spectrometer*

The EM27/SUN FTIR spectrometer was designed/developed by KIT in close cooperation with Bruker Optics^{TM}. Briefly, it is a mobile unit capable of measuring direct solar radiation in the NIR spectral region with two detectors, the main covering the range: 5500 to 11000 cm^{-1} and the second: 4000 to 5500 cm^{-1} . From the measured spectra the atmospheric abundances of CO_2, CH_4, CO and H_2O can be derived. The Figure 7.5 shows schematically the general instrumental components and the measurement principles.
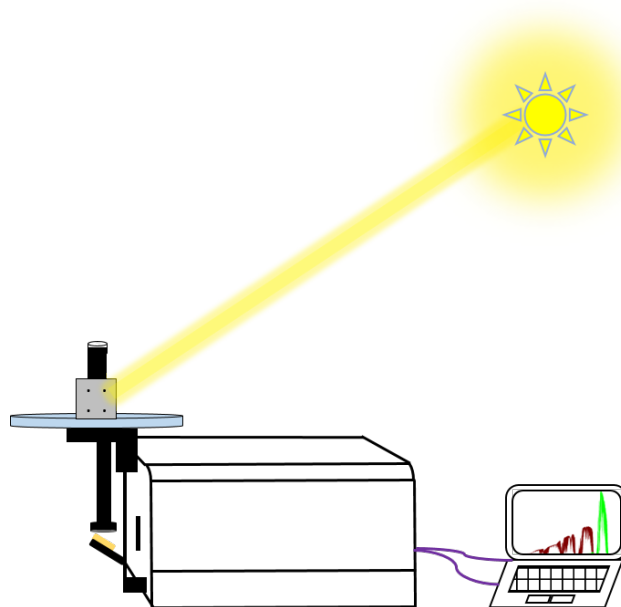
Figure 7.5: EM27/SUN set-up and basics

7.2.1.1 *Description and set-up*

The main component of these instruments are shown in Figure 7.7 and briefly described as follows:

- **Part A**: This is a **RockSolid^{TM}** pendulum interferometer[4] composed of two cube corner mirrors and a Quartz beamsplitter offering high thermal and mechanical stability, supporting a maximum beam diameter up to 40 mm. The pendulum's retroreflectors are gimbal mounted to avoid wear and friction damage. This pendulum allows an OPD of 1.8 cm, approximating a spectral resolution of 0.5 cm^{-1} that permits double-sided interferogram recording.

- **Part B**: This is a standard **CMOS USB-camera** that helps to monitor and control the solar tracking by giving real-time optical feedback of the diffusely backscattered

---

4 As an FTIR spectrometer, the core is an interferometer, as described previously.

radiation emerging from the field stop wheel (see Figure 7.6 **A**) showing a real-time image of the solar disk alignment into the field-stop of the instrument, photo of the camera view is shown in Figure 7.6 **B**. More details can be found in (Gisi et al., 2011).
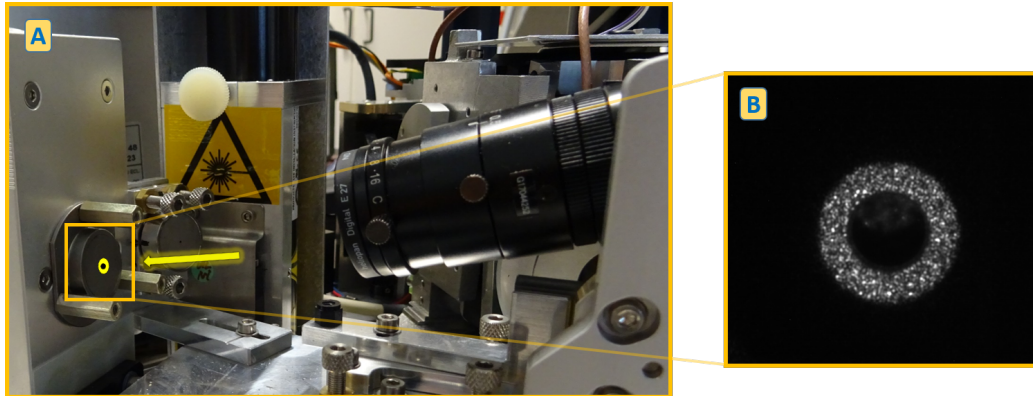
Figure 7.6: Illustration of the camera tracking system; in **A**, the illuminated field stop of the main channel and the camera placed right in front is shown; and in **B**, an example of one digital image of the solar disk recorded by the software CamTracker.

- **C** and **Part D**: They are the instrument's main and CO channel detectors, respectively. Both are Indium Gallium Arsenide (InGaAs) detectors, which cover the wavelength range: 5500-11000 cm^{-1}, and 4000-5500 cm^{-1} for the primary and CO channel, respectively. The second channel uses an extended InGaAs detector element and a wedged Germanium (Ge) filter to define a spectral bandpass beyond the spectral coverage of the standard spectrometer. More details can be found in Hase et al. (2016).

- **Part E**: It is a standard non frequency stabilized HeNe laser that controls the interferogram sampling.

- **Part F**: It is the outer part of the **CamTracker** system, which is an altazimuthal solar tracker; more information can be found in (Gisi et al., 2011). The rest are the camera described previously, and the software controlling it.

7.2.1.2 *Instrumentation software*

CAMTRACKER: It is the software controls the solar tracking system in the EM27/SUN instrument. It uses the coordinates of the measurement site (latitude, longitude, altitude), the instrument should face towards South. Once this is done, the solar disk has to be manually centered in the instrument's field stop and saved for future measurements. The ellipse and circle parameters of the fitted solar disk (see Figure 7.6 **B**) must be adjusted, and then the tracking system is ready to work.
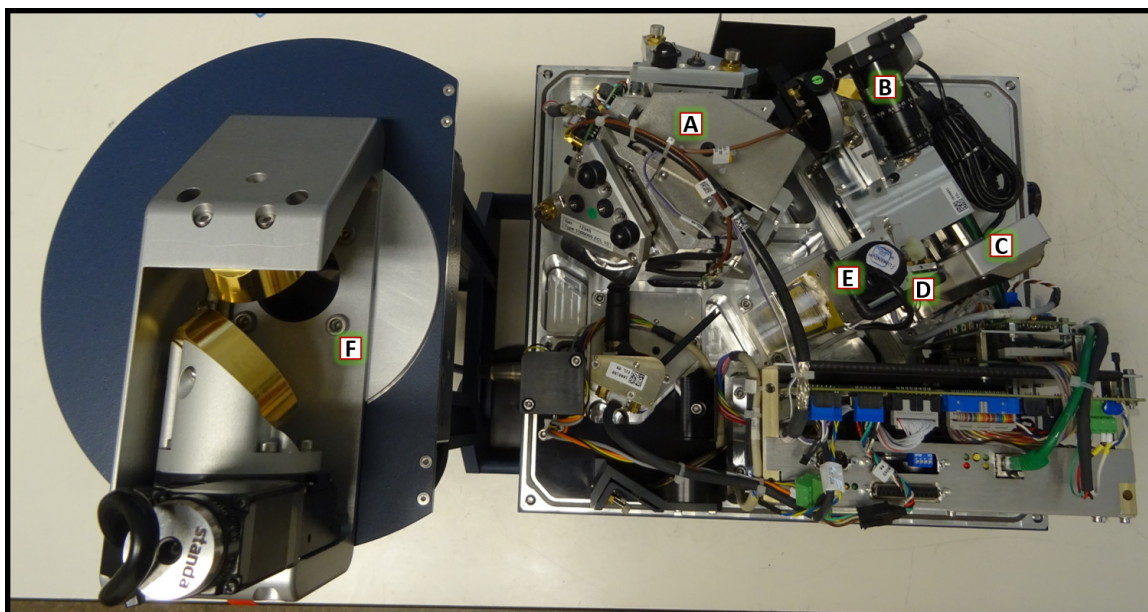
Figure 7.7: The main components of the EM27/SUN can be seen in this figure. A., B., C., D, and E represent the internal parts of the instrument while F. is the outdoor part.

OPUS: The software provided by the manufacturer Bruker controls the collection of the interferograms. For daily solar measurements, the procedure is automatized by a script called "macro," which contains the settings of the desired measurement acquisition.

7.2.2 *Bruker FTS-125HR*

The Ground-Based FTIR Remote Sensing group operates a high-resolution FTIR spectrometer, Bruker IFS 125HR, at KIT Campus North ($49.100°$ N, $8.439°$ E, 112 m a.s.l.). This spectrometer is part of the TCCON and NDACC network, a complete description of this instrument can be found in Kiel (2016).

The instrument operated at KIT is set up in a controlled temperature shipping container to ensure a constant temperature throughout the year. In order to satisfy the requirements of the NDACC and TCCON network measurement routines and specifications, the spectrometer uses a devoted dichroic beamsplitter arrangement (Optics Balzers Jena GmbH, Germany) with a cut-off wavenumber of 5250 cm^{-1}. The core of this instrument is a cube-corner Michelson interferometer with a calcium Fluoride (CaF2) beamsplitter and a linear moving scanner.

This spectrometer can measure solar radiation in the MIR and NIR spectral regions, covering the wavelength region 1900 - 11000 cm^{-1}; experimentally done by using two different detectors: (1) an indium antimonide (InSb) covering the wavelength from 1900 to 5250 cm^{-1} that requires a cryogenically cooling system done by liquid nitrogen (LN$_2$); and (2) an indium gallium arsenide (InGaAs), covering the spectral range 5250 to 11 000 cm^{-1}, which works at room temperature; more information can be found in Kiel (2016). The di-

rect sunlight radiation is collected using a camera-based tracking system (Gisi et al., 2011).

IMPROVED CALIBRATION PROCEDURES FOR THE EM27/SUN SPECTROMETERS OF THE COCCON NETWORK.

In this chapter, an extension on the previously reported status of the COllaborative Carbon Column Observing Network's (COCCON) calibration procedures incorporating refined methods is presented. COCCON is a global network of portable Bruker EM27/SUN FTIR spectrometers for deriving column-averaged atmospheric abundances of greenhouse gases. The original laboratory open-path lamp measurements for deriving the instrumental line shape (ILS) of the spectrometer from water vapour lines, see (Frey et al., 2019), have been refined and extended to the secondary detector channel incorporated in the EM27/SUN spectrometer for detection of carbon monoxide (CO). The refinements encompass improved spectroscopic line lists for the relevant water lines and a revision of the laboratory pressure measurements used for the analysis of the spectra. In addition, a new calibration cell for ILS measurements was designed, constructed and put into service. Spectrometers calibrated since January 2020 were tested using both methods for ILS characterization, open-path (OP) and cell measurements. Finally, a revision and extension of the COCCON network instrument-to-instrument calibration factors for XCO_2, XCO and XCH_4 is presented, incorporating 47 new spectrometers (of 83 in total by now). This calibration is based on the reference EM27/SUN spectrometer operated by the Karlsruhe Institute of Technology (KIT) and spectra collected by the collocated TCCON station Karlsruhe.

8.1 ADVANCING THE OPEN-PATH METHOD FOR ILS CHARACTERIZATION

The method described in Frey et al. (2015), of characterizing the ILS of low-resolution spectrometers using open-path measurements, is improved and extended; the method is briefly summarized here along with a description of the main improvements. The idea of the approach is to use the absorption of infrared radiation from an external tungsten lamp by strong water vapour lines along a laboratory path of a few metres. A fit to the spectrum is performed by adjusting the H_2O column, a spectral scaling factor, a spectrally variable background transmission level and a parameterized ILS.

Two parameters are used for describing deviations from the nominal ILS shape: the "modulation efficiency amplitude" (MEA) describes a deviation from the expected ILS width, and the "phase error" (PE) quantifies the asymmetry of the ILS (Hase, Blumenstock, and Paton-Walsh, 1999). Because the widths of the spectral lines generated along the open path depend on pressure and temperature, these parameters need to be recorded for the analysis of the measurements. The self-broadening of H_2O is a non-negligible contribution; therefore, the absorption path length needs to be known. The H_2O partial pressure is calculated from the retrieved H_2O column amount, pressure and temperature, so the analysis of the spectrum is an iterative procedurem (repeated until convergence to a self-consistent solution is reached).

8.1.1 *Procedure and set-up*

The general set-up is described by Frey et al. (2015) and Gisi et al. (2012) and illustrated in Figure 8.1. At least 2 h before the first interferograms are collected, the spectrometer is powered up. Two openings in the spectrometer's shelter are uncovered for allowing exchange between the air trapped inside the spectrometer and the external laboratory air. This equilibrates the water vapour mixing ratio inside the spectrometer with the environment and allows the spectrometer to reach a stable operating temperature, thereby minimizing spectral drifts of the He–Ne laser which controls the interferogram sampling. For the radiation source, a commercial halogen lamp attached to a lens collimator is used. The lamp bulb is grounded on the outside and is tilted with respect to the optical axis to minimize channelling artefacts (Blumenstock et al., 2021). The spectrometer resides on a table, while the lamp is mounted on a tripod at about 4.20 m (4.0 m for instruments calibrated before January 2020) from the first mirror of the solar tracker attached to the spectrometer. The position of the lamp is level with the tracker, and the beam is steered towards the first tracker mirror.
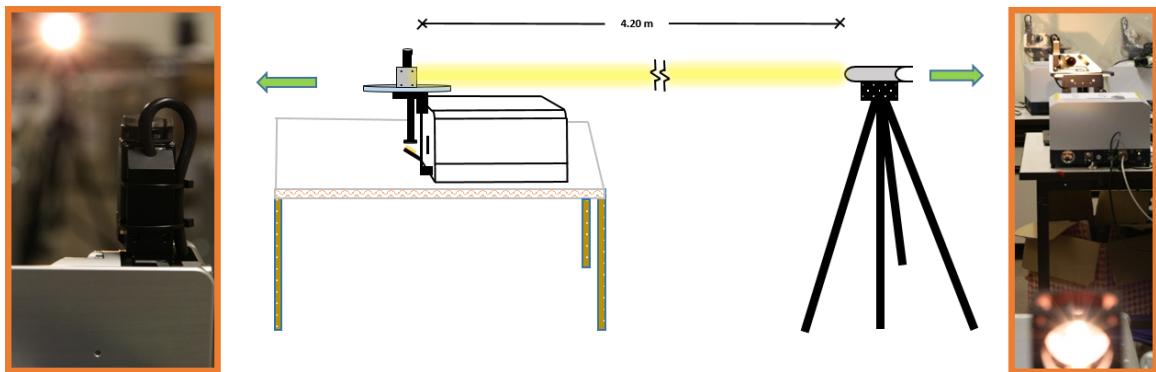
Figure 8.1: Set-up of the open-path measurements. The central part of the illustration schematically shows all the components and the alignment of the experimental set-up, while in left and right sides photographic close-up views are presented. The left photograph shows the view in the opposite direction from the spectrometer towards the lamp unit, while the right photograph shows a view from the lamp unit (bottom) towards the spectrometer with its solar tracker (top): the lamp in the bottom part and the instrument located at a distance of 4.20 m.

8.1.2 *Updated measurement procedures*

The main changes with respect to the old method are described in the following subsections.

8.1.2.1 *Geometry of the set-up*

In addition to the open-path procedure (January 2020), a cell set-up has now been implemented for the calibration of the EM27/SUN spectrometers; the geometrical arrangement previously used was slightly reconfigured to support both OP and cell measurements. The

spectrometer is now oriented in such a way that the cell can be conveniently located in the infrared beam on top of the spectrometer housing (see Figures 8.1 and 8.4 **a)** and 8.4 **b)**. This modification results in a slightly larger distance between the lamp and the first tracking mirror; in the past that distance was 4.0 m, and it is now 4.2 m.

8.1.2.2 *Distance travelled by the beam inside the instrument*

We decided to re-check and thereby noticed that the previously assumed optical path length inside the spectrometer was underestimated. In order to derive this distance properly, an optical method was applied. The set-up of the method is illustrated in Figure 8.2 and described as follows: it uses a digital camera **J**, a finely structured optical target printed on a piece of paper **E'** and pocket lamp **E''** for illumination of the target. The aim is to optically measure the inaccessible path section from the instrument entrance window **E'** until position **E**, as shown in that figure.

Where:
- ✓ A') Instrument's entrance
- ✓ A) Long-pass filter
- ✓ B) Reflecting mirrors
- ✓ C) Beam splitter
- ✓ D) Moving mirror
- ✓ E) Aperture ~ 3 mm
- ✓ E') Finely structured optical target
- ✓ E'') Pocket lamp
- ✓ F) Mirror
- ✓ G) Aperture ~ 0.6 mm
- ✓ H) Diffusor
- ✓ I) First channel detector InGaAS
- ✓ J) Professional camera
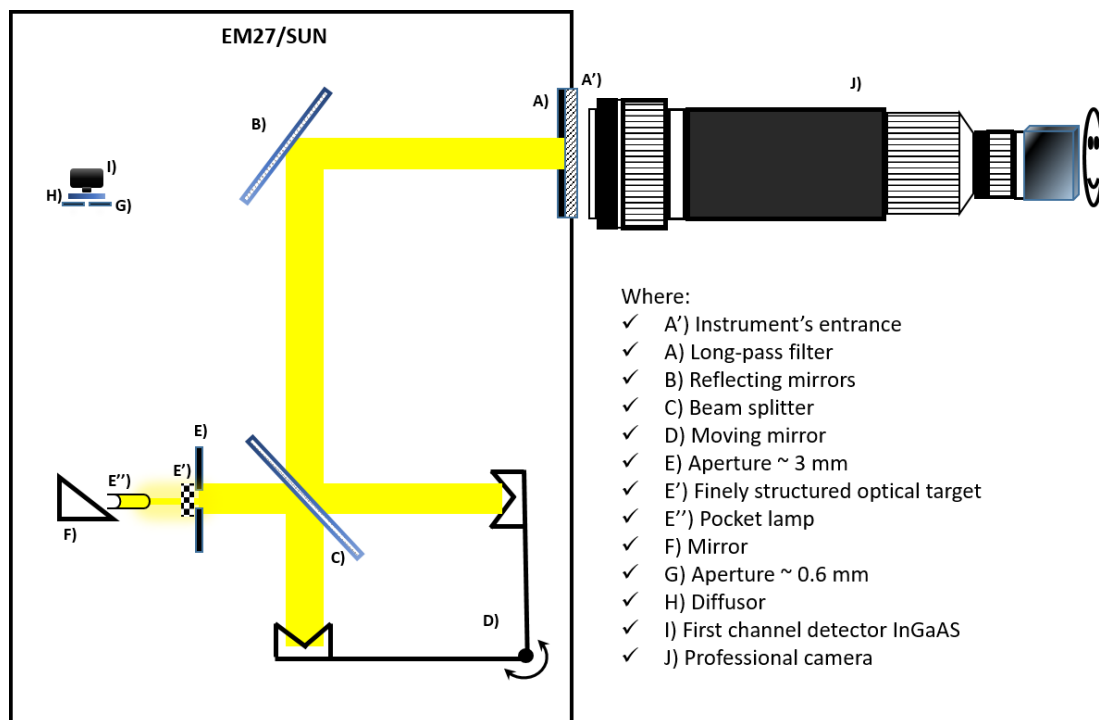
Figure 8.2: Light path of the beam inside the instrument coming from the lamp in **E''** to the camera at the instrument's entrance **A'**.

For performing the distance measurement, the solar tracker was unmounted to gain access to the entrance window. The paper target was located at position **E** and illuminated with the pocket lamp. The digital camera equipped with a telescopic lens was positioned directly in front of the entrance window for observing the target. The target is focused properly, and the focus position of the lens is maintained while the spectrometer is removed. Next, the target is arranged at such a distance from the lens that a sharp image is re-created. This distance can easily be measured geometrically, and we estimate the accuracy of the method to be better than 5 cm. In order to determine the complete optical path

inside the instrument, the distances **E** to **F** and **F** to **I** are measured with a conventional ruler and added to the distance calculated with the previously explained method.

Length	Old	New (cm)	Difference abs(new − old)/old
Lamp to first tracking mirror	400.0	430.0	7.5 % (note: deliberate adjustment)
First tracking mirror to spectrometer housing entrance	38.0	33.0	−13.2 %
Spectrometer housing entrance to detector	58.0	74.0	+27.6 %

Table 8.1: Description of the main changes in the path distance used in the past and the current ones.

In Table 8.1, the old and new results for the relevant distances are presented. Note that the distance between lamp and first tracker mirror has been changed deliberately. The corrected other two contributions to the total path length, which are used for the proper calculation of the H_2O partial pressure, have been considered in the reanalysis of the old lamp measurements. For the analysis of the lamp measurements after mid-January 2020, the updated values as provided in Table 8.1 have been used. The effect on the ILS parameters via the resulting change in H_2O partial pressure is small, but detectable. We discuss this effect in Section 8.3.1.

8.1.2.3 *Measurement procedure*

Before the collection of measurements, the tracking mirrors (elevation and azimuth) are carefully adjusted in order to centre the lamp image on the field stop. The image of the lamp needs to surpass the field stop's diameter. This procedure is conveniently carried out using the camera, which is incorporated in the spectrometer for controlling the solar tracking.

8.1.3 *Data acquisition and improved processing*

Before the interferograms are recorded (either with or without the cell in the path), the pre-gain and gain settings of both detectors are checked. The manufacturer's data acquisition software OPUS is used to perform the measurements and to process the DC-coupled interferograms. Ten double-sided full-resolution scans recorded with 10 kHz scan speed are co-added into one averaged interferogram, and 30 to 40 averaged interferograms of this kind are recorded in total to achieve a spectral signal-to-noise ratio in the range of 2000 to 3000; see Section 8.5.3. As the DC level of the EM27/SUN is slightly variable as a function of optical path difference, a DC correction is applied (because the solar observations also undergo a DC correction). The resulting spectra are normalized to about

unity in the spectral range required for the ILS analysis and are stored with a zero-filling factor of 8 to support the visual inspection of the spectral fit quality.

8.1.3.1 *Required auxiliary data*

In order to correctly derive the H_2O column and ILS parameters, pressure and temperature need to be measured, both inside the instrument and outside in the laboratory. The temperature inside the spectrometer is recorded using the sensor built into the spectrometer by the manufacturer. The temperature of the laboratory air is recorded using digital thermometers offering $0.8\,°C$ accuracy (Lutron MHB-382SD data loggers or thermo hygrometer barometers of type PCE-THB 40 were used). While in the previous data analysis the pressure readings of the aforementioned portable sensors were used, we migrated for the analysis of new measurements as well as for the re analysis of previous measurements to the pressure record from the nearby meteorological tall tower. This tower is operated by the Institute for Meteorology and Climate Research – Department Troposphere (IMK-TRO), see Kohler, Metzger, and Kalthoff (2018). The pressure sensor used at the tower is calibrated in regular intervals, and the data accuracy is expected to be within 0.5 hPa. The tower is located at a distance of about $800\,m$ from our laboratory. We apply a barometric correction to the pressure data measured at the tower, as the elevation of the laboratory is higher than the location of the pressure sensor by approximately $11\,m$.

8.1.3.2 *Data processing*

For the retrieval of the ILS parameters, the LINEFIT software version 14.8 (Hase, Blumenstock, and Paton-Walsh, 1999) is used. In order to retrieve the H_2O column, a simple two-parameter ILS model is utilized as described in Frey et al. (2015). The main extension in the retrieval set-up is that the ILS is now characterized for both the primary and the CO channel. Two different spectral regions are therefore investigated as shown in Figure 8.3. The previously used spectral window covers 7000–$7400\,cm^{-1}$, and the newly added window covers 5275–$5400\,cm^{-1}$. The latter window resides in the spectral overlap region covered by both detectors, allowing a check for a possibly degraded ILS of the CO channel with respect to the primary channel, because in this spectral window the retrieval of ILS parameters can be performed from both main channel and CO channel spectra. A dedicated check of the CO channel seems advisable, because the primary channel is used as the reference for the interferometric alignment, while the CO channel is only adjusted to match the alignment of the primary channel. By comparing the ILS parameters retrieved from the same spectral window, biases introduced by spectroscopic inconsistencies cancel out. Therefore, according to the new scheme presented here, three sets of ILS parameters are retrieved, and the two additional retrievals performed in the new window are introduced for recognizing a potential misalignment of the CO detector.

8.1.3.3 *Empirical update of H_2O spectroscopic data*

For the previous ILS analysis, the H_2O line list provided by HITRAN version 2008 (including the corrections introduced in 2009) with some minor empirical adjustments was used. The work presented here uses a considerably revised line list. The HITRAN 2016
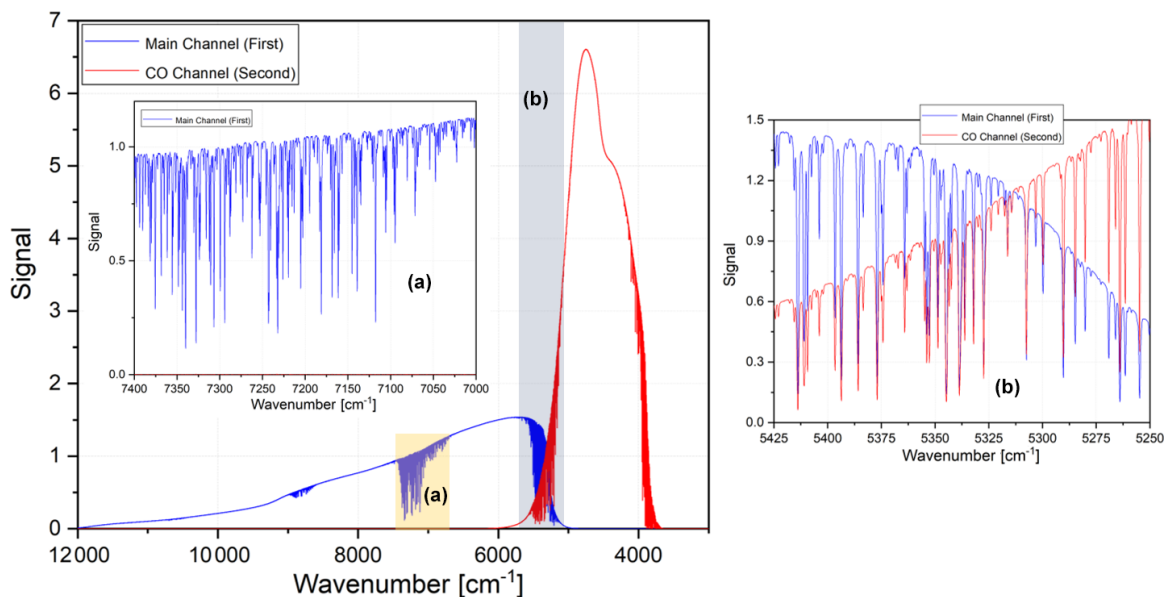
Figure 8.3: Typical spectra for both channels, obtained with the COCCON reference instrument SN37 on 19 March 2021. The highlighted regions **(a)** and **(b)** are the spectral windows used for the ILS retrievals.

H_2O list served as a starting point for fitting empirical H_2O line parameters in the two relevant spectral regions using a pair of high-resolution open-path spectra recorded with the Bruker IFS125HR spectrometer of the TCCON station Karlsruhe. The air condition- ing system of the laboratory container housing the spectrometer was used to adjust the air temperature to 15 and 30 °C, respectively. We assume that this span largely covers the conditions of laboratory ILS measurements. The pair of spectra were then used for a multi-spectrum fit of empirical H_2O line parameters using the LINEFIT software with a wrapper for adjusting the line parameters. Line intensities, line positions and broadening parameters were adjusted (the ratios of the self and foreign broadening parameters were maintained as reported in the HITRAN line list). The fit residuals of the high-resolution spectra after the empirical adjustment are shown in Appendix A (see Figures A.1 and Fig- ure A.2). In order to avoid a significant bias between the ILS parameters reported by Frey et al. (2019) and the results of the reanalysis presented here, a global scaling factor was determined and applied to the new pressure broadening parameters. As expected, the fit quality of EM27/SUN open-path spectra using the new empirical line list are significantly improved, as discussed in Section 8.3.1.

8.2 USE OF A CELL FILLED WITH A C_2H_2−AIR MIXTURE FOR ILS CHARACTERIZA- TION

In addition to the refinements introduced in the open-path method, a new gas cell was developed and has been used in parallel with the open-path measurements. This chapter presents the details of the cell.

8.2.1 *Cell components*

This new method developed for measuring the ILS for EM27/SUN instruments uses a gas cell filled with C_2H_2. This gas is a good choice, because it is easily accessible and easy to handle, and because it offers a strong absorption band at $6550\,cm^{-1}$, a spectral region largely free from H_2O contamination. In the context of calibration work for TCCON, experience with C_2H_2 has already been collected (see Section 8.2.2). The cell has an effective length of 200 mm and an internal diameter of 30 mm. Wedged fused silica windows are glued to the slightly angled end surfaces of the cell body. The cell is closed with a Teflon valve stem, sealing against a Schott Duran valve body. A temperature sensor is attached to the cell in order to monitor this variable during the experiment. To fix the cell into the lamp beam at the level of the tracker beam, a simple support has been built as shown in Figure 8.4 **c)**. A cardboard screen is used to limit the heating of the cell body by the lamp.
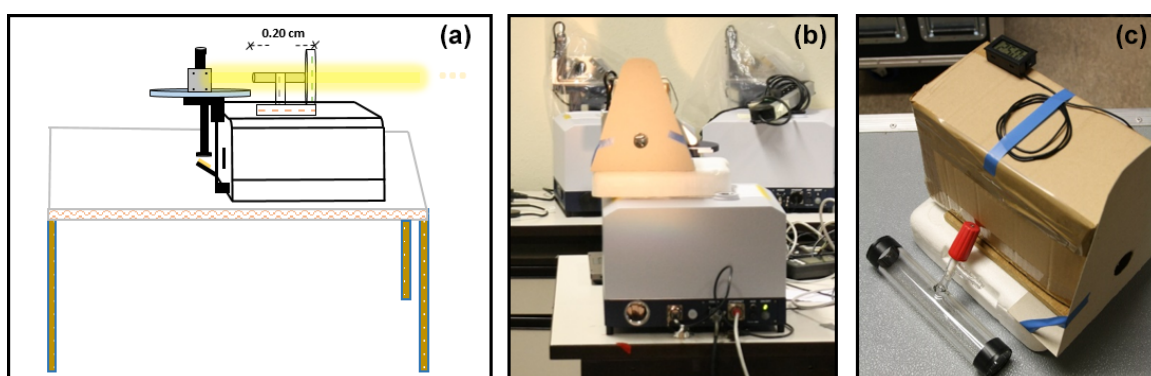
Figure 8.4: The set-up of the cell measurements and the cell components used in this study are shown in **(a)**, **(b)** and **(c)**, respectively.

8.2.2 *Cell content and calibration*

A different cell, which is pressure-monitored and filled with 300 Pa of pure C_2H_2, is used at the TCCON station Karlsruhe for calibration work on the sealed HCl cell as used by the TCCON network; this cell and its application is described in Hase et al. (2013). Inspection of the fit residuals of high-resolution C_2H_2 spectra recorded with the IFS125HR spectrometer indicates that in particular the line positions of the HITRAN 2016 line list are slightly imperfect, so the line positions have been adjusted. This improved empirical C_2H_2 line list is also applied to the low-resolution work presented here.

For low-resolution measurements, we require a higher filling pressure, as pressure broadening is needed to generate absorption lines of sufficient area. In the Doppler limit, even saturated lines generate a very weak signal in the convolved spectrum, because such lines are spectrally much narrower than the ILS of the EM27/SUN spectrometer. Using an available cell body of 200 mm length, a pressure on the order of 100 hPa was found to be a reasonable choice.

After filling of the cell, a pair of high-resolution reference cell spectra were recorded using the IFS125HR spectrometer at temperatures around 288 and 303 K. From these spectra,

the amount of C_2H_2 contained in the cell was retrieved, which also sets the C_2H_2 partial pressure for a given cell temperature. Next, assuming an ideal ILS for the IFS125HR spectrometer, the relevant cell parameters were retrieved using LINEFIT. The results for C_2H_2 total and partial pressure are provided in Table 8.2. While the partial pressure results from the measured line area follow the ideal gas law, the retrieved total pressure which minimizes spectral residuals deviates from the ideal gas law. It should not be regarded as a physical parameter, and it is used to compensate for various imperfections (reported values of self and foreign pressure broadening parameters and their temperature dependence, possible air contamination in the cell, etc.). For adjusting these parameters to other working temperatures, we apply a linear interpolation in both tabulated parameters of the total and partial pressure.

T [K]	p_tot [hPa]	p_part [hPa]
288.2	138.0	121.8
303.2	147.8	128.1

Table 8.2: Measured variables in the cell with respect to the IFS125HR spectrometer at Karlsruhe TCCON station.

8.2.3 *Measurement set-up*

When the cell is positioned in the open-path set-up, we maintain the 4 m distance between the lamp and spectrometer. This does not bring in complications, because the H_2O lines superimposed to the observed C_2H_2 band are sufficiently weak. Therefore, we can easily go back and forth between the open-path and cell configuration. The C_2H_2 cell introduces a slight beam deviation because the window wedges do not fully compensate, but the camera incorporated in the EM27/SUN can be conveniently used for realigning the image of the lamp collimator on the spectrometer's entrance field stop. After the warm-up phase of the spectrometer discussed in Section 8.1.2.1, 10 to 16 interferograms are collected using a 10 kHz scan speed (each interferogram comprised of 10 co-added scans).

8.2.4 *Error budget of the cell measurement for measuring ILS parameters of the EM27/SUN spectrometer*

With the spectral noise level achieved by applying the measurement procedure outlined in Section 8.3.3, the propagation of spectral noise into the retrieved ILS parameters turns out to be a negligible contribution. The error budget of the ILS parameters is dominated by the knowledge of the gas cell temperature, which might vary while the measurement is performed and across the cell body. We assume that the knowledge of cell temperature during the measurement is on the order of 1 to 2 K. A change in the temperature by 1 K changes the retrieved modulation efficiency amplitude by about 0.25 %. The empirical cell pressure parameters described in Section 8.2.2 used for the analysis of cell spectra also suffer from experimental uncertainty. The IFS125HR spectrometer might deviate slightly

from an ideal spectrometer, and the analysis of the spectra used for the calibration of the cell parameters suffers from imperfect measurement of cell temperature. In the subsequent application of the cell, we estimate an uncertainty of the cell pressure parameters on the order of 0.5 %, which produces a systematic error contribution of about 0.36 %. Table 8.3 summarizes the error budget of the cell measurement.

Error source	Uncertainty	Propagation on MEA
Spectral signal-to-noise ratio	2000	1.5×10^{-4}
Temperature	1 K	2.5×10^{-3}
Empirical cell pressure parameters (systematic error contribution)	0.5 %	3.6×10^{-3}

Table 8.3: Estimated error budget of the MEA (modulation efficiency amplitude) ILS parameter for the C_2H_2 cell measurement procedure.

8.2.5 *Data acquisition and pre-processing and final processing*

The OPUS software provided by the manufacturer Bruker is used to collect the interferograms. The settings used for their acquisition are the same as for the open-path method. Once the interferograms are recorded, they are pre-processed using OPUS in the same way as explained in the open-path method; namely a DC correction is included. After generating a spectrum, the ILS is retrieved using LINEFIT 14.8. Figure 8.5 shows an open-path spectrum recorded with the C_2H_2 cell inserted in the beam. The C_2H_2 band located in the wavenumber range 6450–6630 cm^{-1} is utilized for the retrieval of ILS parameters.

8.3 DISCUSSION OF OPEN-PATH RESULTS

In this section, we will discuss the results of the open-path measurements, achieved by applying the improved and extended methods introduced in Section 8.1. Firstly, we apply the new refined analysis procedure to the open-path measurements collected by Frey et al. (2019), and we compare the results of this reanalysis with the previously reported results. Next, the results derived from the standard spectral window are compared with results obtained using the micro window in the spectral overlap region, which is accessible by both detectors. As described in Section 8.1.3, this additional spectral micro window was implemented for detecting a potential misalignment of the CO detector element. This performance test was not included in the previous open-path recipe. Finally, our best estimate of the instrumental line shape parameters is provided for all tested spectrometers. The table summarizing the revised results contains the revised values for those spectrometers investigated in the study by Frey et al. (2019) and new results for the spectrometers, which have been calibrated since then.
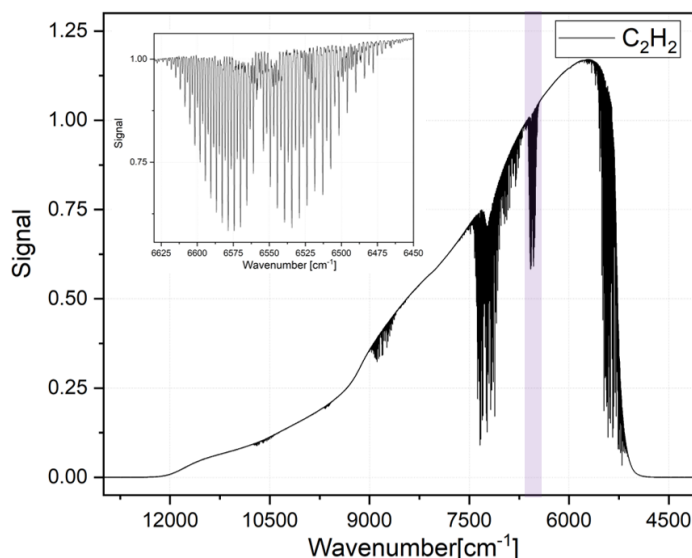
Figure 8.5: An open-path spectrum recorded with the C_2H_2 cell inserted in the beam. The spectrum was recorded using COCCON's EM27/SUN reference spectrometer SN37. The insert shows a zoom-in of the wavenumber range used for the retrieval of ILS parameters from C_2H_2.

8.3.1   *Reanalysis of previous open-path measurements*

Figure 8.6 shows, for all spectrometers treated in the work of Frey et al. (2019), the old and newly derived modulation efficiency amplitudes (MEAs), the phase errors (PEs), the new-minus-old differences for both quantities and the empirical standard deviation of the spectral residuals. The use of the revised H_2O line list significantly reduced the spectral residuals. Figure 8.7 shows an excellent correlation between old and new MEA and PE ($R^2 = 0.95$) results. Figure 8.8 **a** shows that due to the empirical calibration of the H_2O broadening parameters mentioned in Section 8.1, only a small bias in MEA is seen, the mean of the new MEA results being higher by 0.04 %. Figure 8.7 **b** indicates a significant reduction of PE values; so probably part of the previously diagnosed ILS asymmetry was introduced by systematic spectral residuals created by the HITRAN 2008 line parameters. Overall, the revised analysis recipe confirms the results by Frey et al. (2019), as spectrometers showing suspiciously high or low values of MEA or PE versus the average behaviour retain their characteristics. Although we are confident that the new method, using an improved line list, a correction of the optical distance (and thereby H_2O self-broadening effects) and more reliable data for the total pressure, is superior to the original method, the overall effect is only a gradual improvement. The reanalysis of the old spectra is important mainly in order to avoid a systematic bias of reported ILS parameters between previous and current calibrations.
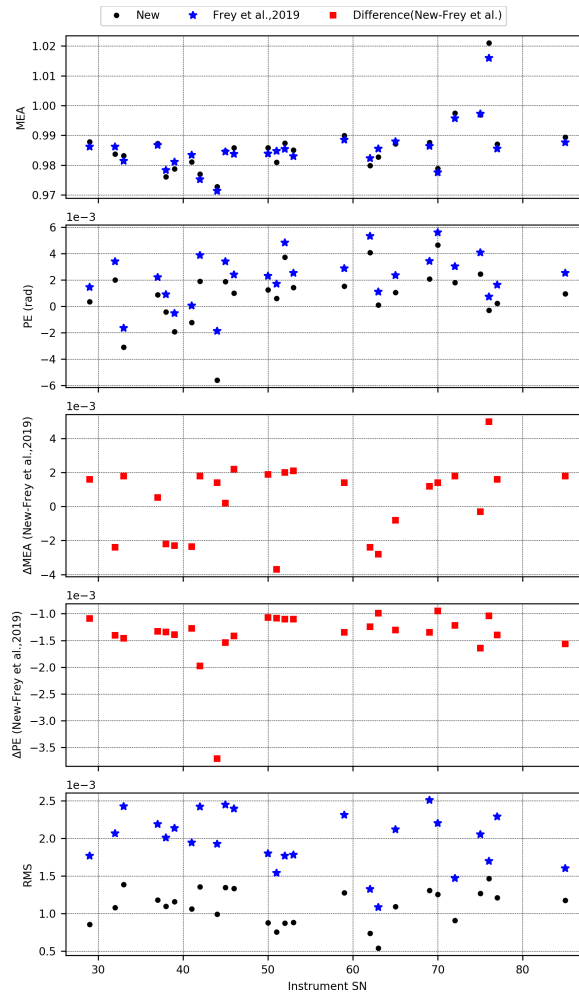
Figure 8.6: Comparison between the old published values (blue star) and the improved ones (black dotes). The MEA, PE and new-minus-old difference for each spectrometer. The bottom panel shows the resulting empirical standard deviation of the spectral fit for the old and the new methods, respectively.

8.3.2 *Open-path results for all spectrometers*

In this section, the ILS parameters for all spectrometers as retrieved with the improved analysis procedure are presented. The left panel of Figure 8.9 provides a graphical overview of these new results, including the reanalysis results for the spectrometers already investigated by Frey et al. (2019). In total 47 new spectrometers were investigated. As can be seen from the figure, the results for new spectrometers are in line with the previous work, but the occurrence of outliers seems reduced (the clearly deviating behaviour of spectrometers 75 and 76 uncovered by the calibration work was later diagnosed to be caused by misassembled detector baseplates). Presumably, this reflects the gain of expert knowledge in the fabrication of the EM27/SUN spectrometer type and in the acceptance and calibration procedures. We suppose that the continued efforts for quality assurance presented in this work contribute to the high level of consistency achieved in the spectrometers' characteristics that is apparent today.
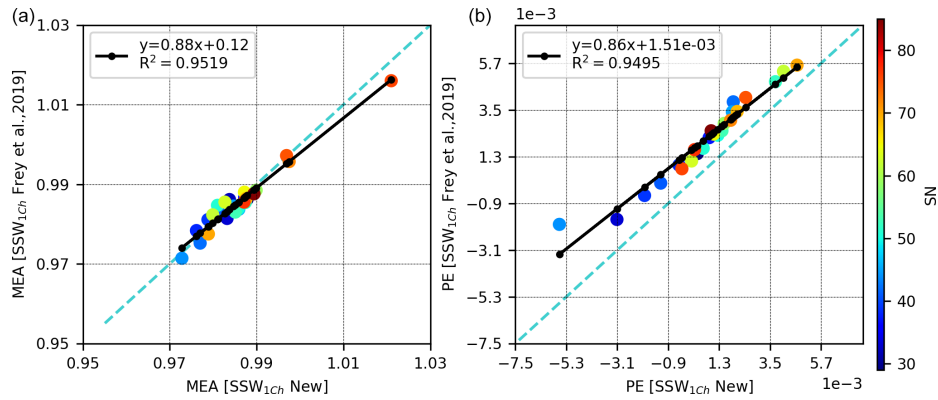
Figure 8.7: **(a)** Correlation between the MEA obtained with the new and the old methods for the shortwave standard micro window (SSW). **(b)** Correlation between the PE obtained with the new and the old methods. The colour bar represents the serial number (SN) of the instruments.
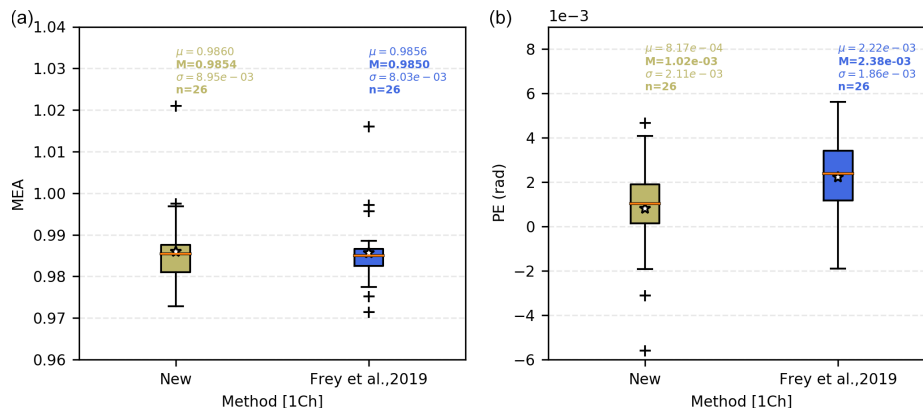
Figure 8.8: Box-and-whisker plots showing the statistics of the original data analysis by Frey et al. (2019) and the reanalysis: median, mean, scatter and interquartile range are presented. **(a)** MEA. **(b)** PE.

8.3.3 *Testing the alignment of the CO channel*

The addition of a further spectral window to the open-path analysis in the spectral overlap region covered by both the main and the CO channel allows the extension of the open-path ILS analysis to the CO channel. The CO channel is an extension of the original design of the EM27/SUN (Hase et al., 2016). CO is an air pollutant and also useful for the source apportionment of CO_2 emissions. CO is measured by space sensors as Measurement of Pollution in the Troposphere (MOPITT) (Drummond and Mand, 1996; Drummond et al., 2010) and the TROPOspheric Monitoring Instrument (TROPOMI) (Veefkind et al., 2012). Today, all EM27/SUN spectrometers incorporate both detector channels. Therefore, it is desirable to include a procedure in the calibration which recognizes the potential for a significant misalignment of the CO detector element with respect to the main detector. Such a misalignment of the CO detector would generate (1) deviating ILS parameters and (2) a deviating spectral scaling factor.
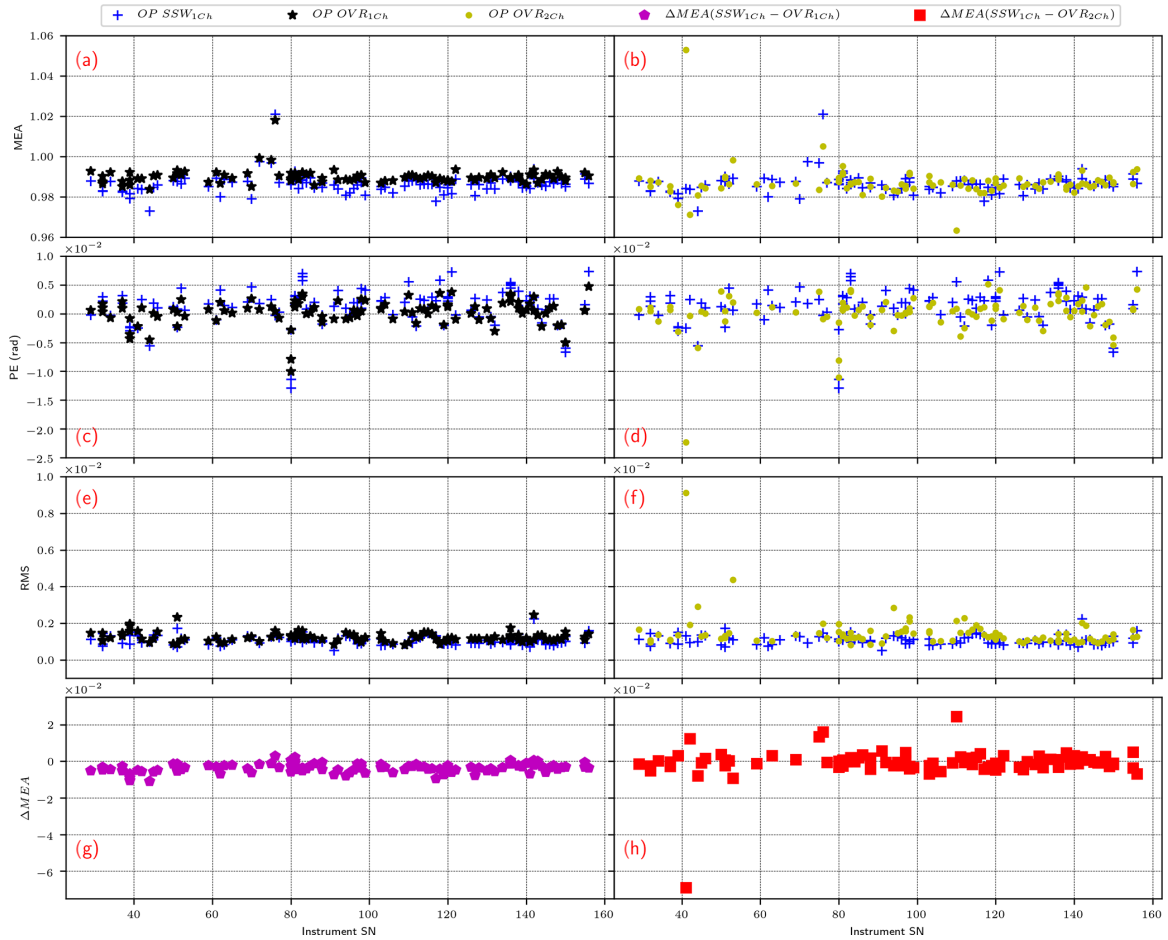
Figure 8.9: Main results for the main **(a, c, e, g)** and CO detector channels **(b, d, f, h)** resulting from the revised open-path method. The modulation efficiency, phase error, rms and relative difference for the first channel by using SSW and OVR are shown in **(a)**, **(c)**, **(e)** and **(g)**, respectively, while the modulation efficiency, phase error, rms and relative difference for the first and second channels using SSW and OVR are presented in **(b)**, **(d)**, **(f)** and **(h)**, respectively.

In this section we compare the consistency of spectral fits in the standard spectral window (SSW) and in the overlap region (OVR) using the spectra recorded with the main detector. We compare the retrieved ILS parameters (MEA and PE) and spectral scaling factors.

8.3.3.1 *Consistency of spectral fitting in the standard spectral window and the overlap region*

Figure 8.10 (top panel) compares the MEA and PE of retrievals performed in the SSW and in the OVR using the main detector. The results show good agreement (MEA: $R^2 = 0.78$, PE $= 0.95$). It is very interesting to observe that the regression line has a slope significantly below $1:1$. Since parameters such as MEA and PE measure fractional wave front errors, their deviations from the nominal value are indeed expected to increase with increasing wavenumber. The wavenumber ratio between OVR and SSW is 0.74, while the slope of the MEA regression line is 0.63, which would support the assumption of a steeper-than-linear

wavenumber dependence of the MEA parameter ($\sim \nu^{1.5}$). The PE results are compatible with the assumption of a linear wavenumber dependence.
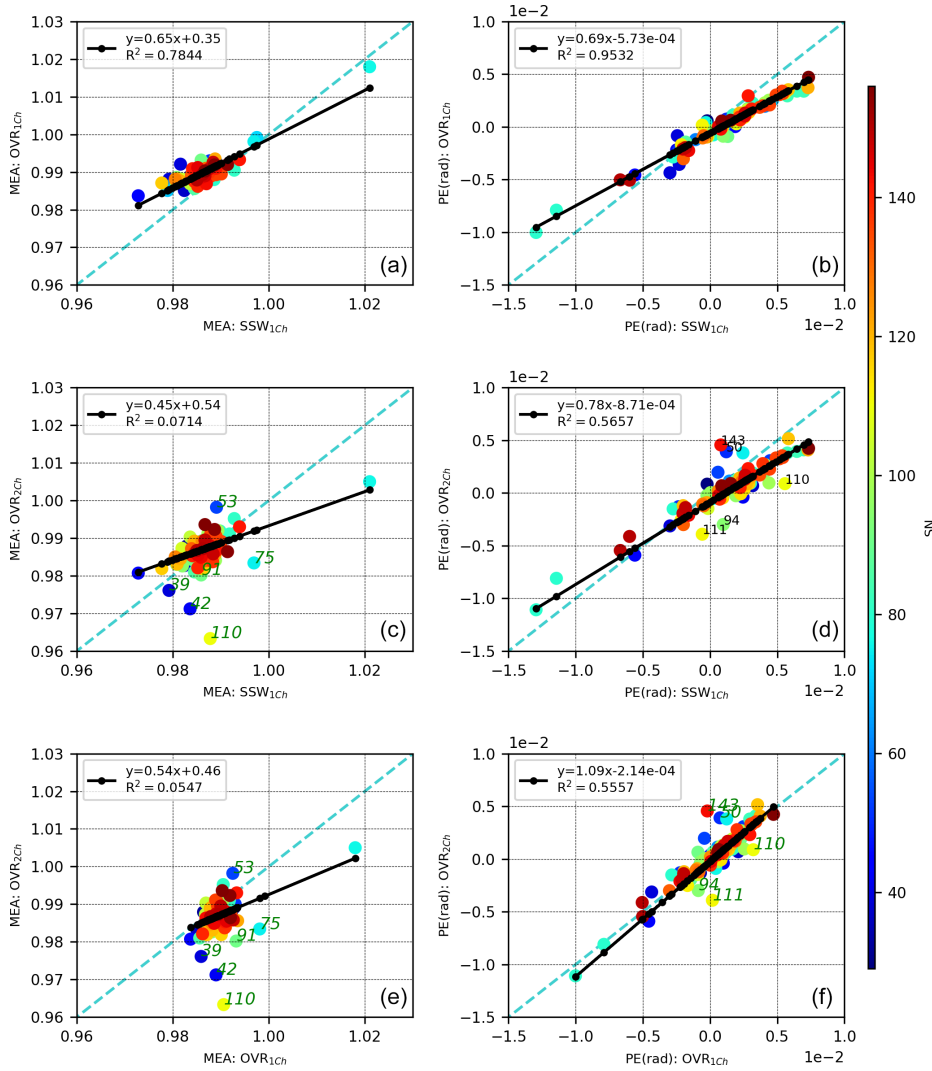
Figure 8.10: Correlation plots between the MEAs **(a, c, e)** and PEs **(b, d, f)**. **(a, b)** The first channel in the SSW and in the OVR region, **(c, d)** the first channel in the SSW and the second channel in the OVR region, and **(e, f)** the first channel in the OVR and the second channel in the OVR region. Additionally, the obvious outliers are labelled in order to assess them.

As can be seen from Figure 8.11, there is a small bias of 0.3 % in MEA between the primary channel results deduced from the SSW and OVR spectral regions: the values retrieved in the OVR are slightly higher than those from the SSW. The PE retrieved in the OVR is significantly smaller, which might indicate that the revised spectroscopic description of the SSW spectral window – although the new line list reduced the retrieved PE by a factor of 2 (see Section 8.3.1) – still simulates a spurious PE bias. The spectral fit quality in the SSW and OVR regions is quite comparable for the primary channel (Figure 8.10, bottom panels), while the OVR spectral fits to the measurements recorded with the CO detector indicate a somewhat higher noise level.
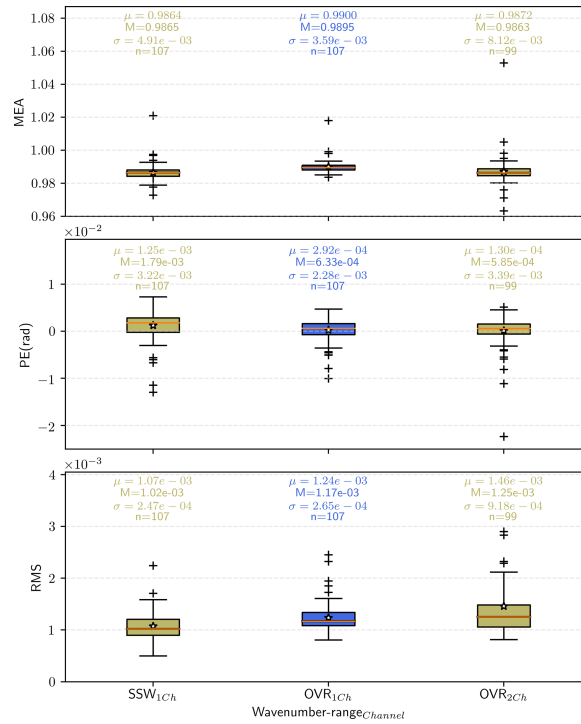
Figure 8.11: Box plots comparison for the three-wavenumber ranges used with the open-path method showing the MEAs, PEs and rms.
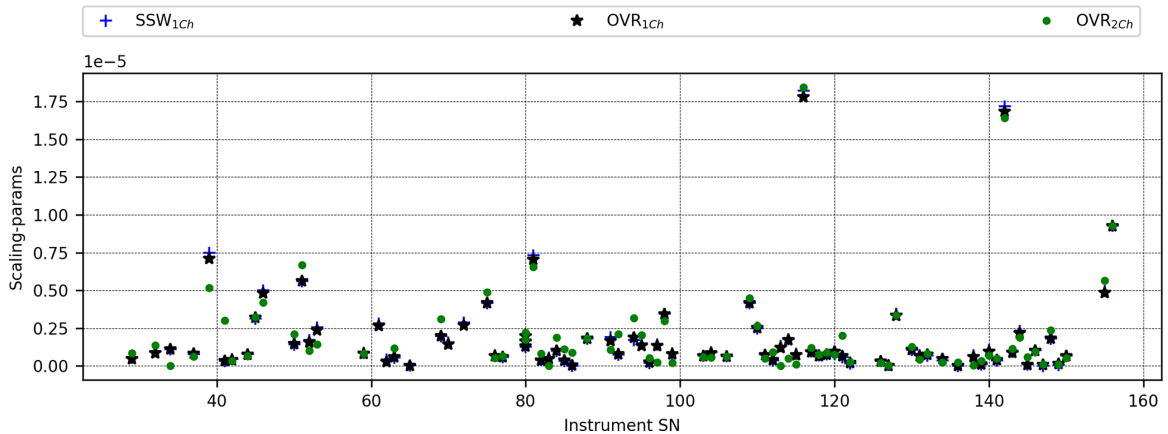
Figure 8.12: Instrumental variation in the spectral scaling factors in each of the spectral windows used and for both channels.

Figure 8.12 summarizes the results for the spectral scaling factors for both spectral windows as resulting from the LINEFIT fits. Figure 8.13 **a** compares the spectral scaling factors of OVR and SSW fits as deduced from main detector spectra. As one would expect, the slope is near 1 : 1, and the correlation is very high.
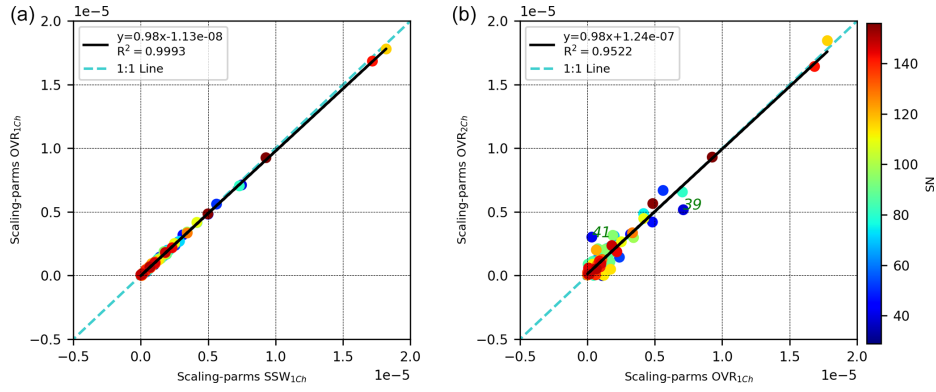
Figure 8.13: Correlations between the scaling factors derived from OVR and SSW spectral windows using the main channel spectra **(a)** and using CO channel results for the OVR spectral window **(b)**.

8.3.3.2 *Evaluation of the CO detector alignment using the spectral overlap region*

Figure 8.10 (middle and lower panels) shows the MEA and PE correlations as deduced from the main detector and the CO detector, respectively. Figure 8.10, middle panel, shows the correlation of MEA between the CO detector (OVR) and main detector (SSW). While the shallower slope is comparable with the results reported in the previous section, the correlation between the two different detectors is significantly poorer. There are several outliers from the MEA regression line: these are spectrometers 39, 42, 53, 75, and 110. In the PE regression, the five results furthest from the regression line are 50, 94, 110, 111 and 143.

Figure 8.13 **b** compares the spectral scaling factors of OVR fits for the two CO and main detectors. While the slope is in excellent agreement with the results derived from the main detector, there is more scatter ($R^2 = 0.95$). The results for spectrometers 39 and 41 are furthest from the regression line.

In summary, although the correlation of ILS parameters and spectral scaling factors is noisier between the main and CO detectors, only one consistent outlier appears, which is spectrometer SN39. Altogether the applied OVR tests do not detect unacceptable misalignments of the CO detector. The relative spectral detuning of SN39 between SSW and OVR is on the order of 2×10^{-6}, which, by applying $\frac{\Delta v}{v} = \frac{1}{2}\alpha^2$ using $\alpha \sim 1.5\,\mathrm{mrad}$, is equivalent to about one-seventh of the apparent solar diameter. Here α denotes the maximum inclination of a ray still accepted by the interferometer. The effect of a misadjusted field stop on spectral scale is discussed by Kauppinen and Saarinen (1992). The majority of spectral detuning results are located within $\pm 1.5 \times 10^{-6}$, equivalent to an angular misalignment of 1/14 of the apparent solar diameter, which is in reasonable agreement with the expected alignment precision of the CO detector. Because the air mass reference is deduced from the oxygen band observed in the main channel, such a misalignment introduces an error in the XCO data. If we assume a misalignment of 1/10 of the apparent solar disc diameter along the vertical, the resulting relative error in XCO at an 80° solar zenith angle amounts to 0.5 %.

8.4 DISCUSSION OF C$_2$H$_2$ CELL RESULTS

In Section 8.2, the construction and calibration of a cell filled with C$_2$H$_2$ are described. Here, we compare in detail the results obtained from the open-path measurements (OP) using the H$_2$O lines forming in the laboratory air with those obtained with the cell method. Because the cell measurements were implemented in the beginning of 2020, only for spectrometers tested afterwards are cell results available. The comparison is based on the standard H$_2$O window covering 7000–7400 cm^{-1} discussed in Section 8.1 and the C$_2$H$_2$ spectral window covering 6450–6630 cm^{-1} discussed in Section 8.2, so spectra recorded with the main detector are used.

8.4.1 *Intercomparison of repeated open-path and cell measurements using the reference spectrometer*

In order to investigate the stability of both methods, OP and cell measurements were taken repeatedly under different laboratory conditions using the COCCON reference instrument SN37. On a total of 16 d, measurements were performed during February and March 2021. For each daily set of measurements, included sequential OP and cell measurements were taken within 45 min to ensure the laboratory conditions were comparable. We collected 15 interferograms for the cell test and 30 for the OP method.

Figure 8.14 shows the internal variability of the results. Both methods seem to offer similar repeatability. While we do not see a clear advantage of the cell approach from the comparison in this regard, we need to acknowledge the fact that the C$_2$H$_2$ line widths are properly calibrated. If we assume that the TCCON spectrometer used to calibrate the empirical C$_2$H$_2$ cell parameters can be regarded as an ideal reference (see Section 8.2.2), this finding suggests that the OP MEA results indeed suffer from a systematic low bias of about 0.015 (1.5 %) and that the ILS performance of the EM27/SUN is on average closer to the nominal expectation than indicated by the OP measurements (see Figure 8.15). This adjustment will be included in a future version of the PROFFAST software used by COCCON for the analysis of atmospheric spectra. The current version of the code uses the MEA values resulting from the OP measurements, so the currently incorporated values of the air-mass-independent and air-mass-dependent calibrations are partly mitigating the bias in MEA.

Even though the cell method does not provide a significant improvement in the determination of MEA and PE values, we plan to maintain the cell measurements in the calibration procedure. That the cell measurement delivers a column value, which can be measured with excellent precision and provides an invariant for the comparison of different spectrometers, seems a useful addition. The relative 1-sigma standard deviation of the C$_2$H$_2$ column indicated by the repeated measurements is 0.0008 % (individual column results are shown in Figure 8.14c).

8.4.2 *Intercomparison of cell results with open-path results*

This section summarizes the main results of the ILS characterization for the first channel by using the OP and the cell method for the spectrometers tested since 2020 (see Fig-
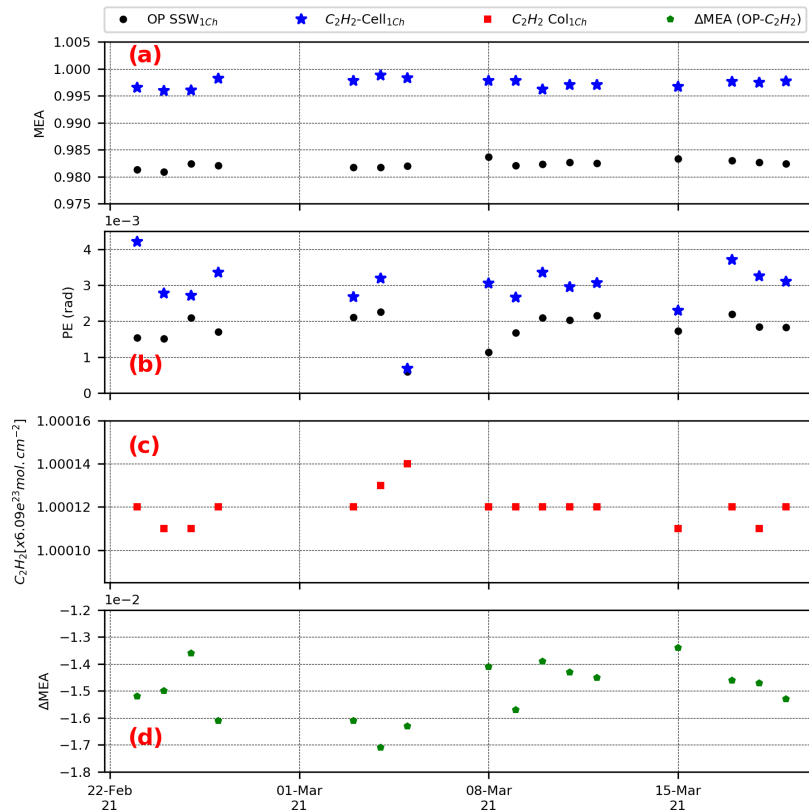
Figure 8.14: Time series of the MEAs, PEs, C_2H_2 retrieved column and difference between the MEAs retrieved with OP and cell method for the COCCON reference instrument SN37 (**a**, **b**, **c** and **d**, respectively).
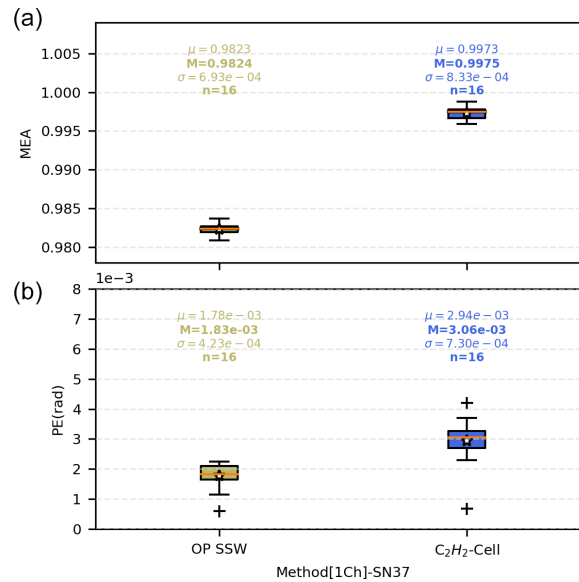
Figure 8.15: Same as Figure 8.8 but for the sensitivity study for the COCCON reference instrument SN37. Left part of the display: open-path results; right part: cell results.

ures 8.16–8.18). Figure 8.16 shows the instrumental variation in the MEA and PE, C$_2$H$_2$ column, and rms according to both methods. The MEA retrieved with the cell method is higher and closer to the ideal ILS in comparison with the OP method, which supports the finding discussed in the previous section that the cell method retrieves $\sim 1.5\,\%$ higher MEA values. The C$_2$H$_2$ columns do show more scatter between different spectrometers than the repeated measurements performed using the reference spectrometer, but still is very low, at a level of 0.0003 %. Figure 8.17 shows the correlation between the OP and the cell MEA and PE results, and Figure 8.18 shows a statistical comparison. We find a reasonable correlation, which indicates that despite the tendency that the spectrometers become more uniform in their characteristics, we are still able to detect – using the described laboratory procedures – actual variations in the MEA and PE values. The sensitivities differ between the methods: while the slope of the MEA regression line is compatible with our assumption of a $\sim \nu^{1.5}$ wavenumber dependence of the MEA parameter (see discussion in Section 8.3.3.2), the slope of the PE regression line is surprisingly steep, as we would expect PE to be proportional to wavenumber. However, the spectral scenes are quite different; the C$_2$H$_2$ lines offer a significantly smaller width than the H$_2$O lines. Therefore, the ILS deviations associated with contributions emerging from larger optical path difference (OPD) will gain importance in the C$_2$H$_2$ spectral fitting. The assumption of a constant PE might be too coarse and therefore introduces the observed discrepancy between the two methods. When regarded from this perspective, the continuation of the C$_2$H$_2$ measurements in addition to OP might also become useful for introducing further refinements of the ILS model in the future. Figure 8.18 summarizes the performance of both methods.
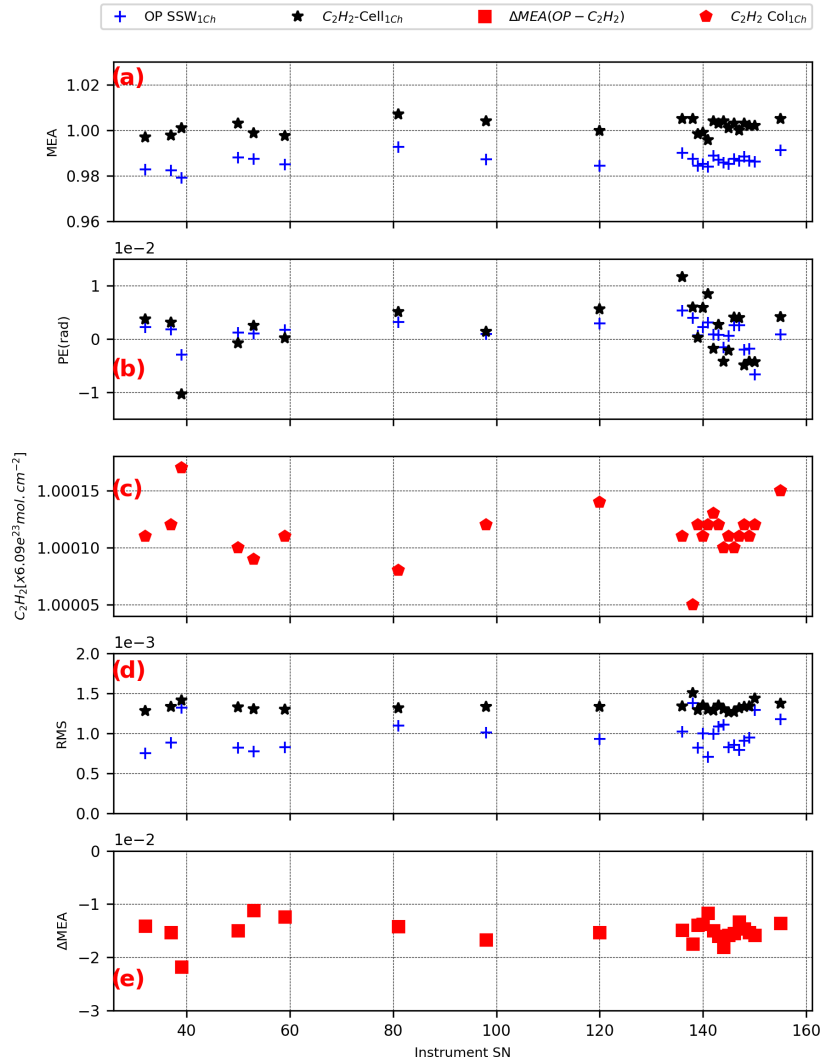
Figure 8.16: The modulation efficiency as a function of the instrumental SN, phase error, C_2H_2 column, rms of the spectral fit and the relative difference between the open-path method and the cell method are presented in **(a)**, **(b)**, **(c)**, **(d)** and **(e)**, respectively.
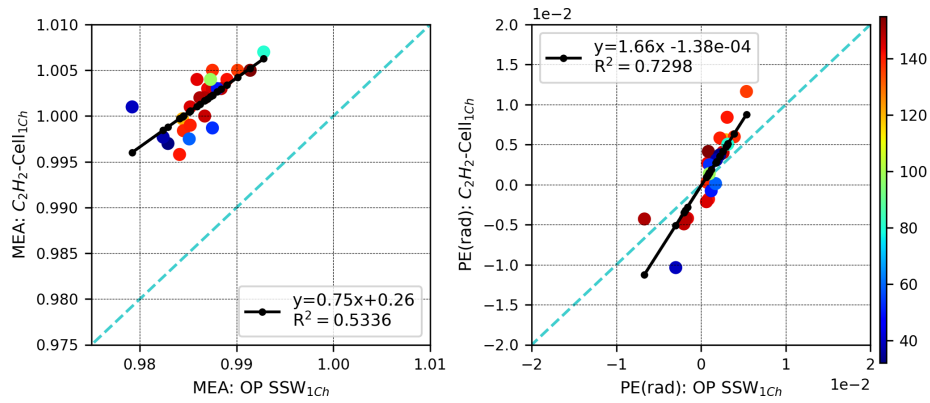
Figure 8.17: Correlations between the MEAs obtained with the OP and cell methods for the first channel.
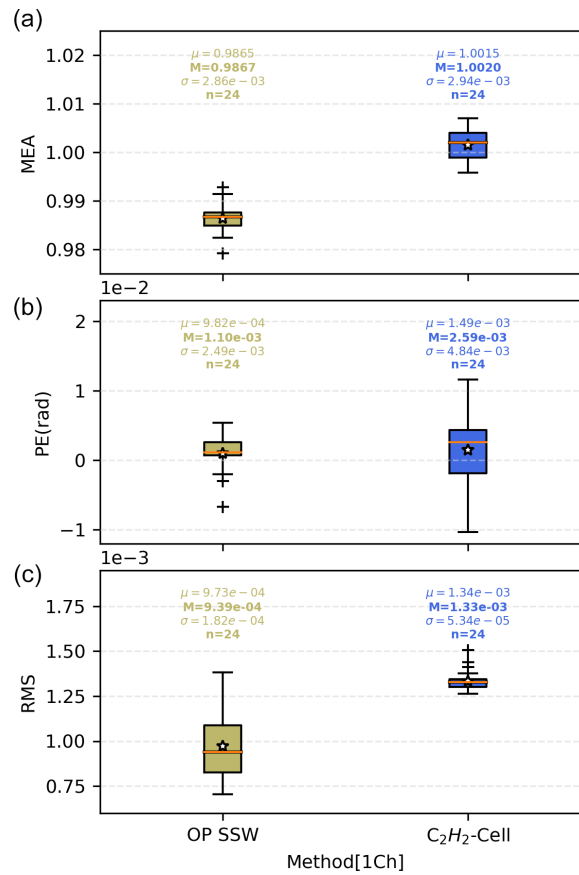
Figure 8.18: MEA and rms statistical results from the ILS retrievals by using the OP and the cell methods for the first channel of the available instruments (left part of the display: open path; right part: cell).

8.5 DISCUSSION OF SOLAR SIDE-BY-SIDE CALIBRATION MEASUREMENTS

8.5.1 *Long-term stability of reference unit*

In this section the historic time series of the COCCON reference instrument SN37 is assessed by comparing the main target gases: XCO_2, XCO, XCH_4 and XH_2O with the results obtained from the high-resolution spectrometer IFS125HR located at KIT Campus North, which contributes to the TCCON network. Two different kinds of measurements were collected with the IFS125HR spectrometer: standard TCCON measurements using a spectral resolution equivalent to max. OPD of 45 cm and double-sided low-resolution spectra for mimicking the EM27/SUN observations (maximum OPD 1.8 cm). The COCCON and the low-resolution data recorded with the IFS125HR were analysed using PROFFAST, while the high-resolution spectra were used for generating the official TCCON product using the GGG software suite version 2014 (Wunch et al., 2015)). Because it provides a very sensitive indication for instrumental drifts and operation problems, we also investigate results for X_{AIR} here. This quantity compares the spectroscopically determined dry-air column as extrapolated from the observed vertical column of O_2 VC_{O_2} with the dry-air column calculated from ground pressure and spectroscopically observed water vapour column VC_{H_2O}, as given in Equation 8.1.

$$X_{AIR} = \frac{0.2095}{VC_{O_2} \cdot \overline{\mu}} \cdot \left(\frac{P_S}{g} - VC_{H_2O} \cdot \mu H_2O \right) \tag{8.1}$$

8.5.1.1 *COCCON reference EM27/SUN spectrometer*

As mentioned in Chapter 6, Section 6.5.1, the EM27/SUN data is analyzed with PROFFAST. It is important in the context of this work that PROFFAST is capable of taking into account the ILS parameters as determined by the open-path measurements. If this information is neglected, additional scatter between the atmospheric trace gas results achieved with different spectrometers would result, and different gas-specific empirical calibration factors would result from the side-by-side solar observations for each spectrometer (these factors are reported in Section 8.5.2).

The EM27/SUN spectrometer SN37 has served as the COCCON reference spectrometer since 2014. The spectrometer participated in the Berlin campaign (Hase et al., 2015) and was upgraded with the CO channel in early 2018. Figure 8.19 presents the time series of XCO_2, XCO, XCH_4, XH_2O and X_{AIR} covering 2015 to the end of 2020. Shown are the official TCCON data generated with the GGG2014 software suite and data derived from the low-resolution spectra recorded with the IFS125HR spectrometer and the COCCON reference spectrometer, respectively, using the PROFFAST code. For the target gases, no obvious drifts are noticeable between the different data sets. The bias in X_{AIR} between the TCCON and low-resolution data is due to the trivial fact that X_{AIR} is not generated as a calibrated quantity by GGG2014, while PROFFAST attempts a normalization to unity. However, there is a change of X_{AIR} apparent in the COCCON reference data during the first 4 years, which we investigate further in the next section. We will show that these changes are small enough not to detectably affect the results of the target gases apart from XCH_4.
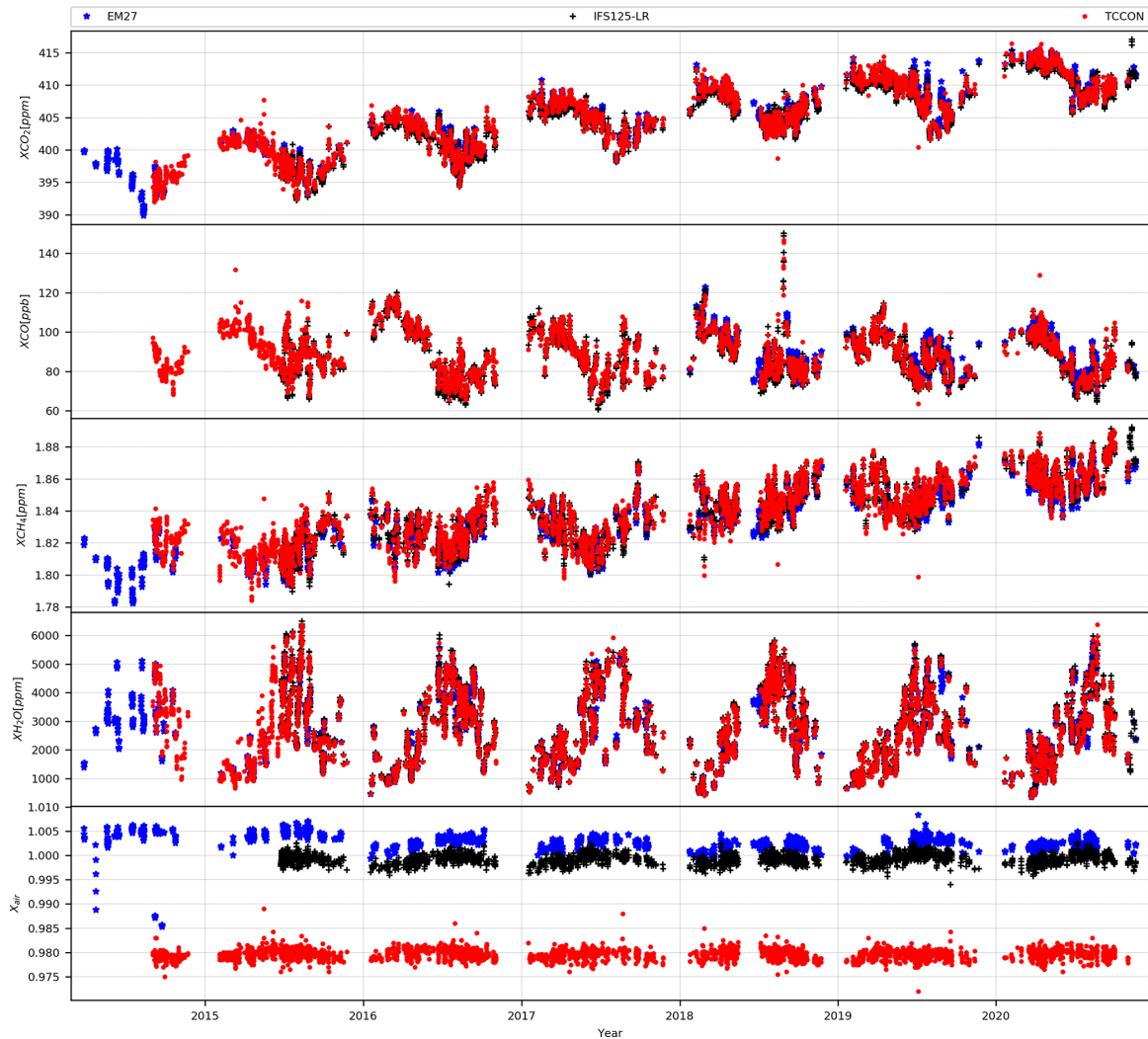
Figure 8.19: Time series of XCO_2, XCO, XCH_4, XH_2O and X_{AIR} measured with the COCCON reference instrument (blue), from the TCCON station Karlsruhe (derived from high-resolution IFS125-HR spectra using GGG2014, red) and derived from low-resolution IFS125-LR spectra (black). The low-resolution measurements were processed with PROFFAST.

8.5.1.2 *Changes of X_{AIR} in time series of reference spectrometer*

Figure 8.21 shows the variations in X_{AIR} of the COCCON reference unit with respect to the low-resolution IFS125HR data. At least two step changes appear, at the end of 2015 and at the end of 2017. Since 2018, the results appear stable. The step change at the end of 2017 is very likely associated with the CO channel upgrade of the spectrometer, while the earlier event might be associated with a realignment of the spectrometer performed in the winter period after participation of the unit in the Berlin campaign between June and July 2014 (Hase et al., 2015). The analysis of atmospheric spectra collected with the reference unit was performed twice: in one analysis, it was assumed that the ILS is time independent (the ILS parameters used for the analysis were derived from averaging the parameters

from all available ILS measurements performed with the reference spectrometer). In the other analysis, yearly values for the ILS parameters were applied as deduced from the available open-path measurements. With the exception of 2015, the X_{AIR} results appear more consistent if time-dependent ILS parameters are used for the data analysis. In 2015, only a single ILS measurement was performed and might for some reason be of inferior quality. A reanalysis of the open-path spectra uncovered at least the use of an erroneous ground pressure value in the original analysis of this measurement reported by Frey et al. (2019) and resulted in less anomalous values for the ILS parameters. The revised set of values (MEA = 0.98417 and 0.98430 and PE = −0.00061 and −0.00068 instead of MEA = 0.98555 and 0.98940 and PE = −0.00086 and 0.08658) has been used in the current analysis for the 2014 and 2015 period, but the MEA value is still suspiciously high. The OP procedures were less refined in the beginning (e.g. no venting of the spectrometer was performed), so the measurements are less reliable than current OP measurements.

The consideration of the variable ILS brings the X_{AIR} results from 2016 and 2017 in better agreement with the more recent results, with only the 2014 to 2015 period remaining as an outlier. We therefore conclude that the assumption that real ILS changes occurred in the early years due to instrumental interventions and upgrades is the best choice. The results shown in Figures 8.19, 8.20 and 8.22 all refer to the analysis run using the variable ILS parameters.

Figures 8.20 and 8.22 investigate the correlation of the retrieved dry-air mole fractions between the reference spectrometer and the data derived from IFS125-LR measurements. While no significant changes are detectable for XCO_2, XCO and XH_2O, the XCH_4 regression line in Figure 8.20 is shallower than the 1 : 1 line. Figure 8.22 investigates the correlation year by year. Again, the changes for XCH_4 become apparent. We therefore assume for the XCH_4 time series from the COCCON reference unit the existence of a non-negligible drift over the first years. We assume that the reference spectrometer has reached a stable configuration since 2018, and during this period we use the XCH_4 side-by-side results without further corrections. Before this period, we derive from Figure 8.22 the existence of a low bias of the reference unit and therefore apply a low XCH_4 bias of the reference unit of 0.0001 during 2017, 0.0002 in 2016, and 0.00135 in 2015 (relative detuning of XCH_4 calibration). The instrument-specific XCH_4 calibration factors provided in Section 8.5.2 take these corrections of the reference unit into account.

The variable bias of the reference unit's XCH_4 despite the fact that a time-dependent ILS is used in the data analysis might indicate that the ILS model currently used by PROFFAST is too simple or that the assumptions made on the wavenumber dependence of the ILS parameters are incorrect (the current version of PROFFAST assumes a linear wavenumber dependence for MEA and PE while the open-path analysis suggests a quadratic dependence for MEA; see Section 8.3.3.1) or that additional influencing factors are affecting the trace gas results.

8.5.2 *Empirical X_{GAS} calibration factors for all tested spectrometers*

To harmonize the retrieved species when using any COCCON spectrometer, empirical instrument-specific calibration factors for XCO_2, XCO, XCH_4 and XH_2O are calculated from the side-by-side solar measurements with the reference spectrometer SN37. The in-
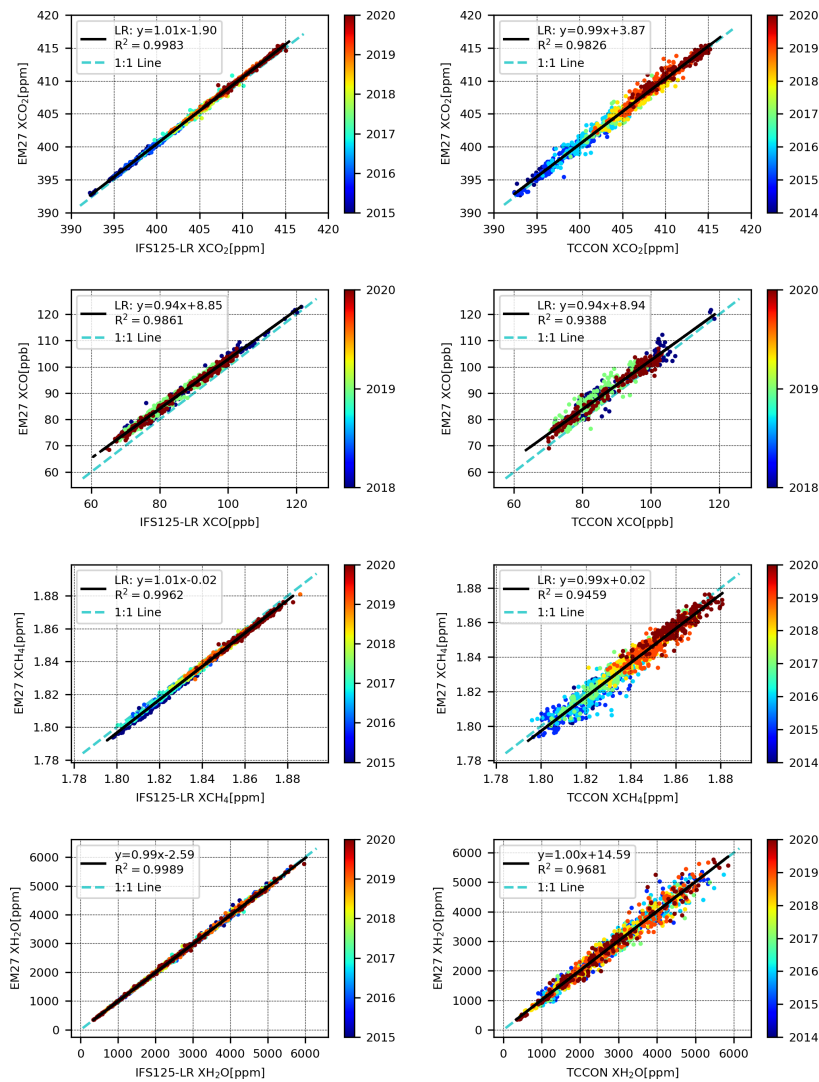
Figure 8.20: Correlations between XCO_2, XCO, XCH_4 and XH_2O between the ones retrieved by using the COCCON reference and the IFS125-LR low-resolution data (left panels) and between COCCON reference and TCCON station (right panels).

struments are set up on the seventh floor at the Meteorology and Climate Research – Atmospheric Trace Gases and Remote Sensing (IMK-ASF) building located at KIT Campus North (49°05′38.7″ N, 8°26′11.5″ E, 134 m a.s.l.). After the measurements are taken, the data are processed using the PROFFAST software. In this processing, the ILS parameters derived previously from OP measurements are included for both spectrometers, the spectrometer under test and the reference unit. Ideally, the resulting gas abundances measured by the spectrometers would be found to be identical. The residual biases give rise to instrument-specific empirical calibration factors that are reported in the following for each spectrometer and target gas. These empirical adjustments consider all remaining instrumental imperfections which are not properly quantified in the calibration process or not properly reflected in the trace gas analysis.
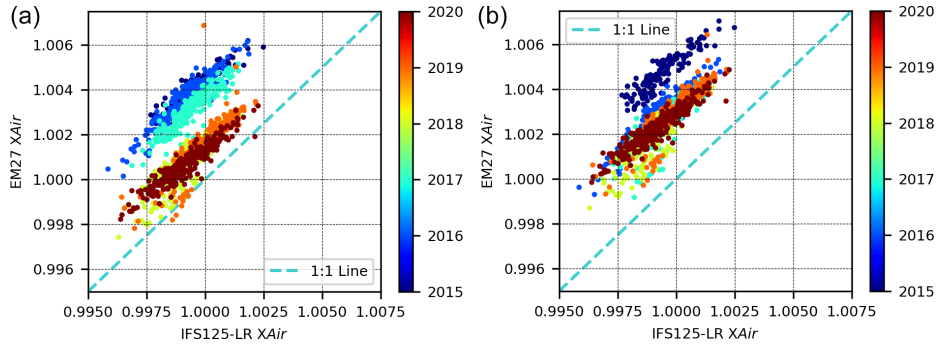
Figure 8.21: Correlations for the retrieved X_{AIR} by using the instrument SN37 and IFS125-LR. Panel **(a)** shows the results of the analysis of atmospheric spectra under the assumption of a constant ILS, and **(b)** shows the results under the assumption of a variable ILS (ILS parameters adjusted on a yearly basis).
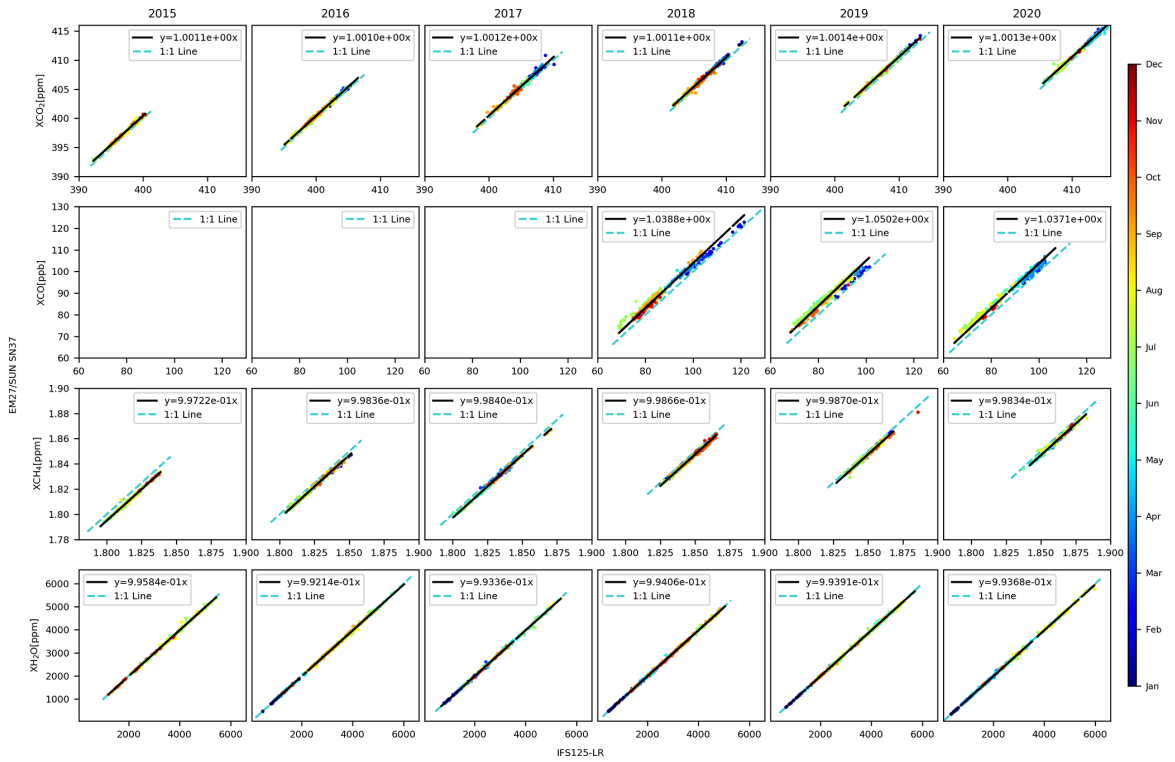
Figure 8.22: Correlations between the species: XCO_2, XCO, XCH_4 and XH_2O retrieved with the COCCON reference instrument and the TCCON instrument in low-resolution measurement mode in each row (top-down), respectively, treated separately by year from 2015 to 2020 in each column for each species.

The correction factors are defined in Equation 8.2, where the K_{gas}^{SN} is the correction factor and $X_{gas}^{no\text{-}corr}$ is the dry-air amount of a defined gas without any correction for a defined gas and instrument. The correction factors are calculated by comparing a defined

gas retrieved with any EM27/SUN instrument with the reference instrument; a linear fit forced to zero intercept is performed, and then the slope is taken as its value.

$$X_{gas}^{corr} = K_{gas}^{SN} \cdot X_{gas}^{no\text{-}corr} \qquad (8.2)$$

Figure 8.23 shows and lists the empirical calibration factors for XCO_2, XCH_4, XCO and XH_2O for each spectrometer investigated. Several spectrometers were calibrated repeatedly, in such cases the values are mean values. The table also provides the X_{AIR} value for each spectrometer. While the Xgas values are derived from the measurements taken with the spectrometer under test and the reference unit, the X_{AIR} result is independent of the reference unit.

Figure 8.23 provides a graphical overview of the tabulated values. The 1-sigma error bars are shown if several calibrations were performed on a spectrometer. Similar to what has been observed and discussed before for the ILS parameters (see Section 8.4.1), a trend towards improved consistency of the calibration factors is suggested, especially for XCO_2 and XCH_4. XCO is a very weak absorber, and therefore the scatter is largely dominated by residual channelling (Blumenstock et al., 2021), which continues to show variable characteristics between individual spectrometers.

8.5.3 *Spectral signal-to-noise ratio of the EM27/SUN spectrometers*

In order to assess the distribution of the spectral signal-to-noise ratio (SNR) of different instruments, these values were calculated for both solar and laboratory spectra. For both cases the SNR is calculated for several spectral windows covering both detector channels. The procedure applied is based on the formula described in the Bruker OPUS © software manual (Bruker, 2017); the SNR is calculated from the ratio of two consecutively measured spectra. A wavenumber region largely free of absorption gases lines is selected. A parabola is fitted to the ratio spectrum in the investigated spectral window and serves as a nominal signal. The rms of the fit residuals is calculated. This rms value is divided by $\sqrt{2}$ to deliver the SNR of a single spectrum (because a pair of spectra is used in the procedure). The wavenumber ranges used for each kind of measurements in each channel are provided in Table 8.4. It is important to mention that for the evaluation of the SNR in solar measurements, two spectra recorded during noontime were selected in order to minimize the variability of the solar zenith angle and to use spectra recorded when solar intensity is maximal. For both solar and laboratory open-path spectra, 10 scans recorded with 10 kHz scan speed were coadded (total integration time 1 min).

In Figure 8.24, the SNR values in the selected spectral regions and both kinds of measurements – open-path and solar – are presented. For the solar measurements higher scatter of the SNR is found in comparison with the OP laboratory measurements, which are more consistent. The SNR values of the solar measurements show a much stronger correlation between the two channels than the SNR values of the open-path measurements (see Figure 8.25). This higher level of correlation is expected if the variable SNR is due to variable weather conditions. Therefore, the SNR values deduced from the open-path measurements are better suited as an indicator of the SNR performance of each spectrometer. However, even for the laboratory measurements we expect some artificial variability, as
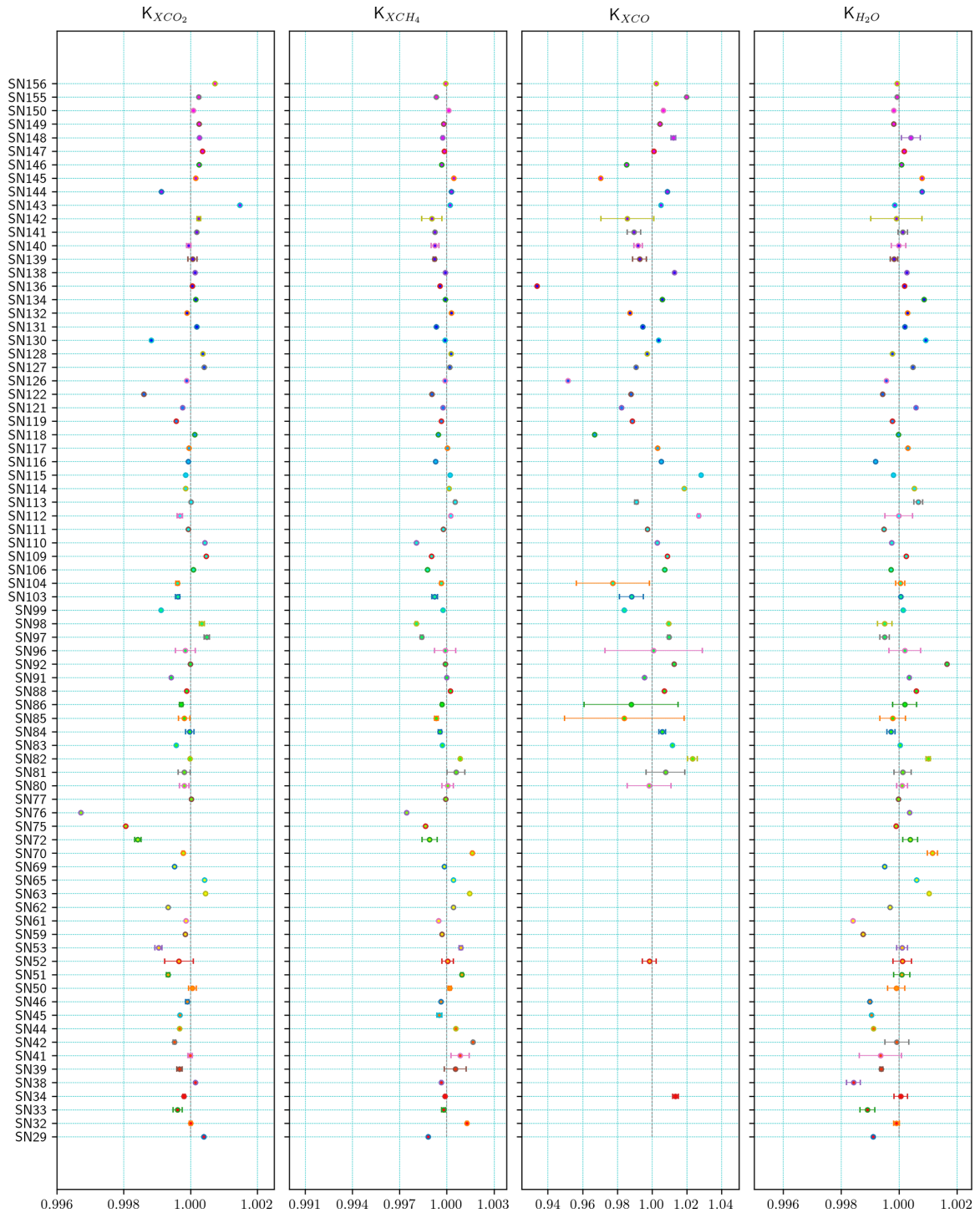
Figure 8.23: Correction factors for XCO_2, XCH_4, XCO and XH_2O from left to right, respectively, calculated for all EM27/SUN spectrometers. The error bar represents the standard deviation, and it is shown only for the instruments with more than one side-by-side measurement in Karlsruhe. The dashed line represents the ideal value "1.0" (practically realized by the COCCON reference spectrometer SN37).

Type of measurements	Instrument's channel	Wavenumber range used [cm^{-1}]
Solar	First	6515–6415
	Second	4500–4400
OP at laboratory	First	6200–6000
	Second	4500–4300

Table 8.4: Description of the wavenumber region utilized for each channel and for each kind of measurement.
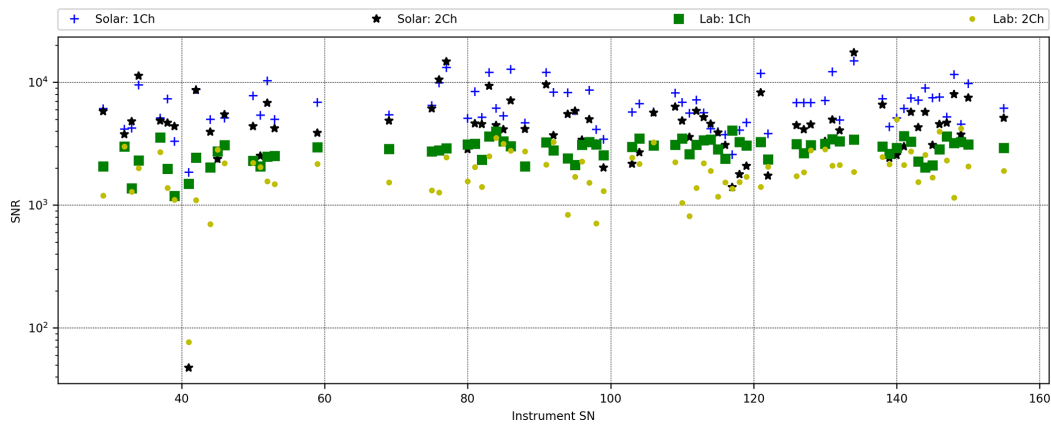
Figure 8.24: Instrumental distribution of the SNR for both channels with both kinds of measurements: solar and OP in the laboratory.
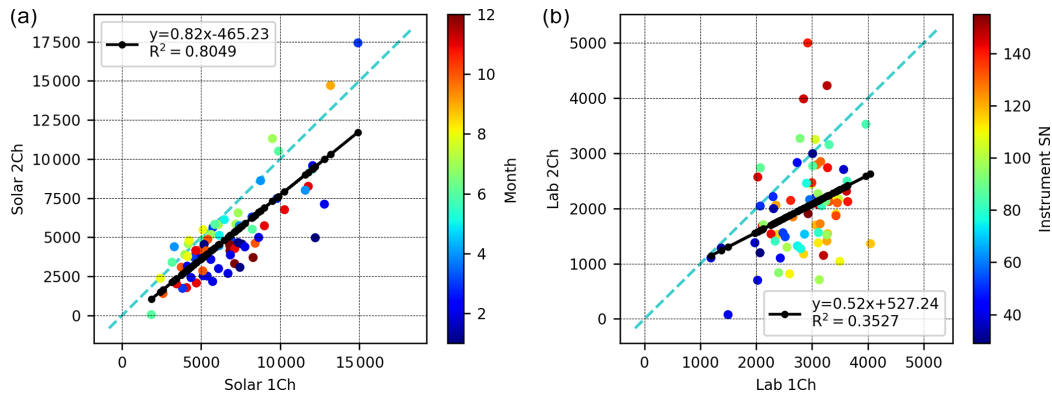
Figure 8.25: Correlations of the SNR obtained in channels 1 and 2, for the solar and OP measurements in **(a)** and **(b)**, respectively. In **(a)** the colour code represents the month of the year when the solar measurements were carried out, for demonstrating the absence of an obvious seasonal signal in the SNR characteristics. In **(b)**, the colour code represents the instrument's serial number because these measurements are carried out under controlled laboratory conditions by using a lamp as a light source. There might be a slight tendency towards higher SNR in recently built spectrometers.

the preamplifier stages are not identical. As a consequence different pre-gain and gain settings were used for optimally exploitation of the analog-to-digital converter (ADC) range. Nevertheless, we can conclude that the SNR typically achieved by the EM27/SUN in a solar spectrum spans the 3000 to 10 000 cm^{-1} range, and the SNR of a laboratory open-path spectrum is in the 2000 to 4000 cm^{-1} range for the main channel and 1000 to 3000 cm^{-1} for the CO channel.

8.5.4 *Effects of improved calibration procedures on XCO$_2$ calibration*

Ideally, the explicit description of the instrumental characteristics from the nominal behaviour as resulting from the calibration procedure would remove any discrepancy between X_{GAS} results derived from different EM27/SUN spectrometers. Instrument-specific calibration factors for each gas as shown in Figure 8.23 would not be required (they would have identical values across different spectrometers). In practice, this is not achievable; instead, the values should be reported and used in the retrieval work. This is due to the fact that (1) the use of instrument-specific ILS parameters very likely does not cover all kinds of possible instrumental imperfections and (2) the ILS description resulting from the calibration procedure itself has limited accuracy.

This opens up a way to test for verifying progress made in the calibration procedure; as such, progress is expected to make the resulting XGAS calibration factors more uniform across different spectrometers. However, the quality of the XCO calibration is limited by other factors not treated in this work: the main impact factor being weak channelling in the spectra (Blumenstock et al., 2021), because CO is a very weak absorber. In case of XCH$_4$, we unfortunately face the drift of the reference spectrometer calibration during the early years; see Section 8.5.1. Therefore, the instrument-specific XCO$_2$ calibration factor appears to be the best available diagnostic. Table 8.5 provides the scatter of the gas-specific calibration factor for XCO$_2$ between different spectrometers following three different recipes: (1) assuming nominal ILS parameters, (2) using the ILS parameters of the previous work by Frey et al. (2019) and (3) using the ILS results obtained in this study. The numbers indicate that either method developing instrument-specific ILS parameters delivers more consistent calibration factors than the "nominal ILS" assumption, and the refined calibration approach creates the least amount of scatter.

Procedure	Empirical standard deviation of XCO$_2$ calibration factors between different spectrometers
Nominal ILS	9.49839×10^{-4}
ILS results from Frey et al. (2019)	8.56409×10^{-4}
ILS results from this work	7.16057×10^{-4}

Table 8.5: Impact of ILS parameters on XCO$_2$ calibration factors (this statistic encompasses the subset of spectrometers that has been treated in the study by Frey et al. (2019).

COCCON OBSERVATIONS IN ST. PETERSBURG AND YEKATERINBURG RUSSIA

Part of this thesis work was done within the work packages (WP) two and three of the EU project VERIFY (https://verify.lsce.ipsl.fr/, last access: 21 August 2022), aiming to quantify and estimate the anthropogenic and natural GHG emissions based on atmospheric measurements, emission inventories and ecosystem data.

This chapter presents the most important results of the COCCON observations carried out in Russia. In general terms, this chapter is divided into two major studies: (1) The COCCON results obtained during the EMME campaign in 2019 are used for the calculation of the emission rates of St. Petersburg and compared with the available bottom-up values (see (Makarova et al., 2021)). Furthermore, (2): The ground-based results obtained during the "long-term" campaigns in Peterhof and Yekaterinburg are compared with space-based observations and model data available for XH_2O, XCO_2, XCH_4 and XCO.

9.1 STABILITY OF THE COCCON SPECTROMETERS DURING THE CAMPAIGN PERIOD

Measurements of very high precision and accuracy are required for correctly retrieving the columnar GHG abundances in the atmosphere, which can be well achieved with the portable EM27/SUN spectrometer.

The two instruments were checked, characterized, and calibrated. The residual instrument-specific calibration factors of XCO_2, XCO, XCH_4 and XH_2O with respect to the COCCON reference were determined, similarly to described in Chapter 8; this was done to ensure the optimum level of accuracy, prior to the campaign, The calibration procedures were repeated after the campaign to demonstrate the stability of the spectrometers.

9.1.1 *Instrumental line shape (ILS) characterization*

A vital step for achieving optimal instrumental performance is the laboratory calibration described in Chapter 8. The instrumental stability and performance during the campaign period were assessed via ILS characterization prior to and after the measurement period at KIT Germany. The modulation efficiency and phase error obtained for both instruments are shown in Table 9.1.

9.1.2 *Side-by-side measurements*

After the instruments were calibrated, side-by-side solar measurements between the instruments used in the campaign (FTS#80 and FTS#84), the COCCON reference, and the TCCON spectrometer operated at the same location were carried out at KIT, as described in Section 8.5. Such measurements occurred before (18 and 19 April 2018) and during the

Instrument	Date	M.E.	Phase error
FTS#80	17 April 2018	0.9865	−0.00275
	4 June 2020	0.9861	−0.01295
FTS#84	27 March 2018	0.9900	−0.00009
	4 June 2020	0.9871	0.00083

Table 9.1: MEA and PE calculated before and after the campaign for instruments FTS#80 and FTS#84.
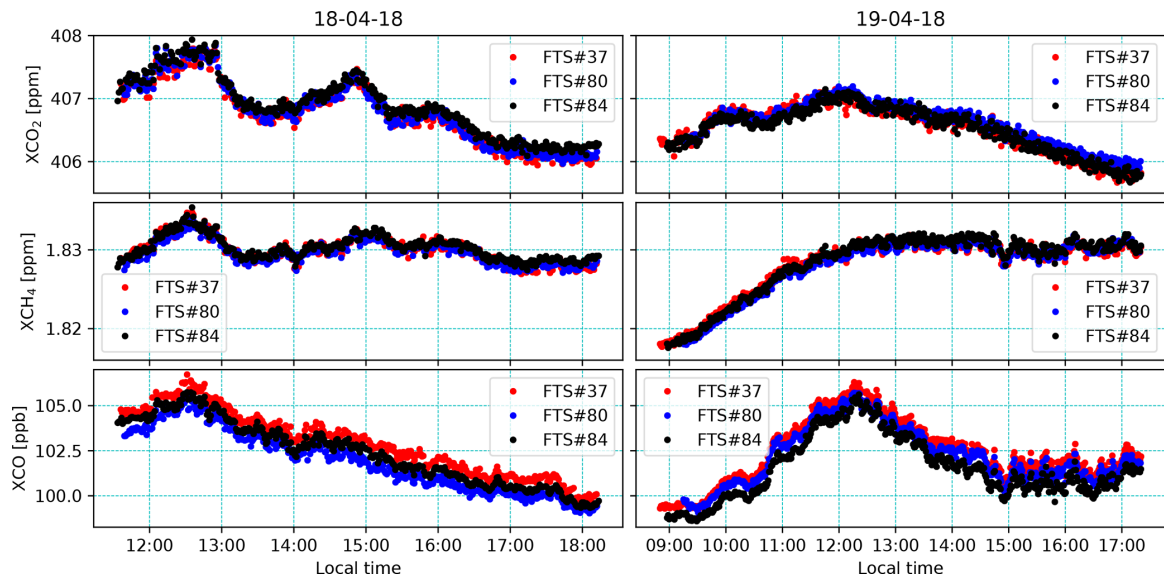
Figure 9.1: Side-by-side measurements before the instruments were shipped to Russia. Comparisons between COCCON reference FTS#37, and instruments FTS#80 and FTS#84.

campaign(12 April 2019). The latter cross-checked whether the instruments kept the same behavior and performance. These results can be seen in Figures 9.1 and 9.2, respectively; the correction factors are listed in Table 9.2.

From the measurements shown in Figure 9.1, the correction factors for XCO_2, XCO and XCH_4 measured by the two instruments are calculated as described in Section 8.5. These results are averaged and later used for scaling the results for each of the retrieved GHGs analysed in this study as presented in Table 9.2.

9.2 EMME CAMPAIGN

9.2.1 *General idea and aim*

The EMME campaign is described in detail by Makarova et al. (2021), and here we summarize only the most relevant details of it. Because this campaign aimed to quantify the CO_2 emissions; CO/CO_2 emission ratios; and the estimation of the CO_2, CH_4, and CO fluxes, two mobile COCCON FTIR spectrometers were used in order to retrieve the required
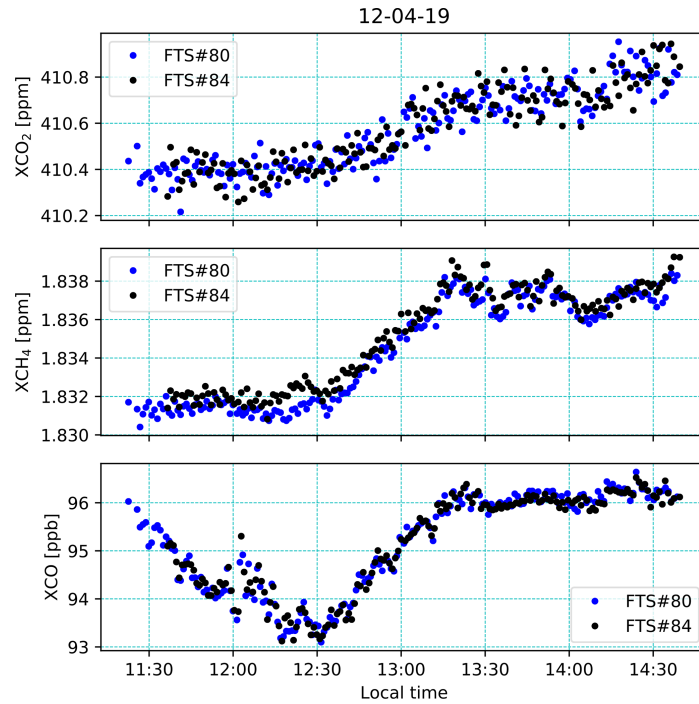
Figure 9.2: Side-by-side measurements during the campaign but only with instruments FTS#80 and FTS#84.

Instrument	Date	XCO$_2$ factor	XCH$_4$ factor	XCO factor
FTS#80	18–19 April 2018	0.99988	1.00013	1.00636
	31 October 2020	0.99981	1.00042	1.00264
	Absolute drift	6.765×10^{-5}	2.966×10^{-4}	3.721×10^{-3}
	Used value	*0.99984*	*1.00028*	*1.00450*
FTS#84	18–19 April 2018	0.99990	0.99987	1.00748
	13 June 2021	0.99967	0.99953	1.00171
	Absolute drift	2.242×10^{-4}	3.333×10^{-4}	5.774×10^{-3}
	Used value	*0.99978*	*0.99970*	*1.00460*

Table 9.2: Correction factors for instruments FTS#80 and FTS#84. The italicized values show the small drift of the instruments and the used values on the analysis.

GHG species. These instruments need to be deployed in up and downwind directions within the St Petersburg city ring[1], which was the federal highway A-118, see Figure 9.3.

---

1 For this campaign the city ring is delimited by the federal public highway A-118, more information can be found in https://en.wikipedia.org/wiki/Saint_Petersburg_Ring_Road, last access: September 03, 2022

Figure 9.3: Map describing the positions of the instruments based on the wind direction

9.2.2 *Daily set-up on a predicted sunny day*

9.2.2.1 *Initial instrumental deployment*

Two teams took care of each spectrometer and carried out the measurements. Because the instruments required sunlight, they were not deployed for continuous measurements but only when good-weather conditions were forecasted; additionally, an essential key point was the forecasted wind direction which gave the initial deployment site. The instruments were stored at the Atmospheric Remote Sensing Laboratory of Saint-Petersburg State University, located in Peterhof (59.88°N, 29.83°E), which is $\approx$ 35 km southwest of the city center. This location was the initial and end point for a measurement day, which means that the instruments need to be moved roundtrip from here to the selected up/downwind location for each spectrometer.

Due to the enormous logistic arrangements required for a single day of measurements, the instruments were not deployed randomly relaying only on the wind forecast of the previous day. Instead, a set of possible locations (up and downwind) were selected based on the historical wind data of St. Petersburg, the accessibility with cars, and convenience, as shown in Figure 9.4. Two of them were selected as positions of the COCCON spectrometers one day before based on two prediction tools: (1) the wind forecast and (2) the orientation of the city's NO_2 plume as modeled by HYSPLIT (HYbrid Single-Particle Lagrangian Integrated Trajectory) (`https://www.ready.noaa.gov/HYSPLIT_traj.php`, last access: 22 August 2022).

9.2.2.2 *Hysplit NO_2 plume forecast*

The second prediction tool used during the campaign was the NO_2 plume forecast calculated with HYSPLIT on the previous day. For a better illustration, here, April 04, 2019, is
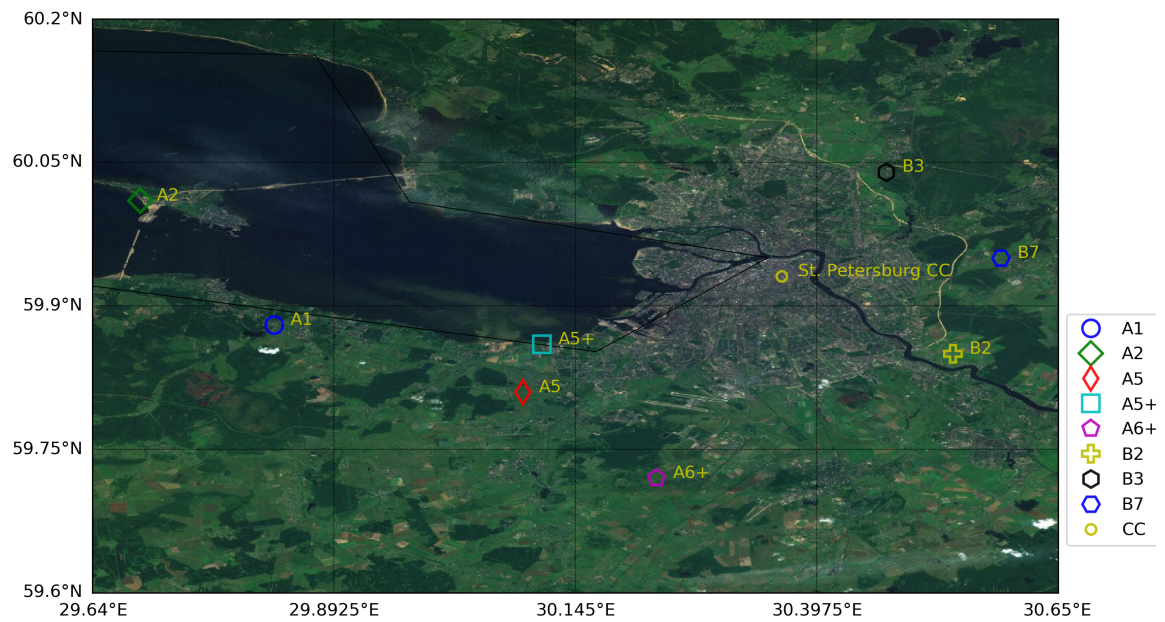
Figure 9.4: Map showing all posible positions of the instruments based on the historical wind direction and the technical and practical convenience

taken as an example. The results for that day are presented in Figure 9.5, which, together with the wind prediction, helped to choose the locations shown in Table 9.3.
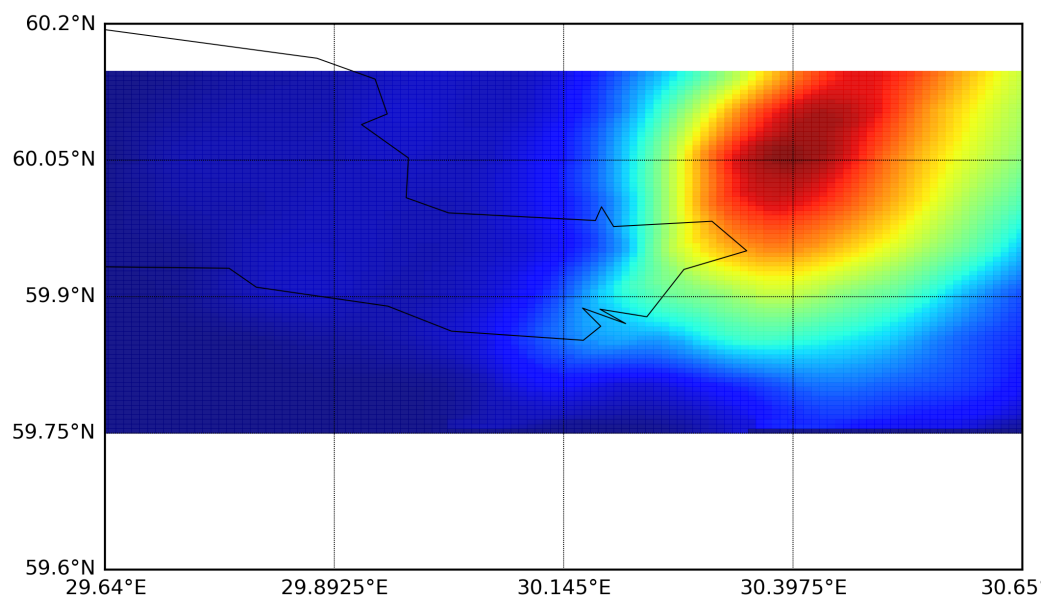
Figure 9.5: Hysplit NO_2 forecast for April 04, 2019.

Date of 2019	Outside the city plume		Inside the city plume		DOAS mobile
	Loc	FTS SN	Loc	FTS SN	
21 March	A1	80	B7	84	no
27 March	A2	84	B2	80	yes
1 April	A2	84	B2	80	yes
3 April	A1	84	B3	80	yes
4 April	A5	84	B3	80	yes
6 April	B7	84	A2	80	no
16 April	A2	84	A5+	80	yes
18 April	B3	80	A5, A6+	84	yes
24 April	A2	84	B2	80	yes
25 April	B3	80	A5	84	yes
30 April	B2	80	A2	84	yes

Table 9.3: Description of the spectrometer location deployment for each campaign day in 2019. Each instrument's location (Loc) is denoted by a letter and a number described in Figure 9.4. Finally, the availability of Mobile DOAS measurements is stated.

9.2.2.3 *Zenith DOAS near-real time total NO_2 along city ring*

During a measuring day, once the mobile FTS were set up following the two prediction tools, mobile zenith DOAS measurements were carried out to derive the NO_2 total column flux over the city in a near-real time manner. The last result was used to derive the actual plume orientation and helped to move one or both instrumFents in case these results differed from the predictions. As an example and following the previous one, the NO_2 total column around the city ring for April 04, 2019, is shown in Figure 9.6; luckily, the results were in good agreement with the wind forecast, and the HYSPLIT simulated NO_2 plume.

9.2.3 *COCCON's results*

Following this approach, 11 successful measurement days were carried out from March to April 2019. An overview of the collected COCCON data is presented in Figure 9.7; especially, the enhancement observed on 25 April 2019 is remarkable. This measurement day is presented as a plume transport event in a city-scale domain detectable by TROPOMI in Section 9.3.
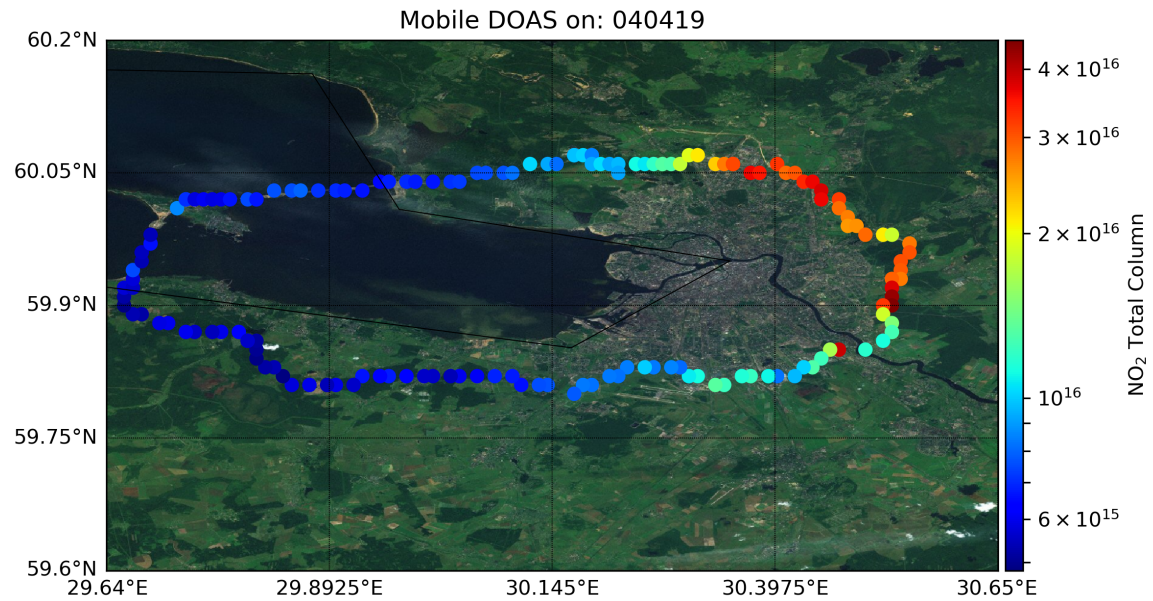
Figure 9.6: NO$_2$ total column over the city ring retrieved with mobile zenith DOAS for April 04, 2019.
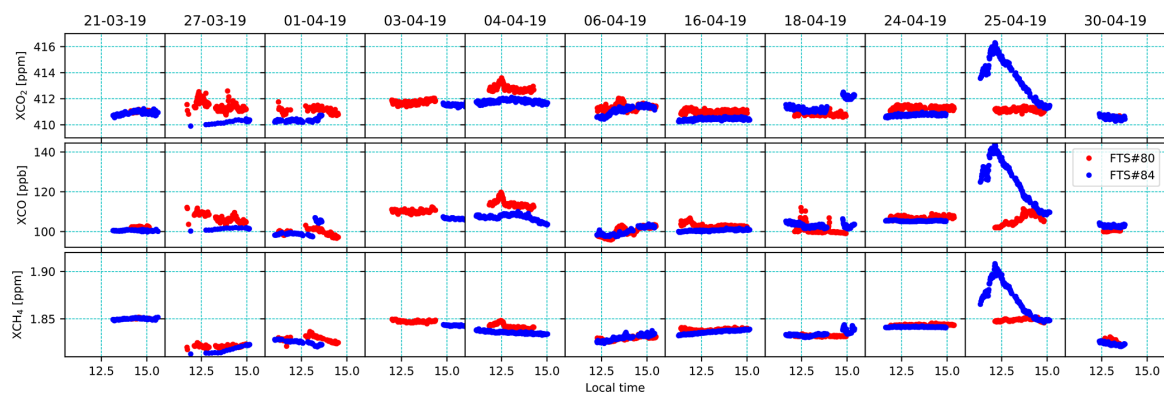
Figure 9.7: General overview of the full campaign results collected with the COCCON spectrometers.

9.2.4 *Flux estimations based on COCCON's results*

9.2.4.1 *Mass-balance approach*

A simple column model based on the mass balance approach (Jacob, 1999) is used in this section to calculate the anthropogenic emission strengths of CO$_2$, CH$_4$, and CO in St. Petersburg.

The built model is purely based on Lagrangian-trajectory dispersion assumptions. Here the emitted particles are transported away from their origin point by the interpolated wind, see Figure 9.8.

With this simple model, the development of a well-mixed column of air that extends from the surface to an altitude h (mixing depth) and travels along the surface can be tracked. Furthermore, in order to correctly used this approach during the transport event, several conditions need to be met:

- The mass exchange with the air above the altitude h is considered negligible.

- Wind speed and direction are constant.

- The extra/interpolated wind vector describes the actual atmospheric state.

- The gas emission remains constant, and there is no accumulation.

- Lifetime of the trace gases much longer than transport time.
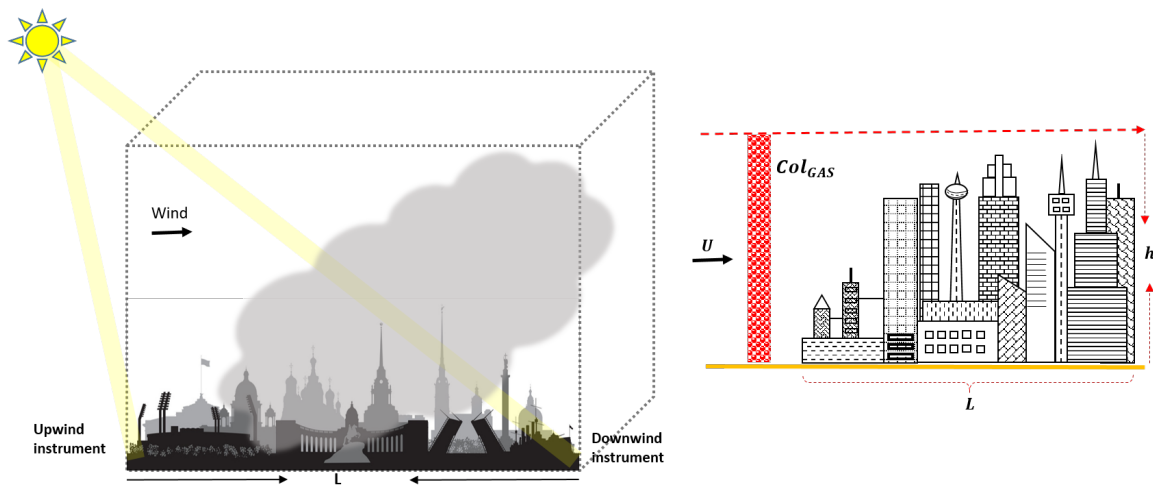
Figure 9.8: Illustration of the main components of the column model utilized for the areal fluxes calculations based on COCCON's observations in two and one dimension respectively.

If all the conditions mentioned above are fulfilled, the area flux can be determined by using the Equation 9.1

$$\Delta X_G = X_G^d - X_G^u = \frac{L}{\bar{U}} \times \frac{E_G}{Col_{dry-air}}$$
(9.1)

Where ΔX_G is the mean column-averaged dry air mole fraction difference between the amounts retrieved by the down-and-up-wind spectrometers ($X_G^d - X_G^u$), E_G is the mean area emission flux along the line crossing St. Petersburg urban area, L is the mean value of the transect, $\bar{U}$ is the mean wind velocity in the horizontal plane, and $Col_{dry-air}$ is the mean column of dry-air, which can be calculated by using Equation 9.2.

$$Col_{dry-air} = \frac{P_{gnd}}{g \times (\mu_{Air} + XH_2O \times \mu_{H_2O})}$$
(9.2)

Where P_{gnd} is the ground pressure in $[Pa]$ units; g is the gravitational acceleration in m/s^2 units; and μ_{Air} and μ_{H_2O} are calculated from the atomic mass unit (amu) and the weight of the molecule, measured in amu units.

As Equation 9.1 dictates, wind speed, direction, and transect distance must be available for the areal flux calculations. The values used in this thesis are described as follows:

WIND DATA SOURCE: While Makarova et al. (2021), used wind data from: (1) the Global Data Assimilation System (GDAS) from the Global Forecast System (GFS) of the National Centers for Environmental Prediction (NCEP) model, and (2) from HYSPLIT. For the results presented in this thesis, ERA5 has been used. ERA5 is the fifth generation of atmospheric global climate reanalysis produced by the European Centre for Medium-Range Weather Forecasts (ECMWF) (Setchell, 2020).

ERA5 data has a horizontal resolution of $30 \times 30 \ km^2$, provides values on 37 pressure levels covering 1 hPa to 1000 hPa, and has a temporal resolution of 1 hour. Based on this information, the wind data has been taken to an altitude corresponding to half of the estimated daily boundary layer height[2] closest to the FTIR observations.

Finally, the wind utilized for the areal flux calculations has been averaged within the FTIR observation period.

AIR PARCEL PATH LENGTH: A critical step that requires an enormous amount of work is the estimation of the air parcel transect within the sources L, in this case, the St. Petersburg city ring. In this thesis, a simple approach was used to daily estimate this value, which considered the wind direction, the position of the downwind spectrometer, and the road city ring as a boundary of the box and, therefore, the limits of the anthropogenic emission area. The wind direction and the position of the downwind spectrometer helped to find an infinite line that went through the city center and the instrument; this line was cut based on the box used, i.e., the ring road A118 shown in Figure 9.3. Finally, L is the distance of that straight line.

9.2.4.2 *Area fluxes results and comparison with inventories*

The simple model described before was applied to each day of the measurement campaign, not considering three days for the following reasons:

- 03 April: because, on that day, one of the instruments did not work at the assigned location.

- 18 April: because the upwind instrument was set up in the proximity of a thermal power plant, which in combination with the wind direction, added not expected pollution from this source.

- 30 April: due to the presence of clouds which developed faster after the instruments were deployed.

The eight remaining days were utilized for the area flux calculation, and the results are presented in Figure 9.9,

---

2 In the middle of the PBL, the wind is considered with constant speed and direction (Stull, 1988)
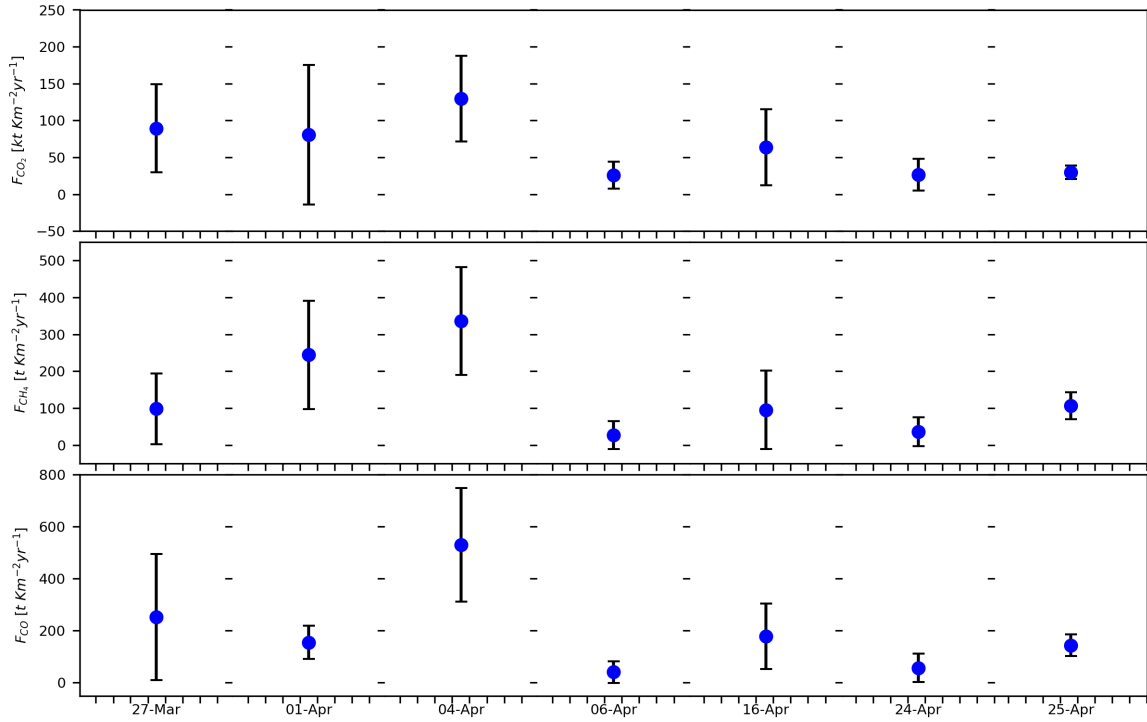
Figure 9.9: Daily mean fluxes for CO_2, CH_4 and CO calculated for the best days of the EMME campaign. The bars represent the estimated standard deviation.

AREA FLUX UNCERTANTY ESTIMATION: This thesis uses the combined standard deviation to assess the total uncertainty of the fluxes. A simple uncertainty propagation over Equation 9.3 was carried out as follows:

$$\delta E_G = \left[\left(\frac{\delta TC_G}{|TC_G|} \right)^2 + \left(\frac{\delta \vec{U}}{|\vec{U}|} \right)^2 + \left(\frac{\delta L}{|L|} \right)^2 \right]^{\frac{1}{2}} \tag{9.3}$$

Where TC_G is the total column of the gas, and is defined by $\Delta X_G Col_{dry-air}$ from Equation 9.1 and 9.2.

Equation 9.3 requires individual uncertainty calculations for (1) the total column difference derived from up and downwind instruments, (2) the derived wind speed, and (3) the estimation of the effective length. These uncertainties are calculated following the corresponding propagation rule based on their algorithms. The relative uncertainty calculated for each gas area flux using Equation 9.3 is presented in Table 9.4 and on the y-axis bars in Figure 9.9.

The EDGAR's yearly averaged area emissions for CO_2, CH_4, and CO for St. Petersburg, presented in Table 9.4, were averaged considering St. Petersburg urban area. No results for 2019 were available; therefore the latest available were taken: 2018.

The results presented in this thesis were independently analyzed in comparison with Makarova et al. (2021). By checking the Table 9.4, which resumes the area fluxes estimated

Area Fluxes	This thesis	Makarova et al. (2021) (9 days)	Russian official reports (Serebritsky, 2017, 2018)	EDGAR v6.0 (Crippa et al., 2021a,b,c)
E_{CO_2} [$kt\ Km^{-2}yr^{-1}$]	64 ± 40	89 ± 28	31	39
E_{CH_4} [$t\ Km^{-2}yr^{-1}$]	118 ± 80	135 ± 68	25	87
E_{CO} [$t\ Km^{-2}yr^{-1}$]	194 ± 98	251 ± 104	410	70

Table 9.4: Annual area fluxes calculated in this thesis and comparison with the results published by (Makarova et al., 2021), Russian reports for the St. Petersburg city taken from (Makarova et al., 2021) and EDGAR inventory v6.0 for 2018. The EDGAR values presented were averaged considering St. Petersburg urban area.

in this thesis, and by (Makarova et al., 2021) for the city of St. Petersburg[3]; one can conclude that the emission strengths estimated in this thesis are smaller for the three species by $\approx$ 28%,13%, and 23% for CO_2, CH_4, and CO, respectively. Nevertheless, all reported quantities agree, considering their uncertainty limits. The most significant facts in the presented calculations that could lead to differences concerning the results presented by Makarova et al. (2021) are the following:

- Trace gases were retrieved with PROFFAST considering the instrument's ILS estimated based on the calibrations performed at KIT before and after the campaign.

- The COCCON results for both instruments were harmonized and intercalibrated to the network's reference unit.

- No smoothing, intra-, or extrapolation between the daily time series of the retrieved column abundances was performed for the area flux calculations.

- The wind data information was taken from ERA5 instead of the Global Data Assimilation System (GDAS) from the Global Forecast System (GFS) model (See `https://www.nco.ncep.noaa.gov/pmb/products/gfs/#GDAS`, last access: 9 September 2022).

- The air parcel transect L estimation did not consider the land-use patterns over the city.

Ionov et al. (2021) have quantified the CO_2 integral emissions by coupling the FTIR results with HYSPLIT, using the Open-Data Inventory for Anthropogenic CO2 (ODIAC) data as a priori for St. Petersburg emissions; finding an emission strength of $\sim$ 76 ± 58 kt yr^{-1}, which is in better agreement with the result estimated in this thesis, 64 ± 45 kt yr^{-1}, being smaller by $\sim$ 13%

When comparing the estimated area fluxes with the municipal reports of the city, these are two times higher for CO_2 and CO and five times for CH_4, making studies like this a great success for the scientific community.

---

3 St. Petersburg municipal reports and EDGAR inventory reported values are exhibited as well.

The estimated area fluxes with EDGAR inventory results (see Table x) for the three species are higher by $\sim$ 40%, 26%, and 64% for CO_2, CH_4, and CO, respectively. Comparing these results with others is always tricky because they depend on the measurement technique, the method applied for the final calculations, spatial and time resolution, season and actual meteorological conditions, and so on. The main reason for the differences may be the seasonal and daily cycle for CO_2 and CH_4; and the anthropogenic emissions occurring during this period (especially for undestanding CO) when the EMME campaign was carried out (March-April, mainly in the afternoon). Such time is considered for maximum anthropogenic emissions mainly due to the heating sector (Ionov et al., 2021; Makarova et al., 2021)

9.3 INVESTIGATION OF SPACEBORNE TRACE GAS PRODUCTS OVER ST PETERSBURG AND YEKATERINBURG USING COCCON OBSERVATIONS

This section focuses on the complete set of COCCON measurements collected in the framework of VERIFY to validate and compare TROPOMI, OCO-2, GOSAT, MUSICA IASI, and Copernicus Atmosphere Monitoring Service (CAMS). Additionally, a scaling method is developed, and its results are used to better inter-compare satellite products. This method is based on COCCON measurements at both sites to scale CAMS XCO_2, XCH_4, and XCO. The effectiveness of this method is proved by using different subsets of XCH_4 retrieved from the densest observations from the reference COCCON spectrometer (FTS#37) at Karlsruhe during the period of January 2018–December 2020. Because GHGs surface fluxes are imprinted in the atmospheric concentrations, in order to learn about them, it is imperative to estimate their respective atmospheric gradients accurately. The gradients for XCO_2, XCH_4, and XCO are calculated between both studied cities during the shared measurement period. Finally, a city-scale transport event that occurred during the city campaign and was tracked by TROPOMI is presented in this study.

9.3.1 *Ground-based FTIR measurements at Peterhof and Yekaterinburg*

For the continuous, long-baseline campaign, the instrument FTS#80 remained at Peterhof station at the Saint Petersburg State University and continued operation there, while the other spectrometer (FTS#84) was moved to Yekaterinburg.

9.3.1.1 *Peterhof (59.88° N, 29.83° E)*

Peterhof is a suburb of St. Petersburg located approximately 35 km southwest from the city centre. The instrument in Peterhof was operated at the Atmospheric Physics Department of the Faculty of Physics at Saint Petersburg State University. The instrument was set up on every sunny day (outside the city campaign period) at the second floor of the FTIR remote-sensing group. Eighty-four measurement days were collected between January 2019 and March 2020 as can be seen in Figure 9.10. From that figure, the larger XCO observed values on 6 August 2019 in comparison to all the other days is remarkable. For more details, see Figure 9.11a and b, where the spatial distribution of TROPOMI XCH_4 and XCO, as well as wind speed and direction, respectively, for this day are presented. Additionally Figure 9.11c shows the time series for COCCON XCO_2, XCH_4 and XCO for that day, and the enhancements are all observed in the three species. It seems that these large values could be related to a plume transport from a heavily industrialized area coming from Lappeenranta, which is located in the southeast of Finland and approximately 160 km away from Peterhof (see Figure 9.12a). In order to confirm this, Figure 9.12a shows the yearly CO emissions coming from the "Combustion from manufacturing sector" taken from the EDGAR V05 inventory (latest available: 2015), together with the backward trajectories calculated by using the HYSPLIT model and arrived in Peterhof on that day (see Figure 9.12b). This confirms that the wind comes from the area where huge anthropogenic CO sources are located. Another possibility could be an even closer local source, like a small fire.
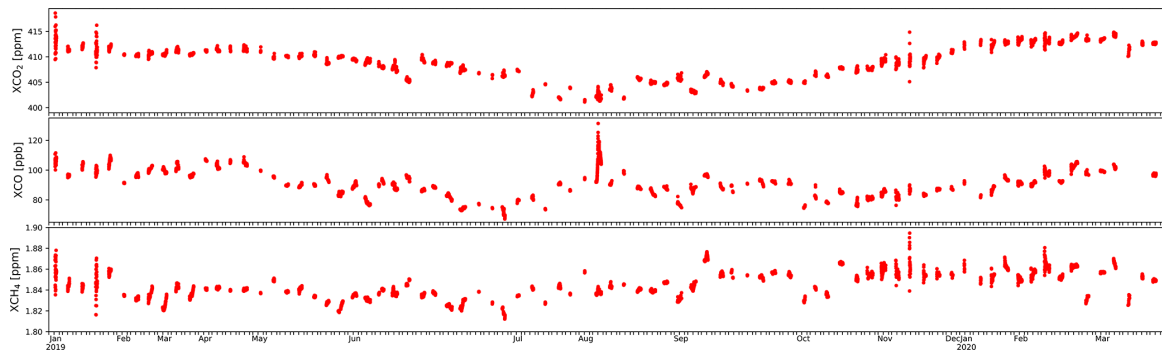
Figure 9.10: Time series for XCO_2, XCO and XCH_4 obtained in Peterhof during the continuous campaign.
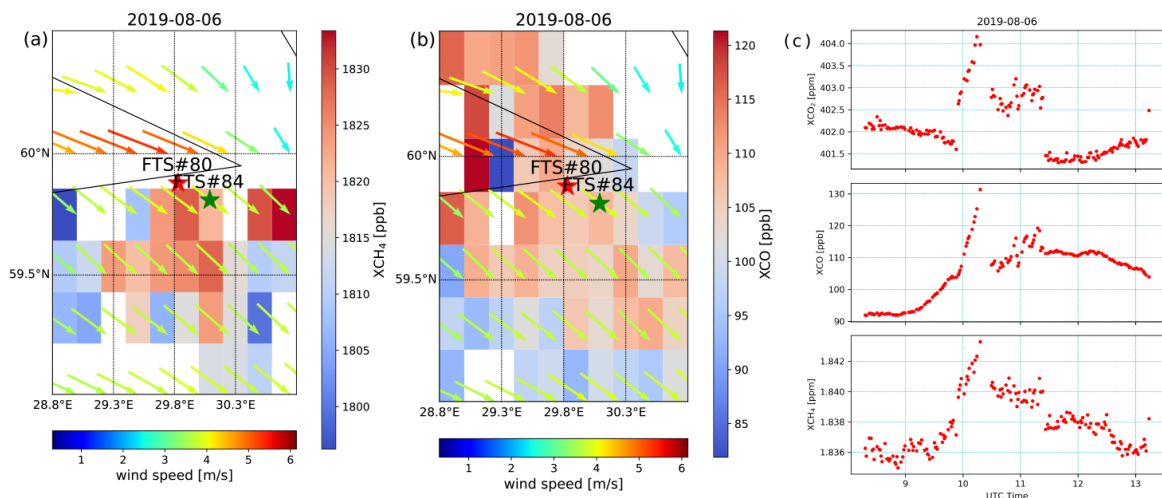
Figure 9.11: Spatial distribution of XCH_4 **(a)** and XCO **(b)** on a 0.1×0.1 latitude $\times$ longitude grid together with the ERA5 wind at 12:00 UTC, and **(c)** daily time series of XCO_2, XCO and XCH_4 (top, middle and bottom panels, respectively) on 6 August 2019.

9.3.1.2 *Yekaterinburg (56.8° N, 60.6° E)*

It was planned that immediately after the EMME campaign the instrument FTS#84 would be transported to Yekaterinburg. Unfortunately, unforeseen organizational problems significantly delayed moving the instrument from St. Petersburg to Yekaterinburg. The instrument was finally operational in Yekaterinburg in October 2019 and kept measuring until the very last day before being shipped back to KIT (April 2020). The instrument was operated at the Climate and Environmental Physics Laboratory INSMA of the Ural Federal University (UrFU). The instrument was set up in an internal yard of the UrFU building. However, the building structure, which blocked the sunlight, was a limitation. Sometimes high trucks passing through the yard blocked the field of view of the instrument. The spectrometer rested on the windowsill of the basement, so it was located exactly at ground level ~ 260 m. Under good weather conditions, measurements were carried out approximately between 11:00 and 14:30 LT. In total, 22 d of measurements were collected as can be seen in Figure 9.13.
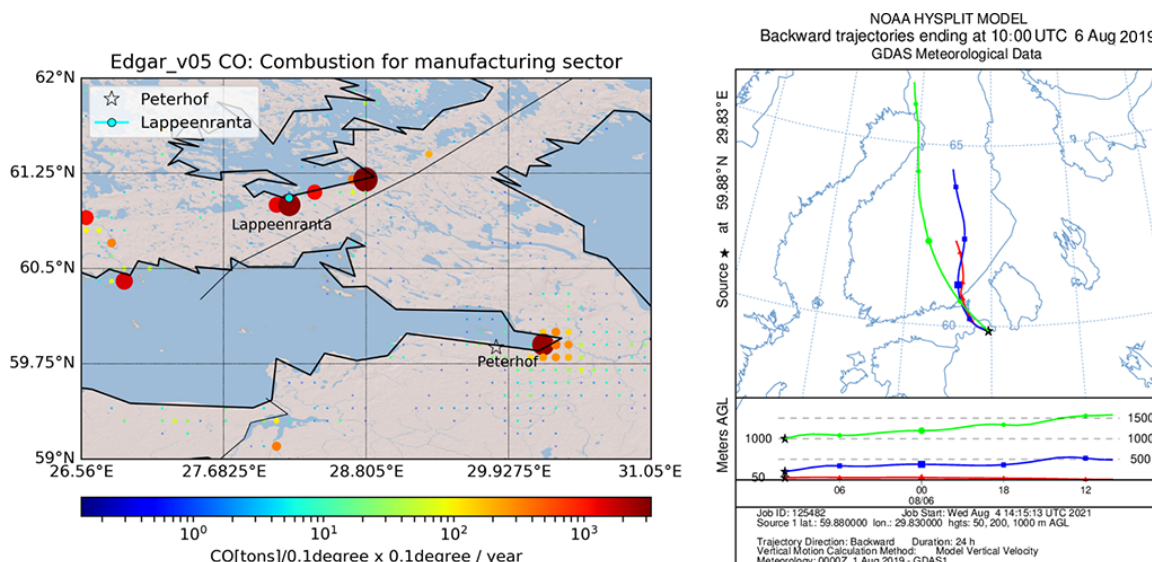
Figure 9.12: **(a)** Spatial distribution of CO emissions (tonnes per $0.1 \times 0.1°\,yr^{-1}$) from "Sector-Specific Gridmaps": combustion for manufacturing. Data source: EDGAR v5.0, 2015 (`https://edgar.jrc.ec.europa.eu/dataset_ap50`, last access: 9 September 2022); the map was generated with Python basemap toolkit by using ArcGIS from a world shaded relief model; **(b)** backward trajectories arriving in Peterhof on 6 August 2019, calculated by using the HYSPLIT model.
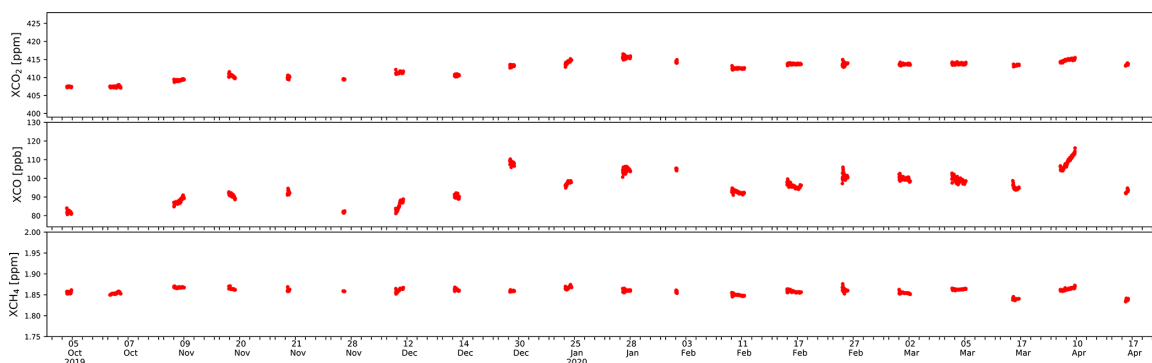
Figure 9.13: Time series of XCO_2, XCO and XCH_4 data observed at Yekaterinburg.

9.4 DATASETS

All the datasets used in this study are summarized in Appendix B. Table 9.5 gives an overview of all products used and the essential characteristics.

9.5 SEASONAL VARIABILITY OF GHGS

9.5.1 *Peterhof*

The seasonal patterns of the retrieved GHGs are shown in Figure 9.14, which illustrates the time series of daily mean XCO_2, XCH_4, XCO and XH_2O from different data prod-

Data product	Species	Algorithm or model	Product version or level	qa	References	Data provider and data access information
COCCON	XCH$_4$, XCO, XH$_2$O	PROFFAST			(Alberti et al., 2022a; Frey et al., 2019)	
TROPOMI	XCH$_4$	RemoTeC	level 2	qa= 1.0	(Lorente et al., 2021)	http://ftp.sron.nl/open-access-data-2/TROPOMI/ tropomi/ch4/14_14_Lorente_et_al_2020_AMTD/ (last access: 9 September 2022)
	XCO	SICOR (Shortwave Infrared CO Retrieval)	offline, level 2, v1.2	qa= 1.0	(Borsdorff et al., 2018b, 2019; Landgraf et al., 2016)	https://s5phub.copernicus.eu/dhus/#/home (last access: 9 September 2022)
	XH$_2$O	SICOR	level 2, v8.1		(Scheepmaker et al., 2016; Schneider et al., 2022a)	http://ftp.sron.nl/open-access-data-2/TROPOMI/ tropomi/hdo/10_3/ (last access: 9 September 2022)
OCO-2	XCO$_2$	ACOS (Atmospheric CO$_2$ Observations from Space)	v10r	qa = 0	(Kiel et al., 2019; Osterman et al., 2020)	Product OCO2_L2_Lite_FP 10r Obtained from NASA's Earthdata GES DISC website: https://doi.org/10.5067/E4E140XDMP02
OCO-2 FOCAL	XCO$_2$	FOCAL	v09		(Reuter and Buchwitz, 2021; Reuter et al., 2017a,b)	University of Bremen
GOSAT	XCH$_4$, XCO, XH$_2$O		V02.90		(Kuze et al., 2009)	https://data2.gosat.nies.go.jp/ (last access: 9 September 2022)
MUSICA IASI	XH$_2$O	PROFFIT (nadir version)	v3.2.1 and v3.3.0	spectral fit quality check according to Schneider et al. (2022)	(Schneider et al., 2022b)	https://www.imk-asf.kit.edu/english/ musica-data.php (last access: 9 September 2022)
CAMS	XCO$_2$	PyVAR	v20r1		(Chevallier, 2020, 2021)	https://ads.atmosphere.copernicus.eu/cdsapp#!/dataset/ cams-global-greenhouse-gas-inversion?tab=form (last access: 9 September 2022)
	XCH$_4$	TM5-4DVAR	v19r1		(Segers, 2020a,b)	
	XCO	Integrated Forecast System	control run		(Flemming et al., 2017; Inness et al., 2019)	on request

Table 9.5: Overview of the satellite and model data products used in this study.

ucts at Peterhof. The CAMS-COCCON data product presented in Figures 9.14 and 9.15 is discussed in Section 9.6. The TROPOMI satellite has a higher spatial resolution and therefore, the available retrieved species from TROPOMI were daily averaged within a collection radius of 50 km around Peterhof. For the GOSAT and MUSICA IASI datasets, a collection radius of 100 km around Peterhof is used, and for OCO-2 data, a collection radius of 200 km is used. The choice of collecting radius is considered based on the available satellite observations and the bias between a single satellite observation and the coincident COCCON observation (see Figure B.1). The measurements from the different ground- and space-based observations and model data generally show good agreements and similar seasonal variability.

CAMS and the satellite products show a high bias of about 0.81 to −3.1 with respect to COCCON. GOSAT (Figure 9.14) also shows some obvious outliers compared to the other products, which have similar behaviours. The amount of XCO$_2$ varies along the year, and much of this variation is driven by respiration, which never stops but increases between autumn and winter due to reduced uptake (no photosynthesis). In this case the atmo-
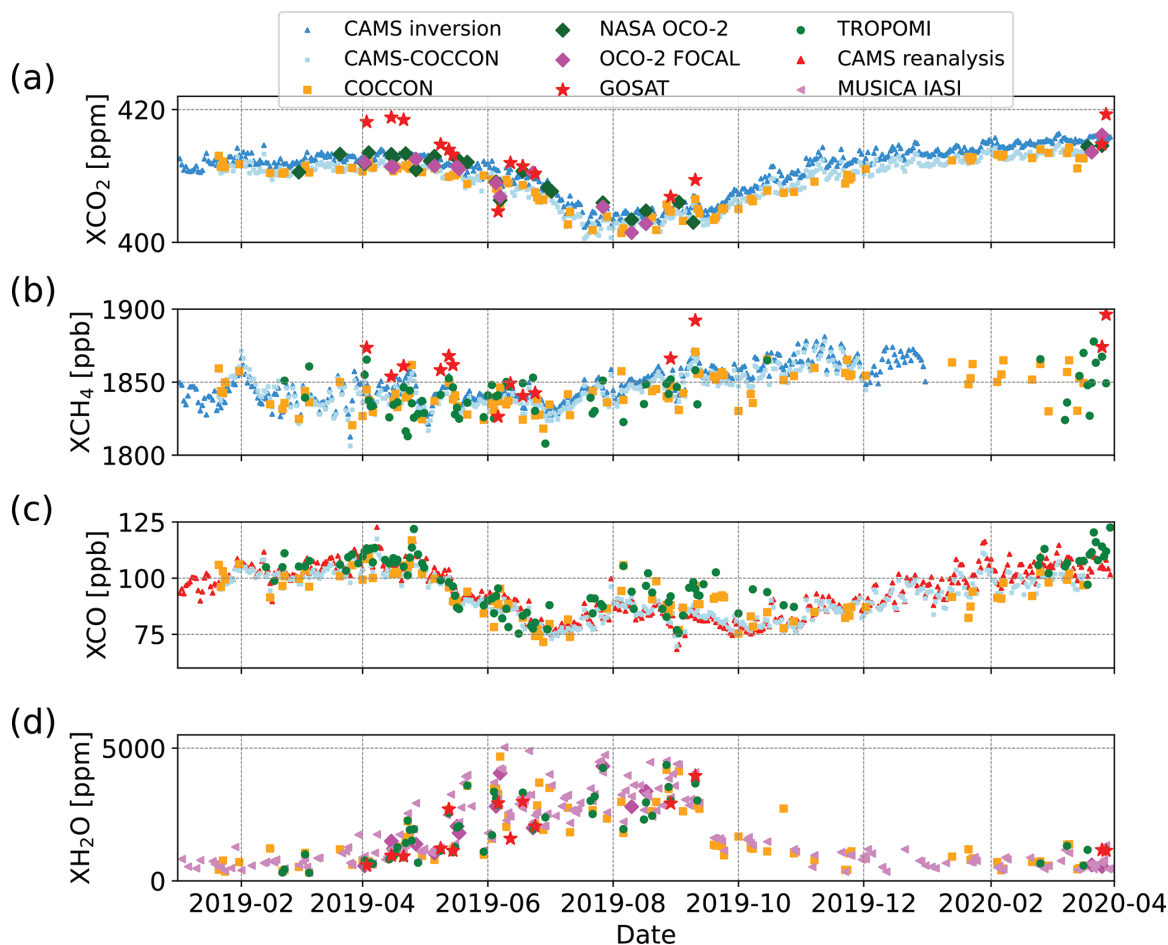
Figure 9.14: Time series of daily mean **(a)** XCO_2, **(b)** XCH_4, **(c)** XCO and **(d)** XH_2O for different data products at Peterhof.

spheric XCO_2 concentration is stable between January and April. It started to decrease from May to end of July, during which the growing season and the photosynthetic activities increase. Similar behaviour in 2019 was also observed by Timofeyev et al. (2021) and in previous years by Nikitenko et al. (2020) and Timofeyev et al. (2019). The amount of XCO_2 stays around 403 ppm between the end of July and middle of September and starts to increase afterwards.

For XCH_4, COCCON shows a similar behaviour as TROPOMI and CAMS. Slightly higher mean values and variability can be seen in GOSAT XCH_4 with a few outliers. Compared to XCO_2, XCH_4 shows generally less seasonal variabilities with more short-term enhancements of about a week duration, probably related to synoptic variations. The seasonal variation is comparable to the results of Gavrilov et al. (2014), Makarova et al. (2015a,b), and Timofeyev et al. (2016). A slightly higher XCH_4 is observed at the end of 2019 for all data products.

XCO shows seasonal variability with a maximal value of 110 ppb in late April and decreases by nearly 40 % to 70 ppb in the beginning of July. A secondary local maximal reaching $\sim$ 95 ppb occurs in August. This feature needs further investigation. The COCCON XCO matches well to the CAMS reanalysis data. Moreover, COCCON agrees better
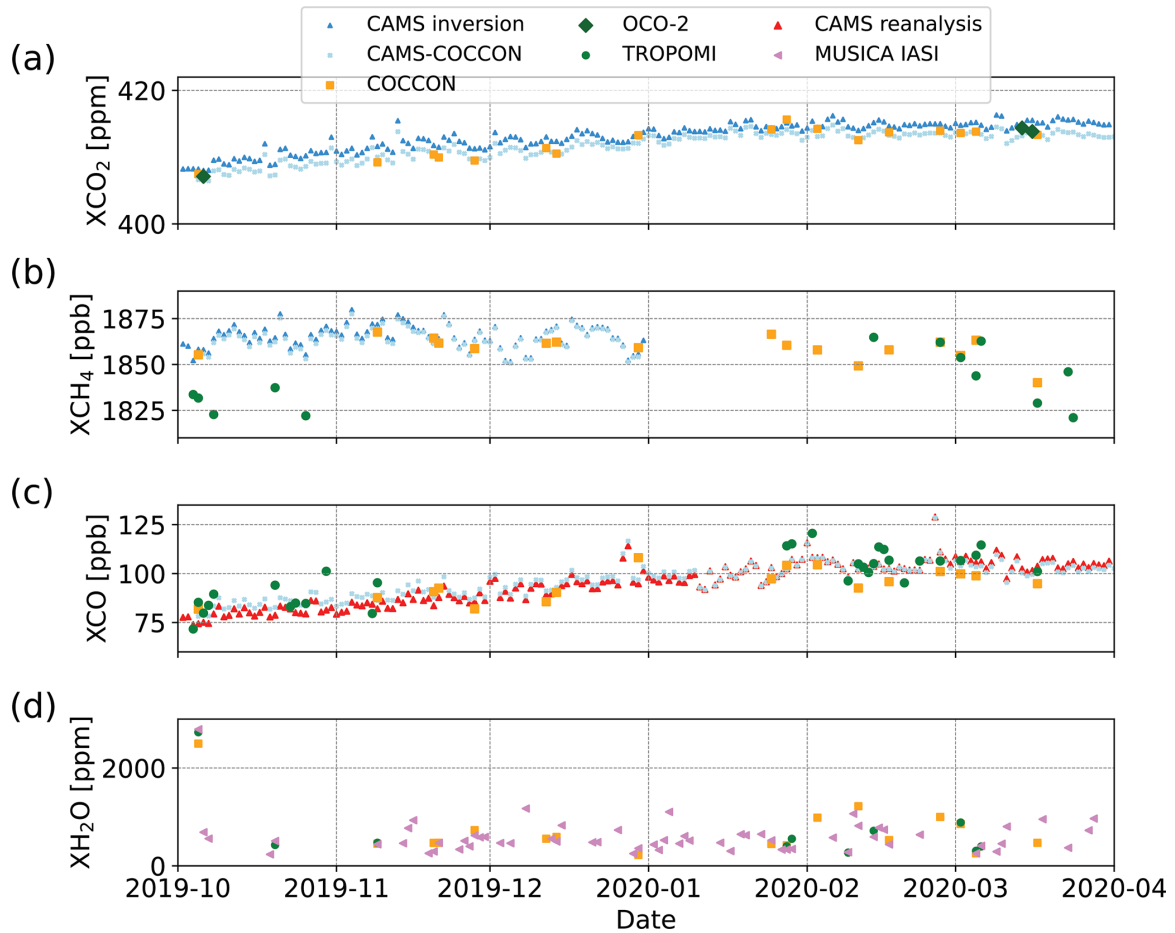
Figure 9.15: Time series of daily mean **(a)** XCO_2, **(b)** XCH_4, **(c)** XCO and **(d)** XH_2O for different data products at Yekaterinburg.

with the TROPOMI data in summer than in spring and late autumn, when TROPOMI measured higher values.

XH_2O shows a strong seasonal cycle with a maximal amount of $\sim 4700\,\text{ppm}$ in summer and minimal amount of $\sim 320\,\text{ppm}$ in winter. All products show quite similar behaviour with high variability, which is similar to those in Semenov et al. (2015), Timofeyev et al. (2016), Virolainen et al. (2017), and Virolainen et al. (2016). The GOSAT data have higher mean values since the measurement period covers only the time range from later spring to summer, during which higher XH_2O is observed.

9.5.1.1 *Yekaterinburg*

The measurement period covered winter and spring, from 5 October 2019 to 17 April 2020 at Yekaterinburg (Figure 9.15). Here we use a larger radius (100 km) to collect the TROPOMI observations, because there are much fewer overpasses at Yekaterinburg during this period. Table 9.6 lists the number of coincidences (pixel-wise) for 50 and 100 km radius, and the number of coincident satellite pixels is reduced by a factor of 3 to 5 for the narrower radius. From Figure B.2, we do see a tendency of slightly reduced differences

with better co-location within the 100 km limit in case of XCH_4 but not clearly for the other species. Due to the low number of coincident measurements when using 50 km, we decided to accept the 100 km distance criterion for the Yekaterinburg observations.

Species	$R = 50$ km	$R = 100$ km
XCH_4	101	345
XCO	265	1111
XH_2O	19	136

Table 9.6: Number of TROPOMI measurements within 50 km and within 100 km.

XCO_2 shows a clearly increasing tendency from October of 408 ppm to a maximal value of 415 ppm in the middle of February, which covers later autumn and winter. This is because on top of the increase due to the anthropogenic emissions there are variations due to photosynthesis and respiration (https://atmosphere.copernicus.eu/carbon-dioxide-levels-are-rising-it-really-simple, last access: 9 September 2022). During that period the plants notably reduce or stop the photosynthesis processes which could increase the amount of CO_2 in the atmosphere. Later this maximal value stays constant until the middle of March. It tends to decrease, and a similar behaviour is observed in Peterhof.

For XCH_4, COCCON shows a good agreement with CAMS data, though there are not so many COCCON observations. XCH_4 shows generally decreasing tendency but with more short-term variabilities. Such variabilities are observed in Peterhof as well. A few TROPOMI observations in October are deviating from the other two datasets, and it seems that TROPOMI underestimates XCH_4. This might be because most TROPOMI measurements are located in the rim of the collecting radius and thus away from the location of Yekaterinburg, introducing some errors (see Figure B.3). Further, this underestimation could be due to the difficulty for retrieving CH_4 in low- and high-albedo scenes (Lorente et al., 2021).

XCO shows in general a similar behaviour of XCO_2, with a steady increase during late autumn and winter. It seems that the increasing behaviour of XCO has an inverse relationship with XCH_4. This is probably due to the fact that atmospheric CO is mainly produced by incomplete combustion of fossil fuels (Kasischke and Bruhwiler, 2002) and the oxidation of methane (Cullis and Willatt, 1983).

As expected, most XH_2O values are below 1000 ppm, similar to Peterhof in that period. This can be explained by the saturation concentration of water vapour in air, which reduces for lower temperatures.

9.5.2 *Removal of the smoothing error bias*

Because we aim at comparing different data products (such as spaceborne and COCCON products) and each of them use different sensitivities and different a priori profiles, it is important to account for these differences when comparing a defined Xgas species as described by Connor et al. (2008) and Rodgers and Connor (2003). Such procedures have been applied in similar studies (Hedelius et al., 2016; Sha et al., 2021; Yang et al., 2020).

In this study, we used the method described in Connor et al. (2008). We took as starting point their Equation (13); then the state vector can be written as:

$$\vec{V}_{\text{gas, obs}} = \vec{V}_{\text{gas, apr}} + \mathbf{A} \left(\vec{V}_{\text{true}} - \vec{V}_{\text{gas, apr}} \right) , \tag{9.4}$$

where V represents the volume mixing ratio (VMR). The left-hand term of the equation represent the retrieved value, while the right-hand term represents the VMR calculated based on the a priori profiles plus the effect of the averaging kernel matrix **A** applied to the difference of the VMR between the true atmospheric gas concentration and the a priori profiles. By dividing the atmosphere into k layers, this equation can be written as follows:

$$X_{\text{gas, obs}} = X_{\text{gas, apr}} + \sum_{0}^{k} h_k a_k \left(V_{\text{true},k} - V_{\text{apr},k} \right) , \tag{9.5}$$

where $X_{\text{gas},y} = \sum_{k} h_k \cdot V_{y,k}$ with y being a defined a priori profile used and h_k being the pressure-weighting function in a defined layer k (Connor et al., 2008), i.e.

$$h_k = \frac{(p_{k-1} - p_k)}{p_0}. \tag{9.6}$$

By using Equation 9.5 with "new" and "old" satellite a priori profiles, we obtain (*) and (**) as follows:

$$X_{\text{gas, obs}-\text{new}} = X_{\text{gas, apr}-\text{new}}$$
$$+ \sum_{0}^{k} h_k a_k \left(V_{\text{true},k} - V_{\text{apr}-\text{new},k} \right) \quad (^*)$$
$$X_{\text{gas, obs}-\text{sat}} = X_{\text{gas, apr}-\text{sat}}$$
$$+ \sum_{0}^{k} h_k a_k \left(V_{\text{true},k} - V_{\text{apr}-\text{sat},k} \right) \quad (^{**}).$$

Then we subtract (*) from (**):

$$X_{\text{gas, obs}-\text{new}} = X_{\text{gas, obs}-\text{sat}} + \left(X_{\text{gas, apr}-\text{new}} - X_{\text{gas, apr}-\text{sat}} \right)$$
$$+ \sum_{0}^{k} h_k a_k V_{\text{true},k}$$
$$- \sum_{0}^{k} h_k a_k V_{\text{apr}-\text{new},k}$$
$$- \sum_{0}^{k} h_k a_k V_{\text{true},k}$$
$$+ \sum_{0}^{k} h_k a_k V_{\text{apr}-\text{sat},k},$$

which turns into

$$
\begin{aligned}
X_{\text{gas, obs}-\text{new}} \\
= X_{\text{gas, obs}-\text{sat}} + \left(X_{\text{gas, apr}-\text{new}} - X_{\text{gas, apr}-\text{sat}}\right) \\
+ \sum_0^k h_k a_k \left(V_{\text{apr}-\text{sat},k} - V_{\text{apr}-\text{new},k}\right),
\end{aligned}
\tag{9.7}
$$

where $X_{\text{gas, obs}-\text{new}}$ in Equation 9.7 becomes the smoothed satellite product, which takes into account the a priori profiles used for the COCCON retrievals.

When using Equation 9.7, both a priori profiles need to be resampled on the same pressure grid. The vertical profiles used for the COCCON analysis are interpolated to the pressure levels of different satellite products (TROPOMI CO, GOSAT CO_2 and CH_4, OCO-2 CO_2, and OCO-2 FOCAL CO_2) by using the mass conservation method described in Langerock et al. (2015).

The smoothing correction is not applied to XH_2O, because the natural variability of XH_2O is very high anyway.

9.6 CORRELATION BETWEEN COCCON AND SATELLITE PRODUCTS

All satellite XCO_2, XCH_4 and XCO data used in this section were adjusted for the COCCON a priori profile (TCCON a priori profiles were used) as described above.

Figures 9.16 to 9.19 show the correlations between COCCON and different satellite products at Peterhof (triangle symbols) and at Yekaterinburg (dot symbols). The satellite products and CAMS generally agree well with COCCON. Figure 9.20 illustrates the averaged bias and standard deviation of each product of the coincident Xgas (XCO_2, XCH_4 and XCO) values (in space-time) with respect to COCCON for the available gases at both sites. In order to find the coincident COCCON data, the mean value of the observations 2 h before and after a centralized time reference is taken. Such a time reference differs for each of the products as follows: the overpass time for satellite and each of the timestamps for CAMS.

The measuring period at Yekaterinburg for COCCON was mostly in winter and early spring, from October 2019 to April 2020, in which there were fewer sunny days. This results in fewer COCCON and satellite observations. There is only one coincident point between COCCON and NASA operational OCO-2 (Figure 9.17c) and no coincident points between COCCON and OCO-2 FOCAL or GOSAT products at Yekaterinburg. Even a much larger collection circle with a radius of 100 km is used for TROPOMI at Yekaterinburg, and there are fewer coincidence measurements than those in Peterhof, where more than 1 year of measurements were performed.

Due to the short period of ground-based measurements, poor weather condition, and poorer coverage of satellites at high latitudes in the winter hemisphere (OCO-2; (Patra et al., 2017), and GOSAT; https://data2.gosat.nies.go.jp/galleryfts_l2_swir_co2_gallery_en.html, last access: 9 September 2022), it becomes more difficult to validate satellite products with ground-based measurements at locations like Yekaterinburg.

At Peterhof OCO-2 FOCAL XCO_2 data have the lowest bias with respect to COCCON, while GOSAT data show the highest bias and standard deviation (3.6 ppm $\pm$ 2.8 ppm, Figure 9.20). NASA operational OCO-2 and CAMS show similar biases. CAMS, TROPOMI
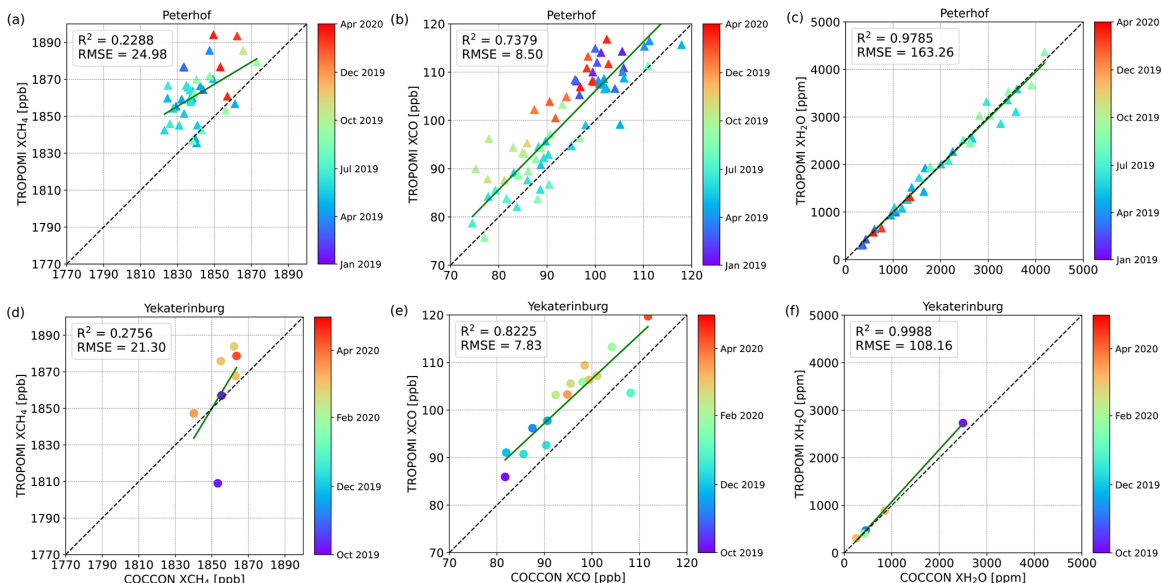
Figure 9.16: Correlation plots between TROPOMI and COCCON for XCH_4, XCO and XH_2O at Peterhof **(a–c)** and at Yekaterinburg **(d–f)**. All satellite data except XH_2O were adjusted for the COCCON a priori profile (TCCON a priori profiles were used).
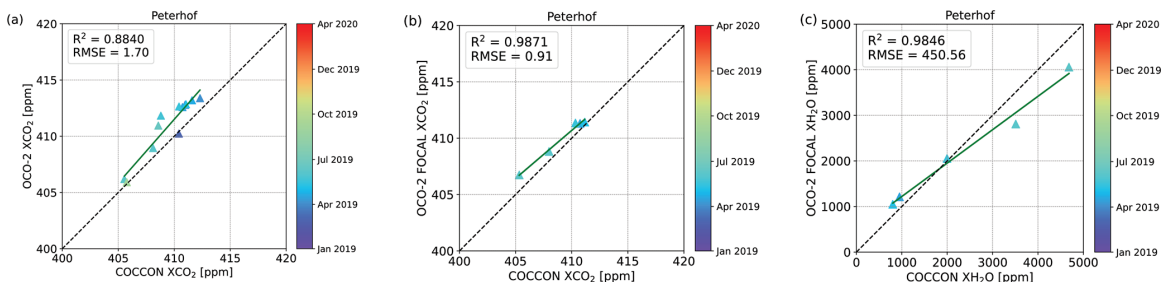
Figure 9.17: Correlation plots **(a–b)** between NASA's operational and the FOCAL OCO-2 product and COCCON for XCO_2 and **(c)** between OCO-2 FOCAL and COCCON for XH_2O at Peterhof. All satellite data except XH_2O were adjusted for the COCCON a priori profile (TCCON a priori profiles were used).
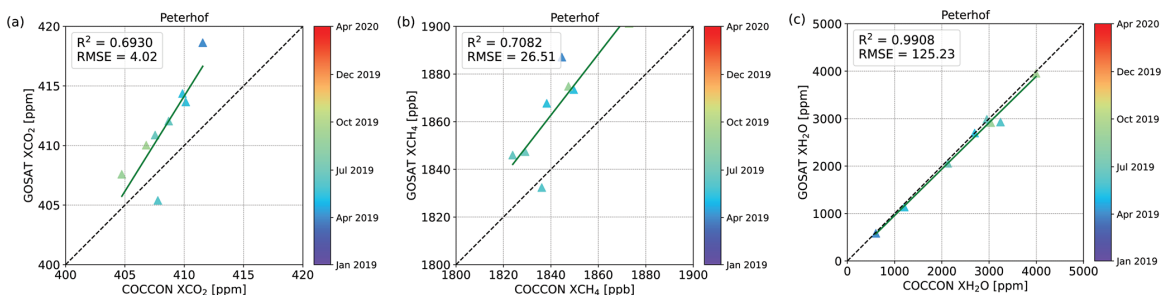
Figure 9.18: Correlation plots between GOSAT and COCCON for **(a)** XCH_4, **(b)** XCO and **(c)** XH_2O at Peterhof. All satellite data except XH_2O were adjusted for the COCCON a priori profile (TCCON a priori profiles were used).

and GOSAT measure higher XCH_4 than COCCON, among which GOSAT has the highest
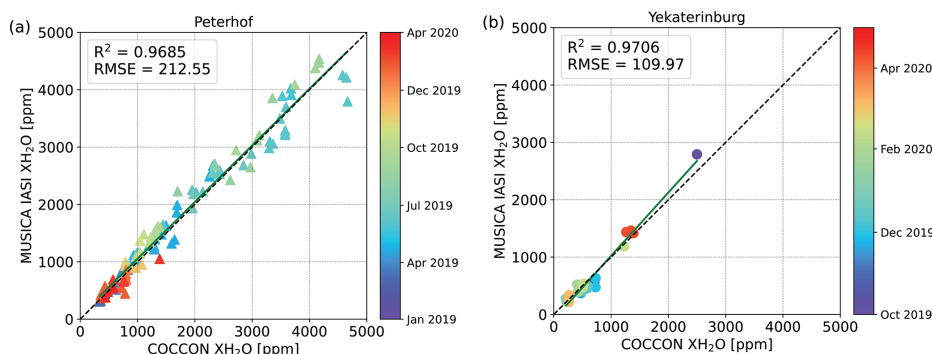
Figure 9.19: Correlation plots of XH_2O between MUSICA IASI and COCCON at **(a)** Peterhof and **(b)** Yekaterinburg.
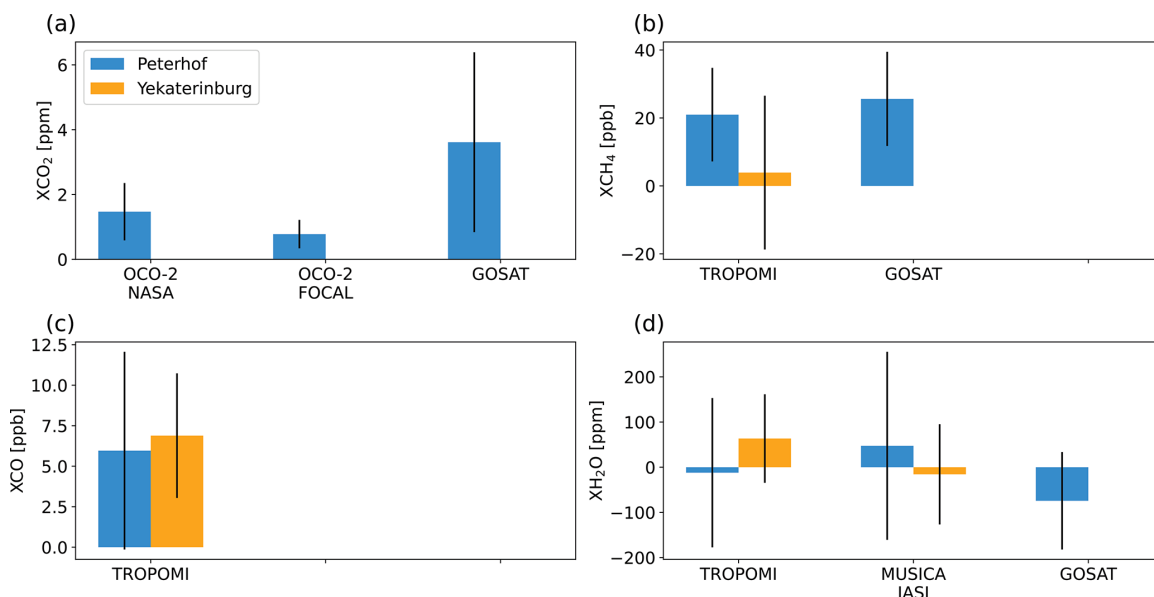
Figure 9.20: Bar plots of the averaged bias derived from different products with respect to COC-CON for **(a)** XCO_2, **(b)** XCH_4, **(c)** XCO and **(d)** XH_2O at Peterhof and Yekaterinburg. The error bars represent the standard deviation of the averaged bias.

biases at Peterhof. The high negative bias in TROPOMI at Yekaterinburg is mainly due to the underestimation of the TROPOMI product in October 2019. At both sites TROPOMI XCO shows higher biases than CAMS with respect to COCCON, which can be seen in Figures 9.14c and 9.15c – TROPOMI with higher values than COCCON. TROPOMI and GOSAT generally measure lower XH_2O than COCCON, whereas MUSICA IASI shows high bias and standard deviation. However, good correlations can be found between satellite XH_2O and COCCON in Figures 9.16c, f, 9.18c and 9.19.

9.7 USING CAMS MODEL FIELDS FOR UPSCALING COCCON OBSERVATIONS

Unfortunately, during the continuous campaign carried out at Peterhof and Yekaterinburg, there are just a few coincident measurement days with satellite observations, especially

in comparison to GOSAT and OCO-2 (see Figure 9.20). Although these satellites offer a global coverage, for our measurement period (even with quite relaxed coincidence criteria), the comparisons do not use the majority of the ground-based observations. This is especially the case in Yekaterinburg during the observations from October 2019 to April 2020, i.e. GOSAT and OCO-2 have none or just a couple of measurements in the winter and early spring period at high latitudes. Even in Peterhof where more than 1 year of measurements were taken, the number of coincident measurements between the aforementioned satellites is rather few.

For that reason, we employ a novel method which uses model fields for upscaling the ground-based FTIR measurements, thereby generating additional virtual coincidences. Such upscaling does not use one global scaling factor but a time-resolved one, as shown in Figures B.4, B.5 and B.6. Although some noise is superimposed on the temporal evolution of scaling factors, a seasonal cycle becomes apparent.

In a first step, CAMS model data are adjusted to match the value for COCCON. Then, the adjusted model fields are compared with the available satellite results data for XCO_2, XCH_4 and XCO. The assumption of this method is that the bias of the model field is a smooth function in space and time, which seems well justified due to the long atmospheric lifetime of the gases under consideration. Since the model considers all relevant aspects of dynamics (advection, changes in tropopause altitude) and attempts to even reproduce abundance changes due to sources and sinks, we expect that our approach is superior to ad hoc schemes typically used for enlarging the co-location area (e.g. using the potential temperature; see Keppel-Aleks, Wennberg, and Schneider (2011)). In order to avoid circular reasoning in the validation based on the adjusted model fields, the method should avoid model simulations which include the assimilation of satellite data.

9.7.1 *Generation of the CAMS fields adjusted to COCCON observations*

CAMS inversion results with surface air-sampled observations as input have been used for XCO_2 and XCH_4 (Segers, 2020a). Unfortunately, no XCO data are available on that model run. No XCO product from CAMS limits us from comparing one of the main data products of S5-P (XCO), which offers a greater number of measurements with a high horizontal resolution in comparison to any other satellite. Instead, the CAMS team has provided special profiles of CO from CAMS reanalysis data (control run). On that run, two important points have to be mentioned: (1) no total columns for CO_2 and CH_4 were available from this special dataset, and (2) no satellite data have been assimilated. Such results are available on a daily basis as described in Table 9.7. CAMS inversion is available on a daily basis for XCO_2 and XCH_4 but with different time frames. Unfortunately, there are no XCH_4 results from CAMS for 2020, which adds a new constraint when simply comparing both results, especially for Yekaterinburg where approximately 4 out of 6 months were measured in 2020.

As explained before, the main idea is to adjust XCO_2, XCH_4 and XCO from CAMS by using COCCON results. This is achieved by performing a time-resolved scaling of the model data, which is informed by the available ground-based observations. The detailed workflow encompasses the following steps, which are represented in Figure 9.21.

Species	Method	Measurement availability	Time frame (UTC)
XCO_2	CAMS inversion	1 January 1979 to 31 December 2020	00:00–21:00; each 3 h
	COCCON: Peterhof	21 January 2019 to 17 March 2020	∼ 09:00–13:00
	COCCON: Yekaterinburg	5 October 2019 to 17 April 2020	∼ 06:00–09:00
XCH_4	CAMS inversion	1 January 1990 to 31 December 2019	00:00–18:00; each 6 h
	COCCON: Peterhof	21 January 2019 to 17 March 2020	∼ 09:00–13:00
	COCCON: Yekaterinburg	5 October 2019 to 17 April 2020	∼ 06:00–09:00
XCO	CAMS reanalysis (control run)	1 January 2003 to 31 December 2020	00:00–21:00; each 3 h
	COCCON: Peterhof	21 January 2019 to 17 March 2020	∼ 09:00–13:00
	COCCON: Yekaterinburg	5 October 2019 to 17 April 2020	∼ 06:00–09:00

Table 9.7: Time range and usual daily time frame of the analysed results from CAMS and COCCON.

1. As shown in Table 9.7, CAMS XCO_2 and XCH_4 are available on a daily basis in different prescribed time frames, while COCCON results are only available when specific conditions were fulfilled: good weather conditions (sunny or almost sunny conditions), no mobile campaign or manpower available to start the measurements, because the instruments were manually operated. These conditions made the measurements rather sparse, but nevertheless there still is a significant number of measurements available. Therefore, the first step is to find the coincident days between CAMS and COCCON and then the COCCON results are averaged around each CAMS time if available. As the COCCON observations require sunlight, all CAMS points before 06:00 UTC and later than 18:00 UTC were filtered out. For the aforementioned, each averaged CAMS time was considered reference, and all the COCCON results ±2 h were averaged as the coincident data. After these steps, we have both results on the same time gridding.

2. The outputs from the first step are time series with coincident measurement days and time frames. These time series, which have the same date boundaries, are then divided into n smaller intervals or sub-windows. These sub-windows have the characteristics of being non-overlapping, and they form equally sized bins on the time axis, as defined in the Equation 9.8, where "DT" stands for "Date–Time", which goes from the first to the last point of the measurement period. The user only needs to define the number of sub-windows n.

$$\Delta t = \frac{DT_{initial} - DT_{final}}{n} \tag{9.8}$$

3. Additionally, a sliding sub-window, with the same size described in step 2, is run over both time series with the main difference being shifted by half of the size of the initial sub-window but still being not overlapping between them. Therefore, after step 2, step 3 is done in order to look at the neighbours.

4. In each of these sub-windows (described above, steps 2 and 3), a correlation analysis is carried out independently of the other sub-windows. In order to make the COCCON time series adjust better to CAMS results, a linear correlation with the intercept forced to zero is carried out; therefore, the slope gives the scaling factor for the CAMS data.

5. Each sub-window defined in step 2 is taken as a base with its slope calculated in step 4. After that, the slopes in the neighbourhood are also calculated in each overlapping sub-window defined in step 3, Finally, all the slopes are then averaged. Such averaged slope represents the scaling factor in that sub-window. It is important to mention that this number of sub-windows (and then its size) was adjusted until good results were achieved as described below.

6. Finally, with the scaling factor calculated in step 5, the original CAMS fields keeping their original temporal sampling are scaled in the whole range of each sub-window.

9.7.2 *Selection criteria for the best number of windows*

In order to choose the best number of windows, the scaling code is run starting from windows = 1 and stops when two different conditions are fulfilled:

1. The root-mean-square deviation (RMSD), which is calculated with the Equation 9.9, where k stands for the number of points considered during the scaling in each sub-window, between COCCON and the CAMS-COCCON data, must be the lowest possible.

$$\text{RMSD} = \sqrt{\frac{\sum_1^k \left(\text{CAMS}_{\text{Scaled}} - \text{COCCON}\right)^2}{k}} \qquad (9.9)$$

2. The number of measurement points in each of the windows must be larger than four.

The second condition is very important, because if the number of windows increases, the window size (number of measurement points) decreases until no more points are available in some windows as the distribution of measurement points in the time domain is non-homogeneous.

9.7.3 *Verification of the method*

In order to test the method before it is applied to the study area, a much denser dataset in COCCON is used to prove its performance. Two years of measurements (January 2018–December 2020) taken in Karlsruhe with the instrument FTS#37, which is the reference in
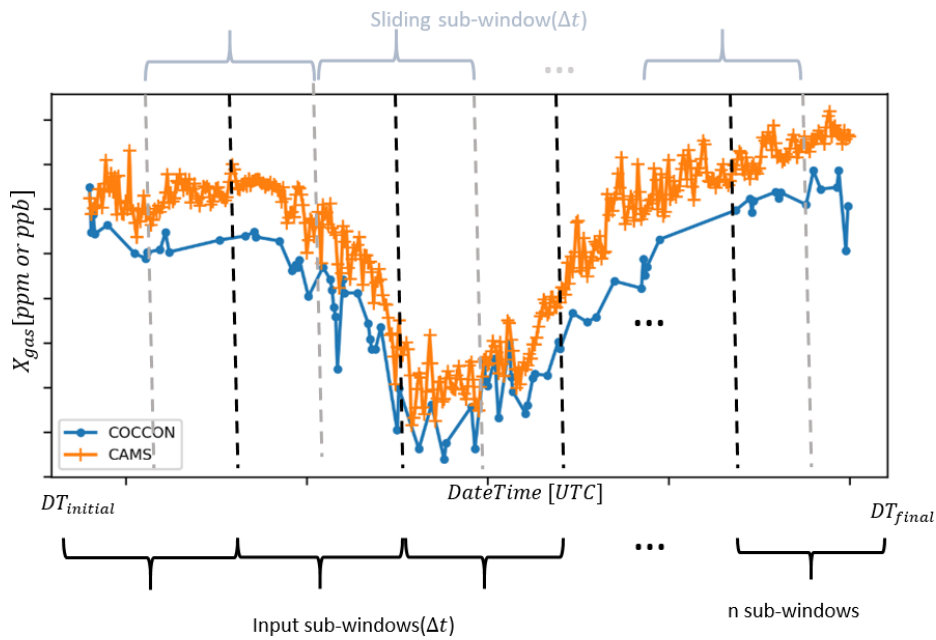
Figure 9.21: Principle of the scaling method. Sub-windows are separated with black dotted lines and sliding sub-windows with grey dotted lines. The window size (Δt) is defined in Equation 9.8).

COCCON, were selected for this purpose. For the sensitivity study, three different subsets were generated from the original dataset. Such subsets consist of a percentage (40 %, 60 % and 80 %) of the total amount of measurement days, which are randomly selected. This is done in order to simulate the reduced number of observations available in the study area. The GHG used for this short sensitivity study is XCH_4, because a comparison between each of the scaling results (for each dataset) can be compared with TROPOMI as well. The main results of this verification exercise are presented in Figures B.7 to B.9. In Figure B.7, a plot showing RMSD as a function of the number of windows is presented for each subset. Such results are used in order to decide the best number of windows. The correlations between CAMS and the original COCCON XCH_4 measurements are presented in Figure B.8a, whereas Figure B.8b, c and d show the results between COCCON XCH_4 and its CAMS-COCCON for 40 %, 60 % and 80 % of the original COCCON data, respectively. The satellite comparisons of the original COCCON XCH_4 with TROPOMI are shown in Figure B.9a, whilst Figure B.9b, c and d show the TROPOMI XCH_4 comparison but for CAMS-COCCON by using 40 %, 60 % and 80 % of the original COCCON measurement days. The most important conclusion can be drawn from Figures B.9 and B.4. Figure B.9 indicates a small bias between CAMS and COCCON (of about 0.12 %), which is successfully removed in the CAMS-COCCON fields, so the latter data approximate the missing observational value in an optimal sense. Figure B.4 shows the scaling factor as a function of time, clarifying that the correction is not just the trivial removal of a constant bias factor but that some seasonal variation in the model – observation difference can be corrected as well. Note that we do not require in our approach that the COCCON values are superior over the CAMS values. This test is performed to clarify that the CAMS fields adjusted in

the manner we described before provide the best prediction for what COCCON would have observed on a certain date.

9.8 COMBINED DATA RESULTS BY USING THE SCALING METHOD

In order to generate the CAMS-COCCON product, we reprocessed the COCCON observations with the CAMS-Xgas a priori data.

The scaling method described above is applied to XCO_2, XCH_4 and XCO at Peterhof and Yekaterinburg. The numbers of selected windows for XCO_2, XCH_4, and XCO were 11, 10, and 11 at Peterhof and 5, 2, and 4 at Yekaterinburg, respectively. These scaled results are then compared with all the available satellite products as described in this study.

In order to correctly compare each of the satellite products to the CAMS-COCCON ones, the a priori profiles of the satellite retrievals were adjusted (replacing the original a priori profile by CAMS profiles) using the method previously described..

9.8.1 *Peterhof*

After using the scaling method, the COCCON-adjusted CAMS data show close agreement with COCCON for XCO_2, XCH_4 and XCO (see Figure B.10 and Table B.1). From Table B.1, it can be observed that the bias and the standard deviation between scaled CAMS and COCCON is significantly smaller than the CAMS variability of the original dataset. This further demonstrates the "close agreement" between adjusted model and observation.

The CAMS-COCCON data fill the gap during the measurements, providing a continuous period of a new intermediate or combined (CAMS-COCCON) data product, which helps to have more coincident data with satellite observations. Figures 9.22 to 9.24 show the CAMS-COCCON data in comparison to the available observations from different satellite products. There are more coincident data points for the operational OCO-2 product than OCO-2 FOCAL XCO_2, which could be because the OCO-2 product has approximately 3 times more soundings (https://climate.esa.int/sites/default/files/ATBDv1_OCO2_FOCAL.pdf, last access: 9 September 2022). However, their correlations and patterns are quite similar, whereas OCO-2 FOCAL shows better agreement with CAMS-COCCON data. GOSAT XCO_2 has a similar correlation with CAMS-COCCON as found for OCO-2 data but with some outliers. For XCH_4, the CAMS-COCCON data are mostly higher than TROPOMI but lower than GOSAT, and this shows a good agreement with GOSAT with $R^2 \sim 0.7$, contrary to TROPOMI where $R^2 \sim 0.12$. The CAMS-COCCON XCO agrees well with TROPOMI data with an $R^2 \sim 0.7$.

9.8.2 *Yekaterinburg*

The scaled data are much more important in Yekaterinburg, because in this city there are just a few coincident measurement days between the COCCON spectrometer and satellite results, mainly because of the season of the measurements taken in winter and spring. That makes a real challenge in finding the best number of sub-windows to better adjust COCCON to CAMS results, which is rather small (between 2 and 3). Neverthe-
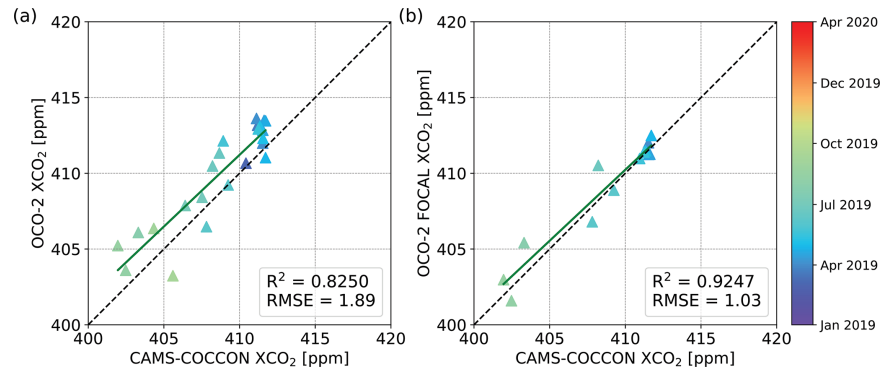
Figure 9.22: Correlation plots of **(a)** OCO-2 and **(b)** OCO-2 FOCAL with respect to CAMS-COCCON XCO_2 at Peterhof. All satellite data were adjusted for the CAMS a priori profile.
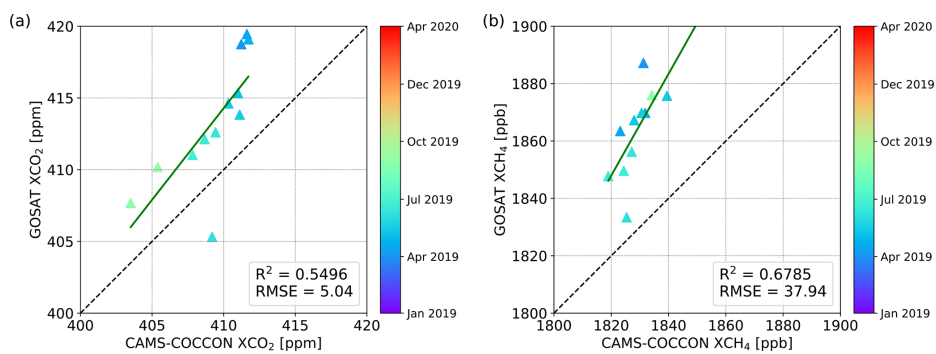
Figure 9.23: Correlation plots of **(a)** GOSAT XCO_2 and **(b)** GOSAT XCH_4 with respect to CAMS-COCCON at Peterhof. All satellite data were adjusted for the CAMS a priori profile.
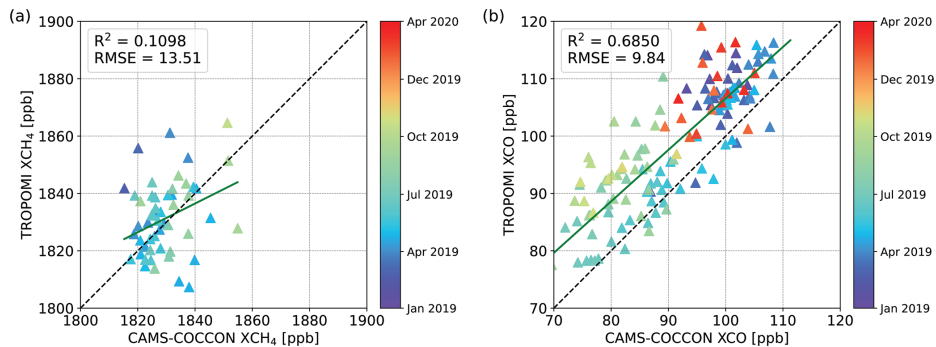
Figure 9.24: Correlation plots of **(a)** TROPOMI XCH_4 and **(b)** TROPOMI XCO with respect to CAMS-COCCON at Peterhof. All satellite data were adjusted for the CAMS a priori profile.

less, as can be seen in Figure B.11 and Table B.1, the CAMS-COCCON data agree better with the coincident COCCON observations, which indicates that the scaling improves the compatibility of CAMS data with COCCON, although the number of sampling points is extremely small.

The correlations between CAMS-COCCON and the OCO-2 and TROPOMI data are presented in Figure 9.25. There are not too many coincident data points than those at

Peterhof due to the lesser COCCON and satellite observations and mostly poor weather condition in winter. The COCCON measurement ended on 17 April 2020. Here we use a larger radius (100 km) to collect TROPOMI data for coincident COCCON observations.
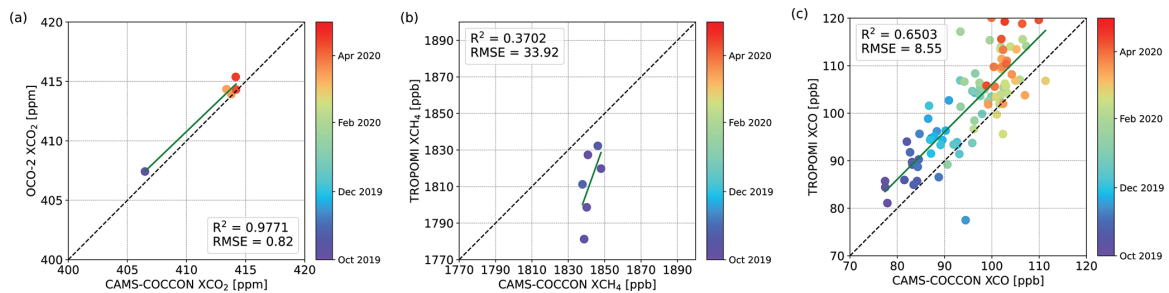
Figure 9.25: Correlation plots of **(a)** XCO_2 between OCO-2 and CAMS-COCCON, **(b)** XCH_4 between TROPOMI and CAMS-COCCON, and **(c)** XCO between TROPOMI and CAMS-COCCON observations at Yekaterinburg. All satellite data were adjusted for the CAMS a priori profile.

The averaged biases between satellite products with respect to CAMS-COCCON are presented in Figure 9.26. Table 9.8 summarizes selected biases and standard deviations of satellite products compared to COCCON and CAMS-COCCON data. Here, only when the coincident data between satellite observations and COCCON and CAMS-COCCON are both available (at least at one site) are they shown. For XCO_2, the biases decrease slightly when OCO-2 is compared with COCCON and to CAMS-COCCON. The absolute bias between TROPOMI XCH_4 and CAMS-COCCON increased mostly twice at both sites in comparison to the direct TROPOMI XCH_4 to COCCON comparison. The increased low bias at Peterhof is mainly driven by the TROPOMI outliers in April (Figure 9.14b). The increased low bias at Yekaterinburg is due to the fact that the CAMS-COCCON data are only available up to the end of 2019, and all TROPOMI data in autumn 2019 are biased low (Figure 9.15b). For XCO, the bias increased slightly at Peterhof and decreased by nearly half at Yekaterinburg when using CAMS-COCCON as the reference instead of COCCON at both sites.
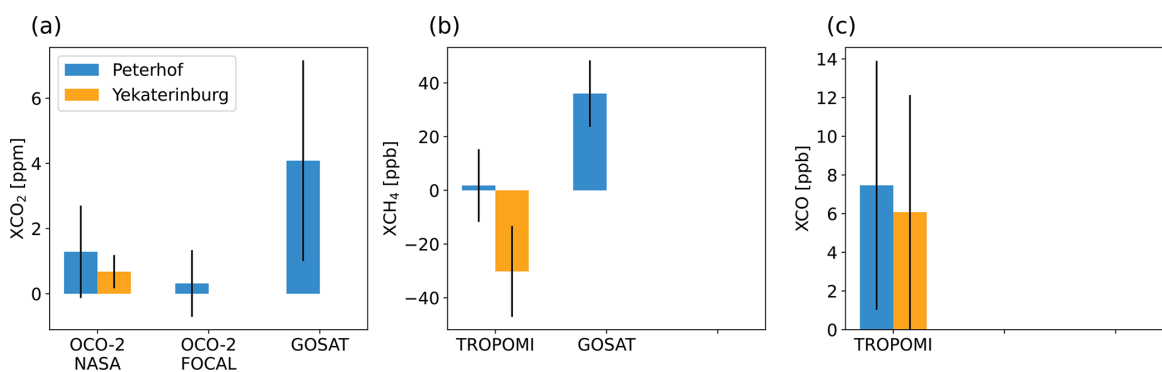
Figure 9.26: Bar plots of the averaged bias derived from different products with respect to CAMS-COCCON for **(a)** XCO_2, **(b)** XCH_4 and **(c)** XCO at Peterhof and Yekaterinburg. The error bars represent the standard deviation of the bias.

		OCO-2 XCO$_2$ (ppm)	TROPOMI XCH$_4$ (ppb)*	TROPOMI XCO (ppb)
Peterhof	COCCON	1.47 ± 0.88 (15)	20.97 ± 13.76 (39)	5.96 ± 6.10 (73)
	CAMS-COCCON	1.29 ± 1.42 (23)	1.80 ± 13.52 (53)	7.46 ± 6.43 (137)
Yekaterinburg	COCCON	$-$ (1)	3.91 ± 22.62 (7)	6.89 ± 3.85 (17)
	CAMS-COCCON	0.68 ± 0.51 (5)	-30.02 ± 16.93 (6)	6.08 ± 6.05 (91)

Table 9.8: Selected averaged bias and standard deviation between satellite products and COCCON and between satellite products and CAMS-COCCON at Peterhof and Yekaterinburg. The number of coincident results is shown in parentheses.

* No CAMS XCH$_4$ in 2020.

9.8.3 *Gradients between Peterhof and Yekaterinburg*

For the comparison shown in this section, the COCCON-CAMS product by using CAMS-Xgas a priori data have been used. This choice removes the comparisons for XCH$_4$ in 2020 for both cities, because no XCH$_4$ from CAMS is available by now.

The gradients (ΔXgas) are the difference of each product between the two sites during the same time period. The gradients between Peterhof and Yekaterinburg (Peterhof–Yekaterinburg) are presented in Figure 9.27. The measuring time of COCCON at Yekaterinburg is less than that at Peterhof. We therefore use monthly means at each site to compute the gradients. A collecting circle with a radius of 100 km is used for TROPOMI at both sites. The coincident measurement days at both sites start from October 2019 until April 2020.
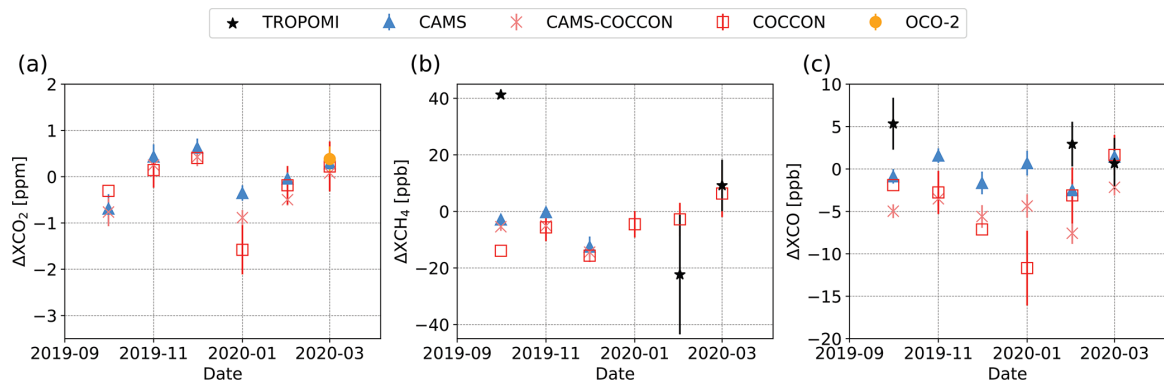
Figure 9.27: Monthly mean of gradients for different gases (ΔXgas) between Peterhof and Yekaterinburg (Peterhof–Yekaterinburg) for different products. The error bars are calculated based on the standard deviation at two sites.

For XCO$_2$, the gradients between COCCON at both sites are mostly negative and lower than those of CAMS and CAMS-COCCON datasets. Higher absolute gradients are observed in the early part of the year for COCCON. In November and December both CAMS and CAMS-COCCON ΔXCO$_2$ show positive values, whereas COCCON has negative val-

ues. This discrepancy might be due to the limited number of COCCON observations during winter in Yekaterinburg (only 12 d of measurements from November to Mach were available). The gradients of different datasets generally fit well for XCH_4, except that of TROPOMI in October due to the low number of observations in winter. COCCON ΔXCO shows highest absolute value in January, when the CAMS value is near to zero. The large variations in ΔXCO are in reasonable agreement with the COCCON gradients.

9.9 ST PETERSBURG CITY EMISSION TRANSPORT EVENT TRACKED BY TROPOMI

In this section we show how a satellite with a high temporal and spatial resolution can measure and track a large transport of pollutants in a megacity like St Petersburg. During the EMME campaign, we have been lucky to have the overpass of the TROPOMI satellite during one of the days with strong transport gradient as presented in section 9.2. Such results are presented in Figure 9.28, which illustrates the XCH_4 and XCO observations on a sample day on 25 April 2019 when the wind flowed from northeast to east before noon. The coincident TROPOMI data are the mean value collected within a circle of 15 km radius. The downwind COCCON instrument FTS#84 measured significant enhancements of XCH_4 and XCO around 09:00 UTC. The higher XCH_4 measured by FTS#84 than that by FTS#80 is later observed by TROPOMI as well at 10:40 UTC, though the absolute values are lower in TROPOMI than the corresponding COCCON observations. When comparing the observations with COCCON and TROPOMI at the two locations where the spectrometers were set up on that day, the measured differences are about 10.6 ppb and 9.4 ppb for COCCON and TROPOMI, respectively (Figure 9.28e – bottom panel). For XCO, TROPOMI observes higher values than COCCON. The difference between the two locations at 10:40 UTC is 9.5 ppb for COCCON and 12.5 ppb for TROPOMI. The increase in XCO at the FTS#80 location measured by COCCON can also be detected by TROPOMI, as it increased from 107.0 to 115.7 ppb.

When comparing the observations with COCCON and TROPOMI in each of two places where the spectrometers were setup on that day, at the TROPOMI overpassing time 10:40 UTC, the measured difference (delta) is 10.6 ppb and 9.5ppb for COCCON and TROPOMI respectively.

Figure 9.28: Time series of COCCON and coincident TROPOMI observations for XCH_4 **(a)** and XCO **(b)**; spatial distribution of XCH_4 **(c)** and XCO **(d)** on a 0.1×0.1 latitude $\times$ longitude grid together with the ERA5 wind at 12:00 UTC; **(e)** bar plot for XCH_4 and XCO gradients by COCCON and TROPOMI on 25 April 2019.
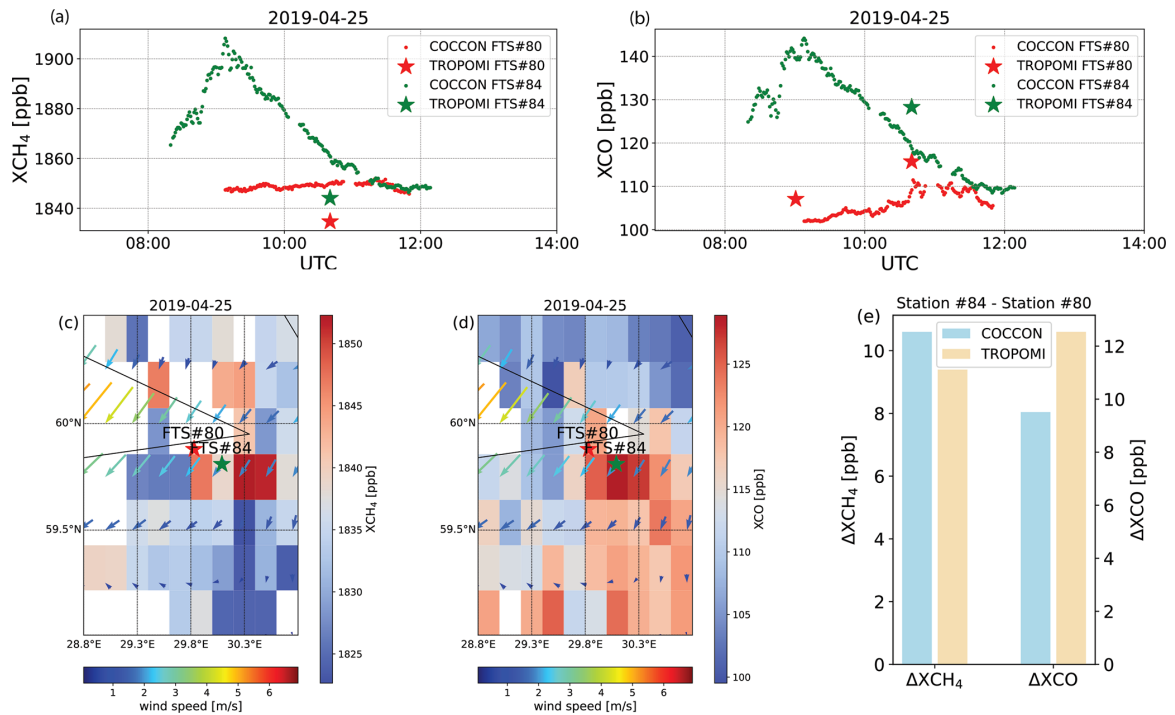
TEMPORAL VARIATIONS OF PROXY/FFCO$_2$ RATIOS

This Chapter presents the most important results obtained using two ground-based atmospheric remote sensing techniques within the framework of the European project VERIFY in the "key-study" region located in the Rhine valley in South-Western Germany (Karlsruhe). This area was selected because it comprises a mixture of different emission sources, and agricultural and small forestal areas surround it. This complex structure can be regarded as an exemplary test case for European urban agglomerations.

The quantification and continuous monitoring of anthropogenic emissions from fossil fuel combustion (ffCO$_2$) from urban to a global scale represent a big challenge for the scientific community in the context of the Paris Agreement.

Measurements of atmospheric CO$_2$ concentrations alone do not allow to separated their biogenic and anthropogenic components or, for the aim of this thesis, in their fossil and non-fossil elements. Therefore, co-emitted species are required in order to quantify the ffCO$_2$ share. The remote sensing approach used in this thesis has no direct handle on ffCO$_2$ mainly because the variations in the CO$_2$ isotopologues are either very small (^{13}C/^{12}C) or too rare (^{14}C) to be detectable by remote sensing techniques. Therefore, the observed short-term variability of the column-averaged mixing ratios of NO$_2$, CO, and CO$_2$ was used to separate signals from local sources. These signals are superimposed to the smoothly varying advected background abundances of the gases. The investigation of the short-term variability supports the determination of empirical correlations between the proxies and CO$_2$.

In order to retrieve the total column of the GHGs (XCO$_2$, XCO, and XCH$_4$) and the trace gas NO$_2$ concentrations, two different techniques and instruments have been used, as described in previous chapters.

The NO$_2$ VCDs retrieved with MAX-DOAS observations are used as proxies for detecting anthropogenic CO$_2$ emissions, together with the total column CO, derived from the TCCON observations at the KIT station. Both observations sites are located at KIT Campus North (CN), see Figure 10.1. The complete approach presented in this chapter requires the total column of CO$_2$, which, similarly to CO is taken from the operationally TCCON product of the Karlsruhe station.

10.1 MEASUREMENT SITE: KEY STUDY LOCATION DESCRIPTION

KIT CN was selected as an essential part of the "study region" in the framework of the European project VERIFY, mainly due to two crucial reasons:

- The measurement site is located in an area surrounded by a complex mixture of CO$_2$ sources and sinks, which is typical for a densely populated area. Furthermore, a heavily industrialized region is located between 6 km to 16 km to the south-west of the KIT tower, including a refinery with 15.5 $Mt\ yr^{-1}$ crude oil processing capacity, a 365 MW gas-fired power plant, and a 1450 MW hard-coal-fired power plant (Hage-

mann et al., 2014). Furthermore, ~ 40 km north (in Mannheim) of KIT CN is located a 2147 MW coal-fired power plant (More details can be found in `https://www.enbw.com/company/the-group/energy-production/fossil-fuel/locations.html`, last access: September 28, 2022.); the emission plume of this power plant can be observed from the tower, as shown at the top of Figure 10.1. The KIT CN is located in the Upper Rhine Valley, 30 to 40 km wide, bordered to the west and east by the Odenwald and the Pfälzer forest. Due to its orography, the Rhine Valley guides the wind from SW or NE prevailing directions, see Figure 10.1.
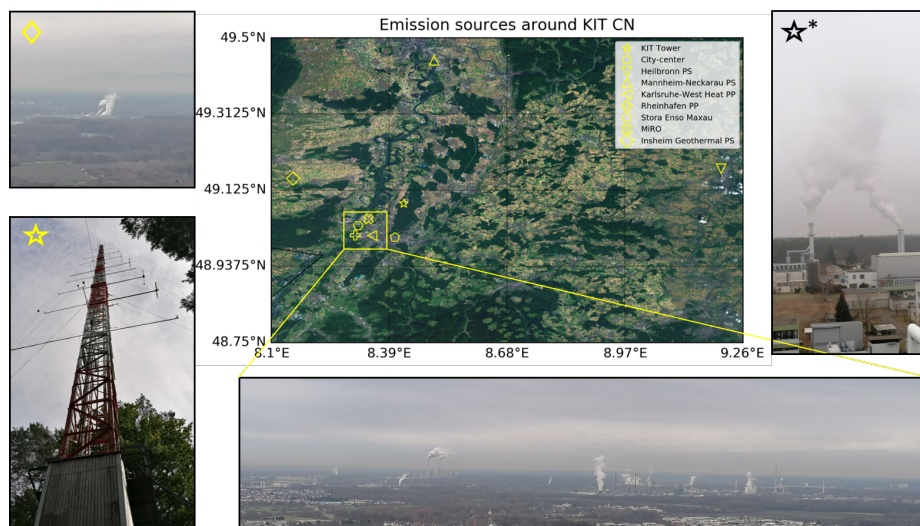
Figure 10.1: Illustration describing the KIT CN location and, most important anthropogenic CO_2 emission sources in the surrounding area. A map with the punctual sources, KIT CN location, and Karlsruhe's city center are highlighted in the middle of the illustration. In the upper left and bottom part of the illustration, pictures of the punctual sources in Karlsruhe's industrial area, observed from the 200-m tall tower, are shown. Furthermore, on the right side of the illustration, a picture of the emission plume coming from the power and heating plant operated at KIT CN as observed from the rooftop of the IMK building towards SE direction (see Figure 10.4), is shown.

- The second one is related to the amount of collocated in-situ and remote sensing atmospheric measurements carried out there, including TCCON, Integrated Carbon Observation System (ICOS), AErosol RObotic NETwork (AERONET), and German Weather Service (DWD) stations.

The ICOS measurements are performed on a 200-m tall tower (see Section 10.7.1) located on the south-western corner of the KIT CN, a prominent former nuclear research facility established 12 km north of the Karlsruhe city center in a forested area (see Figure 10.1). KIT CN ($\sim 4\ 000$ employees) is causing local fossil CO_2 emissions and occasional emissions of $^{14}CO_2$ from radioactive incineration waste (BMU, 2019). Furthermore, the electricity and warm water are generated internally by a 30 MW natural-gas fired power plant and a heating plant that fires natural gas and heating oil, respectively (`https://www.fm.kit.edu/112.php`, last access: September 28, 2022.). In the right side of

the Figure 10.1 the emissions caused by these plants can be observed during a normal day in winter.

10.2   TNO HIGH-RESOLUTION INVENTORY FOR KIT-SURROUNDING AREA

Figure 10.2 gives a general idea about the primary point sources of anthropogenic emissions in the surrounding of KIT CN. However, to better understand how CO_2, CO and NOx emissions are spatially distributed, TNO high-resolution inventory data (Gon et al., 2017; Kuenen et al., 2022) for the year 2020 has been taken and illustrated in Figures 10.2 a, b, and c, respectively.

The TNO inventory distinguishes and reports both punctual and areal emission sources. In Figures 10.2 a), b), and c), all emission categories have been summed up on the 1x1 km resolution grid to get the total emission in the shown area for ffCO$_2$, CO, and NOx. ffCO$_2$ peaks in Karlsruhe urban, and industrialized area, and on the path followed by the A5 highway, which is well known for having a massive traffic flow. Punctual sources of ffCO$_2$ and NOx also coincide. Furthermore, KIT CN is surrounded by a rich agricultural and forested area, which implies additional biogenic sources and sinks of CO_2 (Hagemann et al., 2014).

In summary, KIT CN is located in an unique area where emissions coming from industrial, urban, agricultural, and forest sectors can be measured.
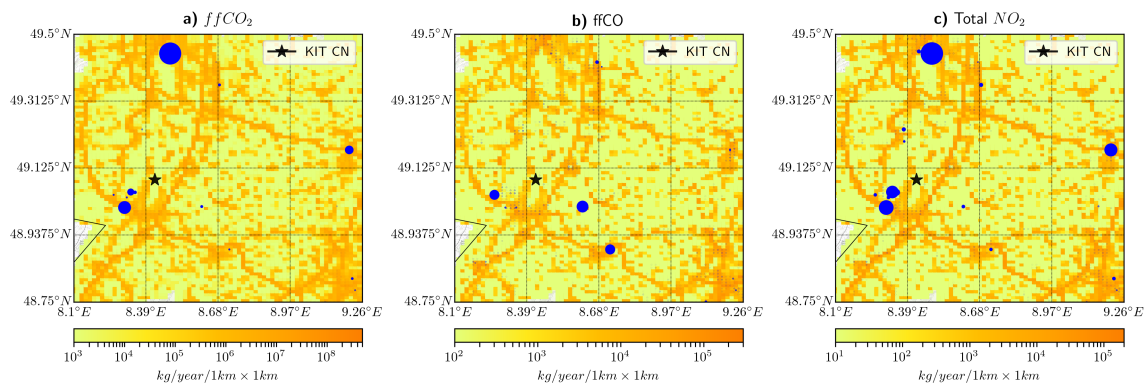
Figure 10.2: Maps showing the area distribution of the annual emission of a) ffCO$_2$,b) CO , and c) NOx in kg per year per grid cell. The blue dots represent annual point source emissions of single facilities, for example, power plants or refineries. The data was taken from the high-resolution TNO emission inventory for 2020.

10.3   FTIR AND MAX-DOAS OBSERVATIONS OF XCO$_2$, XCO, AND NO$_2$

Because there is no direct handle on ffCO$_2$ from remote sensing observations, the measured variability of the column-averaged trace gas abundances is used for achieving an approximative separation between nearby, strong, and localized fossil fuel emissions and other kinds of signals. The underlying rationale is that the variability on short intra-day

time scales of XCO$_2$ is assumed to be dominated by local and regional sources. Therefore, short-term variations in XCO$_2$ can be considered as an approximation for ffXCO$_2$.

The NO$_2$ vertical column amounts derived from the MAX-DOAS observations and the XCO$_2$ and XCO total column amounts from TCCON observations, respectively, are required for the approach presented in this thesis, for assessing Δproxy/ΔXCO$_2$ ratios. Therefore, this section briefly discusses the most critical information about the remote sensing measurements carried out, processing, and results.

10.3.1 TCCON station

As previously mentioned in Chapter 8 the TCCON station located at KIT CN has been operational since 2014; here, the results of the high-resolution observations for XCO$_2$ and XCO are used in Section 10.5 for the proxy/ffCO$_2$ analysis. In Figure 8.19, the long time series of XCO$_2$, XCH$_4$, XCO, XH$_2$O and XAir are presented. The minimal variability of the XAir time series (in the bottom panel) confirms the high instrumental stability; therefore, using TCCON retrieved results in this study guarantees reliable and high-quality scientific results. Figure 10.3 shows the available time series for XCO$_2$ and XCO for Karlsruhe TCCON station located at KIT CN, see Figure 10.4. These results are taken for the approach developed and implemented in this thesis.
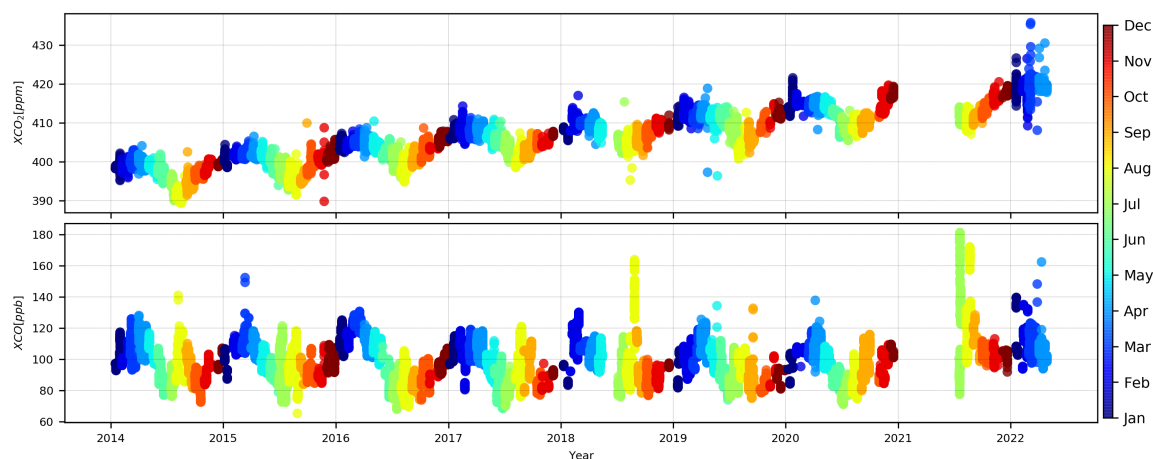
Figure 10.3: TCCON results for XCO$_2$ and XCO during the years 2014 to 2022 for Karlsruhe.

10.3.2 MAX-DOAS retrieval of aerosol and trace gases in the troposphere

As described in Chapters 5 and 6.6, three crucial steps must be followed to get the NO$_2$ gas abundances in the atmosphere, given a set of MAX-DOAS observations. Here, the application of these individual procedures for the final retrieval of NO$_2$ VCD and vertical profiles are summarized, and the intermediate products are also presented.

10.3.3 *Location and viewing geometry*

Figure 10.4 shows that the 2D SkySpect MAX-DOAS instrument was set up at the top of the 200 m tall tower operated by IMK-TRO institute. Because this instrument is capable of measuring at different azimuth angle directions, the instrument was programmed to take measurements at 0° (North), 60°, 120°, 180°, and 240°, as shown by the arrows in Figure 10.4. In each of these azimuth directions, the instruments recorded scattered sunlight at different elevation angles: 1°,2°,3°,5°,10°,20°,40°, and 90° (reference), translating to have a full elevation scan in   10 minutes, and therefore   1 set of azimuth scans per hour. The main idea of the selected measurement sequence was to retrieve NO_2 abundances in all the surrounding areas for later being used as a proxy to try to detect $ffCO_2$.

Figure 10.4: The map shows the locations of the TCCON station and MAX-DOAS instrument within the KIT CN map. The MAX-DOAS instrument is located at the top of the 200-m tall tower from IMK-TRO (https://www.imk-tro.kit.edu/english/7791.php, last access: 02 October 2022.), the arrows represent the different azimuth angle directions used for collecting measurements. A heating and power plant operated by KIT are also shown on the map.

10.3.3.1 *dSCD measured by MAX-DOAS*

The primary processing starting from the raw MAX-DOAS observations data is the DOAS analysis, which is later used for the aerosol and trace gas vertical profile algorithms. Having this retrieval properly tuned is a mandatory prerequisite to achieving reliable results. The DOAS settings used for the retrieval of the NO_2 dSCD are described in C.1 and a fitting example results of the performed retrieval is shown in C.2.

Because the instrument is operated continuously, and sunny conditions are imperative for reliable results, a cloud classification algorithm based on Wagner et al. (2014) was implemented and helped filter out bad data. The algorithm calculates the CI (radiance ratio

between two selected wavelengths) for each elevation angle. In this thesis, the irradiances were taken directly from the corrected measured spectrum at 320 nm and 440 nm.

An example of the NO₂, HCHO, and O₄ dSCDs and the calculated CI at 90° daily behaviors are shown in Figure 10.5 for four typical days: 04, 05, 06, and 07 July 2019.

Based on the CI daily time series observed in Figure 10.5, it can be concluded that 04 July was a completely sunny day, while 07 July was a completely cloudy day. 05 and 06 July presented broken clouds episodes. These findings are confirmed, but the diurnal variations of the dSCDs at different angles, in the presence of sunny conditions, show a smooth behavior, and they are well separated, especially for lower elevation angles (Heckel et al., 2005).
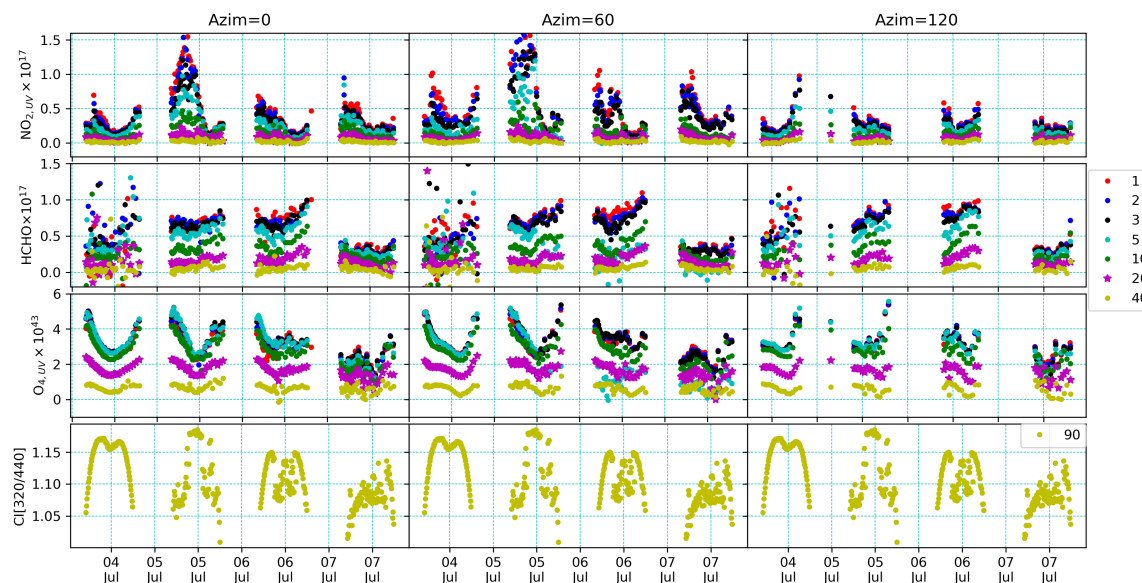
Figure 10.5: NO₂, HCHO and O₄ dSCDs and Color Index (CI) for 04,05, 06 and 07, July 2019. The daily behavior of the dSCD for each specie is shown at different elevation angles and for three different azimuth angle directions. Additionally, the CI calculated at 90° for the wavelength ratio 320/440 is shown in the bottom panel. The units for the dSCD for NO₂ and HCHO are $molec/cm^2$, while for O₄, $molec/cm^5$.

10.3.3.2 *Aerosol and trace gas retrieval profile results*

The aerosol vertical profile retrieval is performed using the dSCDs obtained by the DOAS analysis and the inputs described in Table C.3. Once the aerosol extinction profiles are retrieved, the trace gas vertical profile is determined, both by using HEIPRO, as explained in Chapter 6.6.

Figure 10.6 shows the vertical profiles of NO₂, HCHO, and aerosols retrieved from the MAX-DOAS instrument observations of the instrument located at the tower at 60° azimuth viewing direction, from 23 to 26 February 2021. The aerosol backscatter coefficients measured with a CHM15k ceilometer located at the Rheinstatten[1] station are shown in the bottom panel of the figure. The ceilometer data used was provided by DWD.

---

1 The ceilometer located at Rheinstetten station is part of the DWD ceilometer network across Germany (http://www.dwd.de/ceilomap, last access: 04 October 2022).

The days shown in Figure 10.6 are of unique particularity because, on these days, a huge Saharan transport event crossed the region where the instrument is installed. These days were mainly sunny, which favors remote sensing measurements, except on 26 February, which was mostly cloudy. Millions of tons of dust were transported from the Sahara and crossed Europe (Francis et al., 2022; Hoshyaripour, 2021). This Figure represents one of the essential capabilities of the MAX-DOAS instruments to catch aerosol layers of particles in the atmosphere. This result is significant because accurate aerosol retrieved profiles are a prerequisite for accurate trace gas abundance calculations. It can be observed from the aerosol backscatter coefficients and aerosol extinction profiles that a high dust plume appeared on 23 February and reached ~ 2 km high between 24 and 25 February. These days, NO₂ and HCHO vertical profiles are not representative because the dust particles mainly backscatter the sunlight.
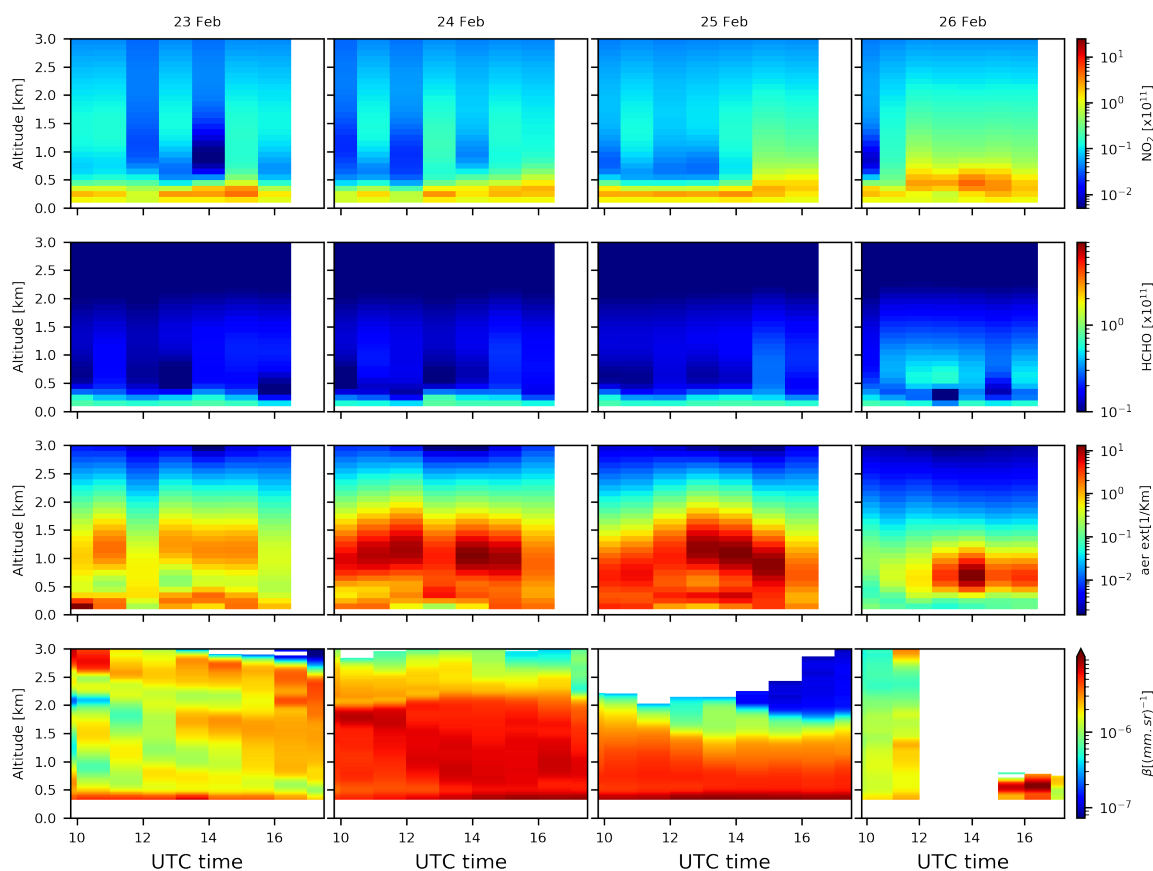

Figure 10.6: NO₂, HCHO and aerosol extinction profiles retrieved at 60° azimuth angle derived from MAX-DOAS observations are shown top-down in the plot; in the lowermost plot, the aerosol backscatter coefficients retrieved with Ceilometer are also shown from 23 to 26 February 2021.

10.3.4 *NO₂ near-ground concentration time series*

Figure 10.7 shows the daily averaged near-ground concentration of NO_2 for the whole available period, which is called "near-ground" because it represents the concentration in the lowermost layer used for the retrieval, i.e., in the first 100 m AGL[2]. A seasonal cycle can be observed in the figure, having its maximum in winter, which can be related to the amount of sunlight and the photolysis of NO_2, and the stability of the boundary layer (BL).

Finally, the NO_2 vertically integrated concentration, previously defined as VCD, is one of the proxies used in this thesis, together with the XCO_2 and XCO from the TCCON observations.
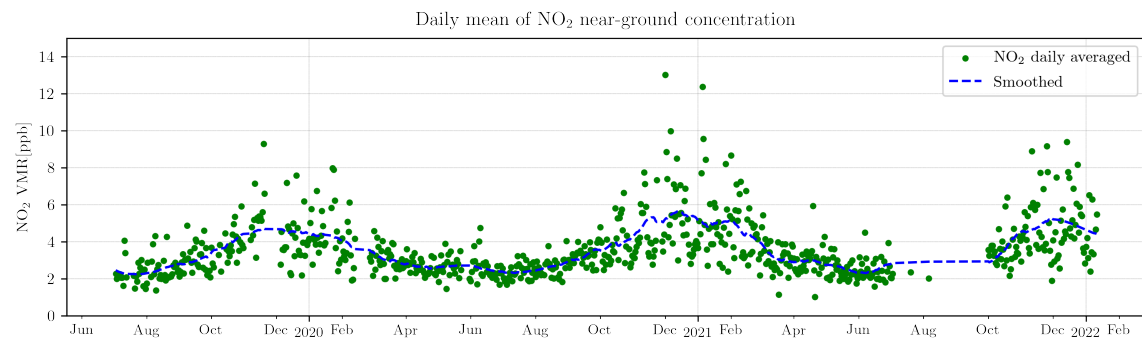
Figure 10.7: Daily averaged NO_2 near-ground concentration retrieved at 60° azimuth angle from July 2019 to January 2022.

10.4 DATA AVAILABILITY

As shown in Figure 10.8, one of the main limitations of the results presented in this thesis is the data availability of the required species in both remote sensing and in-situ observations. Comparisons between in-situ and remote sensing are constrained to Iterative CAvity enhanced DOAS (ICAD)(Horbanski et al., 2019) NO_2 data available only between April 2019 and August 2020, with a gap between mid of January to the end of March 2020. Additionally, MAX-DOAS is only available from July 2019 onward; therefore, the only available range for comparisons is July 2019 to August 2020.

From the remote sensing point of view, TCCON has a long observation time series, while MAX-DOAS was only installed in July 2019. Although there is an observation gap of several months due to TCCON instrumental failure in 2021, the period for the proxy/ΔCO_2 comparisons is around two years.

10.5 DERIVATION OF PROXY/FFCO₂ RATIOS

In order to effectively separate the short-term fluctuations for both total column signals from longer-term variations, two different methods have been applied for XCO and XCO_2

---

2 As described in Chapter 6.6, the vertical algorithm discretized the atmosphere in "n" different layers; for this thesis, a linear grid of 100 m step was used.
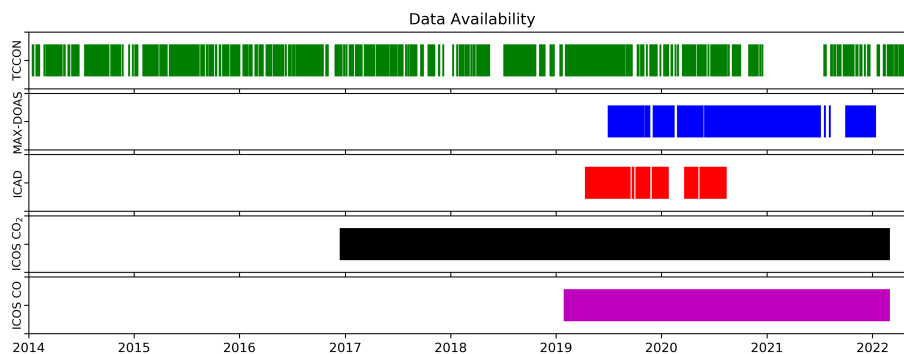
Figure 10.8: Chart showing the data availability for the remote sensing and in-situ observations: TCCON (XCO_2 and XCO) and MAX-DOAS ($NO_{2,VCD}$), ICAD (NO_2), and ICOS (CO_2 and CO) at 200 m.

on the one hand and NO_2 on the other hand. This is enforced by the fact that the cadence of measurements is significantly lower for the MAX-DOAS than for the TCCON measurements (MAX-DOAS: one per hour, TCCON: one per several minutes); therefore, we need to coarsen the procedures used for the TCCON measurements:

10.5.1 $\frac{\Delta XCO}{\Delta XCO_2}$ ratios

For calculating the short term deviations for both species, a median filter, with a 30 minutes window length, has been applied to the XCO and XCO_2 daily time series. The median filter's window length was appropriately adjusted to dampen variations of two hours duration and is shown as red dots in Figure 10.9 in the top panels for XCO_2 and XCO for an example day. This smoothed version of the time series is assumed to approximate the average background CO_2 concentration, which is slowly variable due to superimposed advected signals from various distant sources (and sinks) and due to variations associated with variable meteorological conditions. The imprints of local signals are suppressed in the smooth curve, as these local contributions tend to be variable on shorter time scales (in response to changes of wind direction, vertical exchange, etc.). So we regard $\Delta X_{gas} = X_{gas,individual} - X_{gas,median}$ as a proxy for the local signals for ΔXCO and ΔXCO_2.

10.5.2 $\frac{\Delta NO_{2,VCD}}{\Delta XCO_2}$ ratios

In order to calculate ΔNO_2 VCDs, the daytime mean has been taken as a reference value and then subtracted from each point. It is important to note that because NO_2 VCDs results are only hourly available, while the cadence of the FTIR measurements is in the order of several minutes, the median filter method used for the FTIR data is not applicable for the MAX-DOAS data. Fortunately, due to the shorter atmospheric lifetime of NO_2, the contribution of local signals in comparison to advected background is much higher for
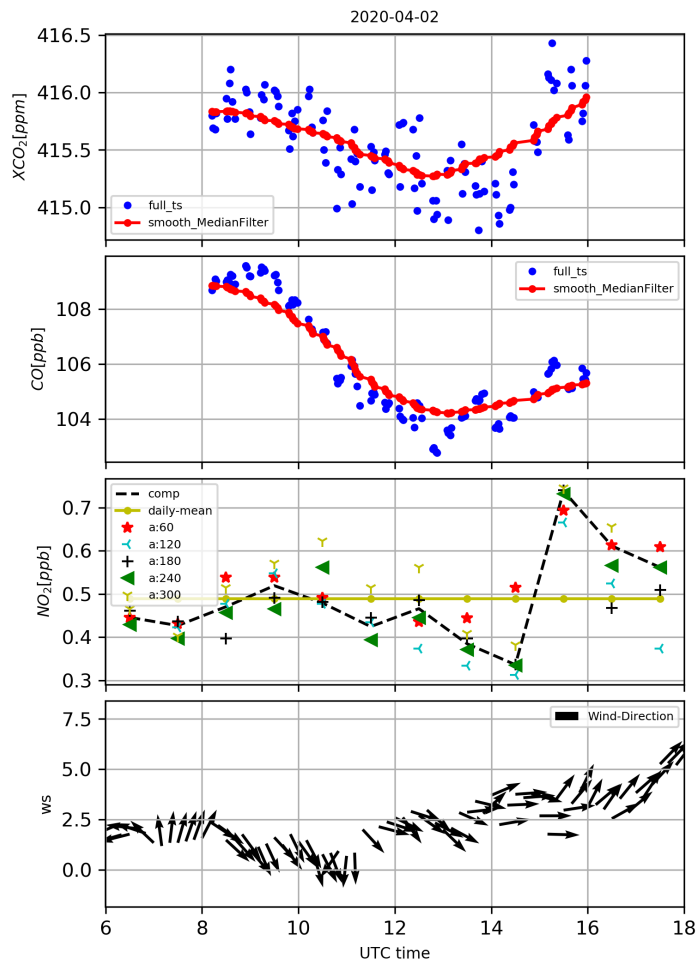
Figure 10.9: Graphic representation of the methods used for the Δ calculation for each gas by using 02.04.2020 as example. In the two uppermost plots, the median is used for defining the slowly variable average CO_2 and CO concentrations (red dots). In addition, the individual measurements (blue points) are shown. In the third plot (top-down), the composed NO_2 VCD (black dashed line) and the NO_2 VCD for all available azimuth angles are shown. In the lowermost panel, the hourly averaged wind velocity is shown. The local time zone (CEST) is ahead of UT by two hours.

NO_2 than for the other gases, so this coarser treatment enforced by the measurement procedure seems acceptable.

In this situation, an equal treatment of XCO_2 appearing in the denominator of $\frac{\Delta NO_{2,VCD}}{\Delta XCO_2}$ (using the daily mean as background) might achieve a better match. However, adopting the NO_2 approach for XCO_2 would introduce significant amounts of background variability in the signal part, due to the very different lifetime of the two gases. The analysis approach described above is the best that can be achieved based on the available observations.

MAX-DOAS measurements are available in 6 different azimuth angle directions, which in practice means having $\sim$ hourly profiles and VCDs in each azimuth direction. In terms

of the time range, these measurements are carried out continuously, and because they depend on sunny conditions, in general, a good measurement day starts at 06:00 and ends at 18:00, local time.

At the same time, TCCON results are related to the slant column derived from the direct sunlight observations (the spectrometer needs to track the solar position during the day). The FTIR measurements are usually available from 10:00 to 18:00 local time. According to the statements above, TCCON results (XCO_2) are shorter in their daily time coverage (while they achieve higher sampling rates than the MAX-DOAS).

The approach used in this thesis requires the combination of the MAX-DOAS and TCCON results. Both techniques sample different parts of the atmosphere: on the one hand, MAX-DOAS instruments sample at six fixed azimuth directions (See Figure 10.4), and on the other hand, TCCON dynamically samples the atmosphere as prescribed by the solar azimuth angle (SAA); therefore, in order to compare the part of the atmosphere that had been sampled with both instruments the following matching procedure has been applied:

- XCO_2 is taken as reference for the time gridding,

- The SAA from the TCCON observations serves as a reference for determining which azimuth directions from MAX-DOAS are considered to match with a selected TC-CON observation.

- Time gridding is used to match with the start and end of the time range as prescribed by TCCON. Finally, time intervals fine enough to preserve the temporal resolution of the MAX-DOAS are selected.

- All the NO_2 VCDs within the (mentioned above) time and SAA range are averaged. The results are presented as a combined NO_2 VCD, which is the most representative NO_2 VCD associated with the given set of TCCON XCO_2 results.

In order to classify the short-time variations of the total column for both gases, daily correlation plots between both gases are used. R^2 values > 0.5 in the linear regression are assumed to indicate significant events. Figures 10.9 and 10.10 demonstrate the data analysis for an example day.

10.6 INTERPRETATION OF PROXY/CO₂ RATIOS DERIVED FROM TOTAL COLUMN DATA

In order to assess the obtained results, in this chapter, the so-called double ratio plots are used similarly as presented for the pure in-situ point of view by (Jäschke et al., 2021; Rosendahl, 2022).

10.6.1 *Double ratio plots based on high-resolution TNO inventory*

A double ratio plot based on the area emissions reported by the high-resolution TNO inventory for 2020 is shown in Figure 10.11. Such a plot can help to characterize the anthropogenic sources by comparing the measured ratios with thoese obtained from high-resolution TNO inventory for different sectors.
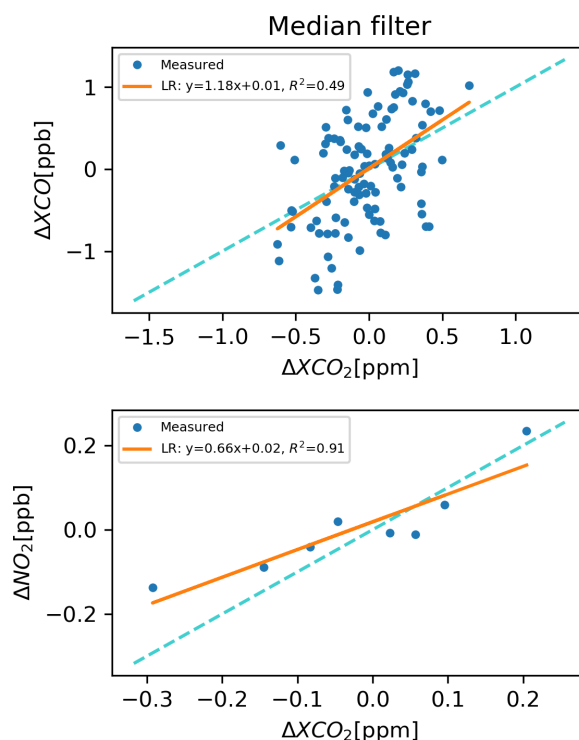
Figure 10.10: Resulting correlation plots for both proxies with respect to ΔXCO_2 for 02 April 2020.
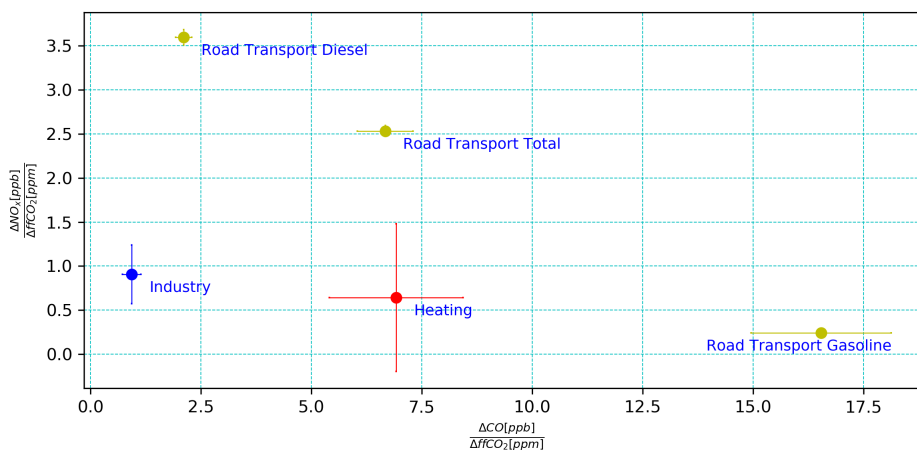
Figure 10.11: Double ratios plots for $\Delta NOx/\Delta XCO_2$ vs $\Delta CO/\Delta XCO_2$ from high-resolution TNO inventory 2020.

10.6.2 *proxy/CO₂ ratios derived from total column observations*

Here we present the events or days when each ratio has a $R^2 > 0.5$, meaning that only when both proxies (NO₂ and CO) have significant enhancements.

Figure 10.12, shows a "double-ratio" relationship between $\Delta NO_{2,VCD}/\Delta XCO_2$ as a function of $\Delta XCO/\Delta XCO_2$ for the identified events based on the total column observations.
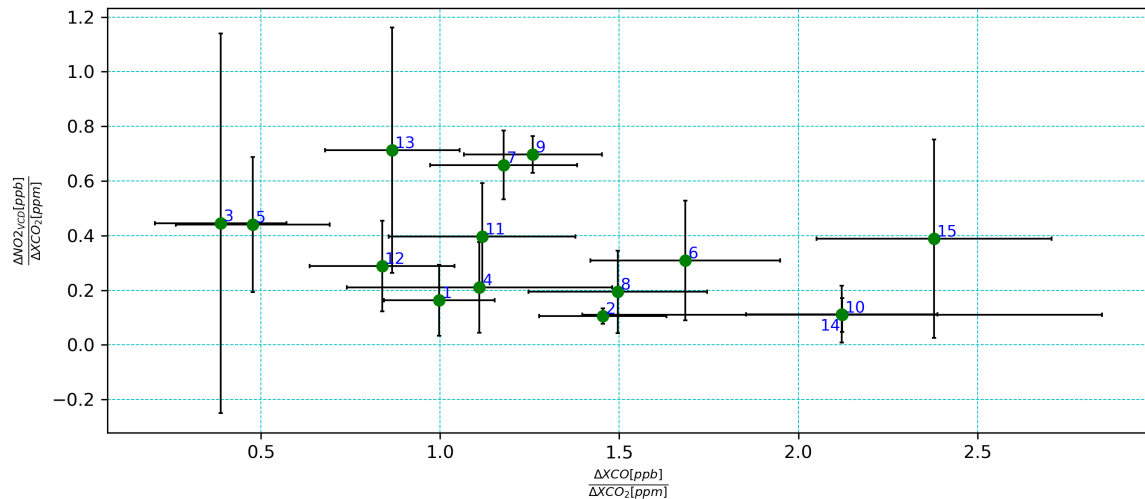
Figure 10.12: Double ratio plot with the events found on the time-period constrained to the MAX-DOAS availability of data, July 2019 to January 2022.

The most important findings based in Figure 10.12 can be summarized as follows:

- Ratio values appear reasonable regarding the values on 10.11.

- Less variability than TNO, probably because the remote sensing measurements generally observe a mix of sources.

- Industry emissions seemed dominant: Mean ratio values $\sim 0.4/1.4$.

Evident variability along both axes of the plot has to be observed above the significance level. The individual events shown in Figure 10.12 are listed in Table 10.1. For testing the assumption whether the strongest events observed (which will be characterized in consequence by highest R^2 values) are plume observations of the hard-coal fired power plant, a possible correlation between R^2 and wind direction is studied for both ratios separately as shown in Figures 10.13 and 10.14. However, no clear preferred direction is found. The number of events seems too low for this kind of analysis. It would be required to continue the observation for several years to increase the number of observed events significantly.

10.6.3 *Individual proxy/CO₂ ratios analysis*

This section evaluates the individual proxy/CO₂ ratios for the whole available period when the condition R^2 is met. Figures 10.15 and 10.16 show the time series of each ratio for the whole available period. From these figures, no clear seasonal change of the proxy ratios (e.g., between winter (heating sector on) and summer season) was found.

Figures 10.17 and 10.18 show no clear correlation between R^2 and wind direction. However, considering the wind speed and direction, the events show two remarkable tendencies: the first one aligned into the SW direction: low $\Delta XCO/\Delta XCO_2$, where a heavily industrialized area is located, as shown in Figure 10.1, suggesting that these events could

Event Corr.No. used in Figure 10.13	Date
1	2019-07-24
2	2019-07-26
3	2019-09-13
4	2019-12-16
5	2019-12-29
6	2020-01-16
7	2020-04-02
8	2020-04-07
9	2020-05-08
10	2020-07-01
11	2020-07-30
12	2020-11-14
13	2020-11-18
14	2020-11-28
15	2021-11-09

Table 10.1: List of events detected by the remote-sensing technique

be related to the anthropogenic emissions that originated in that area; and the second one, in the ENE direction: high $\Delta XCO/\Delta XCO_2$ that could be related to the emissions of the power and heating plant, operated at KIT CN, anthropogenic emissions originated in Bruchsal or even coming from the power plant located in Heilbronn ($\sim$40 east of KIT CN), see Figure 10.1. The validity of this hypothesis is supported by Figure 10.19, which shows the predominant wind direction which coincides with the events location of the events found.

10.7 COMPARISON OF PROXY/CO$_2$ RATIOS WITH INVENTORY DATA AND IN-SITU MEASUREMENTS

10.7.1 *In-situ data*

The in-situ measurements, and data analysis used for the comparison in this chapter, were carried out for the Integrated Carbon Observation System (ICOS) Central Radiocarbon Laboratory from the Institute for Environmental Physics at Heidelberg University. However, a brief description of the data is given in this section.

The ICOS in-situ measurements are carried out continuously at the 200 m high tower of the KIT-TRO station, which allows conducting atmospheric measurements at 200 m, 100 m, 60 m, and 30 m above ground ($\sim$110 masl). Continuous CO_2, CH_4, N_2O, CO measurements, and meteorological parameters are conducted at all platform heights.
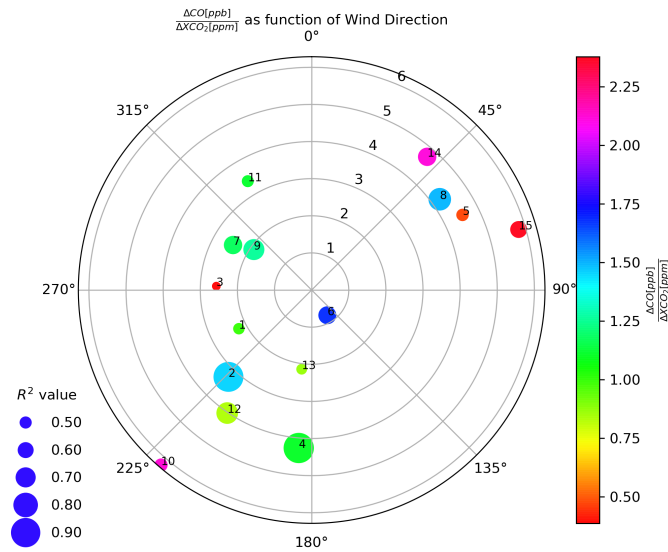
Figure 10.13: Remote-sensing-based $\Delta XCO/\Delta XCO_2$ ratio plot for the days with $R^2 > 0.5$ for both ratios, constrained to the MAX-DOAS availability of data and classified by a correlative number. The angular orientation and radial position of each event in the polar plot are given by the averaged wind direction and speed at noon, respectively. The color and size of the bubbles represent the ratio and the R^2 values, respectively.
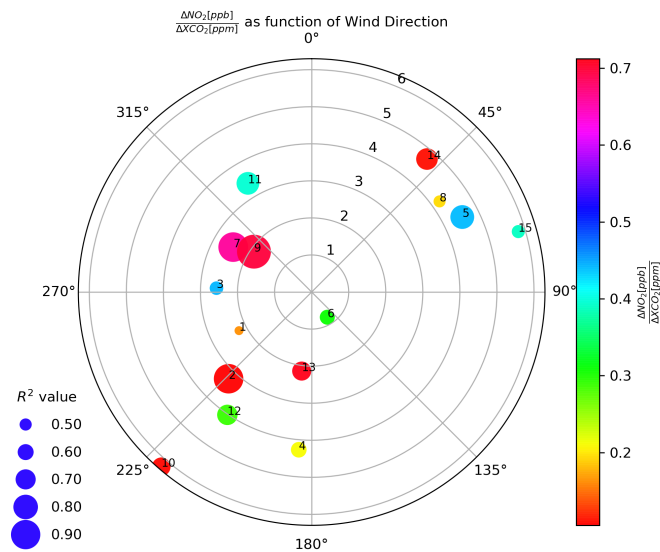
Figure 10.14: Similar to 10.13 but for $\Delta NO_{2,VCD}/\Delta XCO_2$ ratio.

The station[3] uses an automated ICOS flask sampler to collect 1 hour averaged air samples in flasks to measure an extended set of GHGs concentrations, the isotopic composi-

---

3 This station is classified as ICOS class 1 atmospheric station; more information can be found in ICOS and RI (2020).
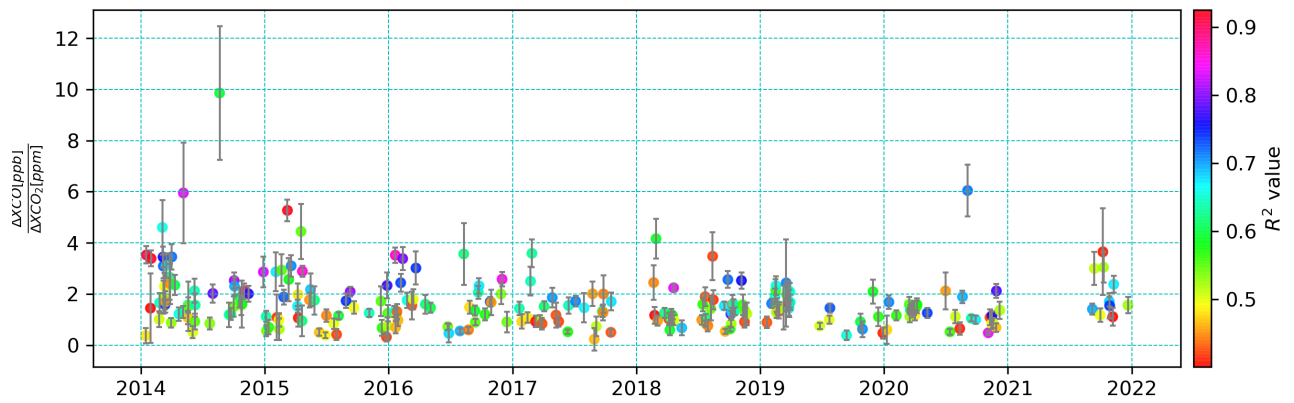
Figure 10.15: Time series for all the correlations with $R^2 > 0.5$ in the period September 2014 to October 2020, for $\Delta XCO/\Delta XCO_2$
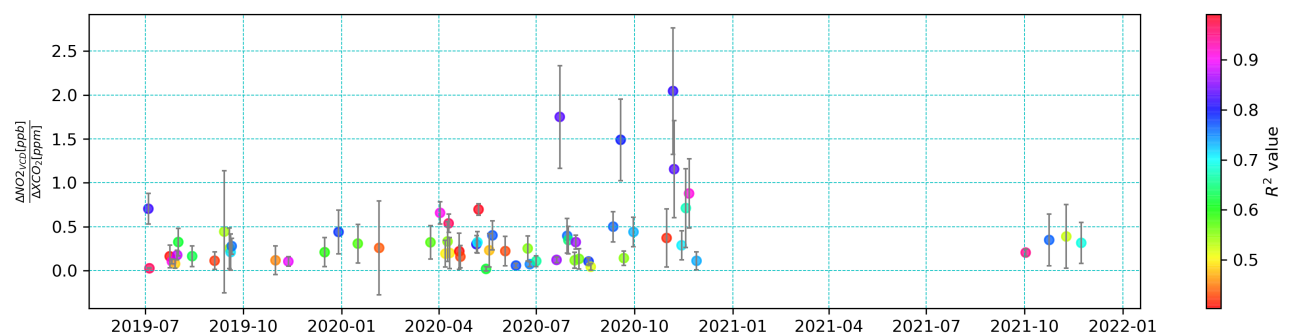
Figure 10.16: Time series for all the correlations with $R^2 > 0.5$ in the period July 2019 to October 2020, for $\Delta NO_{2,VCD}/\Delta XCO_2$

tion of CO_2 and CH_4 and the atmosphere O_2/N_2 ratio. More information about the ICOS flask sampling strategy can be found in Levin et al. (2020).

Additionally, an ICAD system conducted continuous in-situ NOx (NO and NO_2) measurements at 200 m from July 2019 to August 2020.

Figure 10.20 shows an example where clear enhancements were measured for CO_2, CO and NOx on January 10, 2020. Between 11:30 and 12:30, a sizeable CO_2 enhancement of about 30 ppm was observed, accompanied by a minor CO enhancement of only 10 ppb and a NOx enhancement of about 15 ppb. During the entire time period, the wind direction was relatively stable from the South-Westerly wind sector, where the most significant industrial sources are located. Apart from the time when the most significant enhancements occurred, the CO_2 concentrations measured at different altitudes showed minor vertical differences, which is a clear sign that the lower boundary layer was well mixed during that day.
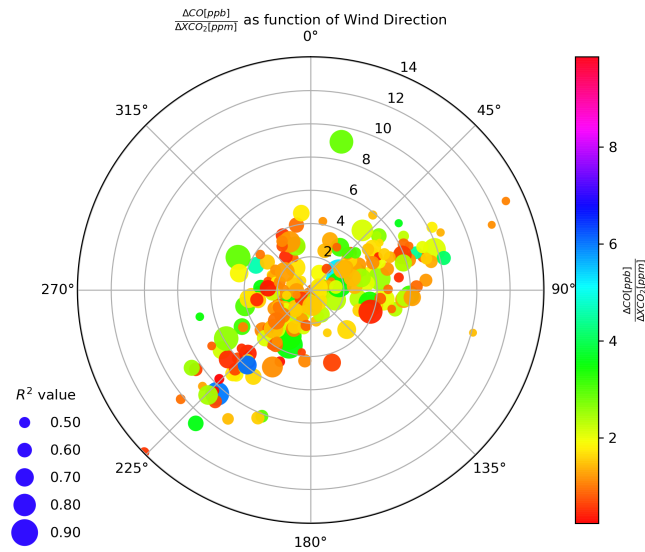
Figure 10.17: Similar to 10.13 but for the whole available measurement period, see 10.4, and Figure 10.15 for more information.
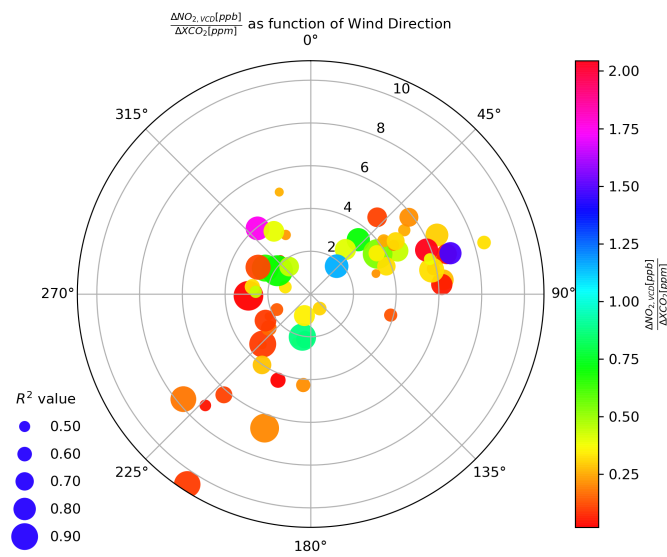
Figure 10.18: Similar to 10.17 but for $\Delta NO_{2,VCD}/\Delta XCO_2$ ratio.

10.7.2 *Comparisons between in-situ, total column and TNO inventory*

Doble ratio plots can help to understand the most probable anthropogenic sources, including the ratios obtained from high-resolution inventory for different sectors, as presented in Figure 10.11. In this thesis, the TNO high-resolution inventory is used.
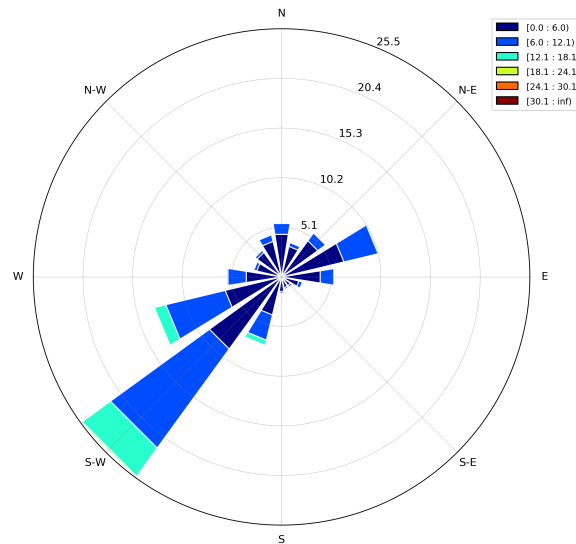
Figure 10.19: Wind rose showing the most predominant wind direction and speed during the period 2014-2021.
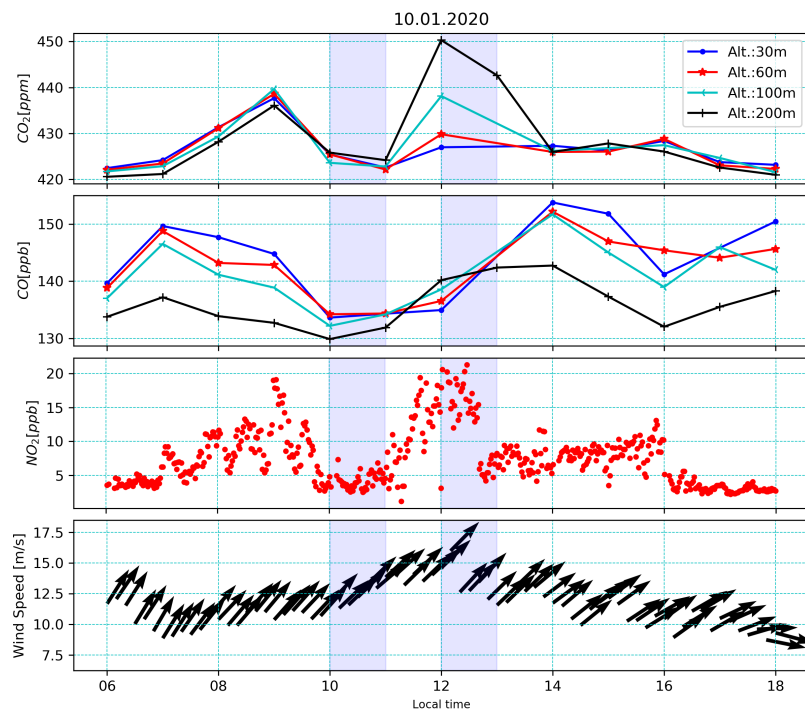
Figure 10.20: An example plot of a transport event detected by the in-situ measurements on January 10, 2020. The uppermost panel shows the continuous measurements of CO_2, followed by CO in the second panel, and then NOx, wind speed and direction, and radon measurements, each referring to the specifications given at the left axis. The colors denote the sampling heights as given in the legend.

Directly comparing the in-situ and total column based proxy/ffCO$_2$ ratios is impossible since the total column measurements cannot measure ffCO$_2$ and NOx. However, in-situ CO$_2$ and NO$_2$ measurements are also available, which are presented in Figure 10.21.

In-situ and total column ratios for the exact quantities are much more comparable in terms of variability, although the in-situ measurements, especially the CO/CO$_2$ variability, are high. Due to the fundamentally different meteorological conditions preferred for the in-situ and the total column measurements[4], there is only one common day for both observation strategies on April 7, 2020, marked in Figure 10.21 as number 13 event of the in-situ data and number 8 by the total column. Though the in-situ signal was sampled between 4:00 and 5:00, the in-situ and the total column observation on that single common day only sample the same event and are unlikely to agree.

The main reason for the discrepancies between in-situ and total column measurements is successfully identified (the transition NOx to NO$_2$ is of minor impact). However, the assumption that individual local and strong emitters dominate the short-term variability seemed generally not justifiable. From the in-situ measurements, we could conclude that the short-term variability in the total column signal has a similar fossil to the non-fossil share as the in-situ signals. However, this is not surprising as the in-situ measurements also exploit the signal's short-term variability.

Thus, for the accurate determination of the source distribution and comparison with inventories, an observational method pinning down the ffCO$_2$ share is required, which unfortunately cannot be achieved by current remote sensing technology.

---

4 Large in-situ enhancements are observed during atmospheric situations with suppressed vertical mixing, while on the other hand, total column observations work only with clear sky conditions, typically associated with enhanced atmospheric mixing

Figure 10.21: Double ratio plot comparison between total column results and in-situ. Black and grey denotes in-situ measur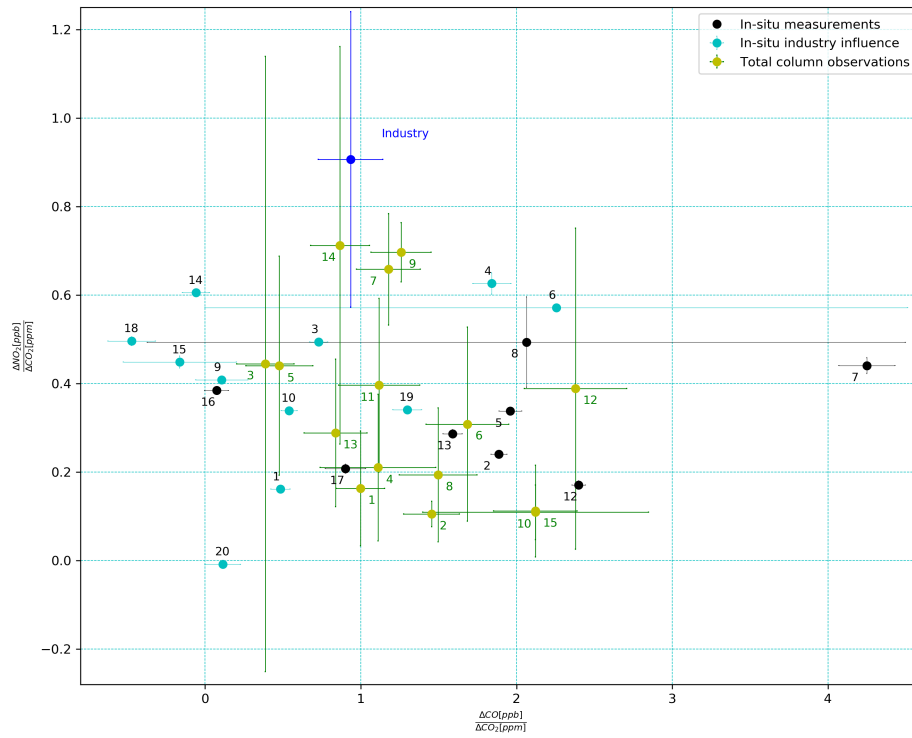ements, light blue measurements obtained from the total column observations. The red marker represents the mean industry ratio from TNO inventory.

11

CONCLUSIONS

This thesis presents three main results chapters that can be considered independent contributions to the study of atmospheric measurements of GHGs. Therefore, the conclusions are separated to give the reader a more consistent idea of the goals achieved in this work.

11.1 IMPROVEMENT OF THE CALIBRATION PROCEDURES FOR THE COCCON NETWORK

The analysis of the open-path measurements for deriving the ILS parameters of EM27/SUN FTIR spectrometers was improved. All previous laboratory open-path measurements for determining ILS parameters in the framework of COCCON were reanalyzed. The elaboration of a revised empirical H_2O line list allowed for a significant reduction of fit residuals. Adding a second spectral window, which can be observed in both channels of the EM27/SUN spectrometer, allowed us to identify and quantify significant CO detector misalignments.

In addition to the open-path measurements, a cell filled with C_2H_2 was constructed and put into service. The cell measurement can be performed sequentially with the open-path procedure without significant additional effort. It offers similar sensitivity to the ILS parameters and adds redundancy to the calibration process, and the C_2H_2 column is expected to be invariant for all EM27/SUN spectrometers. An excellent agreement of the retrieved column amount between different spectrometers was found (1-σ scatter on the order of 0.01 %; see Figure 8.14c). Based on these encouraging results, it is planned to circulate C_2H_2 cells to demonstrate the temporal stability of individual spectrometers and the level of instrument-to-instrument consistency across the network.

The stability of the COCCON reference spectrometer operated at KIT was investigated, and variations in X_{AIR} were found during the first years of operation (2015—2017). This variability has a non-negligible impact on the XCH_4 calibration results during this period of up to 0.14 %. All previous side-by-side measurements reported by Frey et al. (2019) were reanalyzed using the revised ILS parameters and incorporating the correction of the XCH_4 calibration factors for 2015–2017 period.

Forty-seven new spectrometers were calibrated before they became operational, and several previously investigated spectrometers were recalibrated. The resulting ILS parameters and empirical calibration factors for each target gas were derived. I finally investigated the typical spectral SNR achieved by the EM27/SUN spectrometer in solar and open-path measurements.

A tendency towards improved and more consistent instrumental performance in the fabrication series of EM27/SUN spectrometers was noticed. We assume that our continued refinement and continuous application of the quality assurance procedures performed for COCCON in cooperation with the manufacturer of the spectrometers, Bruker, is the reason for this tendency.

11.2   EMME CAMPAIGN: GENERAL RESULTS AND CO$_2$,CH$_4$ AND CO EMISSION ESTIMATIONS

Within the project VERIFY, a joint[1] campaign was carried out in the second largest city in Russia, St. Petersburg, to quantify the emission strengths of CO$_2$, CH$_4$, and CO in a megacity of 5 million inhabitants with a variety of emission sources along its territory.

The central core of this campaign were two EM27/SUN instruments, which were deployed daily in the up and downwind direction within the city ring road (used as a boundary). The initial daily location for each instrument was decided based on the model weather forecast (for clear conditions and wind information) and Hysplit forecasted pollution plume direction. Furthermore, on the measurement day, mobile zenith DOAS measurements were performed to track the actual time plume and then cross-check the correctness of the initial deployment of the instruments.

The whole concept of this campaign is already published by Makarova et al. (2021). However, in this thesis, the measurements obtained with the two EM27/SUN instruments were completely re-analyzed and the evaluation of differential column signals was refined. With these new results and a simple total column model, the emissions strengths for CO$_2$, CH$_4$, and CO were obtained and compared with the published results by Makarova et al. (2021). The results proved that with this set-up, emissions plumes could be detected on an urban scale.

The total column mass balance approach used in this thesis used a different wind source, ERA-5, because it can reproduce observed wind well across whole Europe (Molina, Gutierrez, and Sanchez, 2021). ERA-5 has been used in similar studies with great success (Angevine et al., 2020; Brune, Keller, and Wahl, 2021). Finally, a more straightforward calculation of the air transect length over the source was applied in the analysis.

The estimated emissions strengths for CO$_2$, CH$_4$, and CO in St. Petersburg are slightly smaller than the results published by (Makarova et al., 2021), but all agree within the error range. These can be attributed to the substantial different calculations and inputs, sharing only the pure observational raw data. The estimated results for CO$_2$ and CH$_4$ are higher $\pm$ 2 and 5 times, respectively, in comparison to the official inventory results of the city, and $\pm$ 2 times smaller for CO.

Concerning EDGAR inventory, the campaign results are clearly higher for the three species, possibly due to the elevated heating sector emissions during this time of the year, while EDGAR emissions refer to yearly averaged emissions.

11.3   INVESTIGATION OF SPACE-BORNE TRACE GAS PRODUCTS OVER ST PETERSBURG AND YEKATERINBURG, RUSSIA, BY USING COCCON OBSERVATIONS

Part of this thesis was devoted to the analyses of ground-based COCCON and space-based TROPOMI, OCO-2, OCO-2 FOCAL, GOSAT, and MUSICA IASI observations (XCO$_2$, XCH$_4$, XCO, XH$_2$O), in Peterhof and Yekaterinburg cities. Stationary COCCON observations were performed in the period 2019–2020.

---

1 The campaign was planned and carried out with close cooperation from St. Petersburg State University (Russia), Karlsruhe Institute of Technology (Germany), and the University of Bremen (Germany).

All the data products in Peterhof show similar seasonal variability. However, for XCO_2, the COCCON dataset is generally lower than the other available datasets, among which GOSAT has the highest standard deviation compared to the other datasets. TROPOMI observes slightly lower XCH_4 but slightly higher XCO than the other products. As expected, the most considerable seasonal variability is observed in XH_2O. Higher amounts of XH_2O are observed in summer, primarily due to higher evaporation and precipitation, which is expected. The averaged GOSAT XH_2O is higher than the other products due to its short measurement period, mostly in summer. Yekaterinburg has a shorter measurement period, mainly covering winter and spring, from October 2019 to April 2020. Similar seasonality and concentrations are observed in Peterhof during the same period.

The satellite observations are sparser in the high-latitude regions than in mid- and low-latitude regions, while models provide continuous datasets. Many previous studies have proven the ground-based COCCON observations to be highly accurate. To combine the advantages of CAMS and COCCON datasets, we developed an upscaling method, adjusting CAMS data to the COCCON observations collected at Peterhof and Yekaterinburg to obtain continuous data of virtual COCCON observations (as demonstrated using different subsets of COCCON measurements at Karlsruhe). This method is more critical for Yekaterinburg, where three different problems were faced: (1) fewer measurements in general (around 6 months compared to 15 months in Peterhof), (2) fewer measurement days per month (mainly in winter), and (3) shorter daily period of measurements. As expected, the CAMS-COCCON data show better correlations with COCCON observations than the original CAMS datasets. The CAMS-COCCON data are then compared with satellite products, showing good agreements and generally similar biases to those between satellite products and COCCON observations. This method was also used for the observations at Yekaterinburg, where fewer COCCON measurements were taken. The gradients between the two study sites (ΔXgas) are similar between CAMS and CAMS-COCCON datasets. A few COCCON and satellite ΔXgas measurements fit well with those of CAMS-COCCON. The results presented in this study indicate that our scaling method is working reliably.

11.4 PROXY/FFCO2 EMISSIONS IN THE VERIFY STUDY-CASE REGION

An considerable amount of effort has been used to calibrate, set up, maintain and keep the MAX-DOAS instrument operational, which was the first instrument of this kind to be mounted in the IMK-TRO tall tower. We consider this as a significant achievement, and the high quality of the resulting measurements supported the aims of this thesis.

The presented results indicate that in the proxy/ΔXCO_2 correlations we can detect enhancements due to local emissions. However, the presented approach based on remote sensing observations seems not to resolve the contributions from distinct individual fossil fuel sources (as industry, traffic, heating), but delivers a signal comprised of a mixture of independent sources encountered in the surroundings.

FIT RESIDUALS OF THE HR SPECTRA AFTER THE EMPIRICAL ADJUSTMENT
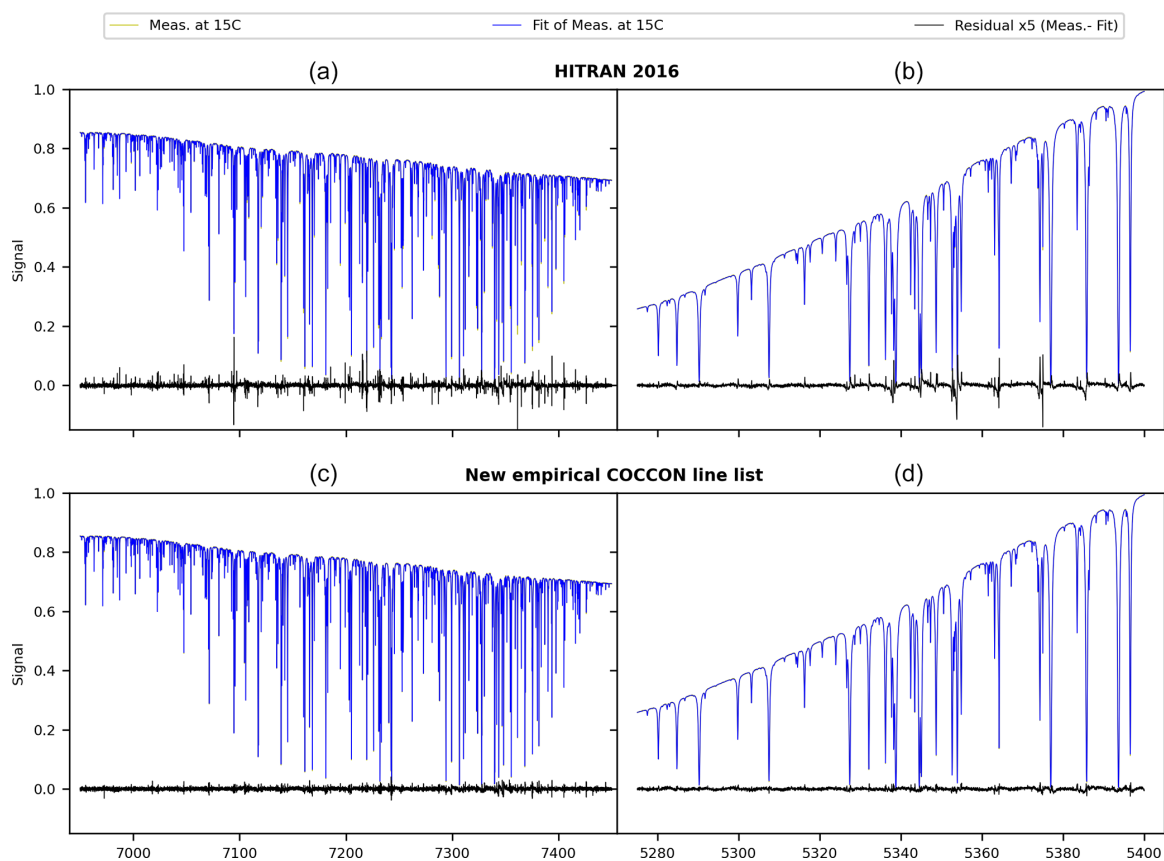
Figure A.1: H_2O spectroscopic lines used for this ILS calibration study. The fits (multi-spectrum fit performed) using HITRAN 2016 and the new empirical COCCON line list are presented in **(a, b)** and **(c, d)**, respectively. The measured spectra were taken with the IFS125HR at KIT Karlsruhe, at 15 °C. The spectral residuals shown are multiplied by 5 in order to be visible.
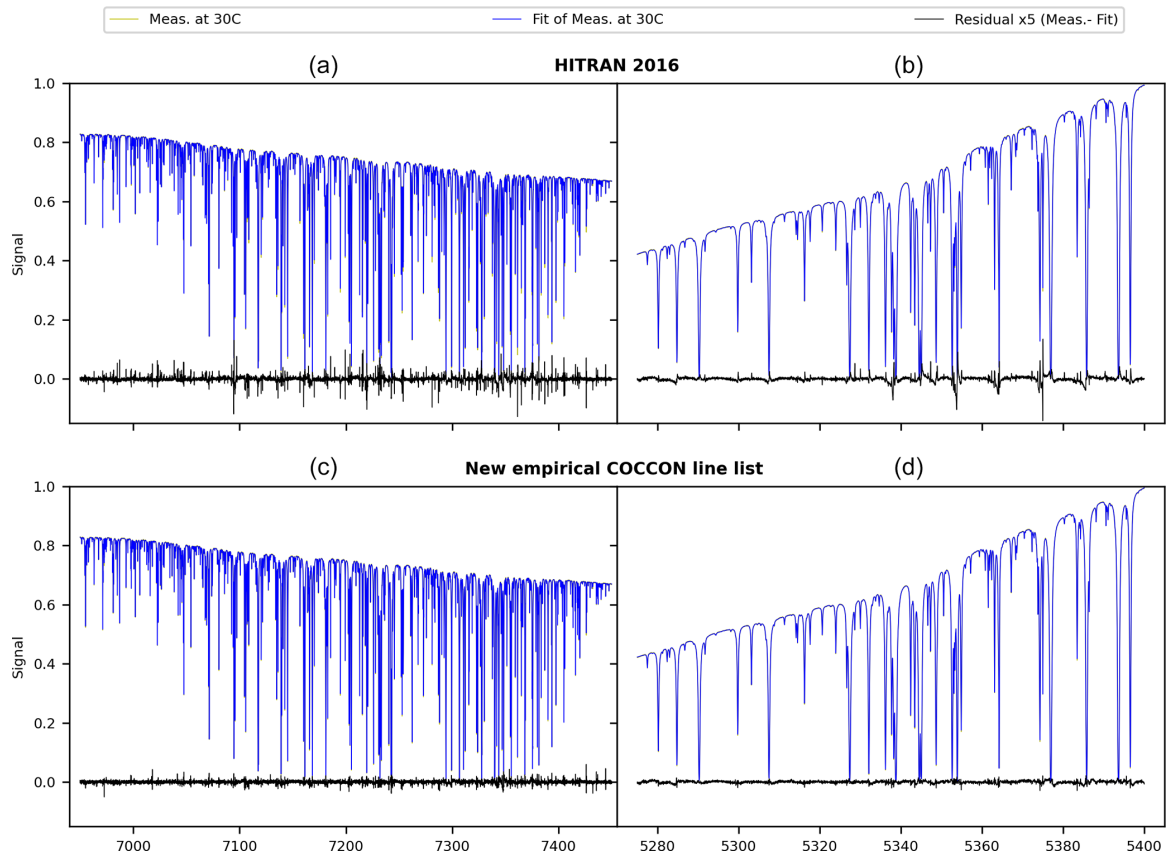
Figure A.2: Same as Figure A.1, but the measured spectra were taken with the IFS125HR at KIT Karlsruhe, at 30 °C.

B

B.1 DATASETS

B.1.1 *TROPOMI*

The Sentinel-5 Precursor (S5-P) satellite with the Tropospheric Monitoring Instrument (TROPOMI) on board as a single payload was launched in October 2017. S5-P is a low-Earth-orbit polar satellite. It aims at monitoring air quality, climate and ozone layer with high spatio-temporal resolution and daily global coverage during an operational lifespan of 7 years (Veefkind et al., 2012). TROPOMI is a nadir-viewing grating-based imaging spectrometer, measuring backscattered solar radiation spectra with an unprecedented resolution of $7 \times 7\,km^2$ (upgraded to $5.5 \times 7\,km^2$ in August 2019; (Lorente et al., 2021)). In this study, we use the improved TROPOMI XCH_4 product derived with the RemoTeC full-physics algorithm (Lorente et al., 2021) and apply the recommended quality value (qa) = 1.0 to the data. For CO, SICOR (Shortwave Infrared CO Retrieval algorithm) is deployed to retrieve the total column density of CO from TROPOMI spectra at $2.3\,\mu m$ (Borsdorff et al., 2018a,b; Landgraf et al., 2016). XCO is computed by dividing the CO total column by the dry air column extracted from the co-located TROPOMI CH_4 file. This dry air column is obtained from the surface pressure and water vapour column as provided by the European Centre for Medium-Range Weather Forecasts (ECMWF) analysis (Lorente et al., 2021; Schneising et al., 2019). H_2O retrievals are also performed with the SICOR algorithm. A similar quality filter is applied to the H_2O product as used in Schneider et al. (2020).

B.1.2 *OCO-2*

The Orbiting Carbon Observatory-2 (OCO-2) is a NASA satellite, launched in July 2014, providing space-based measurements of atmospheric CO_2 (Eldering et al., 2017). These observations have the potential capability to detect CO_2 sources and sinks with unprecedented spatial and temporal coverage and resolution (Crisp, 2015). The OCO-2 mission carries a single instrument incorporated with three high-resolution imaging grating spectrometers, collecting spectra from reflected sunlight by the surface of Earth in the molecular oxygen (O_2) A band at $0.764\,\mu m$ and two CO_2 bands at 1.61 and $2.06\,\mu m$ (Osterman et al., 2020). The OCO-2 satellite has three viewing modes (nadir, glint and target) and a near-repeat cycle of 16 d (98.8 min per orbit, 233 orbits in total). It samples at a local time of about 13:30 LT. The current version (V10r) of the OCO-2 Level 2 (L2) data product, containing bias-corrected XCO_2, is used in this study.

In addition to the operational XCO_2 product derived from OCO-2 observations described above, the data product generated using the Fast atmOspheric traCe gAs retrievaL (FOCAL) algorithm described in Reuter et al. (2017a) had been used. Compared with co-

located TCCON observations, the OCO-2 FOCAL data show a regional-scale bias of about 0.6 ppm and single measurement precision of 1.5 ppm (Reuter and Buchwitz, 2021). In this study, the latest version (v09) covering the time period of 2015–2020 is utilized for further comparison with the COCCON results.

B.1.3   *MUSICA IASI*

The Infrared Atmospheric Sounding Interferometer (IASI) is a payload on board the EMETSAT Metop series of polar-orbiting satellites (Clerbaux et al., 2009). The IASI instrument is a Fourier transform spectrometer that measures infrared radiation emitted from the Earth and emitted and absorbed by the atmosphere. It provides unprecedented accuracy and resolution on atmospheric humidity profile, as well as total column-integrated CO, CH_4 and other compounds twice a day. There are currently three IASI instruments in operation on Metop-A, Metop-B and Metop-C, launched in 2006, 2012 and 2018, respectively. The MUSICA IASI retrievals are based on a nadir version of PROFFIT (Schneider and Hase, 2009), which has been developed in support of the MUSICA project. More details can be found in Schneider et al. (2022b) and Schneider and Hase (2011). A validation of the MUSICA IASI H_2O profile data is presented by Borger et al. (2018).

B.1.4   *GOSAT*

The Greenhouse Gases Observing Satellite (GOSAT) was launched in January 2009, equipped with two instruments (the Thermal And Near-infrared Sensor for carbon Observation Fourier Transform Spectrometer, TANSO-FTS, and the TANSO Cloud and Aerosol Imager, TANSO-CAI) (Kuze et al., 2009). The satellite is placed on a Sun-synchronous orbit and passes the same point on Earth every 3 d. GOSAT is the first mission to monitor the global distribution and sinks and sources of GHGs. For this study, GOSAT FTS shortwave infrared (SWIR) level-2 data, version V02.90, from the National Institute for Environmental Studies (NIES) are used.

B.2   CAMS DATA

B.2.1   *CAMS inversion*

Copernicus Atmosphere Monitoring Service (CAMS) is operated by the European Centre for Medium-Range Weather Forecasts (ECMWF), providing global inversion-optimized GHG concentration products which are updated once or twice per year. For XCO_2 and XCH_4, the latest version datasets (v20r1 for XCO_2 and v19r1 for XCH_4) using surface air-sample as observations input are used in this study. The CAMS global CO_2 atmospheric inversion product is generated by the inversion system, called PyVAR (Python VARiational), with a horizontal resolution of 1.875×3.75 and temporal resolution of 3 h (Chevallier, 2020, 2021). The latest version (V20r1) was released in December 2020, covering the period from January 1979 to May 2020. The V20r1 model data fit TCCON retrievals well with less than 1 ppm of absolute biases (Chevallier, 2021).

For XCH$_4$, we used the latest version V19r1 based on inversion of surface observations only, covering the period between January 1990 and December 2019. The CAMS XCH$_4$ inversion product is based on the TM5-4DVAR (four-dimensional variational) inverse modelling system (Bergamaschi et al., 2013, 2010; Meirink, Bergamaschi, and Krol, 2008) with a horizontal resolution of 2×3 and temporal resolution of 6 h (Segers, 2020a,b). Compared to previous releases, v19r1 data have been adjusted by using new atmospheric CH$_4$ sinks and updated wetland emissions, and the monthly bias is usually less than 10 ppb with respect to TCCON (Segers, 2020b).

B.2.2 *CAMS reanalysis (control run)*

This study aims to compare XCO retrieved from the COCCON measurements with XCO from different satellite and CAMS datasets as well. However, no XCO data are available from the before-mentioned CAMS data. Fortunately, CAMS also provides reanalysis datasets, covering the period of 2003–June 2020. The standard CAMS reanalysis data use 4DVar data assimilation in CY42R1 of ECMWF's Integrated Forecast System (IFS) (Flemming et al., 2017; Inness et al., 2019). The CAMS reanalysis CO profiles under a control run, i.e. without any data assimilation, is obtained from Copernicus Support team. This control run reanalysis CO profiles are using only one IFS cycle with a 0.1×0.1 latitude $\times$ longitude resolution, 3 h of temporal resolution and 25 pressure levels. XCO is obtained when integrating the profiles from the lowest to the highest pressure level.

B.3 COLLECTION RADIUS BASED ON SATELLITE OBSERVATIONS
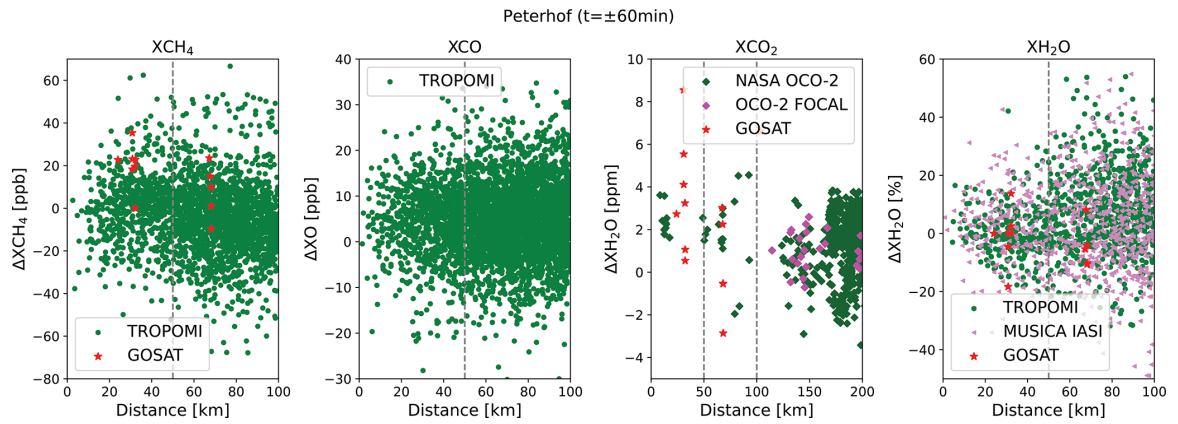
Figure B.1: Difference between a single satellite measurement with the averaged COCCON measurement ($\pm 1\,\mathrm{h}$ of satellite overpass) with respect to their distance.
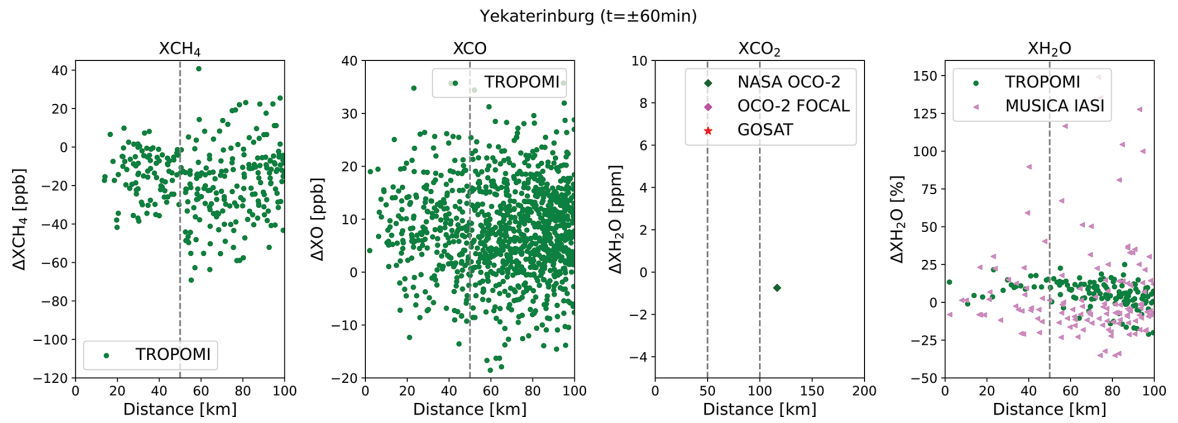
Figure B.2: Same as Figure B.1 but for Yekaterinburg.
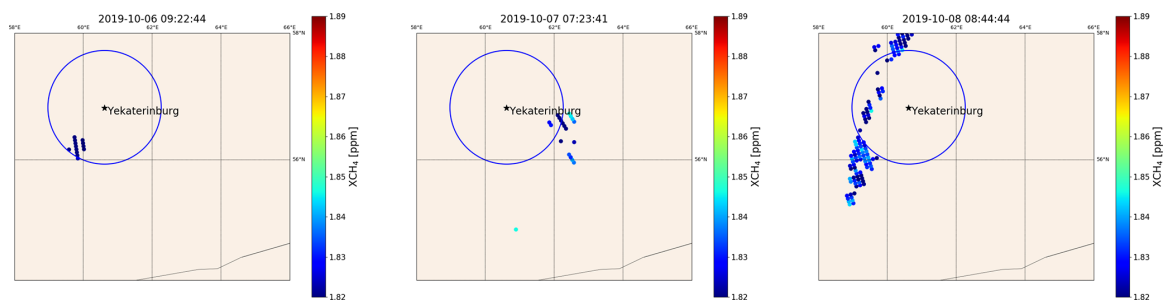
Figure B.3: Sample days for TROPOMI measurements (qa = 1.0) in October 2019. The circle has a radius of 100 km, centred at Yekaterinburg. The colour represents the value of XCH_4.
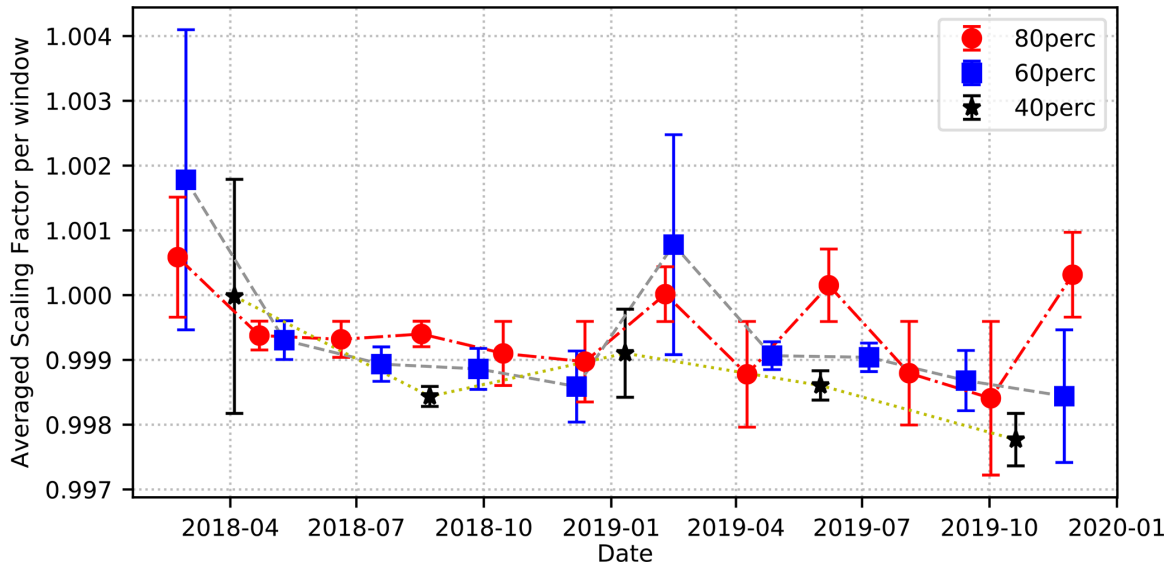
Figure B.4: Temporal variation of the averaged scaling factors in each sub-window for the number of windows selected for each subset of COCCON measurements at Karlsruhe (40 %, 60 % and 80 % of the total measurement days with FTS#37). The error bar represents the standard deviation calculated in each sub-window.
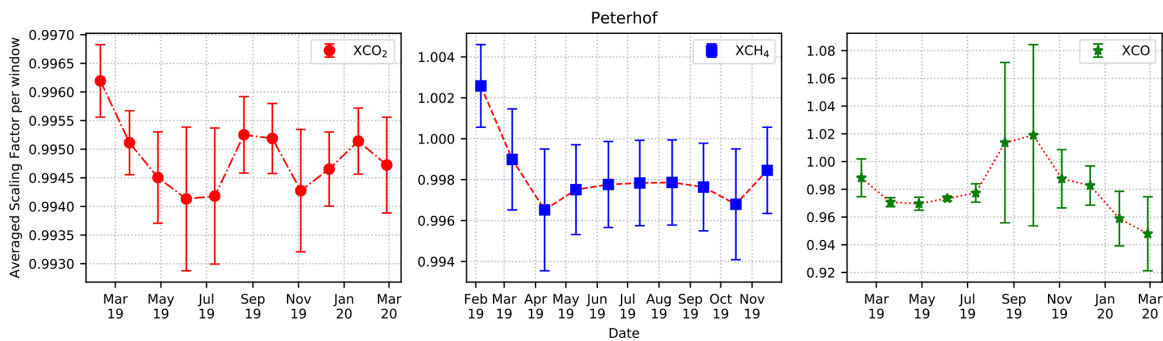
Figure B.5: Temporal variation of the averaged scaling factors per window for each studied gas: XCO_2, XCH_4 and XCO at Peterhof.
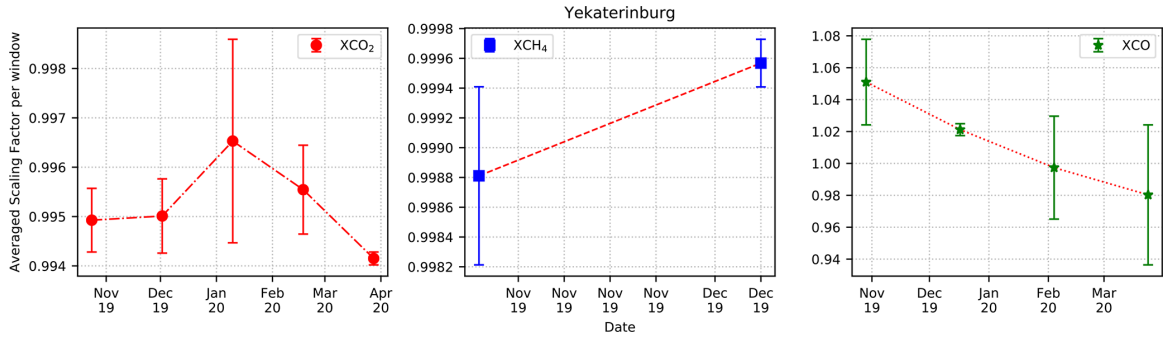
Figure B.6: Same as Figure B.5 but for Yekaterinburg.
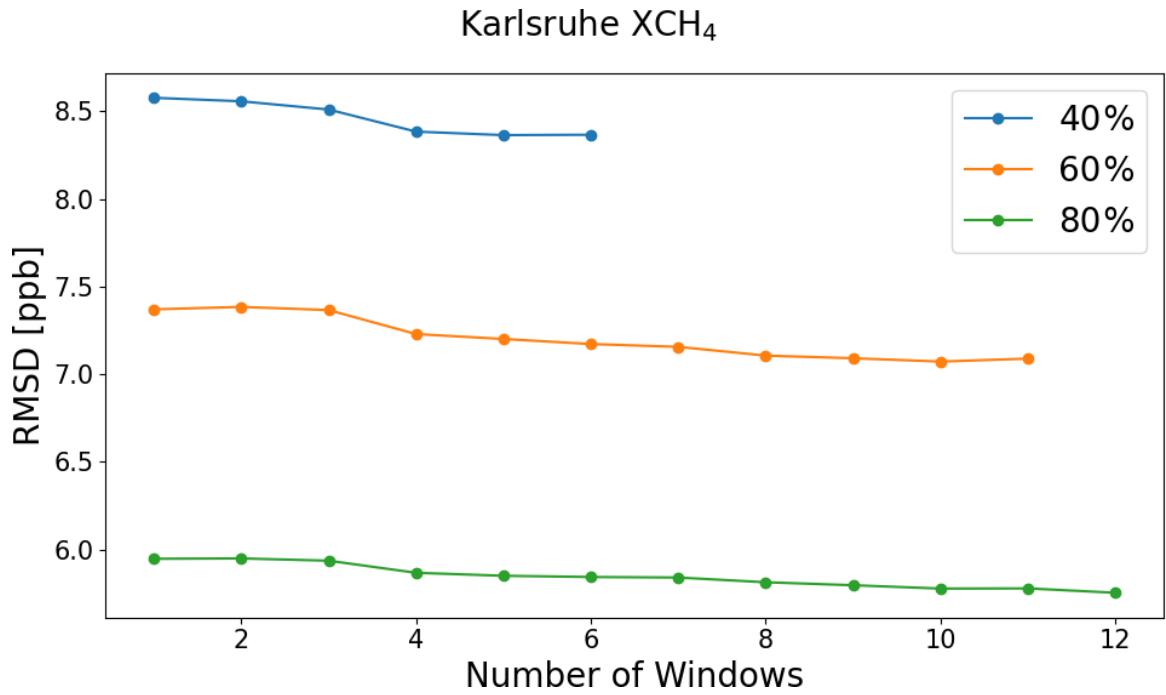
Figure B.7: Root-mean-square deviation between CAMS-COCCON and COCCON with respect to number of windows for XCH$_4$ according to 40 %, 60 % and 80 % COCCON data points at Karlsruhe.
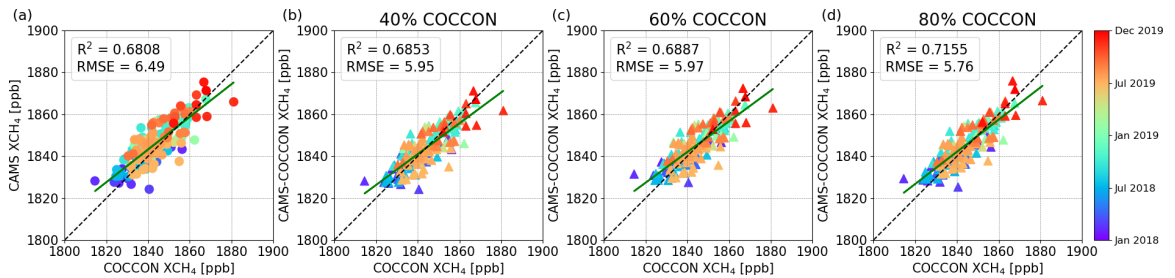
Figure B.8: Correlation plots of **(a)** CAMS and **(b–d)** CAMS-COCCON with respect to COCCON XCH$_4$ at Karlsruhe. The CAMS-COCCON datasets are based on 40 %, 60 % and 80 % of COCCON measurement days.
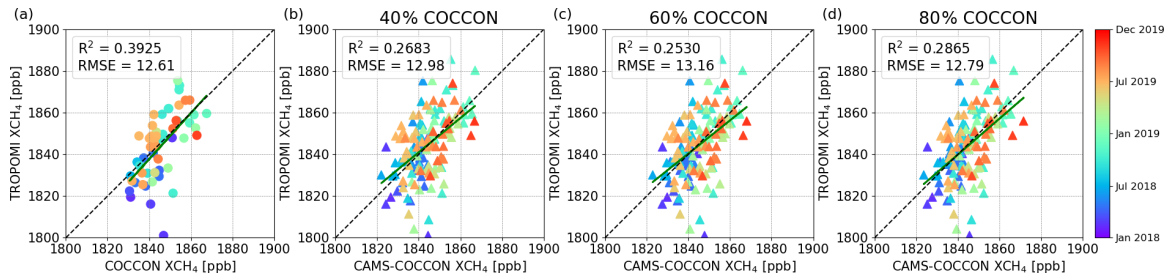
Figure B.9: Correlation plots of **(a)** COCCON and **(b–d)** CAMS-COCCON with respect to TROPOMI XCH_4 at Karlsruhe. The CAMS-COCCON datasets are based on 40 %, 60 % and 80 % of COCCON measurement days.

Species	Peterhof			Yekaterinburg		
	Variability of original CAMS products	CAMS–COCCON	Scaled CAMS–COCCON	Variability of original CAMS products	CAMS–COCCON	Scaled CAMS–COCCON
XCO_2	3.45 ppm	1.76 ± 0.82 ppm	0.18 ± 0.79 ppm	2.24 ppm	1.31 ± 0.69 ppm	−0.008 ± 0.56 ppm
XCH_4	11.81 ppb	14.97 ± 8.7 ppb	−1.95 ± 6.84 ppb	5.95 ppb	19.9 ± 5.88 ppb	−0.58 ± 4.19 ppb
XCO	10.67 ppb	0.59 ± 6.51 ppb	−1.92 ± 4.90 ppb	11.58 ppb	1.96 ± 6.50 ppb	2.16 ± 5.03 ppb

Table B.1: The variability (standard deviation) of the original CAMS products during the COCCON measurement period in each city and bias and standard deviation for the difference between CAMS and COCCON, as well as between scaled CAMS and COCCON.
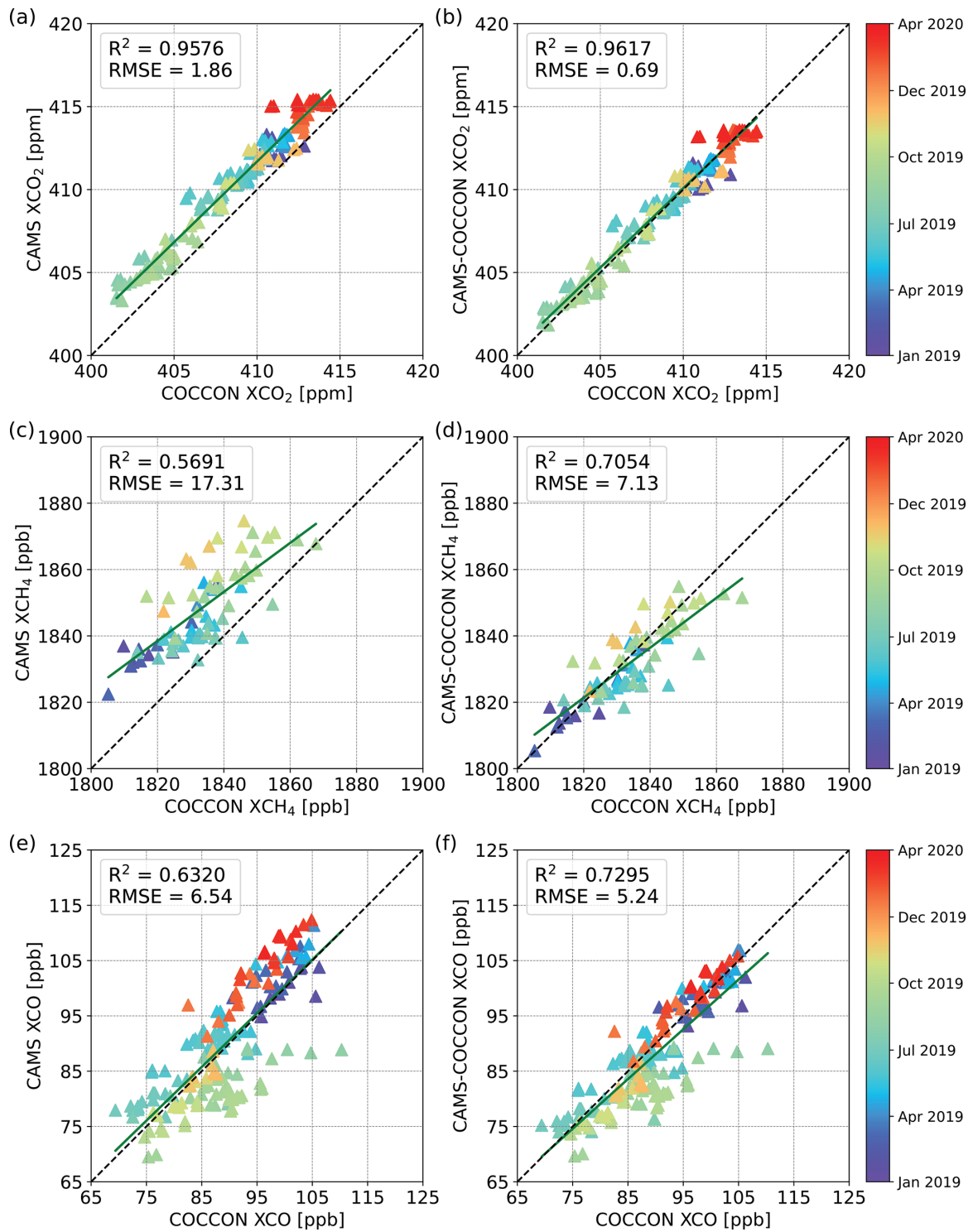
Figure B.10: Correlation plots of CAMS **(a, c, e)** and CAMS-COCCON **(b, d, f)** with respect to COCCON for XCO_2 **(a, b)**, XCH_4 **(c, d)** and XCO **(e, f)** at Peterhof.
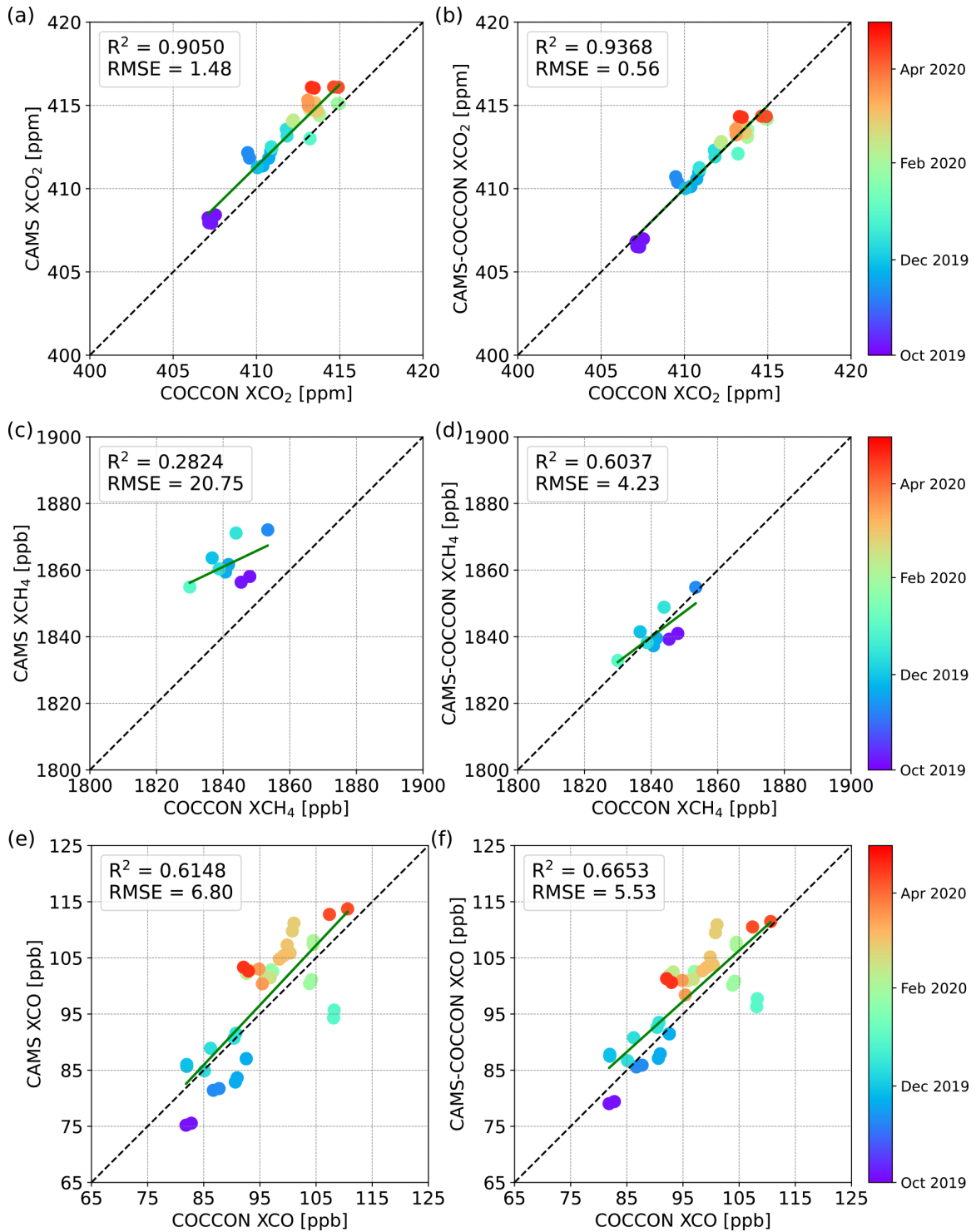
Figure B.11: Correlation plots of CAMS **(a, c, e)** and CAMS-COCCON **(b, d, f)** with respect to COCCON for XCO$_2$ **(a, b)**, XCH$_4$ **(c, d)** and XCO **(e, f)** at Yekaterinburg.

C

APPENDIX FOR MAX-DOAS CAMPAIGN

C.1 DOAS ANALYSIS INPUT SETTINGS

Tables C.1 and C.1 summarized the setting used for the DOAS retrieval of NO_2 and O_4 in the UV and Vis wavelength range.

PARAMETER	BASELINE SETTING
Wavelength range	338-370 nm.
Fraunhofer reference	Sequential.
Polynomial degree	5.
Intensity offset	Constant
Absorption cross sections	
NO_2	At 298 K and 220K. Both from (Vandaele et al., 1998). I_0 corrected (SCD $10^{17} molec.cm^{-2}$)
O_3	At 223K and 243K. Both from (Serdyuchenko et al., 2014). I_0 corrected (SCD $10^{20} molec.cm^{-2}$).
O_4	At 293K. From (Thalman and Volkamer, 2013).
HCHO	At 297K. From (Meller and Moortgat, 2000).
BrO	At 223K. From (Fleischmann et al., 2004).
Ring	Based on reference SAO solar spectra (Chance and Kurucz, 2010).

Table C.1: DOAS fit analysis inputs for NO_2 in the UV wavelength range used in this thesis.

C.2 DOAS FIT EXAMPLE RESULT

The DOAS fit presented in the next figure was done by using DOASIS software (Kraus, 2006) with all the inputs described in Table C.1, and C.3.

PARAMETER	BASELINE SETTING
Wavelength range	425-490 nm.
Fraunhofer reference	Sequential.
Polynomial degree	5.
Intensity offset	Constant
Absorption cross sections	
NO_2	At 298K and 220K. Both from (Vandaele et al., 1998). I_0 corrected (SCD $10^{17} molec.cm^{-2}$)
O_3	At 223K. From (Serdyuchenko et al., 2014). I_0 corrected (SCD $10^{20} molec.cm^{-2}$).
O_4	At 293K. From (Thalman and Volkamer, 2013).
H_2O	At 296K. (Rothman et al., 2010).
Ring	Based on reference SAO solar spectra (Chance and Kurucz, 2010).

Table C.2: As Table C.1 but for NO_2 in the Vis range.
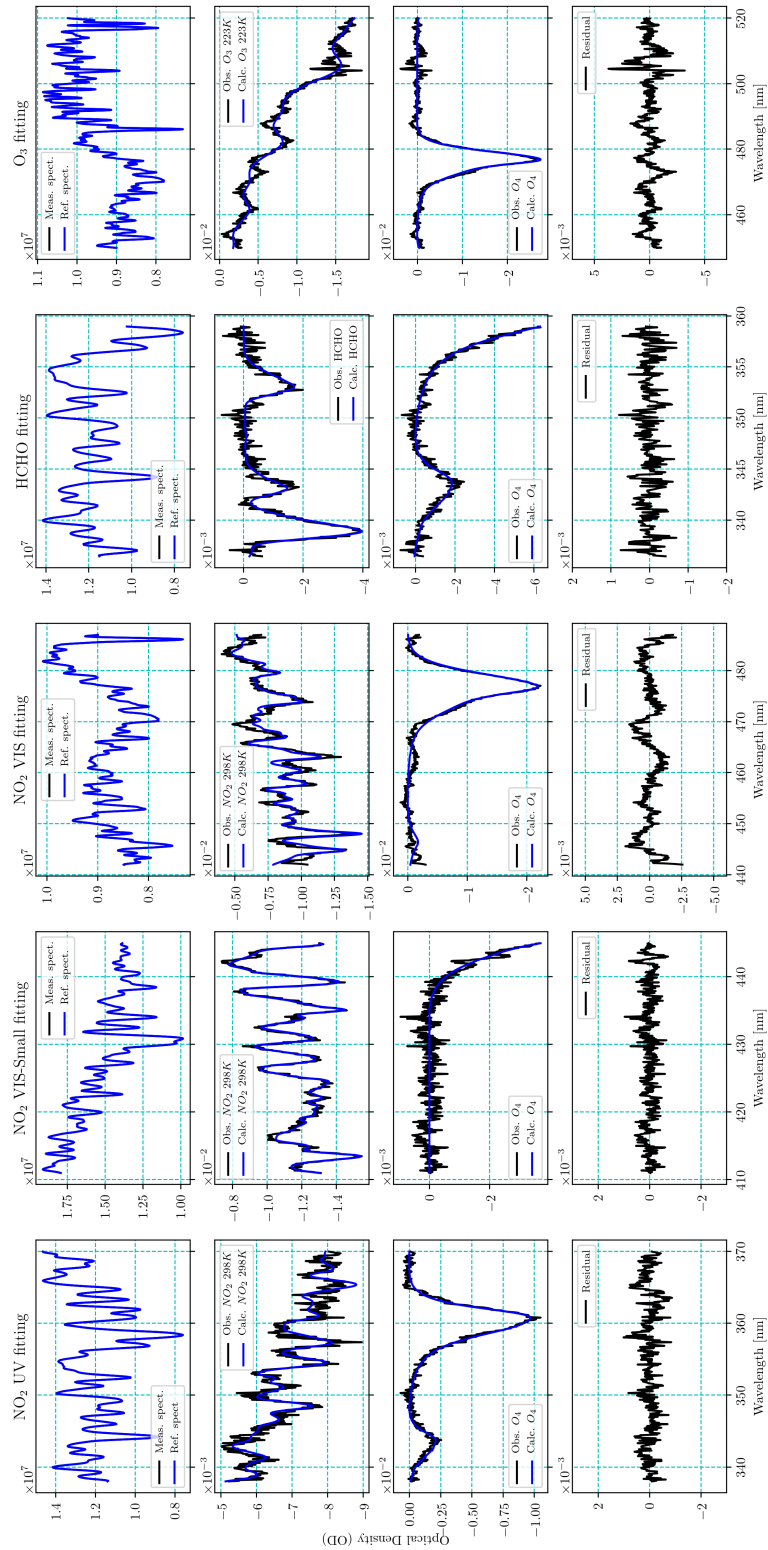
Figure C.1: Typical DOAS fit for NO_2 UV,NO_2 vis-small,NO_2 vis, HCHO and O_3 obtained with DOASIS for a observation at KIT-TRO tower at $5°$ and $\sim$ at noon time on July 25, 2019. Optical densities of the fitted trace gases(blue line) and the observed (black line) are displayed.

C.3 AEROSOL AND RACE GAS VERTICAL PROFILE INPUT SETTINGS

PARAMETER	VALUES USED
Atmosphere definition	Pressure, temperature, total air density, and O_3 vertical profiles averaged from O_3 sonde measurements in De Bilt (09/2013-2015). Surface albedo fixed to 0.06.
Retrieval altitude grid	0-3km/step 100m. The surface height and instrument altitude are fixed to 0m.
Wavelength	360nm for species in the UV range and 477nm for species in the Vis range.
Aerosol settings	Single Scattering Albedo (SSA): 0.92 and the asymmetry factor: 0.68 for both 360 and 477nm.
O_4 scaling	1.0
Elevation angles	1°, 2°, 3°, 5°, 10°, 20° and 40°.
A priori profiles	Exponentially-decreasing profiles derived using the following AOD/VCD and scaling height (SH) values: • AOD: 0.18 for both 360 and 477 nm • NO_2 VCD: 9e15 molec.cm^{-2} • A scaling height of 1 km is used for all species.
A priori covariance matrices	Variance of 50% of the a priori profile for the diagonal terms.
Correlation length of the a priori profile (km)	200 m.

Table C.3: Settings used for the aerosol and trace gas vertical profile retrieval.

BIBLIOGRAPHY

AMS (2022). In: *Climatology. Glossary of Meteorology*. URL: https://glossary.ametsoc.org/wiki/Atmospheric_window (cit. on p. 28).

Airyx (May 2022). *SkySpec 2D Instrument v.250*. Airyx. Justus-von-Liebig-Strasse 14, 69214 Eppelheim. URL: https://airyx.de/wp-content/uploads/2022/05/SkySpec-2D_v250.pdf (cit. on p. 86).

Alberti, C., F. Hase, M. Frey, D. Dubravica, T. Blumenstock, A. Dehn, P. Castracane, G. Surawicz, R. Harig, B. C. Baier, C. Bès, J. Bi, H. Boesch, A. Butz, Z. Cai, J. Chen, S. M. Crowell, N. M. Deutscher, D. Ene, J. E. Franklin, O. García, D. Griffith, B. Grouiez, M. Grutter, A. Hamdouni, S. Houweling, N. Humpage, N. Jacobs, S. Jeong, L. Joly, N. B. Jones, D. Jouglet, R. Kivi, R. Kleinschek, M. Lopez, D. J. Medeiros, I. Morino, N. Mostafavipak, A. Müller, H. Ohyama, P. I. Palmer, M. Pathakoti, D. F. Pollard, U. Raffalski, M. Ramonet, R. Ramsay, M. K. Sha, K. Shiomi, W. Simpson, W. Stremme, Y. Sun, H. Tanimoto, Y. Té, G. M. Tsidu, V. A. Velazco, F. Vogel, M. Watanabe, C. Wei, D. Wunch, M. Yamasoe, L. Zhang, and J. Orphal (2022a). "Improved calibration procedures for the EM27/SUN spectrometers of the COllaborative Carbon Column Observing Network (COCCON)." In: *Atmospheric Measurement Techniques* 15.8, pp. 2433–2463. DOI: 10.5194/amt-15-2433-2022. URL: https://amt.copernicus.org/articles/15/2433/2022/ (cit. on pp. vi, 3, 139).

Alberti, C., Q. Tu, F. Hase, M. V. Makarova, K. Gribanov, S. C. Foka, V. Zakharov, T. Blumenstock, M. Buchwitz, C. Diekmann, B. Ertl, M. M. Frey, H. Kh. Imhasin, D. V. Ionov, F. Khosrawi, S. I. Osipov, M. Reuter, M. Schneider, and T. Warneke (2022b). "Investigation of spaceborne trace gas products over St Petersburg and Yekaterinburg, Russia, by using COllaborative Column Carbon Observing Network (COCCON) observations." In: *Atmospheric Measurement Techniques* 15.7, pp. 2199–2229. DOI: 10.5194/amt-15-2199-2022. URL: https://amt.copernicus.org/articles/15/2199/2022/ (cit. on p. vi).

Alicke, Björn, Kai Hebestreit, Jochen Stutz, and Ulrich Platt (Feb. 1999). "Iodine oxide in the marine boundary layer." In: *Nature* 397.6720, pp. 572–573. DOI: 10.1038/17508 (cit. on p. 51).

Angevine, W. M., J. Peischl, A. Crawford, C. P. Loughner, I. B. Pollack, and C. R. Thompson (2020). "Errors in top-down estimates of emissions using a known source." In: *Atmospheric Chemistry and Physics* 20.20, pp. 11855–11868. DOI: 10.5194/acp-20-11855-2020. URL: https://acp.copernicus.org/articles/20/11855/2020/ (cit. on p. 178).

Arlander, D. W., D. Brüning, U. Schmidt, and Ehhalt. (1995). "The tropospheric distribution of formaldehyde during TROPOZ II." In: *Journal of Atmospheric Chemistry* 22.3, pp. 251–269 (cit. on p. 14).

BMU (Dec. 1, 2019). *Umweltradioaktivität und Strahlenbelastung Jahresbericht 2018*. German. Bonn: Bundesministerium für Umwelt, Naturschutz und nukleare Sicherheit (BMU). URL: https://doris.bfs.de/jspui/bitstream/urn:nbn:de:0221-2021011124821/1/JB2018_2020.pdf. December 2019 (cit. on p. 158).

Ball, Philip (Nov. 2000). "Fast-acting atmospheric detergent." In: *Nature*. DOI: `10.1038/news001109-1` (cit. on p. 12).

Bekker, A., H. Holland, PL. Wang, D. Rumble, H. Stein, J. Hannah, L. Coetzee, and N. Beukes (Jan. 2004). "Dating the rise of atmospheric oxygen." In: *Nature* 427.6970, pp. 117–120. DOI: `10.1038/nature02260` (cit. on p. 9).

Bergamaschi, P., S. Houweling, A. Segers, M. Krol, C. Frankenberg, R. A. Scheepmaker, E. Dlugokencky, S. C. Wofsy, E. A. Kort, C. Sweeney, T. Schuck, C. Brenninkmeijer, H. Chen, V. Beck, and C. Gerbig (2013). "Atmospheric CH4 in the first decade of the 21st century: Inverse modeling analysis using SCIAMACHY satellite retrievals and NOAA surface measurements." In: *Journal of Geophysical Research: Atmospheres* 118.13, pp. 7350–7369. DOI: `https://doi.org/10.1002/jgrd.50480`. eprint: `https://agupubs.onlinelibrary.wiley.com/doi/pdf/10.1002/jgrd.50480`. URL: `https://agupubs.onlinelibrary.wiley.com/doi/abs/10.1002/jgrd.50480` (cit. on p. 184).

Bergamaschi, P., M. Krol, J. F. Meirink, F. Dentener, A. Segers, J. van Aardenne, S. Monni, A. T. Vermeulen, M. Schmidt, M. Ramonet, C. Yver, F. Meinhardt, E. G. Nisbet, R. E. Fisher, S. O'Doherty, and E. J. Dlugokencky (2010). "Inverse modeling of European CH4 emissions 2001-2006." In: *Journal of Geophysical Research: Atmospheres* 115.D22. DOI: `https://doi.org/10.1029/2010JD014180`. eprint: `https://agupubs.onlinelibrary.wiley.com/doi/pdf/10.1029/2010JD014180`. URL: `https://agupubs.onlinelibrary.wiley.com/doi/abs/10.1029/2010JD014180` (cit. on p. 184).

Bernardo, Cirilo and David W. T. Griffith (Oct. 2005). "Fourier transform spectrometer instrument lineshape (ILS) retrieval by Fourier deconvolution." In: 95.2, pp. 141–150. DOI: `10.1016/j.jqsrt.2004.10.001` (cit. on p. 2).

Bernath, Peter F. (2016). *Spectra of atoms and molecules*. Third Edition. New York: Oxford University Press, p. 488. ISBN: 9780199382576 (cit. on p. 35).

Blumenstock, T., F. Hase, A. Keens, D. Czurlok, O. Colebatch, O. Garcia, D. W. T. Griffith, M. Grutter, J. W. Hannigan, P. Heikkinen, P. Jeseck, N. Jones, R. Kivi, E. Lutsch, M. Makarova, H. K. Imhasin, J. Mellqvist, I. Morino, T. Nagahama, J. Notholt, I. Ortega, M. Palm, U. Raffalski, M. Rettinger, J. Robinson, M. Schneider, C. Servais, D. Smale, W. Stremme, K. Strong, R. Sussmann, Y. Té, and V. A. Velazco (2021). "Characterization and potential for reducing optical resonances in Fourier transform infrared spectrometers of the Network for the Detection of Atmospheric Composition Change (NDACC)." In: *Atmospheric Measurement Techniques* 14.2, pp. 1239–1252. DOI: `10.5194/amt-14-1239-2021`. URL: `https://amt.copernicus.org/articles/14/1239/2021/` (cit. on pp. 95, 120, 123).

Bobrowski, N., G. Hönninger, B. Galle, and U. Platt (May 2003). "Detection of bromine monoxide in a volcanic plume." In: *Nature* 423.6937, pp. 273–276. DOI: `10.1038/nature01625` (cit. on p. 51).

Borger, C., M. Schneider, B. Ertl, F. Hase, O. E. García, M. Sommer, M. Höpfner, S. A. Tjemkes, and X. Calbet (2018). "Evaluation of MUSICA IASI tropospheric water vapour profiles using theoretical error assessments and comparisons to GRUAN Vaisala RS92 measurements." In: *Atmospheric Measurement Techniques* 11.9, pp. 4981–5006. DOI: `10.5194/amt-11-4981-2018`. URL: `https://amt.copernicus.org/articles/11/4981/2018/` (cit. on p. 183).

Borsdorff, T., J. Aan de Brugh, H. Hu, I. Aben, O. Hasekamp, and J. Landgraf (2018a). "Measuring Carbon Monoxide With TROPOMI: First Results and a Comparison With ECMWF-IFS Analysis Data." In: *Geophysical Research Letters* 45.6, pp. 2826–2832. DOI: https://doi.org/10.1002/2018GL077045. eprint: https://agupubs.onlinelibrary.wiley.com/doi/pdf/10.1002/2018GL077045. URL: https://agupubs.onlinelibrary.wiley.com/doi/abs/10.1002/2018GL077045 (cit. on p. 182).

Borsdorff, T., J. aan de Brugh, H. Hu, O. Hasekamp, R. Sussmann, M. Rettinger, F. Hase, J. Gross, M. Schneider, O. Garcia, W. Stremme, M. Grutter, D. G. Feist, S. G. Arnold, M. De Mazière, M. Kumar Sha, D. F. Pollard, M. Kiel, C. Roehl, P. O. Wennberg, G. C. Toon, and J. Landgraf (2018b). "Mapping carbon monoxide pollution from space down to city scales with daily global coverage." In: *Atmospheric Measurement Techniques* 11.10, pp. 5507–5518. DOI: 10.5194/amt-11-5507-2018. URL: https://amt.copernicus.org/articles/11/5507/2018/ (cit. on pp. 139, 182).

Borsdorff, T., J. aan de Brugh, A. Schneider, A. Lorente, M. Birk, G. Wagner, R. Kivi, F. Hase, D. G. Feist, R. Sussmann, M. Rettinger, D. Wunch, T. Warneke, and J. Landgraf (2019). "Improving the TROPOMI CO data product: update of the spectroscopic database and destriping of single orbits." In: *Atmospheric Measurement Techniques* 12.10, pp. 5443–5455. DOI: 10.5194/amt-12-5443-2019. URL: https://amt.copernicus.org/articles/12/5443/2019/ (cit. on p. 139).

Brasseur, Guy P., John J. Orlando, and Geoffrey S. Tyndall (1999). *Atmospheric Chemistry and Global Change*. Oxford University Press, Inc. (cit. on pp. 14, 15).

Bruker (2017). *OPUS/IR Reference Manual version 7.0*. Bruker Optik GmbH. Ettlingen Germany (cit. on p. 120).

Brune, S., J. D. Keller, and S. Wahl (2021). "Evaluation of wind speed estimates in reanalyses for wind energy applications." In: *Advances in Science and Research* 18, pp. 115–126. DOI: 10.5194/asr-18-115-2021. URL: https://asr.copernicus.org/articles/18/115/2021/ (cit. on p. 178).

Butz, A., A. S. Dinger, N. Bobrowski, J. Kostinek, L. Fieber, C. Fischerkeller, G. B. Giuffrida, F. Hase, F. Klappenbach, J. Kuhn, P. Lübcke, L. Tirpitz, and Q. Tu (2017). "Remote sensing of volcanic CO_2, HF, HCl, SO_2, and BrO in the downwind plume of Mt. Etna." In: *Atmospheric Measurement Techniques* 10.1, pp. 1–14. DOI: 10.5194/amt-10-1-2017. URL: https://amt.copernicus.org/articles/10/1/2017/ (cit. on p. 2).

Chance, K. and R. L. Kurucz (2010). "An improved high-resolution solar reference spectrum for earth's atmosphere measurements in the ultraviolet, visible, and near infrared." In: *Journal of Quantitative Spectroscopy and Radiative Transfer*, pp. 1289–1295 (cit. on pp. 57, 61, 66, 191, 192).

Chen, J., F. Dietrich, H. Maazallahi, A. Forstmaier, D. Winkler, M. E. G. Hofmann, H. Denier van der Gon, and T. Röckmann (2020). "Methane emissions from the Munich Oktoberfest." In: *Atmospheric Chemistry and Physics* 20.6, pp. 3683–3696. DOI: 10.5194/acp-20-3683-2020. URL: https://acp.copernicus.org/articles/20/3683/2020/ (cit. on p. 2).

Chen, J., C. Viatte, J. K. Hedelius, T. Jones, J. E. Franklin, H. Parker, E. W. Gottlieb, P. O. Wennberg, M. K. Dubey, and S. C. Wofsy (2016). "Differential column measurements using compact solar-tracking spectrometers." In: *Atmospheric Chemistry and Physics*

16.13, pp. 8479–8498. DOI: 10.5194/acp-16-8479-2016. URL: https://acp.copernicus.org/articles/16/8479/2016/ (cit. on p. 2).

Chevallier, F. (Apr. 27, 2020). *Description of the CO2 inversion production chain 2020*. English. ECMWF COPERNICUS REPORT. Version 1.0. European Centre for Medium-Range Weather Forecasts (ECMWF). 15 pp. URL: https://atmosphere.copernicus.eu/sites/default/files/2020-06/CAMS73_2018SC2_D5.2.1-2020_202004_CO2inversionproductionchain_v1.pdf (visited on 09/09/2022) (cit. on pp. 139, 183).

— (Sept. 8, 2021). *Validation report for the CO2 fluxes estimated by atmospheric inversion, v20r2*. ECMWF COPERNICUS REPORT. European Centre for Medium-Range Weather Forecasts(ECMWF). 22 pp. URL: https://atmosphere.copernicus.eu/sites/default/files/custom-uploads/EQC-GHG/CAMS73_2018SC2_D73.1.4.1-2020-v5_202109_v1.pdf (visited on 09/09/2022) (cit. on pp. 139, 183).

Clémer, K., M. Van Roozendael, C. Fayt, F. Hendrick, C. Hermans, G. Pinardi, R. Spurr, P. Wang, and M. De Mazière (2010). "Multiple wavelength retrieval of tropospheric aerosol optical properties from MAXDOAS measurements in Beijing." In: *Atmos. Meas. Tech.* 3.4, pp. 863–878. DOI: 10.5194/amt-3-863-2010. URL: https://www.atmos-meas-tech.net/3/863/2010/ (cit. on p. 84).

Clerbaux, C., A. Boynard, L. Clarisse, M. George, J. Hadji-Lazaro, H. Herbin, D. Hurtmans, M. Pommier, A. Razavi, S. Turquety, C. Wespes, and P.-F. Coheur (2009). "Monitoring of atmospheric composition using the thermal infrared IASI/MetOp sounder." In: *Atmospheric Chemistry and Physics* 9.16, pp. 6041–6054. DOI: 10.5194/acp-9-6041-2009. URL: https://acp.copernicus.org/articles/9/6041/2009/ (cit. on p. 183).

Connor, Brian J., Hartmut Boesch, Geoffrey Toon, Bhaswar Sen, Charles Miller, and David Crisp (2008). "Orbiting Carbon Observatory: Inverse method and prospective error analysis." In: *Journal of Geophysical Research: Atmospheres* 113.D5. DOI: https://doi.org/10.1029/2006JD008336. eprint: https://agupubs.onlinelibrary.wiley.com/doi/pdf/10.1029/2006JD008336. URL: https://agupubs.onlinelibrary.wiley.com/doi/abs/10.1029/2006JD008336 (cit. on pp. 142, 143).

Crippa, M., D. Guizzardi, E. Schaaf, E. Solazzo, M. Muntean, F. Monforti-Ferrario, J. G. J. Olivier, and E. Vignati (Sept. 6, 2021a). *EDGAR v6.0 Greenhouse Gas Emissions*. English. URL: http://data.europa.eu/89h/97a67d67-c62e-4826-b873-9d972c4f670b (cit. on p. 134).

— (Sept. 6, 2021b). *Emissions Database for Global Atmospheric Research (EDGAR) v6.0*. English. URL: https://edgar.jrc.ec.europa.eu/index.php/dataset_ghg60 (visited on 09/16/2022) (cit. on p. 134).

— (May 12, 2021c). *Fossil CO2 and GHG emissions of all world countries - 2021*. Tech. rep. Joint Research Centre, European Commission. (in prep.) (Cit. on p. 134).

Crisp, D. (Sept. 2015). "Measuring atmospheric carbon dioxide from space with the Orbiting Carbon Observatory-2 (OCO-2)." In: ed. by James J. Butler, Xiaoxiong (Jack) Xiong, and Xingfa Gu. San Diego, California, United States, p. 960702. DOI: 10.1117/12.2187291. URL: http://proceedings.spiedigitallibrary.org/proceeding.aspx?doi=10.1117/12.2187291 (cit. on p. 182).

Crisp, D., H. R. Pollock, R. Rosenberg, L. Chapsky, R. A. M. Lee, F. A. Oyafuso, C. Frankenberg, C. W. O'Dell, C. J. Bruegge, G. B. Doran, A. Eldering, B. M. Fisher, D. Fu, M. R. Gunson, L. Mandrake, G. B. Osterman, F. M. Schwandner, K. Sun, T. E. Taylor, P. O.

Wennberg, and D. Wunch (2017). "The on-orbit performance of the Orbiting Carbon Observatory-2 (OCO-2) instrument and its radiometrically calibrated products." In: *Atmospheric Measurement Techniques* 10.1, pp. 59–81. DOI: 10.5194/amt-10-59-2017. URL: https://amt.copernicus.org/articles/10/59/2017/ (cit. on p. 2).

Crutzen, Paul J. (1979). "The Role of NO and NO2 in the chemistry of the troposphere and stratosphere." In: *Annual Review of Earth and Planetary Sciences* (cit. on pp. 13, 14).

Cullis, C. F. and B. M. Willatt (1983). "Oxidation of methane over supported precious metal catalysts." In: *Journal of Catalysis* 83.2, pp. 267–285. ISSN: 0021-9517. DOI: https://doi.org/10.1016/0021-9517(83)90054-4. URL: https://www.sciencedirect.com/science/article/pii/0021951783900544 (cit. on p. 142).

D., Ehhalt, Prather M., Dentener F., Derwent R., Dlugokencky E., Holland E., Isaksen I., Katima J., Kirchhoff V., Matson P., Midgley P., and Wang M. (2001). "Concentrations and Distributions of Atmospheric Trace Gases. In: Climate Change 2001: The Scientific Basis. Contribution of Working Group I to the Third Assessment Report of the Intergovernmental Panel on Climate Change." In: *Cambridge University Press*. Ed. by Houghton J.T., Y. Ding, D.J. Griggs, M. Noguer, P.J. van der Linden, X. Dai, K. Maskell, and C.A. Johnson, p. 881. eprint: https://www.ipcc.ch/site/assets/uploads/2018/03/WGI_TAR_full_report.pdf (cit. on pp. 13, 16).

Danckaert, T., C. Fayt, I. Van Roozendael M. De Smedt, V. Letocart, A. Merlaud, and G. Pinardi (2017). *QDOAS Software user manual*. Royal Belgian Institute for Space Aeronomy. URL: http://uv-vis.aeronomie.be/software/QDOAS/QDOAS_manual.pdf (cit. on pp. 61, 66).

Demtröder, Wolfgang (2006). *Atoms, Molecules and Photons: An Introduction to Atomic-, Molecular and Quantum-Physics*. Springer. ISBN: 9783540206316 (cit. on pp. 41, 45).

Deutschmann, Tim, Steffen Beirle, Udo Friess, Michael Grzegorski, Christoph Kern, Lena Kritten, Ulrich Platt, Cristina Prados-Román, Janis Pukite, Thomas Wagner, Bodo Werner, and Klaus Pfeilsticker. (2010). "The Monte Carlo atmospheric radiative transfer model McArtim: Introduction and validation of Jacobians and 3D features." In: *Journal of Quantitative Spectroscopy & Radiative Transfer* 112.6, pp. 1119–1137 (cit. on pp. 70, 82).

Dietrich, F., J. Chen, B. Voggenreiter, P. Aigner, N. Nachtigall, and B. Reger (2021). "MUCCnet: Munich Urban Carbon Column network." In: *Atmospheric Measurement Techniques* 14.2, pp. 1111–1126. DOI: 10.5194/amt-14-1111-2021. URL: https://amt.copernicus.org/articles/14/1111/2021/ (cit. on p. 2).

Dix, B., C. Brenninkmeijer, U. Friess, T. Wagner, and U. Platt (Nov. 2, 2009). "Airborne multi-axis DOAS measurements of atmospheric trace gases on CARIBIC long-distance flights." In: *Atmospheric Measurement Techniques* 2.2, pp. 639–652. DOI: 10.5194/amt-2-639-2009 (cit. on p. 51).

Dix, Barbara (2007). "Spectroscopic Measurements of Atmospheric Trace Gases on Long-Distance Flights." PhD thesis. Combined Faculties for the Natural Sciences and for Mathematics of the Ruperto-Carola University of Heidelberg, Germany (cit. on pp. 13, 15).

Dlugokencky, Ed (Sept. 27, 2022). *Trends in CO2, CH4, N2O, SF6O*. English. NOAA/GML. URL: https://gml.noaa.gov/ccgg/trends/ (visited on 09/27/2022) (cit. on p. 9).

Donner, S., J. Kuhn, M. Van Roozendael, A. Bais, S. Beirle, T. Bösch, K. Bognar, I. Bruchk-
   ouski, K. L. Chan, S. Dörner, T. Drosoglou, C. Fayt, U. Frieß, F. Hendrick, C. Hermans,
   J. Jin, A. Li, J. Ma, E. Peters, G. Pinardi, A. Richter, S. F. Schreier, A. Seyler, K. Strong,
   J.-L. Tirpitz, Y. Wang, P. Xie, J. Xu, X. Zhao, and T. Wagner (2020). "Evaluating different
   methods for elevation calibration of MAX-DOAS (Multi AXis Differential Optical Ab-
   sorption Spectroscopy) instruments during the CINDI-2 campaign." In: *Atmospheric
   Measurement Techniques* 13.2, pp. 685–712. DOI: 10.5194/amt-13-685-2020. URL:
   https://amt.copernicus.org/articles/13/685/2020/ (cit. on p. 88).

Drummond, James R. and G. S. Mand (1996). "The Measurements of Pollution in the
   Troposphere (MOPITT) Instrument: Overall Performance and Calibration Require-
   ments." In: *Journal of Atmospheric and Oceanic Technology* 13.2, pp. 314–320. DOI: 10.
   1175/1520-0426(1996)013<0314:TMOPIT>2.0.CO;2. URL: https://journals.ametsoc.
   org/view/journals/atot/13/2/1520-0426_1996_013_0314_tmopit_2_0_co_2.xml
   (cit. on p. 105).

Drummond, James R., Jiansheng Zou, Florian Nichitiu, Jayanta Kar, Robert Deschambaut,
   and John Hackett (2010). "A review of 9-year performance and operation of the MO-
   PITT instrument." In: *Advances in Space Research* 45.6, pp. 760–774. ISSN: 0273-1177. DOI:
   https://doi.org/10.1016/j.asr.2009.11.019. URL: https://www.sciencedirect.
   com/science/article/pii/S0273117709007224 (cit. on p. 105).

EPA (2022a). *Facts About Formaldehyde*. English. Accessed: 2012-07-27. United States En-
   vironmental Protection Agency (EPA). URL: https://www.epa.gov/formaldehyde/
   facts\-about\-formaldehyde\#whatisformaldehyde (cit. on p. 15).

— (2022b). *Ozone Pollution*. English. Accessed: 2022-07-27. United States Environmental
   Protection Agency. URL: https://www.epa.gov/ozone\-pollution (cit. on p. 13).

Eldering, A., T. E. Taylor, C. W. O'Dell, and R. Pavlick (2019). "The OCO-3 mission: mea-
   surement objectives and expected performance based on 1 year of simulated data." In:
   Atmospheric Measurement Techniques 12.4, pp. 2341–2370. DOI: 10.5194/amt-12-2341-
   2019. URL: https://amt.copernicus.org/articles/12/2341/2019/ (cit. on p. 2).

Eldering, A., P. O. Wennberg, D. Crisp, D. S. Schimel, M. R. Gunson, A. Chatterjee, J.
   Liu, F. M. Schwandner, Y. Sun, C. W. O'Dell, C. Frankenberg, T. Taylor, B. Fisher,
   G. B. Osterman, D. Wunch, J. Hakkarainen, J. Tamminen, and B. Weir (2017). "The
   Orbiting Carbon Observatory-2 early science investigations of regional carbon dioxide
   fluxes." In: *Science* 358.6360, eaam5745. DOI: 10.1126/science.aam5745. eprint: https:
   //www.science.org/doi/pdf/10.1126/science.aam5745. URL: https://www.science.
   org/doi/abs/10.1126/science.aam5745 (cit. on pp. 2, 182).

Emde, C., R. Buras-Schnell, A. Kylling, B. Mayer, J. Gasteiger, U. Hamann, J. Kylling,
   B. Richter, C. Pause, T. Dowling, and L. Bugliaro (2016). "The libradtran software
   package for radiative transfer calculations (version 2.0.1)." In: *Geoscientific Model De-
   velopment* 9.5. DOI: 10.5194/gmd-9-1647-2016. URL: https://www.geosci-model-
   dev.net/9/1647/2016/ (cit. on pp. 22–24, 72).

Fleischmann, Oliver C., Matthias Hartmann, John P. Burrows, and Johannes Orphal. (2004).
   "New ultraviolet absorption cross-sections of BrO at atmospheric temperatures mea-
   sured by time-windowing Fourier transform spectroscopy." In: *Journal of Photochem-
   istry and Photobiology A: Chemistry* 168.1, pp. 117–132. DOI: 10.1016/j.jphotochem.

2004.03.026. URL: http://www.sciencedirect.com/science/article/pii/S1010603004001522 (cit. on p. 191).

Flemming, J., A. Benedetti, A. Inness, R. J. Engelen, L. Jones, V. Huijnen, S. Remy, M. Parrington, M. Suttie, A. Bozzo, V.-H. Peuch, D. Akritidis, and E. Katragkou (2017). "The CAMS interim Reanalysis of Carbon Monoxide, Ozone and Aerosol for 2003–2015." In: *Atmospheric Chemistry and Physics* 17.3, pp. 1945–1983. DOI: 10.5194/acp-17-1945-2017. URL: https://acp.copernicus.org/articles/17/1945/2017/ (cit. on pp. 139, 184).

Forster, P, T Storelvmo, K Armour, W Collins, J.-L Dufresne, D Frame, D Lunt, T Mauritsen, M Palmer, M Watanabe, M Wild, H Zhang, V Masson-Delmotte, P Zhai, A Pirani, S Connors, C Péan, S Berger, N Caud, Y Chen, L Goldfarb, M Gomis, M Huang, K Leitzell, E Lonnoy, J Matthews, T Maycock, T Waterfield, O Yelekçi, R Yu, and B Zhou (2021). *The Earth's Energy Budget, Climate Feedbacks, and Climate Sensitivity, in: Climate Change 2021: The Physical Science Basis, Contribution of Working Group I to the Sixth Assessment Report of the Intergovernmental Panel on Climate Change.* DOI: 10.1017/9781009157896.009 (cit. on pp. 28–30).

Francis, Diana, Ricardo Fonseca, Narendra Nelli, Deniz Bozkurt, Ghislain Picard, and Bin Guan (2022). "Atmospheric rivers drive exceptional Saharan dust transport towards Europe." In: *Atmospheric Research* 266, p. 105959. ISSN: 0169-8095. DOI: https://doi.org/10.1016/j.atmosres.2021.105959. URL: https://www.sciencedirect.com/science/article/pii/S0169809521005159 (cit. on p. 163).

Frankenberg, C., R. Pollock, R. A. M. Lee, R. Rosenberg, J.-F. Blavier, D. Crisp, C. W. O'Dell, G. B. Osterman, C. Roehl, P. O. Wennberg, and D. Wunch (2015). "The Orbiting Carbon Observatory (OCO-2): spectrometer performance evaluation using prelaunch direct sun measurements." In: *Atmospheric Measurement Techniques* 8.1, pp. 301–313. DOI: 10.5194/amt-8-301-2015. URL: https://amt.copernicus.org/articles/8/301/2015/ (cit. on p. 2).

Frey, M., F. Hase, T. Blumenstock, J. Groß, M. Kiel, G. Mengistu Tsidu, K. Schäfer, M. K. Sha, and J. Orphal (2015). "Calibration and instrumental line shape characterization of a set of portable FTIR spectrometers for detecting greenhouse gas emissions." In: *Atmospheric Measurement Techniques* 8.7, pp. 3047–3057. DOI: 10.5194/amt-8-3047-2015. URL: https://amt.copernicus.org/articles/8/3047/2015/ (cit. on pp. 2, 3, 94, 95, 98).

Frey, M., M. K. Sha, F. Hase, M. Kiel, T. Blumenstock, R. Harig, G. Surawicz, N. M. Deutscher, K. Shiomi, J. E. Franklin, H. Bösch, J. Chen, M. Grutter, H. Ohyama, Y. Sun, A. Butz, G. Mengistu Tsidu, D. Ene, D. Wunch, Z. Cao, O. Garcia, M. Ramonet, F. Vogel, and J. Orphal (2019). "Building the COllaborative Carbon Column Observing Network (COCCON): long-term stability and ensemble performance of the EM27/SUN Fourier transform spectrometer." In: *Atmospheric Measurement Techniques* 12.3, pp. 1513–1530. DOI: 10.5194/amt-12-1513-2019. URL: https://amt.copernicus.org/articles/12/1513/2019/ (cit. on pp. 2, 94, 99, 102–104, 117, 123, 139, 177).

Friess, U., P. S. Monks, J. J. Remedios, A. Rozanov, R. Sinreich, T. Wagner, and U. Platt (2006). "MAX-DOAS O_4 measurements: A new technique to derive information on atmospheric aerosols: 2. Modeling studies." In: *Journal of Geophysical Research: Atmospheres* 111.D14. DOI: https://doi.org/10.1029/2005JD006618. eprint: https://

agupubs.onlinelibrary.wiley.com/doi/pdf/10.1029/2005JD006618. URL: https://agupubs.onlinelibrary.wiley.com/doi/abs/10.1029/2005JD006618 (cit. on pp. 70, 80–82).

Friess, U., H. Sihler, R. Sander, D. Pöhler, S. Yilmaz, and U. Platt (Sept. 27, 2011). "The vertical distribution of BrO and aerosols in the Arctic: Measurements by active and passive differential optical absorption spectroscopy." In: *Journal of Geophysical Research* 116, D00R–04. DOI: 10.1029/2011jd015938 (cit. on p. 51).

Friess, Udo (2001). "Spectroscopic measurements of atmospheric trace gases at Neumayer-Station, Antarctica." PhD thesis. Faculties for the Natural Sciences and for Mathematics of the Ruperto-Carola University of Heidelberg, Germany. DOI: 10.11588/HEIDOK.00001709. URL: http://archiv.ub.uni-heidelberg.de/volltextserver/id/eprint/1709 (cit. on pp. 53, 55).

Gavrilov, N. M., M. V. Makarova, A. V. Poberovskii, and Yu. M. Timofeyev (2014). "Comparisons of CH_4 ground-based FTIR measurements near Saint Petersburg with GOSAT observations." In: *Atmospheric Measurement Techniques* 7.4, pp. 1003–1010. DOI: 10.5194/amt-7-1003-2014. URL: https://amt.copernicus.org/articles/7/1003/2014/ (cit. on p. 140).

Gisi, M., F. Hase, S. Dohe, and T. Blumenstock (2011). "Camtracker: a new camera controlled high precision solar tracker system for FTIR-spectrometers." In: *Atmospheric Measurement Techniques* 4.1, pp. 47–54. DOI: 10.5194/amt-4-47-2011. URL: https://amt.copernicus.org/articles/4/47/2011/ (cit. on pp. 91, 93).

Gisi, M., F. Hase, S. Dohe, T. Blumenstock, A. Simon, and A. Keens (2012). "XCO_2-measurements with a tabletop FTS using solar absorption spectroscopy." In: *Atmospheric Measurement Techniques* 5.11, pp. 2969–2980. DOI: 10.5194/amt-5-2969-2012. URL: https://amt.copernicus.org/articles/5/2969/2012/ (cit. on pp. 2, 95).

Gon, H. A. C. Denier van der, J. J. P. Kuenen, G. Janssens-Maenhout, U. Döring, S. Jonkers, and A. Visschedijk (2017). "TNO_CAMS high resolution European emission inventory 2000–2014 for anthropogenic CO_2 and future years following two different pathways." In: *Earth System Science Data Discussions* 2017, pp. 1–30. DOI: 10.5194/essd-2017-124. URL: https://essd.copernicus.org/preprints/essd-2017-124/ (cit. on p. 159).

Gordon, I. E., L. S. Rothman, R. J. Hargreaves, R. Hashemi, E. V. Karlovets, F. M. Skinner, E. K. Conway, C. Hill, R. V. Kochanov, Y. Tan, P. Wcisło, A. A. Finenko, K. Nelson, P. F. Bernath, M. Birk, V. Boudon, A. Campargue, K. V. Chance, A. Coustenis, B. J. Drouin, J. M. Flaud, R. R. Gamache, J. T. Hodges, D. Jacquemart, E. J. Mlawer, A. V. Nikitin, V. I. Perevalov, M. Rotger, J. Tennyson, G. C. Toon, H. Tran, V. G. Tyuterev, E. M. Adkins, A. Baker, A. Barbe, E. Cane, A. G. Császár, A. Dudaryonok, O. Egorov, A. J. Fleisher, H. Fleurbaey, A. Foltynowicz, T. Furtenbacher, J. J. Harrison, J. M. Hartmann, V. M. Horneman, X. Huang, T. Karman, J. Karns, S. Kassi, I. Kleiner, V. Kofman, F. Kwabia–Tchana, N. N. Lavrentieva, T. J. Lee, D. A. Long, A. A. Lukashevskaya, O. M. Lyulin, V. Yu. Makhnev, W. Matt, S. T. Massie, M. Melosso, S. N. Mikhailenko, D. Mondelain, H. S. P. Müller, O. V. Naumenko, A. Perrin, O. L. Polyansky, E. Raddaoui, P. L. Raston, Z. D. Reed, M. Rey, C. Richard, R. Tóbiás, I. Sadiek, D. W. Schwenke, E. Starikova, K. Sung, F. Tamassia, S. A. Tashkun, J. Vander Auwera, I. A. Vasilenko, A. A. Vigasin, G. L. Villanueva, B. Vispoel, G. Wagner, A. Yachmenev, and S. N. Yurchenko (2022). "The HITRAN2020 molecular spectroscopic

database." In: *Journal of Quantitative Spectroscopy and Radiative Transfer* 277, p. 107949. ISSN: 0022-4073. DOI: https://doi.org/10.1016/j.jqsrt.2021.107949. URL: https://www.sciencedirect.com/science/article/pii/S0022407321004416 (cit. on p. 72).

Gordon, I.E., L.S. Rothman, C. Hill, R.V. Kochanov, Y. Tan, P.F. Bernath, M. Birk, V. Boudon, A. Campargue, K.V. Chance, B.J. Drouin, J.-M. Flaud, R.R. Gamache, J.T. Hodges, D. Jacquemart, V.I. Perevalov, A. Perrin, K.P. Shine, M.-A.H. Smith, J. Tennyson, G.C. Toon, H. Tran, V.G. Tyuterev, A. Barbe, A.G. Császár, V.M. Devi, T. Furtenbacher, J.J. Harrison, J.-M. Hartmann, A. Jolly, T.J. Johnson, T. Karman, I. Kleiner, A.A. Kyuberis, J. Loos, O.M. Lyulin, S.T. Massie, S.N. Mikhailenko, N. Moazzen-Ahmadi, H.S.P. Müller, O.V. Naumenko, A.V. Nikitin, O.L. Polyansky, M. Rey, M. Rotger, S.W. Sharpe, K. Sung, E. Starikova, S.A. Tashkun, J. Vander Auwera, G. Wagner, J. Wilzewski, P. Wcisło, S. Yu, and E.J. Zak (2017). "The HITRAN2016 molecular spectroscopic database." In: *Journal of Quantitative Spectroscopy and Radiative Transfer* 203. HITRAN2016 Special Issue, pp. 3–69. ISSN: 0022-4073. DOI: https://doi.org/10.1016/j.jqsrt.2017.06.038. URL: https://www.sciencedirect.com/science/article/pii/S0022407317301073 (cit. on p. 72).

Grainger, Roy Gordon (Oct. 7, 2013). *Atmospheric Radiative Transfer. In Chapter 4: Electromagnetic Absorption and Emission byAtoms and Molecules*. English. University of Oxford. URL: http://eodg.atm.ox.ac.uk/user/grainger/research/book/protected/Chapter4.pdf (cit. on pp. 32, 33).

Griffiths, Peter R. and James A. de Haseth (Apr. 2007). *Fourier Transform Infrared Spectrometry*. Ed. by J. D. Winefordner. Second. Chemical Analysis: A Series of Monographs on Analytical Chemistry and its Aplications. A John Wiley and Sons, Inc. 556 pp. ISBN: 0471194042. URL: https://www.ebook.de/de/product/5178742/griffiths_de_haseth_fourier_transform_2e_c.html (cit. on pp. 36, 45, 46, 48, 50).

Grossmann, Katja (2014). "Aircraft-borne DOAS limb observations of UV/visible absorbing trace gas species over Borneo: Implications for the photochemistry of iodine, volatile organic oxide degradation, and lightning-produced radicals." PhD thesis. Faculties for the Natural Sciences and for Mathematics of the Ruperto-Carola University of Heidelberg, Germany (cit. on pp. 23, 25, 56, 59, 62, 70, 81).

Guzzi, Rodolfo, Louis J. Lanzerotti, and Ulrich Platt., eds. (2011). *The Remote Sensing of Tropospheric Composition from Space*. Physics of Earth and Space Environments. Springer-Verlag Berlin Heidelberg. ISBN: 978-3-642-14790-6. DOI: 10.1007/978-3-642-14791-3. URL: https://link.springer.com/book/10.1007/978-3-642-14791-3 (cit. on pp. 29, 69).

Hagemann, Rowell, Ulrich Corsmeier, Christoph Kottmeier, Rayk Rinke, Andreas Wieser, and Bernhard Vogel (2014). "Spatial variability of particle number concentrations and NOx in the Karlsruhe (Germany) area obtained with the mobile laboratory AEROTRAM." In: *Atmospheric Environment* 94, pp. 341–352. ISSN: 1352-2310. DOI: https://doi.org/10.1016/j.atmosenv.2014.05.051. URL: https://www.sciencedirect.com/science/article/pii/S1352231014003987 (cit. on pp. 157, 159).

Halla, J., T. Wagner, S. Beirle, J. Brook, K. Hayden, J. O'brien, A. Ng, D. Majonis, M. Wenig, and R. Mclaren (Dec. 13, 2011). "Determination of tropospheric vertical columns of NO2 and aerosol optical properties in a rural setting using MAX-DOAS." In: *Atmo-*

spheric Chemistry and Physics 11.23, pp. 12475–12498. DOI: 10.5194/acp-11-12475-2011 (cit. on p. 51).

Harris, Paul G., Alice S. Y. Chow, and Jonathan Symons (2012). "Greenhouse gas emissions from cities and regions: International implications revealed by Hong Kong." In: *Energy Policy* 44, pp. 416–424. ISSN: 0301-4215. DOI: https://doi.org/10.1016/j.enpol.2012.02.012. URL: https://www.sciencedirect.com/science/article/pii/S0301421512001280 (cit. on p. 1).

Hase, F. (2012). "Improved instrumental line shape monitoring for the ground-based, high-resolution FTIR spectrometers of the Network for the Detection of Atmospheric Composition Change." In: *Atmospheric Measurement Techniques* 5.3, pp. 603–610. DOI: 10.5194/amt-5-603-2012. URL: https://amt.copernicus.org/articles/5/603/2012/ (cit. on p. 2).

Hase, F., B. J. Drouin, C. M. Roehl, G. C. Toon, P. O. Wennberg, D. Wunch, T. Blumenstock, F. Desmet, D. G. Feist, P. Heikkinen, M. De Mazière, M. Rettinger, J. Robinson, M. Schneider, V. Sherlock, R. Sussmann, Y. Té, T. Warneke, and C. Weinzierl (2013). "Calibration of sealed HCl cells used for TCCON instrumental line shape monitoring." In: *Atmospheric Measurement Techniques* 6.12, pp. 3527–3537. DOI: 10.5194/amt-6-3527-2013. URL: https://amt.copernicus.org/articles/6/3527/2013/ (cit. on p. 100).

Hase, F., M. Frey, T. Blumenstock, J. Groß, M. Kiel, R. Kohlhepp, G. Mengistu Tsidu, K. Schäfer, M. K. Sha, and J. Orphal (2015). "Application of portable FTIR spectrometers for detecting greenhouse gas emissions of the major city Berlin." In: *Atmospheric Measurement Techniques* 8.7, pp. 3059–3068. DOI: 10.5194/amt-8-3059-2015. URL: https://amt.copernicus.org/articles/8/3059/2015/ (cit. on pp. 2, 115, 116).

Hase, F., J. W. Hannigan, M. T. Coffey, A. Goldman, M. Höpfner, N. B. Jones, C. P. Rinsland, and S. W. Wood (2004). "Intercomparison of retrieval codes used for the analysis of high-resolution, ground-based FTIR measurements." In: *Journal of Quantitative Spectroscopy and Radiative Transfer* 87.1, pp. 25–52. ISSN: 0022-4073. DOI: https://doi.org/10.1016/j.jqsrt.2003.12.008. URL: https://www.sciencedirect.com/science/article/pii/S0022407303003765 (cit. on p. 73).

Hase, Frank, Thomas Blumenstock, and Clare Paton-Walsh (May 1999). "Analysis of the instrumental line shape of high-resolution Fourier transform IR spectrometers with gas cell measurements and new retrieval software." In: *Appl. Opt.* 38.15, pp. 3417–3422. DOI: 10.1364/AO.38.003417. URL: http://opg.optica.org/ao/abstract.cfm?URI=ao-38-15-3417 (cit. on pp. 2, 94, 98).

Hase, Frank, Matthias Frey, Matthäus Kiel, Thomas Blumenstock, Roland Harig, Axel Keens, and Johannes Orphal (May 2016). "Addition of a channel for XCO observations to a portable FTIR spectrometer for greenhouse gas measurements." en. In: *Atmospheric Measurement Techniques* 9.5, pp. 2303–2313. ISSN: 1867-8548. DOI: 10.5194/amt-9-2303-2016. URL: https://amt.copernicus.org/articles/9/2303/2016/ (cit. on pp. 2, 91, 105).

Hausmann, M. and U. Platt (1994). "Spectroscopic measurement of bromine oxide and ozone in the high Arctic during Polar Sunrise Experiment 1992." In: *Journal of Geophysical Research* 99.D12, p. 25399. DOI: 10.1029/94jd01314 (cit. on p. 51).

Heckel, A., A. Richter, T. Tarsu, F. Wittrock, C. Hak, I. Pundt, W. Junkermann, and J. Burrows (Mar. 21, 2005). "MAX-DOAS measurements of formaldehyde in the Po-Valley." In: *Atmospheric Chemistry and Physics* 5.4, pp. 909–918. DOI: 10.5194/acp-5-909-2005 (cit. on pp. 51, 162).

Hedelius, J. K., C. Viatte, D. Wunch, C. M. Roehl, G. C. Toon, J. Chen, T. Jones, S. C. Wofsy, J. E. Franklin, H. Parker, M. K. Dubey, and P. O. Wennberg (2016). "Assessment of errors and biases in retrievals of X_{CO_2}, X_{CH_4}, X_{CO}, and X_{N_2O} from a $0.5\,cm^{-1}$ resolution solar-viewing spectrometer." In: *Atmospheric Measurement Techniques* 9.8, pp. 3527–3546. DOI: 10.5194/amt-9-3527-2016. URL: https://amt.copernicus.org/articles/9/3527/2016/ (cit. on pp. 2, 142).

Hendrick, F., J-F. Müller, K. Clémer, P. Wang, M. De Mazi`ere, C. Fayt, C. Gielen, C. Hermans, J. Ma, G. Pinardi, T. Stavrakou, T. Vlemmix, and M. Van Roozendael (Jan. 22, 2014). "Four years of ground-based MAX-DOAS observations of HONO and NO2 in the Beijing area." In: *Atmospheric Chemistry and Physics* 14.2, pp. 765–781. DOI: 10.5194/acp-14-765-2014 (cit. on p. 51).

Henyey, L. G. and J. L. Greenstein (Jan. 1941). "Diffuse radiation in the Galaxy." In: *Astrophysical Journal* 93, pp. 70–83. DOI: 10.1086/144246 (cit. on p. 24).

Hilboll, Andreas (2014). "Tropospheric nitrogen dioxide from satellite measurements: SCIAMACHY limb / nadir matching and multi-instrument trend analysis." PhD thesis. University of Bremen (cit. on p. 19).

Holmes, Christopher D. (2018). "Methane Feedback on Atmospheric Chemistry: Methods, Models, and Mechanisms." In: *Journal of Advances in Modeling Earth Systems* 10.4, pp. 1087–1099. DOI: https://doi.org/10.1002/2017MS001196. eprint: https://agupubs.onlinelibrary.wiley.com/doi/pdf/10.1002/2017MS001196. URL: https://agupubs.onlinelibrary.wiley.com/doi/abs/10.1002/2017MS001196 (cit. on p. 7).

Hönninger G., von Friedeburg C. and U. Platt (2004). "Multi axis differential optical absorption spectroscopy (MAX-DOAS)." In: *Atmos. Chem. Phys.* 4. DOI: https://doi.org/10.5194/acp-4-231-2004 (cit. on p. 57).

Hönninger, G., N. Bobrowski, E. Palenque, R. Torrez, and U. Platt (2004a). "Reactive bromine and sulfur emissions at Salar de Uyuni, Bolivia." In: *Geophysical Research Letters* 31.4, p. L04101. DOI: 10.1029/2003gl018818 (cit. on p. 51).

Hönninger, G., H. Leser, O. Sebastián, and U. Platt (2004b). "Ground-based measurements of halogen oxides at the Hudson Bay by active longpath DOAS and passive MAX-DOAS." In: *Geophysical Research Letters* 31.4, p. L04111. DOI: 10.1029/2003gl018982 (cit. on p. 51).

Hönninger, Gerd (2002). "Halogen Oxide Studies in the Boundary Layer by Multi Axis Differential Optical Absorption Spectroscopy and Active Longpath-DOAS." PhD thesis. Combined Faculties for the Natural Sciences and for Mathematics of the Ruperto Carola University of Heidelberg, Germany (cit. on p. 55).

Horbanski, M., D. Pöhler, J. Lampel, and U. Platt (2019). "The ICAD (iterative cavity-enhanced DOAS) method." In: *Atmospheric Measurement Techniques* 12.6, pp. 3365–3381. DOI: 10.5194/amt-12-3365-2019. URL: https://amt.copernicus.org/articles/12/3365/2019/ (cit. on p. 164).

Hoshyaripour, Ali (Apr. 3, 2021). *February 2021: A dusty month for Europe*. English. Ed. by Athanasios Nenes and Mengze Li. Atmospheric Sciences (AS) Division of the Euro-

pean Geosciences Union (EGU). URL: https://blogs.egu.eu/divisions/as/2021/
04/03/february-2021-a-dusty-month-for-europe/ (visited on 10/04/2022) (cit. on
p. 163).

Hosseinpour, Saman and Johnson Magnus (2017). "Vibrational Spectroscopy in Studies of
Atmospheric Corrosion." In: *Materials(Basel)*. DOI: 10.3390/ma10040413 (cit. on p. 25).

ICOS and RI (2020). "ICOS Atmosphere Station Specifications V2.0 (editor: O. Laurent)."
In: DOI: 10.18160/GK28-2188 (cit. on p. 171).

IPCC (2021). "Summary for Policymakers." In: *Climate Change 2021: The Physical Science
Basis. Contribution of Working Group I to the Sixth Assessment Report of the Intergovern-
mental Panel on Climate Change*. Ed. by V. Masson-Delmotte, P. Zhai, A. Pirani, S.L.
Connors, C. Pean, S. Berger, N. Caud, Y. Chen, L. Goldfarb, M.I. Gomis, M. Huang,
K. Leitzell, E. Lonnoy, J.B.R. Matthews, T.K. Maycock, T. Waterfield, O. Yelekci, R.
Yu, and B. Zhou. Cambridge, United Kingdom and New York, NY, USA: Cambridge
University Press, pp. 3–32. DOI: 10.1017/9781009157896.001 (cit. on pp. iv, 1).

Inness, A., M. Ades, A. Agustí-Panareda, J. Barré, A. Benedictow, A.-M. Blechschmidt,
J. J. Dominguez, R. Engelen, H. Eskes, J. Flemming, V. Huijnen, L. Jones, Z. Kipling,
S. Massart, M. Parrington, V.-H. Peuch, M. Razinger, S. Remy, M. Schulz, and M.
Suttie (2019). "The CAMS reanalysis of atmospheric composition." In: *Atmospheric
Chemistry and Physics* 19.6, pp. 3515–3556. DOI: 10.5194/acp-19-3515-2019. URL:
https://acp.copernicus.org/articles/19/3515/2019/ (cit. on pp. 139, 184).

Ionov, D. V., M. V. Makarova, F. Hase, S. C. Foka, V. S. Kostsov, C. Alberti, T. Blumenstock,
T. Warneke, and Y. A. Virolainen (2021). "The CO_2 integral emission by the megacity
of St Petersburg as quantified from ground-based FTIR measurements combined with
dispersion modelling." In: *Atmospheric Chemistry and Physics* 21.14, pp. 10939–10963.
DOI: 10.5194/acp-21-10939-2021. URL: https://acp.copernicus.org/articles/21/
10939/2021/ (cit. on pp. 134, 135).

Irie, H., H. Takashima, Y. Kanaya, K. F. Boersma, L. Gast, F. Wittrock, D. Brunner, Y.
Zhou, and M. Van Roozendael (2011). "Eight-component retrievals from ground-
based MAX-DOAS observations." In: *Atmos. Meas. Tech.* 4.6, pp. 1027–1044. DOI: 10.
5194/amt-4-1027-2011. URL: https://www.atmos-meas-tech.net/4/1027/2011/
(cit. on p. 79).

Jacob, Daniel J. (1999). *Introduction to atmospheric chemistry*. Princeton, N.J: Princeton Uni-
versity Press. ISBN: 9780691001852 (cit. on p. 130).

Jäschke, Cornelia, Carlos Alberti, Samuel Hammer, Frank Hase, and Claudius Rosendahl
(Jan. 29, 2021). *Observation-based system formonitoring and verification of greenhouse gases.
Temporal variations of proxy/ffCO2 ratios*. Tech. rep. University of Heidelberg and Karl-
sruhe Institute of Technology. 69 pp. (cit. on pp. vi, 167).

Johnston, P. V. (1996). "Studies on the I_0 effect" (cit. on p. 56).

Jones, T. S., J. E. Franklin, J. Chen, F. Dietrich, K. D. Hajny, J. C. Paetzold, A. Wenzel, C.
Gately, E. Gottlieb, H. Parker, M. Dubey, F. Hase, P. B. Shepson, L. H. Mielke, and
S. C. Wofsy (2021). "Assessing urban methane emissions using column-observing
portable Fourier transform infrared (FTIR) spectrometers and a novel Bayesian inver-
sion framework." In: *Atmospheric Chemistry and Physics* 21.17, pp. 13131–13147. DOI:
10.5194/acp-21-13131-2021. URL: https://acp.copernicus.org/articles/21/
13131/2021/ (cit. on p. 2).

Kasischke, Eric S. and Lori P. Bruhwiler (2002). "Emissions of carbon dioxide, carbon monoxide, and methane from boreal forest fires in 1998." In: *Journal of Geophysical Research: Atmospheres* 107.D1. DOI: https://doi.org/10.1029/2001JD000461. eprint: https://agupubs.onlinelibrary.wiley.com/doi/pdf/10.1029/2001JD000461. URL: https://agupubs.onlinelibrary.wiley.com/doi/abs/10.1029/2001JD000461 (cit. on p. 142).

Kauppinen, Jyrki and Pekka Saarinen (Jan. 1992). "Line-shape distortions in misaligned cube corner interferometers." en. In: *Applied Optics* 31.1, p. 69. DOI: 10.1364/AO.31.000069. URL: https://opg.optica.org/abstract.cfm?URI=ao-31-1-69 (cit. on p. 109).

Keppel-Aleks, G., P. O. Wennberg, and T. Schneider (2011). "Sources of variations in total column carbon dioxide." In: *Atmospheric Chemistry and Physics* 11.8, pp. 3581–3593. DOI: 10.5194/acp-11-3581-2011. URL: https://acp.copernicus.org/articles/11/3581/2011/ (cit. on p. 147).

Kiel, M., C. W. O'Dell, B. Fisher, A. Eldering, R. Nassar, C. G. MacDonald, and P. O. Wennberg (2019). "How bias correction goes wrong: measurement of X_{CO_2} affected by erroneous surface pressure estimates." In: *Atmospheric Measurement Techniques* 12.4, pp. 2241–2259. DOI: 10.5194/amt-12-2241-2019. URL: https://amt.copernicus.org/articles/12/2241/2019/ (cit. on p. 139).

Kiel, Matthäus (2016). "Trace gas measurements from different spectral regions using FTIR spectroscopy." English. 12.03.01; LK 01. PhD thesis. Karlsruher Institut für Technologie (KIT). 151 pp. DOI: 10.5445/IR/1000056859 (cit. on p. 92).

Kille, Natalie, Randall Chiu, Matthias Frey, Frank Hase, Mahesh K. Sha, Thomas Blumenstock, James W. Hannigan, Johannes Orphal, Daniel Bon, and Rainer Volkamer (2019). "Separation of Methane Emissions From Agricultural and Natural Gas Sources in the Colorado Front Range." In: *Geophysical Research Letters* 46.7, pp. 3990–3998. DOI: https://doi.org/10.1029/2019GL082132. eprint: https://agupubs.onlinelibrary.wiley.com/doi/pdf/10.1029/2019GL082132. URL: https://agupubs.onlinelibrary.wiley.com/doi/abs/10.1029/2019GL082132 (cit. on p. 2).

Kohler, Martin, Jutta Metzger, and Norbert Kalthoff (2018). "Trends in temperature and wind speed from 40 years of observations at a 200 m high meteorological tower in Southwest Germany." In: *International Journal of Climatology* 38.1, pp. 23–34. DOI: https://doi.org/10.1002/joc.5157. eprint: https://rmets.onlinelibrary.wiley.com/doi/pdf/10.1002/joc.5157. URL: https://rmets.onlinelibrary.wiley.com/doi/abs/10.1002/joc.5157 (cit. on p. 98).

Kraus, S. (2006). "DOASIS, A Framework Design for DOAS." PhD thesis. Technische Informatik, Univ. Mannheim. URL: http://d-nb.info/981351662 (cit. on pp. 66, 191).

Kuenen, J., S. Dellaert, A. Visschedijk, J.-P. Jalkanen, I. Super, and H. Denier van der Gon (2022). "CAMS-REG-v4: a state-of-the-art high-resolution European emission inventory for air quality modelling." In: *Earth System Science Data* 14.2, pp. 491–515. DOI: 10.5194/essd-14-491-2022. URL: https://essd.copernicus.org/articles/14/491/2022/ (cit. on p. 159).

Kurucz, R. (Mar. 1992). "Synthetic infrared spectra." In: *Proceedings of the 154th Symposium of the International Astronomical Union (IAU).* Ed. by D.M. Rabin and J.T. Jefferies. Tucson, Arizona: Kluwer, Acad.Norwell, MA. (cit. on p. 23).

Kuze, Akihiko, Hiroshi Suto, Masakatsu Nakajima, and Takashi Hamazaki (Dec. 2009). "Thermal and near infrared sensor for carbon observation Fourier-transform spectrometer on the Greenhouse Gases Observing Satellite for greenhouse gases monitoring." In: *Appl. Opt.* 48.35, pp. 6716–6733. DOI: 10.1364/AO.48.006716. URL: http://opg.optica.org/ao/abstract.cfm?URI=ao-48-35-6716 (cit. on pp. 2, 139, 183).

Kylling, A., K. Stamnes, and S. C. Tsay (June 1995). "A reliable and efficient two-stream algorithm for spherical radiative transfer: Documentation of accuracy in realistic layered media." In: *Journal of Atmospheric Chemistry* 21.2, pp. 115–150. DOI: 10.1007/bf00696577 (cit. on p. 72).

Lampel, Johannes (2014). "Measurements of reactive trace gases in the marine boundary layer using novel DOAS methods." PhD thesis. Combined Faculties for the Natural Sciences and for Mathematics of the Ruperto-Carola University of Heidelberg, Germany (cit. on p. 81).

Landgraf, J., J. aan de Brugh, R. Scheepmaker, T. Borsdorff, H. Hu, S. Houweling, A. Butz, I. Aben, and O. Hasekamp (2016). "Carbon monoxide total column retrievals from TROPOMI shortwave infrared measurements." In: *Atmospheric Measurement Techniques* 9.10, pp. 4955–4975. DOI: 10.5194/amt-9-4955-2016. URL: https://amt.copernicus.org/articles/9/4955/2016/ (cit. on pp. 139, 182).

Langerock, B., M. De Mazière, F. Hendrick, C. Vigouroux, F. Desmet, B. Dils, and S. Niemeijer (2015). "Description of algorithms for co-locating and comparing gridded model data with remote-sensing observations." In: *Geoscientific Model Development* 8.3, pp. 911–921. DOI: 10.5194/gmd-8-911-2015. URL: https://gmd.copernicus.org/articles/8/911/2015/ (cit. on p. 144).

Leser, H., G. Hönninger, and U. Platt (May 15, 2003). "MAX-DOAS measurements of BrO and NO_2 in the marine boundary layer." In: *Geophysical Research Letters* 30.10. DOI: 10.1029/2002gl015811 (cit. on p. 51).

Levenberg, Kenneth (1944). "A method for the solution of certain non-linear problems in least squares." en. In: *Quarterly of Applied Mathematics* 2.2, pp. 164–168. DOI: 10.1090/qam/10666. URL: https://www.ams.org/qam/1944-02-02/S0033-569X-1944-10666-0/ (cit. on pp. 55, 70).

Levin, I., U. Karstens, M. Eritt, F. Maier, S. Arnold, D. Rzesanke, S. Hammer, M. Ramonet, G. Vítková, S. Conil, M. Heliasz, D. Kubistin, and M. Lindauer (2020). "A dedicated flask sampling strategy developed for Integrated Carbon Observation System (ICOS) stations based on CO_2 and CO measurements and Stochastic Time-Inverted Lagrangian Transport (STILT) footprint modelling." In: *Atmospheric Chemistry and Physics* 20.18, pp. 11161–11180. DOI: 10.5194/acp-20-11161-2020. URL: https://acp.copernicus.org/articles/20/11161/2020/ (cit. on p. 172).

Liu, Yi, Jing Wang, Lu Yao, Xi Chen, Zhaonan Cai, Dongxu Yang, Zengshan Yin, Songyan Gu, Longfei Tian, Naimeng Lu, and Daren Lyu (2018). "The TanSat mission: preliminary global observations." In: *Science Bulletin* 63.18, pp. 1200–1207. ISSN: 2095-9273. DOI: https://doi.org/10.1016/j.scib.2018.08.004. URL: https://www.sciencedirect.com/science/article/pii/S2095927318303797 (cit. on p. 2).

Lorente, A., T. Borsdorff, A. Butz, O. Hasekamp, J. aan de Brugh, A. Schneider, L. Wu, F. Hase, R. Kivi, D. Wunch, D. F. Pollard, K. Shiomi, N. M. Deutscher, V. A. Velazco, C. M. Roehl, P. O. Wennberg, T. Warneke, and J. Landgraf (2021). "Methane retrieved

from TROPOMI: improvement of the data product and validation of the first 2 years of measurements." In: *Atmospheric Measurement Techniques* 14.1, pp. 665–684. DOI: 10.5194/amt-14-665-2021. URL: https://amt.copernicus.org/articles/14/665/2021/ (cit. on pp. 139, 142, 182).

Luther, A., R. Kleinschek, L. Scheidweiler, S. Defratyka, M. Stanisavljevic, A. Forstmaier, A. Dandocsi, S. Wolff, D. Dubravica, N. Wildmann, J. Kostinek, P. Jöckel, A.-L. Nickl, T. Klausner, F. Hase, M. Frey, J. Chen, F. Dietrich, J. Neecki, J. Swolkień, A. Fix, A. Roiger, and A. Butz (2019). "Quantifying CH₄ emissions from hard coal mines using mobile sun-viewing Fourier transform spectrometry." In: *Atmospheric Measurement Techniques* 12.10, pp. 5217–5230. DOI: 10.5194/amt-12-5217-2019. URL: https://amt.copernicus.org/articles/12/5217/2019/ (cit. on p. 2).

Macdonald, S., H. Oetjen, A. Mahajan, L. Whalley, P. Edwards, D. Heard, C. Jones, and J. Plane (July 12, 2012). "DOAS measurements of formaldehyde and glyoxal above a south-east Asian tropical rainforest." In: *Atmospheric Chemistry and Physics* 12.13, pp. 5949–5962. DOI: 10.5194/acp-12-5949-2012 (cit. on p. 51).

Makarova, M. V., C. Alberti, D. V. Ionov, F. Hase, S. C. Foka, T. Blumenstock, T. Warneke, Y. A. Virolainen, V. S. Kostsov, M. Frey, A. V. Poberovskii, Y. M. Timofeyev, N. N. Paramonova, K. A. Volkova, N. A. Zaitsev, E. Y. Biryukov, S. I. Osipov, B. K. Makarov, A. V. Polyakov, V. M. Ivakhov, H. Kh. Imhasin, and E. F. Mikhailov (2021). "Emission Monitoring Mobile Experiment (EMME): an overview and first results of the St. Petersburg megacity campaign 2019." In: *Atmospheric Measurement Techniques* 14.2, pp. 1047–1073. DOI: 10.5194/amt-14-1047-2021. URL: https://amt.copernicus.org/articles/14/1047/2021/ (cit. on pp. 2, 3, 124, 125, 132–135, 178).

Makarova, M. V., O. Kirner, Yu. M. Timofeev, A. V. Poberovskii, Kh. Kh. Imkhasin, S. I. Osipov, and B. K. Makarov (Mar. 2015a). "Analysis of methane total column variations in the atmosphere near St. Petersburg using ground-based measurements and simulations." en. In: *Izvestiya, Atmospheric and Oceanic Physics* 51.2, pp. 177–185. DOI: 10.1134/S0001433815010089. URL: http://link.springer.com/10.1134/S0001433815010089 (cit. on p. 140).

— (July 2015b). "Annual cycle and long-term trend of the methane total column in the atmosphere over the St. Petersburg region." en. In: *Izvestiya, Atmospheric and Oceanic Physics* 51.4, pp. 431–438. DOI: 10.1134/S0001433815040088. URL: http://link.springer.com/10.1134/S0001433815040088 (cit. on p. 140).

Marquardt, Donald W. (1963). "An Algorithm for Least-Squares Estimation of Nonlinear Parameters." In: *Journal of the Society for Industrial and Applied Mathematics* 11.2, pp. 431–441. DOI: 10.1137/0111030. eprint: https://doi.org/10.1137/0111030. URL: https://doi.org/10.1137/0111030 (cit. on pp. 55, 70).

Mayer, B. and A. Kylling (2005). "Technical note: The libRadtran software package for radiative transfer calculations - description and examples of use." In: *Atmospheric Chemistry and Physics* 5.7, pp. 1855–1877. DOI: 10.5194/acp-5-1855-2005. URL: https://www.atmos-chem-phys.net/5/1855/2005/ (cit. on pp. 11, 22–24).

Meetham, A. R., D. W. Bottom, and S. Cayton (Jan. 21, 2016). *Atmospheric Pollution*. Elsevier Science and Techn. 244 pp. ISBN: 9781483135847. URL: https://www.ebook.de/de/product/23285324/a_r_meetham_d_w_bottom_s_cayton_atmospheric_pollution.html (cit. on p. 1).

Meirink, J. F., P. Bergamaschi, and M. C. Krol (2008). "Four-dimensional variational data assimilation for inverse modelling of atmospheric methane emissions: method and comparison with synthesis inversion." In: *Atmospheric Chemistry and Physics* 8.21, pp. 6341–6353. DOI: 10.5194/acp-8-6341-2008. URL: https://acp.copernicus.org/articles/8/6341/2008/ (cit. on p. 184).

Meller, Richard and Geert K. Moortgat (2000). "Temperature dependence of the absorption cross sections of formaldehyde between 223 and 323 K in the wavelength range 225-375 nm." In: *Journal of Geophysical Research: Atmospheres* 105.D6. DOI: 10.1029/1999JD901074. URL: https://agupubs.onlinelibrary.wiley.com/doi/abs/10.1029/1999JD901074 (cit. on p. 191).

Miller, Scot M., Steven C. Wofsy, Anna M. Michalak, Eric A. Kort, Arlyn E. Andrews, Sebastien C. Biraud, Edward J. Dlugokencky, Janusz Eluszkiewicz, Marc L. Fischer, Greet Janssens-Maenhout, Ben R. Miller, John B. Miller, Stephen A. Montzka, Thomas Nehrkorn, and Colm. Sweeney (2013). "Anthropogenic Emissions of Methane in the United States." In: *Proceedings of the National Academy of Sciences of the United States of America* 110.50, pp. 20018–20022. DOI: 10.1073/pnas.1314392110. URL: http://www.pnas.org/content/110/50/20018 (cit. on p. 1).

Molina, Maria O., Claudia Gutierrez, and Enrique Sanchez (2021). "Comparison of ERA5 surface wind speed climatologies over Europe with observations from the HadISD dataset." In: *International Journal of Climatology* 41.10, pp. 4864–4878. DOI: https://doi.org/10.1002/joc.7103. eprint: https://rmets.onlinelibrary.wiley.com/doi/pdf/10.1002/joc.7103. URL: https://rmets.onlinelibrary.wiley.com/doi/abs/10.1002/joc.7103 (cit. on p. 178).

Morino, I., O. Uchino, M. Inoue, Y. Yoshida, T. Yokota, P. O. Wennberg, G. C. Toon, D. Wunch, C. M. Roehl, J. Notholt, T. Warneke, J. Messerschmidt, D. W. T. Griffith, N. M. Deutscher, V. Sherlock, B. Connor, J. Robinson, R. Sussmann, and M. Rettinger (2011). "Preliminary validation of column-averaged volume mixing ratios of carbon dioxide and methane retrieved from GOSAT short-wavelength infrared spectra." In: *Atmospheric Measurement Techniques* 4.6, pp. 1061–1076. DOI: 10.5194/amt-4-1061-2011. URL: https://amt.copernicus.org/articles/4/1061/2011/ (cit. on p. 2).

NOAA (2021). *Increase in atmospheric methane set another record during 2021.* English. National Oceanic and Atmospheric Administration. URL: https://www.noaa.gov/news-release/increase\-in\-atmospheric\-methane\-set\-another\-record\-during\-2021 (cit. on p. 16).

Nikitenko, A. A., Yu. M. Timofeev, I. A. Berezin, A. V. Poberovskii, Ya. A. Virolainen, and A. V. Polyakov (Nov. 2020). "The Analysis of OCO-2 Satellite Measurements of CO_2 in the Vicinity of Russian Cities." In: *Atmospheric and Oceanic Optics* 33.6, pp. 650–655. DOI: 10.1134/S1024856020060111 (cit. on p. 140).

Osterman, G., C. O'Dell, A. Eldering, B. Fisher, D. Crisp, C. Cheng, C. Frankenberg, A. Lambert, M. Gunson, L. Mandrake, and D. Wunch (June 8, 2020). *Orbiting Carbon Observatory-2 and 3 (OCO-2 & OCO-3), Data Product User'sGuide, Operational Level 2 Data Versions 10 and Lite File Version 10 andVEarly.* English. Version 1.0. National Aeronautics andSpace Administration Jet Propulsion Laboratory California Institute of Technology. Pasadena, California. 93 pp. URL: https://docserver.gesdisc.eosdis.

`nasa.gov/public/project/OCO/OCO2_OCO3_B10_DUG.pdf` (visited on 09/09/2022) (cit. on pp. 139, 182).

Parker, Stewart F., Vijay Patel, Philip B. Tooke, and Kenneth P. J. Williams (1991). "The effect of apodization and finite resolution on Fourier transform Raman spectra." In: *Spectrochimica Acta Part A: Molecular Spectroscopy* 47.9, pp. 1171–1178. ISSN: 0584-8539. DOI: `https://doi.org/10.1016/0584-8539(91)80204-V`. URL: `https://www.sciencedirect.com/science/article/pii/058485399180204V` (cit. on p. 50).

Patra, Prabir K., David Crisp, Johannes W. Kaiser, Debra Wunch, Tazu Saeki, Kazuhito Ichii, Takashi Sekiya, Paul O. Wennberg, Dietrich G. Feist, David F. Pollard, David W. T. Griffith, Voltaire A. Velazco, M. De Maziere, Mahesh K. Sha, Coleen Roehl, Abhishek Chatterjee, and Kentaro Ishijima (Dec. 2017). "The Orbiting Carbon Observatory (OCO-2) tracks 2-3 peta-gram increase in carbon release to the atmosphere during the 2014-2016 El Nino." en. In: *Scientific Reports* 7.1, p. 13567. ISSN: 2045-2322. DOI: `10.1038/s41598-017-13459-0`. URL: `http://www.nature.com/articles/s41598-017-13459-0` (cit. on p. 144).

Perner, D., D. Ehhalt, H. Pätz, U. Platt, E. Röth, and A. Volz (Aug. 1976). "OH - Radicals in the lower troposphere." In: *Geophysical Research Letters* 3.8, pp. 466–468. DOI: `10.1029/gl003i008p00466` (cit. on p. 51).

Perner, D. and U. Platt (Dec. 1979). "Detection of nitrous acid in the atmosphere by differential optical absorption." In: *Geophysical Research Letters* 6.12, pp. 917–920. DOI: `10.1029/gl006i012p00917` (cit. on p. 51).

Peters, Enno (2013). "Improved MAX-DOAS measurements and retrievals focused on the marine boundary layer." PhD thesis. Institut für Umweltphysik, Fachbereich Physik und Elektrotechnik, Universität Bremen (cit. on p. 81).

Petty, Grant W. (2006). *A First Course in Atmospheric Radiation*. 2nd ed. Sundog Publishing (cit. on p. 19).

Platt, U., D. Perner, and H. Pätz (1980). "Simultaneous measurement of atmospheric CH2O, O3, and NO2by differential optical absorption." In: *Journal of Geophysical Research* 84.C10, p. 6329. DOI: `10.1029/jc084ic10p06329` (cit. on p. 51).

Platt, Ulrich and Jochen Stutz (2008). *Differential Optical Absorption Spectroscopy Principles and Applications*. Springer-Verlag Berlin Heidelberg. DOI: `10.1007/978-3-540-75776-4` (cit. on pp. 24, 51, 52, 54, 55, 59, 61).

Pukite, J., S. Kühl, T. Deutschmann, U. Platt, and T. Wagner (2010). "Extending differential optical absorption spectroscopy for limb measurements in the UV." In: *Atmos. Meas. Tech.* 3.3, pp. 631–653 (cit. on p. 66).

Reuter, M., M. Buchwitz, M. Hilker, J. Heymann, O. Schneising, D. Pillai, H. Bovensmann, J. P. Burrows, H. Bösch, R. Parker, A. Butz, O. Hasekamp, C. W. O'Dell, Y. Yoshida, C. Gerbig, T. Nehrkorn, N. M. Deutscher, T. Warneke, J. Notholt, F. Hase, R. Kivi, R. Sussmann, T. Machida, H. Matsueda, and Y. Sawa (2014). "Satellite-inferred European carbon sink larger than expected." In: *Atmospheric Chemistry and Physics* 14.24, pp. 13739–13753. DOI: `10.5194/acp-14-13739-2014`. URL: `https://acp.copernicus.org/articles/14/13739/2014/` (cit. on p. 3).

Reuter, Maximilian and Michael Buchwitz (Jan. 26, 2021). *Product User Guide Version 3 (PUGv3) for theFOCAL XCO₂ OCO-2 Data Product CO2_OC2_FOCA (v09) for the Essential Climate Variable (ECV) Greenhouse Gases (GHG)*. Version 3. 17 pp. URL: `https:`

//www.iup.uni-bremen.de/carbon_ghg/docs/GHG-CCIplus/CRDP6/PUGv3_GHG-CCI_CO2_OC2_FOCA_v09_20210126.pdf (visited on 09/09/2022) (cit. on pp. 139, 183).

Reuter, Maximilian, Michael Buchwitz, Oliver Schneising, Stefan Noël, Heinrich Bovensmann, and John P. Burrows (2017a). "A Fast Atmospheric Trace Gas Retrieval for Hyperspectral Instruments Approximating Multiple Scattering-Part 2: Application to XCO2 Retrievals from OCO-2." In: *Remote Sensing* 9.11. ISSN: 2072-4292. DOI: 10.3390/rs9111102. URL: https://www.mdpi.com/2072-4292/9/11/1102 (cit. on pp. 139, 182).

Reuter, Maximilian, Michael Buchwitz, Oliver Schneising, Stefan Noël, Vladimir Rozanov, Heinrich Bovensmann, and John P. Burrows (2017b). "A Fast Atmospheric Trace Gas Retrieval for Hyperspectral Instruments Approximating Multiple Scattering-Part 1: Radiative Transfer and a Potential OCO-2 XCO2 Retrieval Setup." In: *Remote Sensing* 9.11. ISSN: 2072-4292. DOI: 10.3390/rs9111159. URL: https://www.mdpi.com/2072-4292/9/11/1159 (cit. on p. 139).

Rodgers, C. D. (1976). "Retrieval of atmospheric temperature and composition from remote measurements of thermal radiation." In: *Reviews of Geophysics* 14.4, pp. 609–624. DOI: https://doi.org/10.1029/RG014i004p00609. eprint: https://agupubs.onlinelibrary.wiley.com/doi/pdf/10.1029/RG014i004p00609. URL: https://agupubs.onlinelibrary.wiley.com/doi/abs/10.1029/RG014i004p00609 (cit. on p. 69).

Rodgers, Clive D. (2000). *Inverse Methods for Atmospheric Sounding: Theory and practice.* Vol. 2. Series on Atmospheric, Ocean and Planetary Physics. World Scientific Publishing Co. Pte. Ltd. (cit. on pp. 69, 71, 80, 81).

Rodgers, Clive D. and Brian J. Connor (2003). "Intercomparison of remote sounding instruments." In: *Journal of Geophysical Research: Atmospheres* 108.D3. DOI: https://doi.org/10.1029/2002JD002299. eprint: https://agupubs.onlinelibrary.wiley.com/doi/pdf/10.1029/2002JD002299. URL: https://agupubs.onlinelibrary.wiley.com/doi/abs/10.1029/2002JD002299 (cit. on p. 142).

Rosa Eugene, A. and Dietz. Thomas (2012). "Human Drivers of National Greenhouse-Gas Emissions." In: *Natural Climate Change* 2.8, pp. 581–582 (cit. on p. 13).

Rosendahl, Claudius Leander (July 12, 2022). "Proxy to fossil-fuel CO2 emission ratios:in-situ versus inventory data." PhD thesis. Combined Faculty of Mathematics, Engineering and Natural Sciences of Heidelberg University. DOI: 10.11588/heidok.00031909. URL: http://www.ub.uni-heidelberg.de/archiv/31909 (cit. on p. 167).

Rothman, L. S., I. E. Gordon, Y. Babikov, A. Barbe, D. Chris Benner, P. F. Bernath, M. Birk, L. Bizzocchi, V. Boudon, L. R. Brown, A. Campargue, K. Chance, E. A. Cohen, L. H. Coudert, V. M. Devi, B. J. Drouin, A. Fayt, J. M. Flaud, R. R. Gamache, J. J. Harrison, J. M. Hartmann, C. Hill, J. T. Hodges, D. Jacquemart, A. Jolly, J. Lamouroux, R. J. Le Roy, G. Li, D. A. Long, O. M. Lyulin, C. J. Mackie, S. T. Massie, S. Mikhailenko, H. S. P. Müller, O. V. Naumenko, A. V. Nikitin, J. Orphal, V. Perevalov, A. Perrin, E. R. Polovtseva, C. Richard, M. A. H. Smith, E. Starikova, K. Sung, S. Tashkun, J. Tennyson, G. C. Toon, Vl. G. Tyuterev, and G. Wagner (2013). "The HITRAN2012 molecular spectroscopic database." In: *Journal of Quantitative Spectroscopy and Radiative Transfer* 130. HITRAN2012 special issue, pp. 4–50. ISSN: 0022-4073. URL: https://www.sciencedirect.com/science/article/pii/S0022407313002859 (cit. on p. 72).

Rothman, L. S., I. E. Gordon, R. J. Barber, H. Dothe, R. R. Gamache, A. Goldman, V. I. Perevalov, S. A. Tashkun, and J. Tennyson (2010). "HITEMP, the high-temperature molecular spectroscopic database." In: *Journal of Quantitative Spectroscopy and Radiative Transfer* 111.15. XVIth Symposium on High Resolution Molecular Spectroscopy (HighRus-2009) (cit. on p. 192).

Rozanov, V. V., A. V. Rozanov, A. A. Kokhanovsky, and J. P. Burrows (Jan. 2014). "Radiative transfer through terrestrial atmosphere and ocean: Software package SCIA-TRAN." en. In: *Journal of Quantitative Spectroscopy and Radiative Transfer* 133, pp. 13–71. DOI: 10.1016/j.jqsrt.2013.07.004. URL: https://linkinghub.elsevier.com/retrieve/pii/S0022407313002872 (cit. on p. 79).

Sanders, R., S. Solomon, M. Carroll, and A. Schmeltekopf (1988). "Visible and near-ultraviolet spectroscopy at McMurdo Station, Antarctica: 4. Overview and daily measurements of NO2, O3, and OClO during 1987." In: *Journal of Geophysical Research* 94.D9. Ed. by R. D. Bjokov and P. Fabian, p. 11381. DOI: 10.1029/jd094id09p11381 (cit. on p. 51).

Sansonetti, Craig J., Marc L. Salit, and Joseph Reader (Jan. 1996). "Wavelengths of spectral lines in mercury pencil lamps." In: *Appl. Opt.* 35.1, pp. 74–77. DOI: 10.1364/AO.35.000074. URL: http://opg.optica.org/ao/abstract.cfm?URI=ao-35-1-74 (cit. on p. 60).

Scheepmaker, R. A., J. aan de Brugh, H. Hu, T. Borsdorff, C. Frankenberg, C. Risi, O. Hasekamp, I. Aben, and J. Landgraf (2016). "*HDO* and *H₂O* total column retrievals from TROPOMI shortwave infrared measurements." In: *Atmospheric Measurement Techniques* 9.8, pp. 3921–3937. DOI: 10.5194/amt-9-3921-2016. URL: https://amt.copernicus.org/articles/9/3921/2016/ (cit. on p. 139).

Schneider, A., T. Borsdorff, J. aan de Brugh, F. Aemisegger, D. G. Feist, R. Kivi, F. Hase, M. Schneider, and J. Landgraf (2020). "First data set of H2O/HDO columns from the Tropospheric Monitoring Instrument (TROPOMI)." In: *Atmospheric Measurement Techniques* 13.1, pp. 85–100. DOI: 10.5194/amt-13-85-2020. URL: https://amt.copernicus.org/articles/13/85/2020/ (cit. on p. 182).

Schneider, A., T. Borsdorff, J. aan de Brugh, A. Lorente, F. Aemisegger, D. Noone, D. Henze, R. Kivi, and J. Landgraf (2022a). "Retrieving H₂O/HDO columns over cloudy and clear-sky scenes from the Tropospheric Monitoring Instrument (TROPOMI)." In: *Atmospheric Measurement Techniques* 15.7, pp. 2251–2275. DOI: 10.5194/amt-15-2251-2022. URL: https://amt.copernicus.org/articles/15/2251/2022/ (cit. on p. 139).

Schneider, M., B. Ertl, C. J. Diekmann, F. Khosrawi, A. Weber, F. Hase, M. Höpfner, O. E. García, E. Sepúlveda, and D. Kinnison (2022b). "Design and description of the MUSICA IASI full retrieval product." In: *Earth System Science Data* 14.2, pp. 709–742. DOI: 10.5194/essd-14-709-2022. URL: https://essd.copernicus.org/articles/14/709/2022/ (cit. on pp. 139, 183).

Schneider, M. and F. Hase (2009). "Ground-based FTIR water vapour profile analyses." In: *Atmospheric Measurement Techniques* 2.2, pp. 609–619. DOI: 10.5194/amt-2-609-2009. URL: https://amt.copernicus.org/articles/2/609/2009/ (cit. on p. 183).

— (2011). "Optimal estimation of tropospheric H2O and delta D with IASI/METOP." In: *Atmospheric Chemistry and Physics* 11.21, pp. 11207–11220. DOI: 10.5194/acp-11-11207-2011. URL: https://acp.copernicus.org/articles/11/11207/2011/ (cit. on p. 183).

Schneising, O., M. Buchwitz, M. Reuter, H. Bovensmann, J. P. Burrows, T. Borsdorff, N. M. Deutscher, D. G. Feist, D. W. T. Griffith, F. Hase, C. Hermans, L. T. Iraci, R. Kivi, J. Landgraf, I. Morino, J. Notholt, C. Petri, D. F. Pollard, S. Roche, K. Shiomi, K. Strong, R. Sussmann, V. A. Velazco, T. Warneke, and D. Wunch (2019). "A scientific algorithm to simultaneously retrieve carbon monoxide and methane from TROPOMI onboard Sentinel-5 Precursor." In: *Atmospheric Measurement Techniques* 12.12, pp. 6771–6802. DOI: 10.5194/amt-12-6771-2019. URL: https://amt.copernicus.org/articles/12/6771/2019/ (cit. on p. 182).

Segers, Arjo (Jan. 24, 2020a). *Description of the CH4 Inversion Production Chain*. ECMWF COPERNICUS REPORT. European Centre for Medium Range Weather Forecasts(ECMWF). 32 pp. URL: https://atmosphere.copernicus.eu/sites/default/files/2020-01/CAMS73_2018SC1_D73.5.2.2-2019_202001_production_chain_v1.pdf (visited on 09/09/2022) (cit. on pp. 139, 147, 184).

— (Dec. 28, 2020b). *Validation of the CH4 surface flux inversion – reanalysis 1990–2019*. ECMWF COPERNICUS REPORT. European Centre for Medium-Range Weather Forecasts(ECMWF). 45 pp. URL: https://atmosphere.copernicus.eu/sites/default/files/2021-02/CAMS73_2018SC2_D73.2.4.1-2020_202012_validation_CH4_1990-2019_v2.pdf (visited on 09/09/2022) (cit. on pp. 139, 184).

Seinfeld, John H. and Spyros N. Pandis (2016). *Atmospheric Chemistry and Physics: From Air Pollution to Climate Change*. John Wiley & Sons (cit. on p. 1).

Semenov, A. O., Ya. A. Virolainen, Yu. M. Timofeyev, and A. V. Poberovskii (Mar. 2015). "Comparison of ground-based FTIR and radio sounding measurements of water vapor total content." en. In: *Atmospheric and Oceanic Optics* 28.2, pp. 121–125. DOI: 10.1134/S1024856015020116. URL: http://link.springer.com/10.1134/S1024856015020116 (cit. on p. 141).

Serdyuchenko, A., V. Gorshelev, M. Weber, W. Chehade, and J. P. Burrows (2014). "High spectral resolution ozone absorption cross-sections - Part 2: Temperature dependence." In: *Atmospheric Measurement Techniques* 7.2, pp. 625–636. DOI: 10.5194/amt-7-625-2014. URL: https://www.atmos-meas-tech.net/7/625/2014/ (cit. on pp. 191, 192).

Serebritsky, I. A. (July 11, 2017). *The Report on Environmental Conditions in St. Petersburg for 2017*. Tech. rep. (In Russian). URL: https://www.gov.spb.ru/static/writable/ckeditor/uploads/2018/06/29/Doklad_EKOLOGIA2018.pdf (visited on 09/16/2022) (cit. on p. 134).

— (Sept. 2, 2018). *The Report on Environmental Conditions in St. Petersburg for 2018*. Tech. rep. (In Russian). URL: https://www.gov.spb.ru/static/writable/ckeditor/uploads/2019/08/12/42/doklad_za_2018_EKOLOGIA2019.pdf (cit. on p. 134).

Setchell, Helen (Feb. 2020). *ECMWF Reanalysis v5*. en. Text. URL: https://www.ecmwf.int/en/forecasts/dataset/ecmwf-reanalysis-v5 (cit. on p. 132).

Sha, M. K., B. Langerock, J.-F. L. Blavier, T. Blumenstock, T. Borsdorff, M. Buschmann, A. Dehn, M. De Mazière, N. M. Deutscher, D. G. Feist, O. E. García, D. W. T. Griffith, M. Grutter, J. W. Hannigan, F. Hase, P. Heikkinen, C. Hermans, L. T. Iraci, P. Jeseck, N. Jones, R. Kivi, N. Kumps, J. Landgraf, A. Lorente, E. Mahieu, M. V. Makarova, J. Mellqvist, J.-M. Metzger, I. Morino, T. Nagahama, J. Notholt, H. Ohyama, I. Ortega, M. Palm, C. Petri, D. F. Pollard, M. Rettinger, J. Robinson, S. Roche, C. M. Roehl, A. N. Röhling, C. Rousogenous, M. Schneider, K. Shiomi, D. Smale, W. Stremme, K.

Strong, R. Sussmann, Y. Té, O. Uchino, V. A. Velazco, C. Vigouroux, M. Vrekoussis, P. Wang, T. Warneke, T. Wizenberg, D. Wunch, S. Yamanouchi, Y. Yang, and M. Zhou (2021). "Validation of methane and carbon monoxide from Sentinel-5 Precursor using TCCON and NDACC-IRWG stations." In: *Atmospheric Measurement Techniques* 14.9, pp. 6249–6304. DOI: 10.5194/amt-14-6249-2021. URL: https://amt.copernicus.org/articles/14/6249/2021/ (cit. on pp. 2, 142).

Shaiganfar, Reza (2012). "Estimation of NOx Emissions from megacities using mobile MAX-DOAS and satellite observations." PhD thesis. Faculties of Natural Sciences and for Mathematics of the Ruperto-Carola University of Heidelberg, Germany (cit. on p. 62).

Sportisse, Bruno (2010). *Fundamentals in Air Pollution: From Processes to Modelling*. Springer Netherlands. DOI: 10.1007/978-90-481-2970-6 (cit. on pp. 20, 22).

Stull, Roland B. (1988). *An Introduction to Boundary Layer Meteorology*. Dordrecht: Springer Netherlands. ISBN: 9789027727695. DOI: 10.1007/978-94-009-3027-8. URL: http://link.springer.com/10.1007/978-94-009-3027-8 (cit. on p. 132).

Stutz, J., J. Thomas, S. Hurlock, M. Schneider, R. Von Glasow, M. Piot, K. Gorham, J. Burkhart, L. Ziemba, J. Dibb, and B. Lefer (Sept. 27, 2011). "Longpath DOAS observations of surface BrO at Summit, Greenland." In: *Atmospheric Chemistry and Physics* 11.18, pp. 9899–9910. DOI: 10.5194/acp-11-9899-2011 (cit. on p. 51).

Stutz, Jochen and Ulrich Platt (1996). "Numerical analysis and estimation of the statistical error of differential optical absorption spectroscopy measurements with least-squares methods." In: *Appl Opt.* (cit. on p. 54).

Suto, H., F. Kataoka, N. Kikuchi, R. O. Knuteson, A. Butz, M. Haun, H. Buijs, K. Shiomi, H. Imai, and A. Kuze (2021). "Thermal and near-infrared sensor for carbon observation Fourier transform spectrometer-2 (TANSO-FTS-2) on the Greenhouse gases Observing SATellite-2 (GOSAT-2) during its first year in orbit." In: *Atmospheric Measurement Techniques* 14.3, pp. 2013–2039. DOI: 10.5194/amt-14-2013-2021. URL: https://amt.copernicus.org/articles/14/2013/2021/ (cit. on p. 2).

Thalman, R. and R. Volkamer (2013). "Temperature dependent absorption cross-sections of O2-O2 collision pairs between 340 and 630 nm and at atmospherically relevant pressure." In: *Physical Chemistry Chemical Physics* 15.37, pp. 15371–15381 (cit. on pp. 80, 191, 192).

Theys, N., M. Van Roozendael, F. Hendrick, C. Fayt, C. Hermans, J-L. Baray, F. Goutail, J-P. Pommereau, and M. De Mazi`ere (Sept. 18, 2007). "Retrieval of stratospheric and tropospheric BrO columns from multi-axis DOAS measurements at Reunion Island (21° S, 56°E)." In: *Atmospheric Chemistry and Physics* 7.18, pp. 4733–4749. DOI: 10.5194/acp-7-4733-2007 (cit. on p. 51).

Timofeyev, Yu. M., I. A. Berezin, Ya. A. Virolainen, M. V. Makarova, A. V. Polyakov, A. V. Poberovsky, N. N. Filippov, and S. Ch. Foka (Jan. 2019). "Spatial-Temporal CO2 Variations near St. Petersburg Based on Satellite and Ground-Based Measurements." en. In: *Izvestiya, Atmospheric and Oceanic Physics* 55.1, pp. 59–64. DOI: 10.1134/S0001433819010109. URL: http://link.springer.com/10.1134/S0001433819010109 (cit. on p. 140).

Timofeyev, Yu. M., G. M. Nerobelov, A. V. Poberovskii, and N. N. Filippov (May 2021). "Determining Both Tropospheric and Stratospheric CO2 Contents Using a Ground-

Based IR Spectroscopic Method." en. In: *Izvestiya, Atmospheric and Oceanic Physics* 57.3, pp. 286–296. DOI: 10.1134/S0001433821020110. URL: https://link.springer.com/10.1134/S0001433821020110 (cit. on p. 140).

Timofeyev, Yury, Yana Virolainen, Maria Makarova, Anatoly Poberovsky, Alexander Polyakov, Dmitry Ionov, Sergey Osipov, and Hamud Imhasin (2016). "Ground-based spectroscopic measurements of atmospheric gas composition near Saint Petersburg (Russia)." In: *Journal of Molecular Spectroscopy* 323. Atmospheric Spectroscopy, pp. 2–14. ISSN: 0022-2852. DOI: https://doi.org/10.1016/j.jms.2015.12.007. URL: https://www.sciencedirect.com/science/article/pii/S0022285215300254 (cit. on pp. 140, 141).

Toon, G. C., C. B. Farmer, P. W. Schaper, L. L. Lowes, and R. H. Norton (1992). "Composition measurements of the 1989 Arctic winter stratosphere by airborne infrared solar absorption spectroscopy." In: *Journal of Geophysical Research* 97.D8. Cited by: 75, pp. 7939–7961. DOI: 10.1029/91JD03114. URL: https://www.scopus.com/inward/record.uri?eid=2-s2.0-0026439831&doi=10.1029%2f91JD03114&partnerID=40&md5=5777bc56cd52bbee699a54a4e7fb6108 (cit. on p. 73).

Van Niel, C. B. (1949). "THE COMPARATIVE BIOCHEMISTRY OF PHOTOSYNTHESIS." In: *American Scientist* 37.3, pp. 371–383. ISSN: 00030996. URL: http://www.jstor.org/stable/27826281 (visited on 10/13/2022) (cit. on p. 7).

Vandaele, A. C. (1996). "Fourier transform measurement of NO2 absorption cross-section in the visible range at room temperature." In: *Journal of Atmospheric Chemistry* 25, pp. 289–305 (cit. on p. 53).

Vandaele, A. C., C. Hermans, P. C. Simon, M. Carleer, R. Colin, S. Fally, M. F. Mérienne, A. Jenouvrier, and B. Coquart (1998). "Measurements of the NO2 absorption cross-section from 42 000 cm^{-1} to 10 000 cm^{-1} (238 -1000 nm) at 220 K and 294 K." In: *Journal of Quantitative Spectroscopy and Radiative Transfer* 59.3, pp. 171–184. DOI: 10.1016/S0022-4073(97)00168-4. URL: http://www.sciencedirect.com/science/article/pii/S0022407397001684 (cit. on pp. 67, 191, 192).

Veefkind, J. P., I. Aben, K. McMullan, H. Förster, J. de Vries, G. Otter, J. Claas, H. J. Eskes, J. F. de Haan, Q. Kleipool, M. van Weele, O. Hasekamp, R. Hoogeveen, J. Landgraf, R. Snel, P. Tol, P. Ingmann, R. Voors, B. Kruizinga, R. Vink, H. Visser, and P. F. Levelt (2012). "TROPOMI on the ESA Sentinel-5 Precursor: A GMES mission for global observations of the atmospheric composition for climate, air quality and ozone layer applications." In: *Remote Sensing of Environment* 120. The Sentinel Missions - New Opportunities for Science, pp. 70–83. ISSN: 0034-4257. DOI: https://doi.org/10.1016/j.rse.2011.09.027. URL: https://www.sciencedirect.com/science/article/pii/S0034425712000661 (cit. on pp. 2, 105, 182).

Viatte, C., T. Lauvaux, J. K. Hedelius, H. Parker, J. Chen, T. Jones, J. E. Franklin, A. J. Deng, B. Gaudet, K. Verhulst, R. Duren, D. Wunch, C. Roehl, M. K. Dubey, S. Wofsy, and P. O. Wennberg (2017). "Methane emissions from dairies in the Los Angeles Basin." In: *Atmospheric Chemistry and Physics* 17.12, pp. 7509–7528. DOI: 10.5194/acp-17-7509-2017. URL: https://acp.copernicus.org/articles/17/7509/2017/ (cit. on p. 2).

Virolainen, Y. A., Y. M. Timofeyev, V. S. Kostsov, D. V. Ionov, V. V. Kalinnikov, M. V. Makarova, A. V. Poberovsky, N. A. Zaitsev, H. H. Imhasin, A. V. Polyakov, M. Schneider, F. Hase, S. Barthlott, and T. Blumenstock (2017). "Quality assessment of inte-

grated water vapour measurements at the St. Petersburg site, Russia: FTIR vs. MW and GPS techniques." In: *Atmospheric Measurement Techniques* 10.11, pp. 4521–4536. DOI: 10.5194/amt-10-4521-2017. URL: https://amt.copernicus.org/articles/10/4521/2017/ (cit. on p. 141).

Virolainen, Yana, Yury Timofeyev, Ivan Berezin, Anatoly Poberovsky, Alexander Polyakov, Nikita Zaitsev, and Hamud Imhasin (2016). "Atmospheric integrated water vapour measured by IR and MW techniques at the Peterhof site (Saint Petersburg, Russia)." In: *International Journal of Remote Sensing* 37.16, pp. 3771–3785. DOI: 10.1080/01431161.2016.1204025. eprint: https://doi.org/10.1080/01431161.2016.1204025. URL: https://doi.org/10.1080/01431161.2016.1204025 (cit. on p. 141).

Vlemmix, T., A. J. M. Piters, P. Stammes, P. Wang, and P. F. Levelt (2010). "Retrieval of tropospheric NO_2 using the MAX-DOAS method combined with relative intensity measurements for aerosol correction." In: *Atmos. Meas. Tech.* 3.5, pp. 1287–1305. DOI: 10.5194/amt-3-1287-2010. URL: https://www.atmos-meas-tech.net/3/1287/2010/ (cit. on p. 80).

Vogel, F. R., M. Frey, J. Staufer, F. Hase, G. Broquet, I. Xueref-Remy, F. Chevallier, P. Ciais, M. K. Sha, P. Chelin, P. Jeseck, C. Janssen, Y. Té, J. Groß, T. Blumenstock, Q. Tu, and J. Orphal (2019). "XCO_2 in an emission hot-spot region: the COCCON Paris campaign 2015." In: *Atmospheric Chemistry and Physics* 19.5, pp. 3271–3285. DOI: 10.5194/acp-19-3271-2019. URL: https://acp.copernicus.org/articles/19/3271/2019/ (cit. on p. 2).

Volkamer, Rainer, L. Molina, M. Molina, T. Shirley, and W. Brune (2005). "DOAS measurement of glyoxal as an indicator for fast VOC chemistry in urban air." In: *Geophysical Research Letters* 32.8, pp. L08–806. DOI: 10.1029/2005gl022616 (cit. on p. 51).

Wagner, T., A. Apituley, S. Beirle, S. Dörner, U. Friess, J. Remmers, and R. Shaiganfar (2014). "Cloud detection and classification based on MAX-DOAS observations." In: *Atmospheric Measurement Techniques* 7.5, pp. 1289–1320. DOI: 10.5194/amt-7-1289-2014. URL: https://www.atmos-meas-tech.net/7/1289/2014/ (cit. on p. 161).

Wagner, T., Kelly Chance, U. Friess, M. Gil, Florence Goutail, G. Hönninger, Paul Johnston, K. Karlsen-Tørnkvist, Ivan Kostadinov, H. Leser, Andrea Petritoli, A. Richter, Michel Van Roozendael, and Ulrich Platt (Jan. 2001). "Correction of the Ring effect and I0-effect for DOAS observations of scattered sunlight." In: (cit. on p. 56).

Wagner, T., T. Deutschmann, and U. Platt (2009). "Determination of aerosol properties from MAX-DOAS observations of the Ring effect." In: *Atmos. Meas. Tech.* (cit. on p. 84).

Wagner, T., B. Dix, C. v. Friedeburg, U. Friess, S. Sanghavi, R. Sinreich, and U. Platt (2004). "MAX-DOAS O_4 measurements: A new technique to derive information on atmospheric aerosol-Principles and information content." In: *Journal of Geophysical Research: Atmospheres* 109.D22. DOI: 10.1029/2004JD004904. URL: https://agupubs.onlinelibrary.wiley.com/doi/abs/10.1029/2004JD004904 (cit. on pp. 80, 81).

Wagner, Thomas, Steffen Dörner, Steffen Beirle, Sebastian Donner, and Stefan Kinne (Mar. 2021). "Quantitative comparison of measured and simulated O_4 absorptions for one day with extremely low aerosol load over the tropical Atlantic." en. In: *Atmospheric Measurement Techniques* 14.5, pp. 3871–3893. ISSN: 1867-8548. DOI: 10.5194/amt-14-3871-2021. URL: https://amt.copernicus.org/articles/14/3871/2021/ (cit. on p. 80).

Wallace, John M. and Peter V. Hobbs (2006). *Atmospheric Science: an introductory survey*. Vol. 92. International geophysics series. Amsterdam ; Boston: Elsevier Academic Press. (cit. on pp. 6, 7, 9, 10, 12, 17, 19).

Wiacek, A., J. R. Taylor, K. Strong, R. Saari, T. E. Kerzenmacher, N. B. Jones, and D. W. T. Griffith (Mar. 2007). "Ground-Based Solar Absorption FTIR Spectroscopy: Characterization of Retrievals and First Results from a Novel Optical Design Instrument at a New NDACC Complementary Station." en. In: *Journal of Atmospheric and Oceanic Technology* 24.3, pp. 432–448. DOI: 10.1175/JTECH1962.1. URL: http://journals.ametsoc.org/doi/10.1175/JTECH1962.1 (cit. on p. 69).

Wunch, Debra, Geoffrey C. Toon, Jean-François L. Blavier, Rebecca A. Washenfelder, Justus Notholt, Brian J. Connor, David W. T. Griffith, Vanessa Sherlock, and Paul O. Wennberg (2011). "The Total Carbon Column Observing Network." In: *Philosophical Transactions of the Royal Society A: Mathematical, Physical and Engineering Sciences* 369.1943, pp. 2087–2112. DOI: 10.1098/rsta.2010.0240. eprint: https://royalsocietypublishing.org/doi/pdf/10.1098/rsta.2010.0240. URL: https://royalsocietypublishing.org/doi/abs/10.1098/rsta.2010.0240 (cit. on pp. 2, 73).

Wunch, Debra, Geoffrey C. Toon, Vanessa Sherlock, Nicholas M. Deutscher, Cate Liu, Dietrich G. Feist, and Paul O. Wennberg (2015). "Documentation for the 2014 TCCON Data Release." en. In: DOI: 10.14291/TCCON.GGG2014.DOCUMENTATION.R0/1221662 (cit. on p. 115).

Yang, Y., M. Zhou, B. Langerock, M. K. Sha, C. Hermans, T. Wang, D. Ji, C. Vigouroux, N. Kumps, G. Wang, M. De Mazière, and P. Wang (2020). "New ground-based Fourier-transform near-infrared solar absorption measurements of XCO_2, XCH_4 and XCO at Xianghe, China." In: *Earth System Science Data* 12.3, pp. 1679–1696. DOI: 10.5194/essd-12-1679-2020. URL: https://essd.copernicus.org/articles/12/1679/2020/ (cit. on p. 142).

Yilmaz, Selami (2012). "Retrieval of Atmospheric Aerosol and Trace Gas Vertical Profiles using Multi-Axis Differential Optical Absorption Spectroscopy." PhD thesis. Faculties for the Natural Sciences and for Mathematics of the Ruperto-Carola University of Heidelberg, Germany (cit. on pp. 24, 25, 55, 56, 70, 79, 81, 82, 84, 85).

Yoshida, Y., N. Kikuchi, I. Morino, O. Uchino, S. Oshchepkov, A. Bril, T. Saeki, N. Schutgens, G. C. Toon, D. Wunch, C. M. Roehl, P. O. Wennberg, D. W. T. Griffith, N. M. Deutscher, T. Warneke, J. Notholt, J. Robinson, V. Sherlock, B. Connor, M. Rettinger, R. Sussmann, P. Ahonen, P. Heikkinen, E. Kyrö, J. Mendonca, K. Strong, F. Hase, S. Dohe, and T. Yokota (2013). "Improvement of the retrieval algorithm for GOSAT SWIR XCO_2 and XCH_4 and their validation using TCCON data." In: *Atmospheric Measurement Techniques* 6.6, pp. 1533–1547. DOI: 10.5194/amt-6-1533-2013. URL: https://amt.copernicus.org/articles/6/1533/2013/ (cit. on p. 2).

Zdunkowski, Wilford, Thomas Trautmann, and Andreas Bott (2007). *Radiation in the atmosphere: a course in theoretical meteorology*. English. Cambridge University Press. ISBN: 9780511275609. URL: https://doi.org/10.1017/CBO9780511535796 (cit. on pp. 37, 45).

Ångström, Anders (1930). "On the Atmospheric Transmission of Sun Radiation II." In: *Geografiska Annaler* 12, pp. 130–159. DOI: 10.2307/519561 (cit. on p. 25).